



U.S. Department of
Transportation

**Federal Railroad
Administration**

Passenger Car Crippling End-Load Test and Analyses

Office of Research,
Development
and Technology
Washington, DC 20590



NOTICE

This document is disseminated under the sponsorship of the Department of Transportation in the interest of information exchange. The United States Government assumes no liability for its contents or use thereof. Any opinions, findings and conclusions, or recommendations expressed in this material do not necessarily reflect the views or policies of the United States Government, nor does mention of trade names, commercial products, or organizations imply endorsement by the United States Government. The United States Government assumes no liability for the content or use of the material contained in this document.

NOTICE

The United States Government does not endorse products or manufacturers. Trade or manufacturers' names appear herein solely because they are considered essential to the objective of this report.

REPORT DOCUMENTATION PAGE*Form Approved*
OMB No. 0704-0188

Public reporting burden for this collection of information is estimated to average 1 hour per response, including the time for reviewing instructions, searching existing data sources, gathering and maintaining the data needed, and completing and reviewing the collection of information. Send comments regarding this burden estimate or any other aspect of this collection of information, including suggestions for reducing this burden, to Washington Headquarters Services, Directorate for Information Operations and Reports, 1215 Jefferson Davis Highway, Suite 1204, Arlington, VA 22202-4302, and to the Office of Management and Budget, Paperwork Reduction Project (0704-0188), Washington, DC 20503.

1. AGENCY USE ONLY (Leave blank)		2. REPORT DATE September 2017	3. REPORT TYPE AND DATES COVERED Technical Report	
4. TITLE AND SUBTITLE Passenger Car Crippling End-Load Test and Analyses			5. FUNDING NUMBERS DTFR53-11-D-00008 Task Order 323	
6. AUTHOR(S) Adam Klopp ¹ , Przemyslaw Rakoczy ¹ , Robert Fries ¹ , Satima Anankitpaiboon ¹ , Ian Bruce ² , Nicholas Christie ² , Michael Willford ² , Andy Thompson ² , and Michael Carolan ³ .			8. PERFORMING ORGANIZATION REPORT NUMBER	
7. PERFORMING ORGANIZATION NAME(S) AND ADDRESS(ES) ¹ Transportation Technology Center, Inc., 55500 DOT Road, Pueblo, CO 81001 ² Arup North America, Ltd., 560 Mission St, Ste 700, San Francisco, CA 94105 ³ Volpe National Transportation Systems Center, 55 Broadway, Cambridge, MA 02142			10. SPONSORING/MONITORING AGENCY REPORT NUMBER DOT/FRA/ORD-17/14	
9. SPONSORING/MONITORING AGENCY NAME(S) AND ADDRESS(ES) U.S. Department of Transportation Federal Railroad Administration Office of Research, Development and Technology 1200 New Jersey Avenue, SE Washington, DC 20590			11. SUPPLEMENTARY NOTES COR: Jeff Gordon	
12a. DISTRIBUTION/AVAILABILITY STATEMENT This document is available to the public through the FRA Web site at http://www.fra.dot.gov .			12b. DISTRIBUTION CODE	
13. ABSTRACT (Maximum 200 words) The Transportation Technology Center, Inc. (TTCI) performed a series of full-scale tests and a finite element analysis (FEA) in a case study that may become a model for manufacturers seeking to use the waiver process of Tier I crashworthiness and occupant protection standards to qualify railcars with alternative designs. The test series included an 800,000-lb quasi-static compressive end-load applied through floor-level crash energy management (CEM) pockets and a crippling compressive load applied through the floor and roof level CEM pockets. Although the first test did not strictly meet the 49 Code of Federal Regulations (CFR) § 238.203, it demonstrated that the passenger railcar can withstand the compressive load along the line of draft. In collaboration with TTCI, Arup North America developed a detailed finite element (FE) model that was calibrated with the linear test results and then used the model to predict the results of the crippling load test. The Volpe National Transportation Systems Center (Volpe) performed an independent FEA of the same test car in parallel to Arup's analysis using different FE software and modeling techniques. The results from the crippling load test showed that the final crippling load was approximately 1,100,000 pounds and the reduction in car length was approximately 3 inches.				
14. SUBJECT TERMS Passenger car, compressive load test, crippling, finite element analysis, crash energy management, finite element model			15. NUMBER OF PAGES 210	
			16. PRICE CODE	
17. SECURITY CLASSIFICATION OF REPORT Unclassified	18. SECURITY CLASSIFICATION OF THIS PAGE Unclassified	19. SECURITY CLASSIFICATION OF ABSTRACT Unclassified	20. LIMITATION OF ABSTRACT	

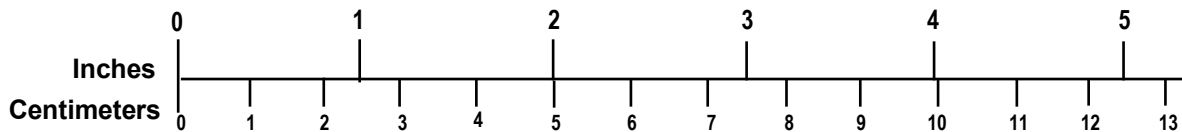
METRIC/ENGLISH CONVERSION FACTORS

ENGLISH TO METRIC

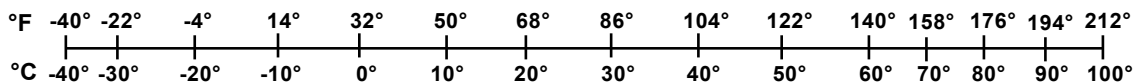
METRIC TO ENGLISH

<p>LENGTH (APPROXIMATE)</p> <p>1 inch (in) = 2.5 centimeters (cm)</p> <p>1 foot (ft) = 30 centimeters (cm)</p> <p>1 yard (yd) = 0.9 meter (m)</p> <p>1 mile (mi) = 1.6 kilometers (km)</p>	<p>LENGTH (APPROXIMATE)</p> <p>1 millimeter (mm) = 0.04 inch (in)</p> <p>1 centimeter (cm) = 0.4 inch (in)</p> <p>1 meter (m) = 3.3 feet (ft)</p> <p>1 meter (m) = 1.1 yards (yd)</p> <p>1 kilometer (km) = 0.6 mile (mi)</p>
<p>AREA (APPROXIMATE)</p> <p>1 square inch (sq in, in²) = 6.5 square centimeters (cm²)</p> <p>1 square foot (sq ft, ft²) = 0.09 square meter (m²)</p> <p>1 square yard (sq yd, yd²) = 0.8 square meter (m²)</p> <p>1 square mile (sq mi, mi²) = 2.6 square kilometers (km²)</p> <p>1 acre = 0.4 hectare (he) = 4,000 square meters (m²)</p>	<p>AREA (APPROXIMATE)</p> <p>1 square centimeter (cm²) = 0.16 square inch (sq in, in²)</p> <p>1 square meter (m²) = 1.2 square yards (sq yd, yd²)</p> <p>1 square kilometer (km²) = 0.4 square mile (sq mi, mi²)</p> <p>10,000 square meters (m²) = 1 hectare (ha) = 2.5 acres</p>
<p>MASS - WEIGHT (APPROXIMATE)</p> <p>1 ounce (oz) = 28 grams (gm)</p> <p>1 pound (lb) = 0.45 kilogram (kg)</p> <p>1 short ton = 2,000 pounds (lb) = 0.9 tonne (t)</p>	<p>MASS - WEIGHT (APPROXIMATE)</p> <p>1 gram (gm) = 0.036 ounce (oz)</p> <p>1 kilogram (kg) = 2.2 lbs (lb)</p> <p>1 tonne (t) = 1,000 kilograms (kg) = 1.1 short tons</p>
<p>VOLUME (APPROXIMATE)</p> <p>1 teaspoon (tsp) = 5 milliliters (ml)</p> <p>1 tablespoon (tbsp) = 15 milliliters (ml)</p> <p>1 fluid ounce (fl oz) = 30 milliliters (ml)</p> <p>1 cup (c) = 0.24 liter (l)</p> <p>1 pint (pt) = 0.47 liter (l)</p> <p>1 quart (qt) = 0.96 liter (l)</p> <p>1 gallon (gal) = 3.8 liters (l)</p> <p>1 cubic foot (cu ft, ft³) = 0.03 cubic meter (m³)</p> <p>1 cubic yard (cu yd, yd³) = 0.76 cubic meter (m³)</p>	<p>VOLUME (APPROXIMATE)</p> <p>1 milliliter (ml) = 0.03 fluid ounce (fl oz)</p> <p>1 liter (l) = 2.1 pints (pt)</p> <p>1 liter (l) = 1.06 quarts (qt)</p> <p>1 liter (l) = 0.26 gallon (gal)</p> <p>1 cubic meter (m³) = 36 cubic feet (cu ft, ft³)</p> <p>1 cubic meter (m³) = 1.3 cubic yards (cu yd, yd³)</p>
<p>TEMPERATURE (EXACT)</p> <p>$[(x-32)(5/9)]\text{ }^{\circ}\text{F} = y\text{ }^{\circ}\text{C}$</p>	<p>TEMPERATURE (EXACT)</p> <p>$[(9/5)y + 32]\text{ }^{\circ}\text{C} = x\text{ }^{\circ}\text{F}$</p>

QUICK INCH - CENTIMETER LENGTH CONVERSION



QUICK FAHRENHEIT - CELSIUS TEMPERATURE CONVERSION



For more exact and or other conversion factors, see NIST Miscellaneous Publication 286, Units of Weights and Measures. Price \$2.50 SD Catalog No. C13 10286

Updated 6/17/98

Contents

Executive Summary	1
1. Introduction	3
1.1 Background	4
1.2 Objectives	4
2. Test Requirements and Methods	6
2.1 800,000-pound Load Test.....	6
2.2 Survey Measurements	8
2.3 Crippling Load Test.....	9
3. Instrumentation.....	13
3.1 Definition of Coordinate Axes	13
3.2 Load Cells.....	14
3.3 Longitudinal Strain Gage Locations.....	14
3.4 Displacement Measurements.....	14
4. Test Results	17
4.1 800,000-pound Load Test Results.....	17
4.2 Crippling Load Test Results.....	23
5. Analysis Overview - Arup.....	34
5.1 Finite Element Model in LS-DYNA	34
5.2 Materials.....	34
5.3 Model Verification	35
5.4 Post-Processing of Test Results	35
5.5 Calibration of the Model to the 800,000-Pound Load Test.....	35
5.6 Comparison of Arup’s FE Analyses with Crippling Load Test Results	36
6. Analysis Overview – Volpe.....	44
6.1 Finite Element Model in Abaqus/Explicit.....	44
6.2 Materials	45
6.3 Model Verification	45
6.4 Post-processing of Test Results.....	45
6.5 Comparison of the Model to the 800,000-pound Load Test	46
6.6 Comparison of Volpe’s FE Analysis with Crippling Load Test Results	49
7. Test Observations	58
8. Discussion.....	59
8.1 Material Characterization	59
8.2 Loading Boundary Conditions	60
8.3 Weld Characterization.....	61
8.4 Pre-existing Damage	61
9. Conclusion.....	63
10. References	64

Appendix A – Instrumentation Locations and Technical Specifications.....	65
Appendix B – Crippling Test Photos	74
Appendix C – Model and Analysis Setup (Arup FE Model).....	86
Appendix D – Material Formulations (Arup FE Model).....	93
Appendix E – 800,000-pound Load Analysis and Test Results (Arup FE Model)	110
Appendix F – Quasi-Static Analysis Verification and Element Formulation Assessment (Arup FE Model)	121
Appendix G – Crippling Load Analysis and Test Results (Arup FE Model).....	126
Appendix H – Discussion of Crippling Load Analysis Results (Arup FE Model).....	144
Appendix I – 800,000-pound and Crippling Load Tests Post-processing (Arup FE Model).....	152
Appendix J – Model and Analysis Setup (Volpe FE Model)	154
Appendix K – Material Formulations (Volpe FE Model)	158
Appendix L – 800,000-pound Load Analysis and Test Results (Volpe FE Model).....	165
Appendix M – Analysis Verification (Volpe FE Model)	180
Appendix N – Crippling Load Analysis and Test Results (Volpe FE Model)	183
Appendix O – Discussion of Future Work	199
Abbreviations and Acronyms	200

Illustrations

Figure 1. Loads Applied at Lower CEM Pockets on F-End.....	6
Figure 2. Loads Reacted at Lower CEM Pockets on B-End.....	6
Figure 3. Target Loading Sequence for 800,000-pound Load Test.....	7
Figure 4. Budd M1 Car 9614 in the Test Fixture.....	7
Figure 5. Locations Surveyed — Fixture.....	8
Figure 6. Locations Surveyed — F-end.....	8
Figure 7. Locations Surveyed — B-end	9
Figure 8. Load Application Sites at F-End CEM Pockets	10
Figure 9. Loads Applied at CEM Pockets on F-End of Car	10
Figure 10. Loads Reacted at CEM Pockets on B-End of Car.....	11
Figure 11. Target Load History for Crippling Test.....	12
Figure 12. Longitudinal Instrumentation Locations	13
Figure 13. Instrumentation Cross-Section	13
Figure 14. Layout of Longitudinal String Potentiometers at Car Ends	15
Figure 15. 800,000-pound Load Test Layout of VLL String Potentiometer Arrays	15
Figure 16. Crippling Load Test Layout of VLL String Potentiometer Arrays.....	16
Figure 17. Budd M1 Car 9614 viewed from the B-end.....	17
Figure 18. Load History for 800,000-pound Load Test.....	18
Figure 19. 800,000-pound Load Test Left Side Sill Longitudinal Compression.....	18
Figure 20. 800,000-pound Load Test Center Sill Longitudinal Compression.....	19
Figure 21. 800,000-pound Load Test Right Side Sill Longitudinal Compression	19
Figure 22. 800,000-pound Load Test Load-Deflection Curve	20
Figure 23. 800,000-pound Load Test Strains.....	21
Figure 24. Damage on Left Side Sill Following 800,000-pound Load Test.....	22
Figure 25. Damage on Right Side Sill Following 800,000-pound Load Test	22
Figure 26. F-End Initial Load Offset	23
Figure 27. B-End Initial Load Offset.....	24
Figure 28. Load History for Crippling Load Test.....	24
Figure 29. Strain versus Time for Strain Gage on Left Roof Rail, Cross-Section 2	25

Figure 30. Buckled Areas of Left Roof Rail and Window Rail at Cross-Section 2	26
Figure 31. First Buckle at Approximately 700,000 lbs Exterior (left) and Interior (right).....	26
Figure 32. Second Buckle at 1,000,000 lb	27
Figure 33. Section 4 Right Side Sill Buckle	28
Figure 34. Section 6 Left Side Sill Buckle	29
Figure 35. Buckled Left Side Sill at Cross-Section 4 (left) and Strain-time History (right)	29
Figure 36. Buckled Center Sill at Cross-Section 4 (left) and Strain-time History (right)	29
Figure 37. Crippling Load Test – Load Deflection Curves	30
Figure 38. Crippling Load Test - Total Load-Deflection Curve Only.....	30
Figure 39. Crippling Load Test Left Side Sill Longitudinal Compression.....	31
Figure 40. Crippling Load Test Center Sill Longitudinal Compression.....	31
Figure 41. Crippling Load Test Right Side Sill Longitudinal Compression	32
Figure 42. Crippling Load Test — Strains.....	33
Figure 43. Finite Element Model of the Budd M1 Railcar	34
Figure 44. Bilinear and Nonlinear Material Formulations.....	34
Figure 45. Force-displacement Curves for the 800,000-pound Load Test and Analysis	36
Figure 46. Maps of Failure Points in Crippling Test (bottom) and Analysis (top).....	38
Figure 47. Force-Displacement Curves for the Crippling Analysis and Crippling Load Test Results at Roof and Floor, Left and Right	39
Figure 48. Force-displacement for the Crippling Load Analysis and Test Results at Roof and Floor, and for Total Overall Load.....	40
Figure 49. Roof Failure in the Simulated and Physical Railcars	41
Figure 50. Buckling at the Repair Location in the Crippling Load Analysis (left) and Test (right)	42
Figure 51. Similar Side Sill Buckles in the Crippling Load Analysis (left) and Test (right)	42
Figure 52. Comparison of Buckles in the Center Sill (top — A3, P3b)	43
Figure 53. Volpe FE Model of M1 Passenger Car.....	44
Figure 54. 800,000-pound Test and Volpe FE Force-displacement Results	46
Figure 55. 800,000-pound test and Volpe FE Vertical Displacement Results	47
Figure 56. 800,000-pound test and Volpe FE Strain Comparison.....	48
Figure 57. Crippling Load Damage in Volpe FE Model	49

Figure 58. Crippling Test and Volpe FE Floor Force-displacement Results.....	50
Figure 59. Crippling Test and Volpe FE Roof Force-displacement Results	51
Figure 60. Crippling Test and Volpe's Pre-test FEA Force-displacement Results.....	52
Figure 61. Roof Buckling in Volpe Crippling FE Model with Inset Showing Interior	53
Figure 62. Buckling in F-end Roof at Cross-Section 2 with Pre-existing Damage Noted	54
Figure 63. Buckling in B-end Roof at Cross-Section 8 with pre-existing Damage Noted.....	55
Figure 64. Damage to Underframe in Volpe Pre-test Crippling Model	56
Figure 65. Center Sill Buckling in Crippling Test (top) and Volpe FE Model (bottom)	56
Figure 66. Side Sill Buckling in Crippling Test (top) and Volpe FE Model (bottom).....	57
Figure 67. Pre- (left) and Post- (right) Test Photographs of Left Side Sill, Cross-Section 6	57

Tables

Table 1. Longitudinal Locations of Cross-Sections.....	14
Table 2. Instrumentation Summary.....	16
Table 3. 800,000-pound Underframe Strain Gage and Volpe FE Results Outside $\pm 20\%$ Envelope	48

Executive Summary

The Transportation Technology Center, Inc. (TTCI) conducted a study sponsored by the Federal Railroad Administration (FRA) on a series of full-scale tests and a finite element analysis (FEA) to investigate the use of a set of criteria and procedures for evaluating the strength of railcar equipment built according to alternative design standards. These criteria and procedures are intended to provide a technical framework for presenting evidence to FRA in support of requests for waivers of the Tier I (up to 125 mph) crashworthiness and occupant protection standards. In the tests and analyses, loads were applied through the crash energy management (CEM) system load paths.

TTCI performed both tests on Budd M1 Car 9614. In collaboration with TTCI, Arup North America Ltd (Arup) developed a detailed finite element (FE) model of the test car and provided predictions prior to each test. Also, a parallel FEA of the same test car was conducted by the John A. Volpe National Transportation Systems Center (Volpe). The Volpe FEA is also documented in this report.

The 800,000-lb load test demonstrated that Car 9614 was acceptable for the crippling load test, and it also provided data for calibrating the FE models.

In the crippling load test, buckling occurred first on the loading end roof at approximately 700,000 pounds, and complete car crippling occurred at approximately 1,100,000 pounds. Crippling occurred on the side sills, center sill, belt rails, roof rails, side walls, and on the roof near the doors. After the test, the total car length had been reduced by approximately 3 inches. The instrumentation for this test measured car strains, displacements, and compressive forces.

Following calibration, Arup's FEA produced reasonable correlation with the physical 800,000-lb load test results. However, there were marked differences between analysis predictions for the crippling test and the actual (physical) test results. When factors that could cause these discrepancies were investigated, several challenges were revealed in predicting nonlinear behavior based on calibration to a linear test:

- The test results appeared to be particularly sensitive to the characterization of material properties, especially as the transition from linear elastic behavior to nonlinear plastic behavior occurred.
- Attention must be paid to spot weld failure. Spot welds often undergo quite complex failures because their performance has as much to do with deformation and tearing of the surrounding metal as the actual connection. For sections where stiffness depends on multiple layers of steel acting compositely, a subtle change in the spot weld performance can have an amplified effect on the load-bearing capacity of the section.
- The results of the crippling load test were moderately sensitive to the nuances of its setup. These included whether the car was properly aligned and all four loading points were engaged simultaneously, as well as whether the rate of loading was sufficiently low to allow buckles to develop in a quasi-static loading condition.
- Volpe's FE also produced reasonable correlation with the 800,000-lb test results after the model's boundary conditions were adjusted to match observations made during the test. Volpe's pre-test FE for the crippling test qualitatively agreed with the results obtained from the test. However, the roof and underframe of the tested car experienced buckling

at loads lower than those expected based on the FE results. Several areas of damage that were known to exist prior to the crippling test had experienced further damage following the crippling test, possibly contributing to the lower crippling load than predicted by either FE model.

1. Introduction

The Federal Railroad Administration (FRA), through its Office of Research, Development and Technology, provides the technical basis for rulemaking that is designed to improve crashworthiness and enhance occupant protection for passenger railroad equipment. This research program addresses both conventional and innovative equipment being introduced more frequently into U.S. service.

In accordance with 49 Code of Federal Regulations (CFR) § 238.203 [1], passenger railcars in Tier I service are required to withstand a static compressive end-load of 800,000 pounds applied longitudinally on the line of draft without permanent deformation. Passenger rail equipment built to alternative design standards may not meet these standards, but may possess at a minimum equivalent performance to equipment meeting the regulation.

For such passenger railcars, which use alternative designs and are equipped with crash energy management (CEM) components, collision loads would be introduced to the occupant volume at the interface between the occupant volume and the CEM components. FRA looked into using a set of criteria and procedures for evaluating the strength of passenger rail equipment built to alternative design standards and applying loads through the collision load path. The criteria and procedures were developed by the Engineering Task Force (ETF) of the Passenger Safety Working Group of the Railroad Safety Advisory Committee [2]. They provide a technical framework for presenting FRA with evidence that supports requests to waive applicable Tier I crashworthiness and occupant protection standards. FRA is currently preparing revised rulemaking which would codify the criteria and procedures, eliminating the need for the waiver process.

To support this effort, FRA contracted TTCI to perform a series of full-scale tests and FEA on Budd M1 Car 9614 that would:

- Reaffirm certain basic assumptions in the criteria and procedures; and,
- Produce a publishable example of the companion finite element analyses that might accompany a report submitted to FRA documenting compliance with relevant regulations.

Car 9614 had been previously modified to include CEM components on both ends. The CEM elements were removed prior to testing, leaving the floor- and roof-level energy absorber pockets in place. These locations represent the locations at which collision loads were introduced into the carbody structure.

This effort included test planning, test implementation, processing of test data, and FE modeling. The FE modeling effort included simulations performed to validate the model and simulations of the test conditions. These tests included the following:

- 800,000-lb Load Test: 800,000-lb quasi-static end-load test using loads applied through the floor-level CEM pockets. This test was conducted on March 13, 2013. Although the first test did not strictly meet the requirements of 49 CFR § 238.203, it demonstrated the car's ability to withstand the compressive load along its underframe and generated data for model validation.

- Crippling Load Test: Quasi-static end-load test to determine the ultimate strength of the car, using loads that were applied through the floor and roof level CEM pockets. This test was conducted on July 17, 2013.

Arup, in collaboration with TTCI, developed a detailed FE model of the test car and provided predictions before each test. Also, FRA directed Volpe to perform an independent FEA for the same test car in parallel with Arup's analysis. FRA investigated the ability of two different modelers, utilizing different approaches (e.g., different modeling techniques, different software packages, etc.) to produce results comparable to the measurements obtained from the tests.

The 800,000-lb load test was conducted to provide data for FE model validation and ensure that Car 9614 was suitable for use in the crippling test. Before the crippling load test, survey measurements verified that Budd M1 Car 9614 was squarely situated in the fixture. Computational work performed by Arup and Volpe predicted the railcar's response for test planning.

Note:

This report was prepared by three independent entities: TTCI prepared the portion describing the physical testing, including setup and instrumentation; Arup and Volpe reported on their respective analyses and efforts to correlate those results with the test data. Conclusions are independently drawn by each participant.

1.1 Background

Before the railcar was used for this series of tests, Budd M1 Car 9614 incurred damage during previous full-scale, high-load tests, which included a train-to-train impact test [3]. Before the compressive end-load tests began, all significant damage sustained by the car was repaired. Wrinkles in the skin on the right-side F-end door and a 0.2-in deep dent on the right-side sill were straightened and strengthened. Two cracks located below the dent were repaired. Another deformation on the right-side sill was strengthened by welding a patch on it. To maintain stiffness symmetry, an identical patch was welded in the same position on the opposite side of the car. The side panel just above the right-side patch was replaced and strengthened with sections similar to the original design. The CEM structures at both car ends were removed for the tests so that loads could be applied to the ends of the occupant volume at the CEM pockets. Material characterization tests using specimens removed from a sister Budd M1 car were performed and the test results were provided to Arup and Volpe in support of the modeling efforts.

1.2 Objectives

These tests had the following objectives:

- 800,000-Lbs Load Test – To provide data for FE model validation and ensure that Budd M1 Car 9614 was structurally sound enough for the crippling load test.
- Crippling Load Test – To determine the ultimate load capability and crush characteristics of Budd M1 Car 9614 by loading it quasi-statically through the floor- and roof-level CEM pockets, until the crippling load was reached.

An additional objective was to compare test results with the results of a quasi-static analysis performed by using the ETF's methodology in an effort to validate that approach.

2. Test Requirements and Methods

2.1 800,000-pound Load Test

An 800,000-lb load test was conducted on Budd M1 Car 9614 in March 13, 2013. Figure 1 shows how the two actuators at the loading end of the car (F-end) applied compressive loads to the two floor-level CEM pockets, while Figure 2 shows how the loads were reacted at the two-floor level CEM pockets on the opposite end of the car (B-end).

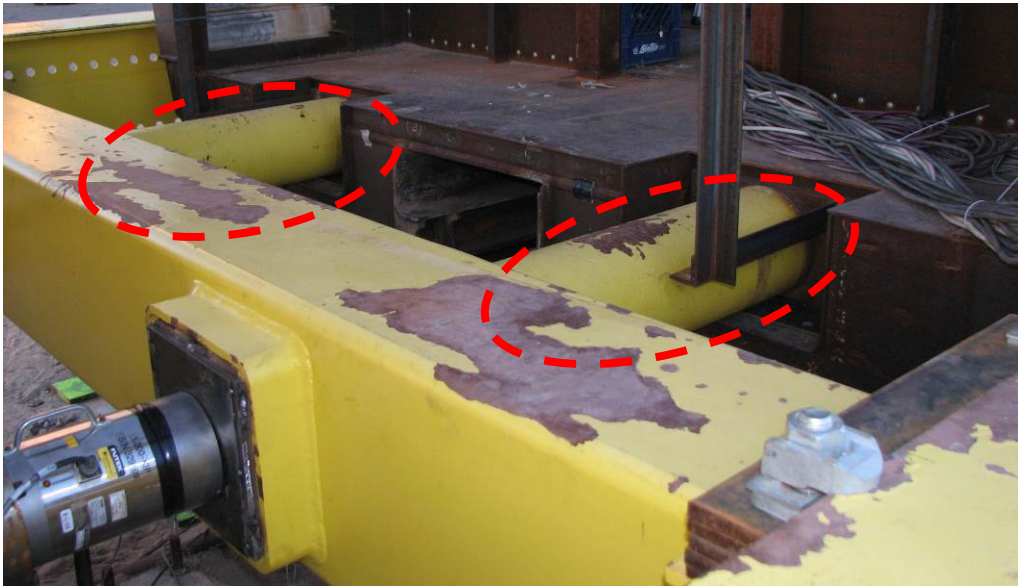


Figure 1. Loads Applied at Lower CEM Pockets on F-End



Figure 2. Loads Reacted at Lower CEM Pockets on B-End

Figure 3 shows the target load sequence for the 800,000-lb load test. A dwell period preceded and followed each load step. After the dwell period at each target load, the load was reduced to approximately 20,000 pounds. Following the 700,000-pound dwell period, the load was reduced

to slightly below 2,000 pounds in preparation for the final 800,000-lb load step. This loading approach is consistent with the test procedures given by industry standards [4] for the conventional 800,000-lb buff strength test. The loading rate during the test was approximately 0.7 in/min. Figure 4 shows Car 9614 in the test fixture. The arrows in this figure indicate the approximate heights of the floor-level loading locations.

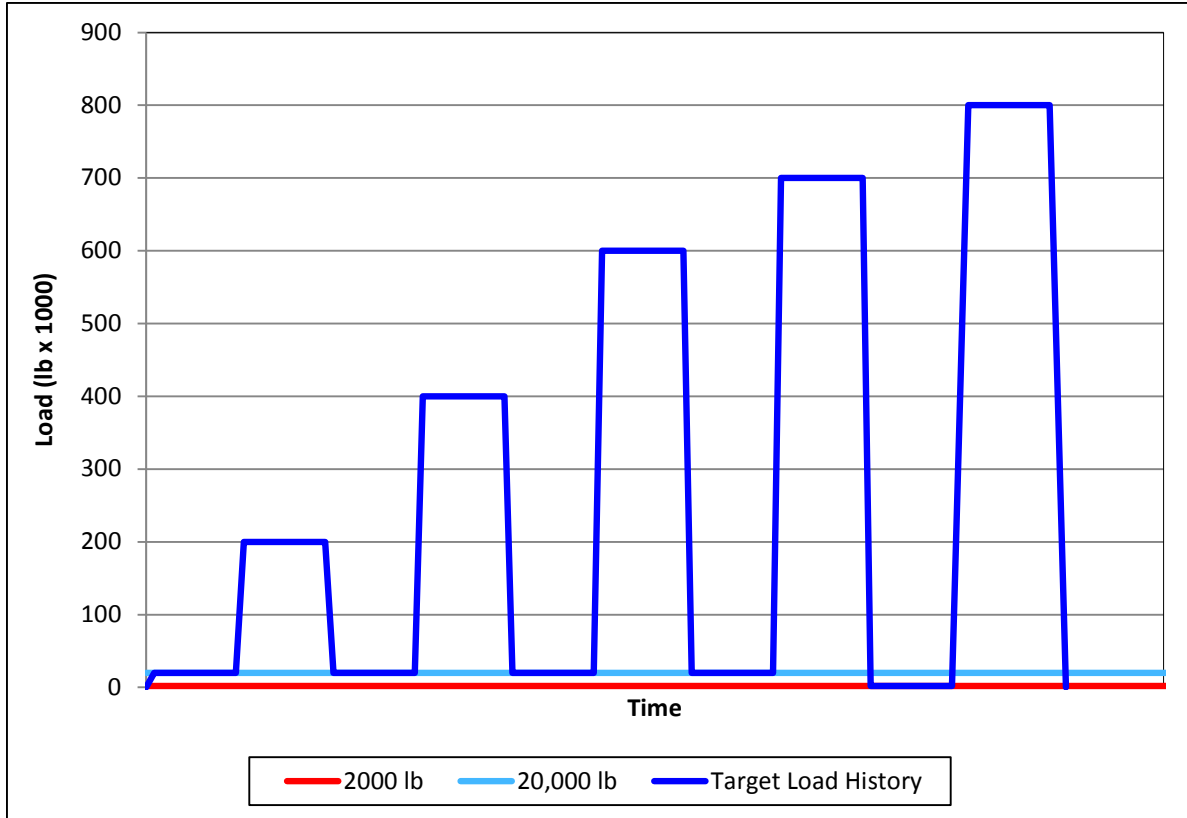


Figure 3. Target Loading Sequence for 800,000-pound Load Test



Figure 4. Budd M1 Car 9614 in the Test Fixture

2.2 Survey Measurements

Before the crippling load test, survey measurements were taken to assess the squareness of Car 9614 in the test fixture. Thirty-two locations were measured on the fixture and the car, as Figure 5, Figure 6, and Figure 7 show. All the locations were surveyed twice under the following conditions:

- Under close to zero load to remove gaps between loading rods and CEM pockets.
- Under low magnitude load (150,000 pounds) to remove all the slack between fixture and car.

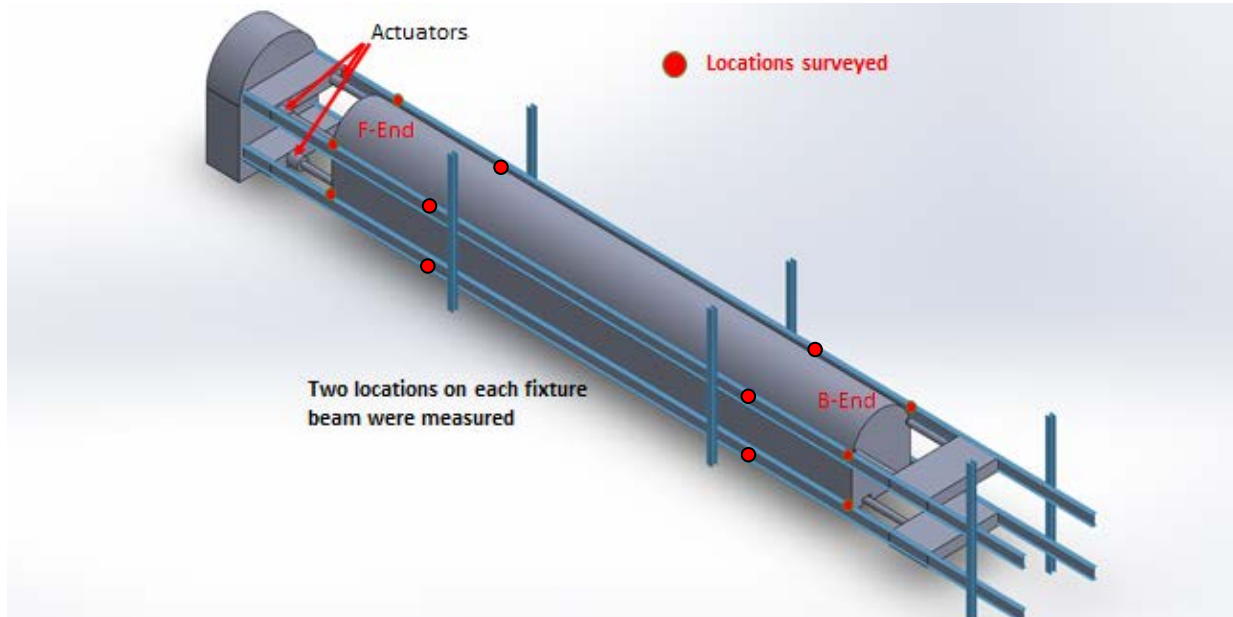


Figure 5. Locations Surveyed — Fixture

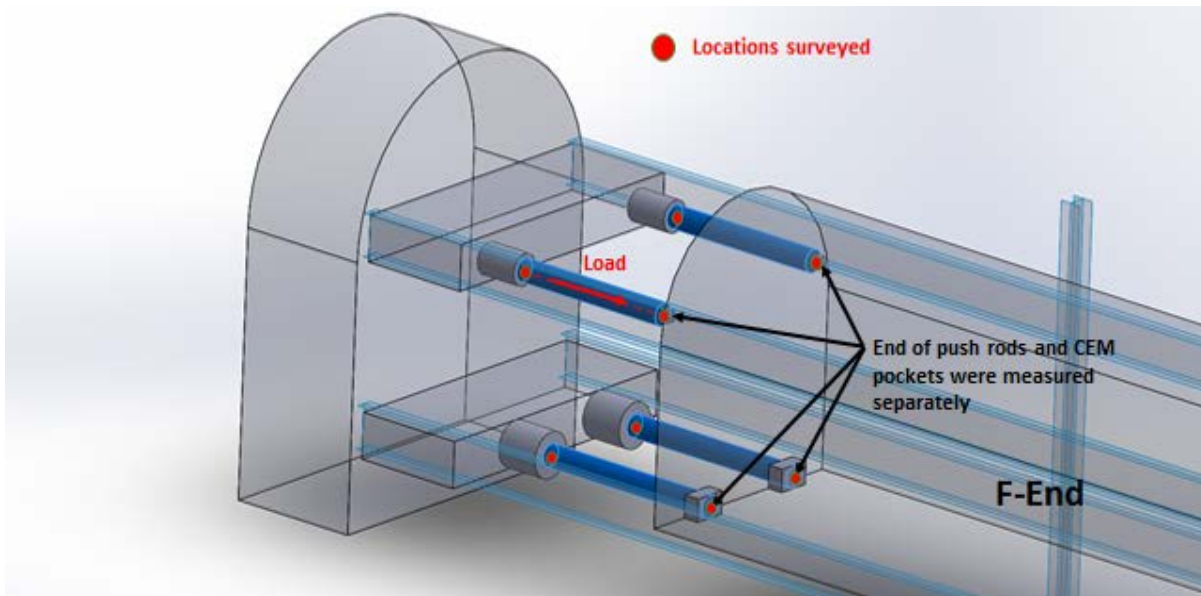


Figure 6. Locations Surveyed — F-end

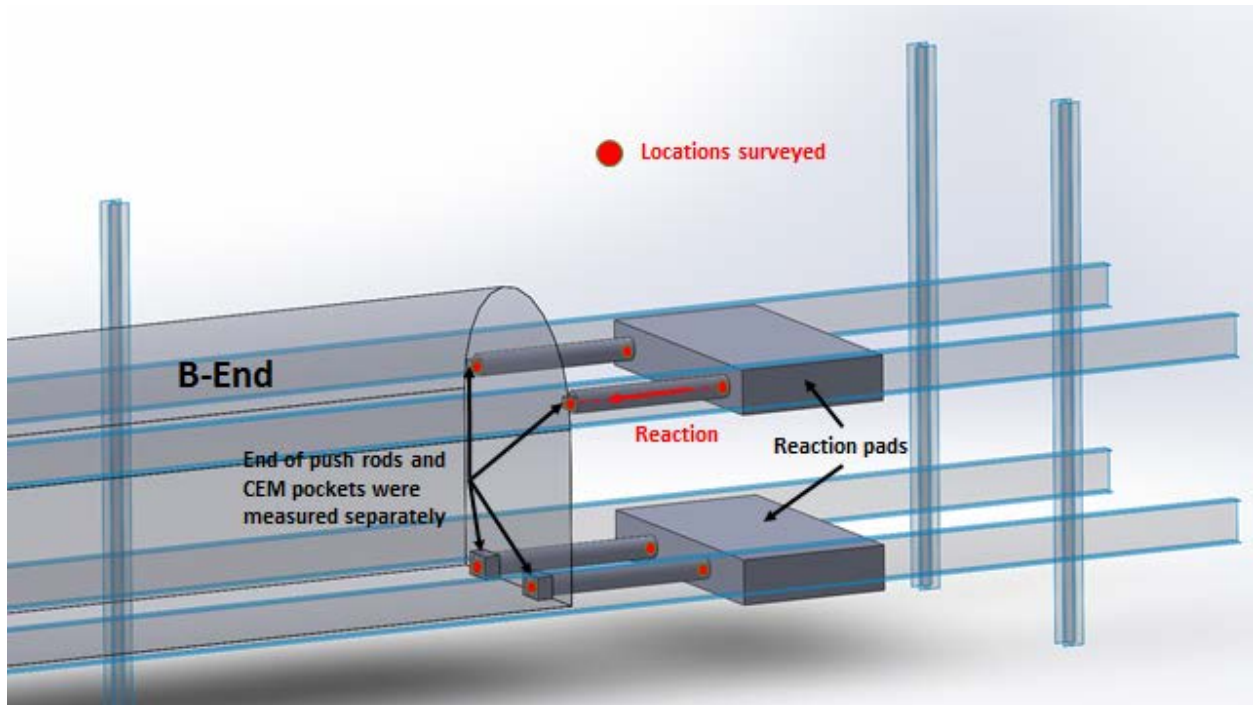


Figure 7. Locations Surveyed — B-end

The survey measurements indicated that the car was not square in the load frame and that the actuators were not perfectly aligned with the longitudinal axis of the car. Instead, the force applied by the actuators was angled slightly with respect to the car centerline. However, the car tended to self-align when under load. The largest angle between the line of force application and the car centerline was noted on the top left CEM pocket in the horizontal direction. The angle measured at zero load was 2.52° which was reduced to 0.51° under load. The imperfections were noted, and the data were provided to Arup and Volpe in support of the modeling efforts.

2.3 Crippling Load Test

Budd M1 Car 9614 was subjected to a crippling load test on July 17, 2013. Figure 8 shows how the car was loaded at all four CEM pockets on the F-end. The loads were reacted at all four CEM pockets on the B-end. Figure 9 shows the loading-end of the car and Figure 10 shows the reaction-end of the car.



Figure 8. Load Application Sites at F-End CEM Pockets

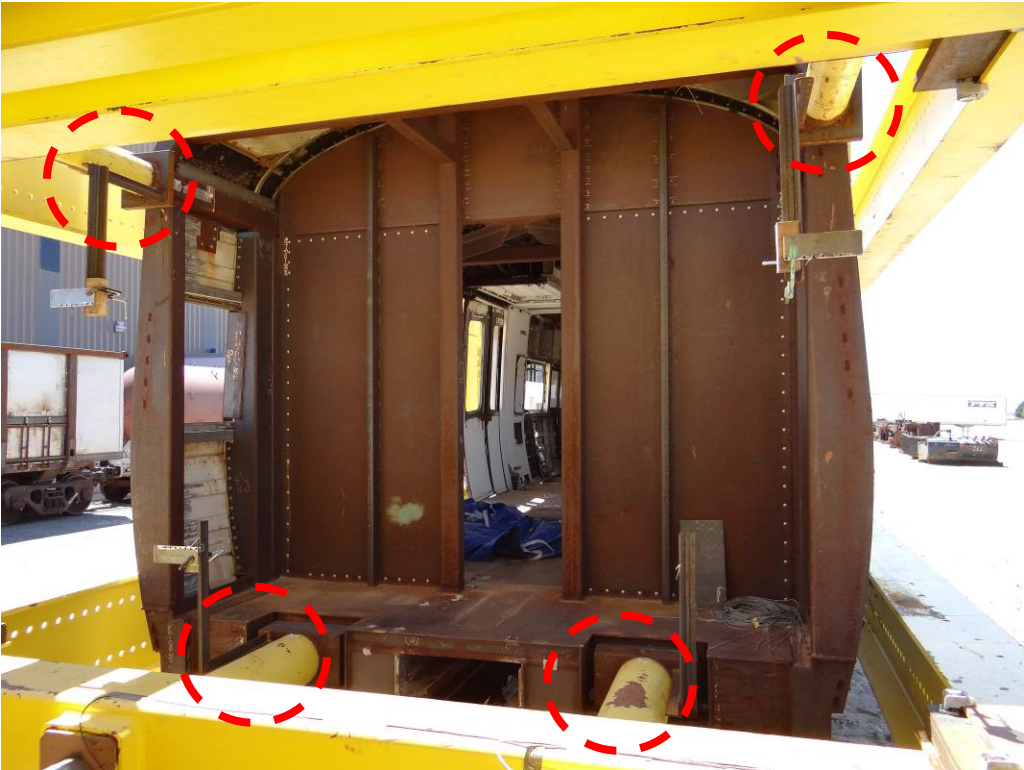


Figure 9. Loads Applied at CEM Pockets on F-End of Car



Figure 10. Loads Reacted at CEM Pockets on B-End of Car

Figure 11 shows the target load history for the crippling load test, in which the car was loaded incrementally to 800,000 pounds. A dwell period preceded and followed each load step. After the dwell period at each target load increment, the load was reduced to approximately 20,000 pounds. After the 600,000-lb dwell period, however, the load was reduced to slightly below 2,000 pounds. in preparation for the 800,000-lb load step. The loading rate was approximately 0.7 in/min for each load cycle. For loads above 800,000 pounds or after the first buckle, the test plan called for the applied load to be increased using increments of displacement instead of force. Above 800,000 pounds, the applied load was not reduced following each increment except if the carbody buckled. Displacement was advanced in 0.25-inch increments until the carbody could no longer sustain the load.

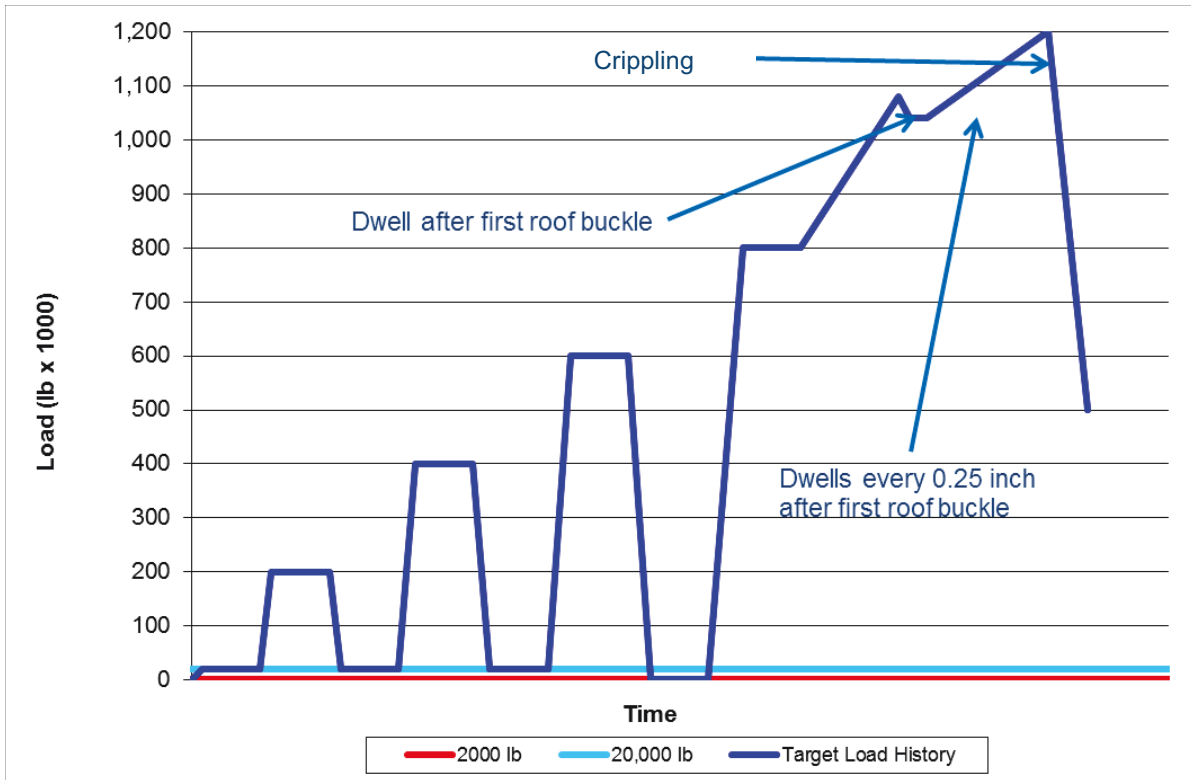


Figure 11. Target Load History for Crippling Test

3. Instrumentation

3.1 Definition of Coordinate Axes

The origin of the coordinate system was at the center of F-end bolster, at floor level, and on the centerline of the test car (see Figures 12 and 13). The z-axis orientation was positive in the upward direction.

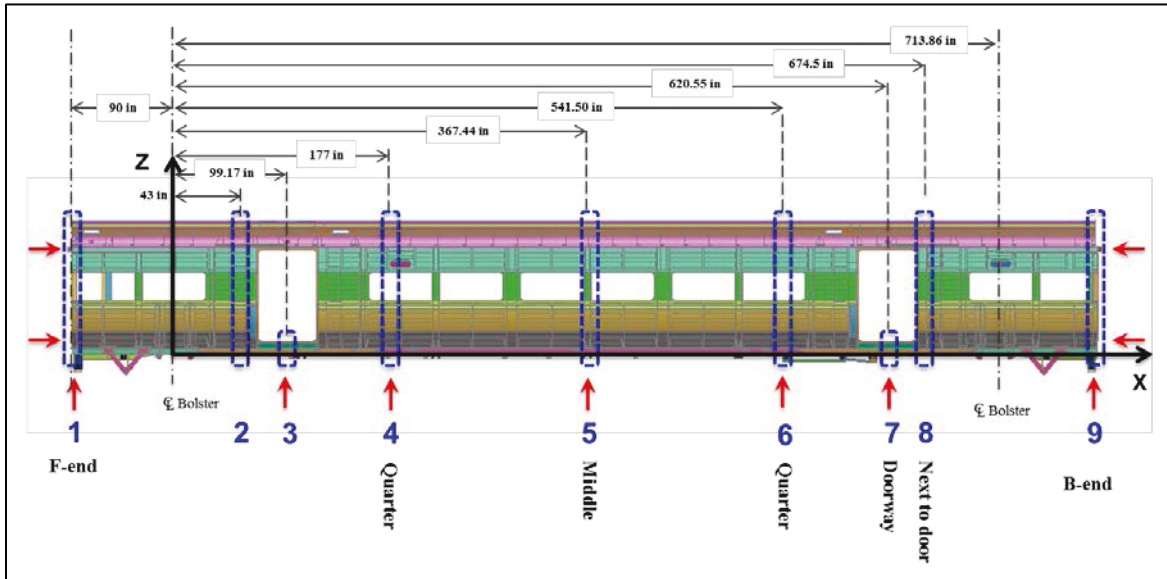


Figure 12. Longitudinal Instrumentation Locations

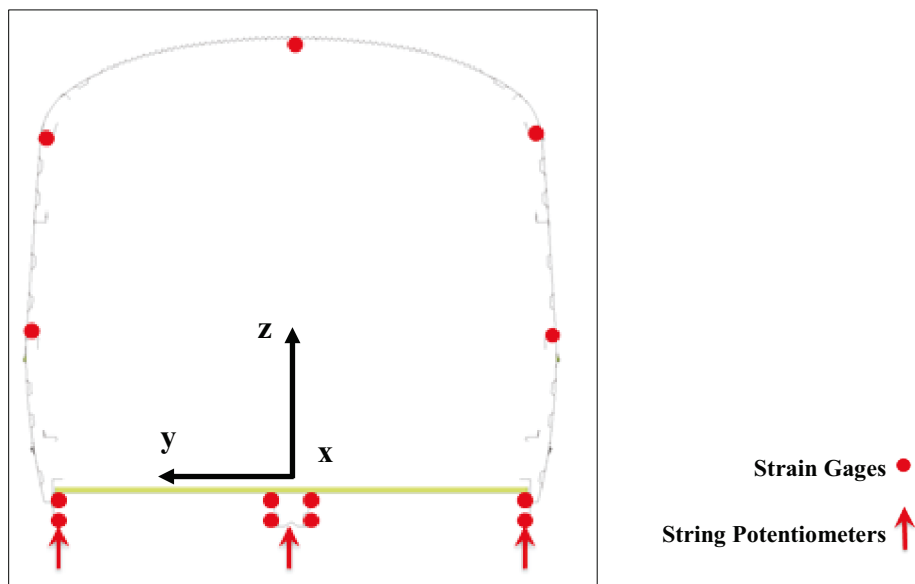


Figure 13. Instrumentation Cross-Section

3.2 Load Cells

For the 800,000-pound test, load cells were installed in series with the floor-level actuators and restraint rods. Before the crippling load test was conducted, additional load cells were installed in sequence with the roof-level actuators and restraint rods. The floor-level load cells had a 1,000,000-pound capacity, and the roof-level load cells had a 500,000-pound capacity. Load cells were applied on both the F- and B-ends of the car in order to infer the load path through the occupant volume. Table A1 in Appendix A includes channel names and location information for the load cells used in both tests.

3.3 Longitudinal Strain Gage Locations

Table 1 shows the cross-sections defined for instrumentation placement in both tests. The cross-sections were numbered 1 through 9 starting at the F-end. Strain gages were placed on the roof rails, belt rails, side sills, and center sill at each cross-section on the car, as Figure 13 shows.

The belt and roof rails were discontinuous at the doorways at Cross-Sections 3 and 7. Consequently, strain gages were placed only on the center sill and side sills at these locations. There were no strain gages installed at the F- and B-ends. Table 1 shows the longitudinal locations of the Cross-Sections. Some strain gages could not be installed at the exact cross-sectional locations because of obstacles or existing imperfections. The gages at these locations were moved slightly to avoid complications, and the deviations were documented. All strain gages used in the tests were of the high-elongation type. Table A2 in Appendix A contains the strain gage naming convention and location details for each strain gage. Figures B1 through B6 in Appendix B give additional details about strain gage installations.

Table 1. Longitudinal Locations of Cross-Sections

Location	Distance From F-End Bolster (inches)
1	90
2	43
3	99.17
4	177
5	367.44
6	541.50
7	620.55
8	674.50
9	803.86

3.4 Displacement Measurements

All actuators contained built-in linear variable differential transformers (LVDT) to measure stroke. Four string potentiometers were installed at each end of the car to measure longitudinal displacements of the carbody relative to the load frame. At each end, two measurements were made at floor level and two were made at roof level on the left and right sides of the car. Figure 14 illustrates the layout of the longitudinal string potentiometers at the car ends. The rectangles in Figure 14 show locations of the side-sill patches.

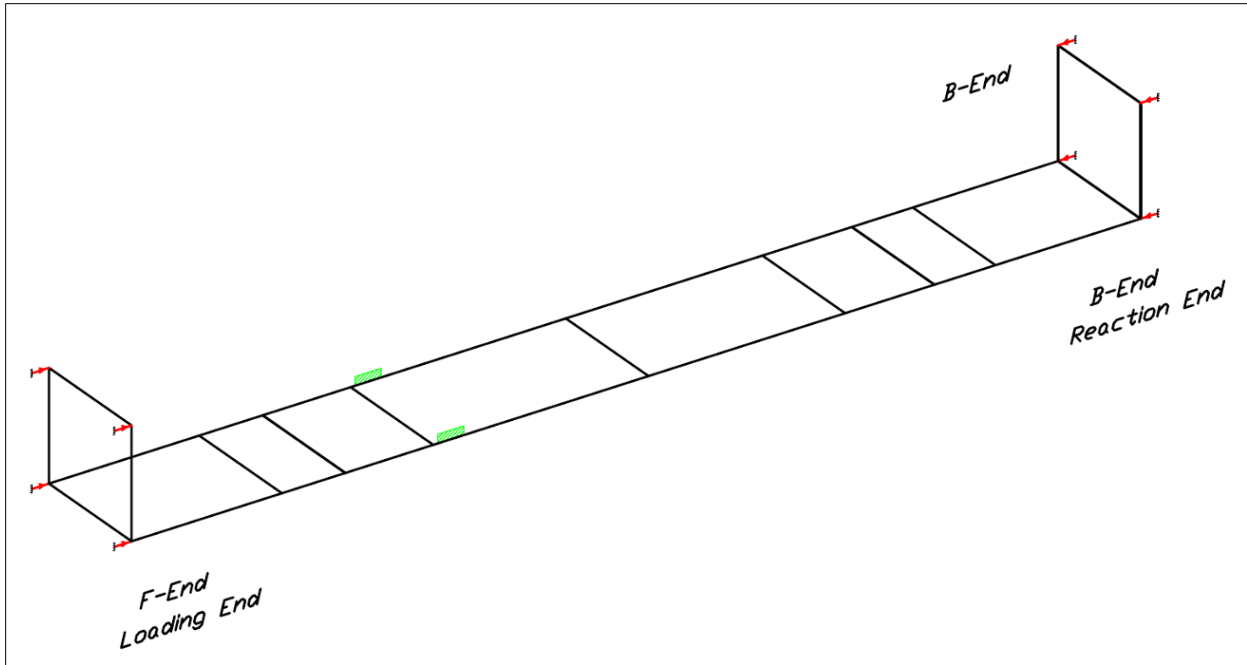


Figure 14. Layout of Longitudinal String Potentiometers at Car Ends

Vertical, lateral, and longitudinal (VLL) string potentiometer arrays were installed along the center sill and side sills at each cross-section, with the exceptions of Cross-Sections 2 and 8. These sections coincided with the bolster locations, which complicated the placement of the VLL arrays. Figure 15 shows the map of VLL string potentiometer arrays for the 800,000-lb load test. Table A3 in Appendix A contains details of the load measuring channels used in the 800,000-lb load test.

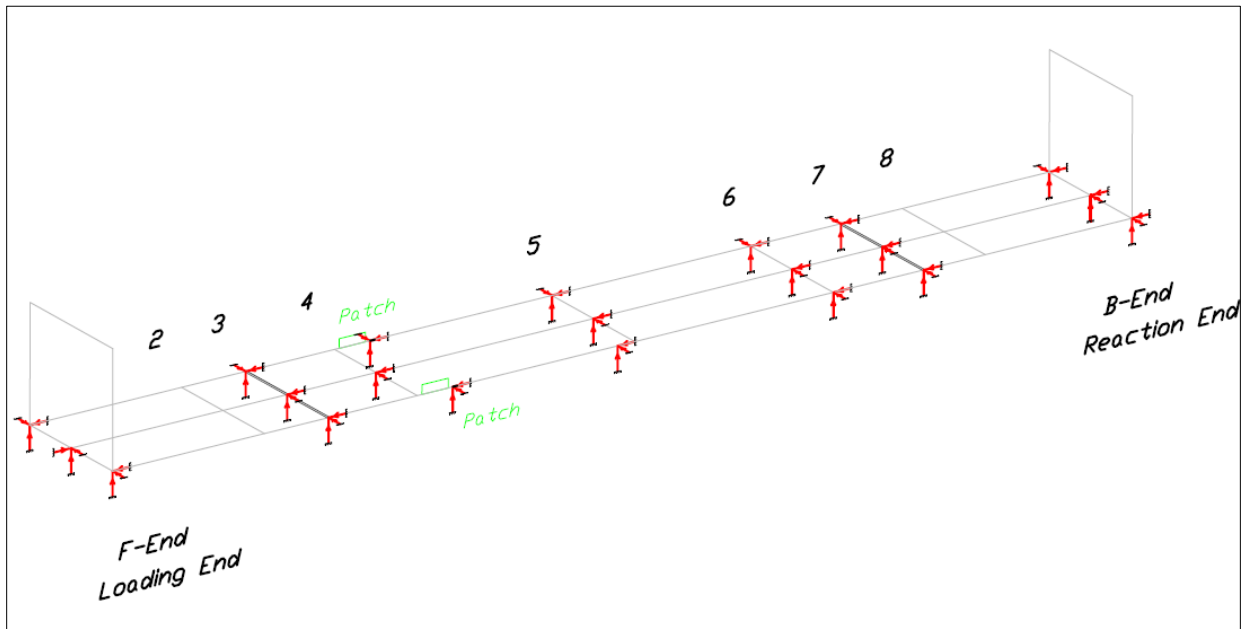


Figure 15. 800,000-pound Load Test Layout of VLL String Potentiometer Arrays

During the crippling test, some of the VLL arrays were moved to avoid damaged or vulnerable areas and the orientations of some arrays were changed. Figure 16 shows the string potentiometer map for the crippling load test. Table A4 in Appendix A contains details of the string potentiometer locations used in the crippling load test. The positions and orientations of the sensors in both tests were consistent with the previously described coordinate system.

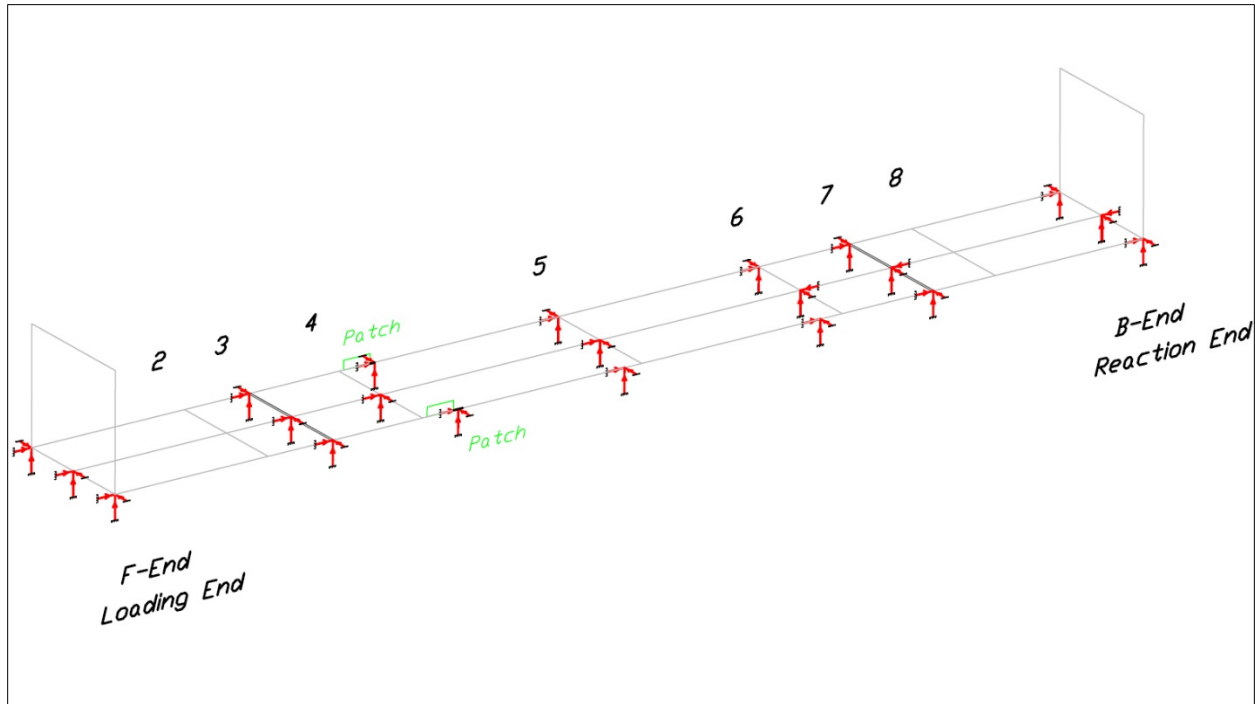


Figure 16. Crippling Load Test Layout of VLL String Potentiometer Arrays

In total, 165 data channels were recorded for the 800,000-lb load test, and 169 data channels were recorded for the crippling load tests. Table 2 shows the instrumentation summary for both tests.

Table 2. Instrumentation Summary

Type of Instrumentation	Channel Count
Strain gages (Longitudinal)	81
Load Cells	4 (8 for crippling load test)
String Potentiometers	71
Pressure Transducers - Actuators	4
LVDTs — Actuators	4
Ambient Temperature	1
Total Data Channels	165 (169 for crippling load test)
Digital Video	2 Cameras (5 for crippling load test)

4. Test Results

4.1 800,000-pound Load Test Results

Budd M1 Car 9614 was subjected to an 800,000-lb quasi-static end-load test on March 13, 2013. Loads were introduced at the two-floor level CEM pockets at the F-end and reacted at the two-floor level CEM pockets at the B-end.

When viewed from the B-end (reaction-end) looking towards the F-end (loading-end), the left side of the car faced north and the right side of the car faced south, as Figure 17 shows.

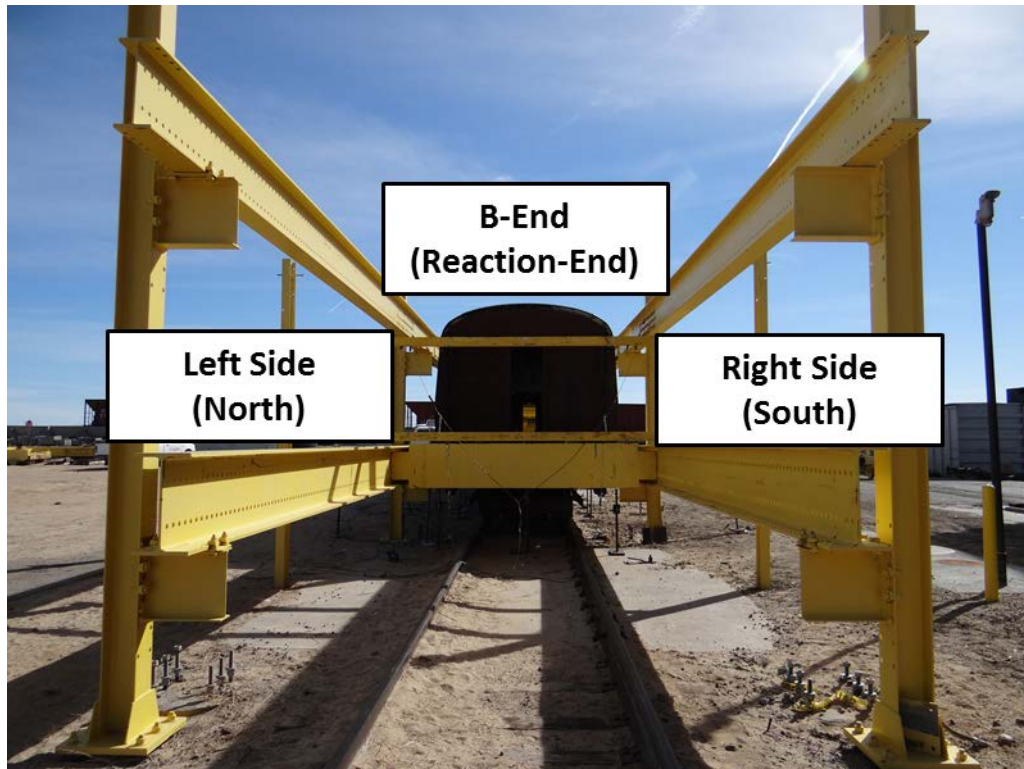


Figure 17. Budd M1 Car 9614 viewed from the B-end

Figure 18 shows the load history for the 800,000-lb load test. The plot includes the loads applied by each floor level actuator and the total load applied to the car.

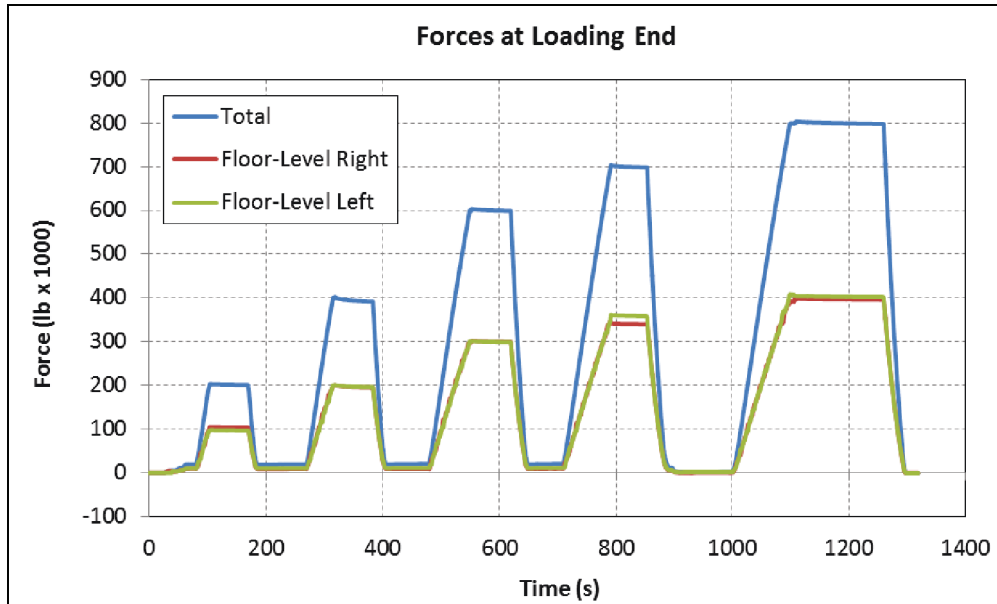


Figure 18. Load History for 800,000-pound Load Test

Figure 19, Figure 20, and Figure 21 show the longitudinal side sill and center sill displacements at the various instrumentation cross sections. The location numbers below the plot represent the cross sections on the car.

The left and right side sills stop displacing longitudinally relative to the ground at the 600,000-lb load step near Section 6, indicating possible weaknesses in the side sills in the vicinity of Cross-Section 6 and potential areas of interest for the crippling test. Both side sills and the center sill also showed sharp drops in longitudinal displacement near Sections 4 and 5, indicating more potential areas for crippling in the next test.

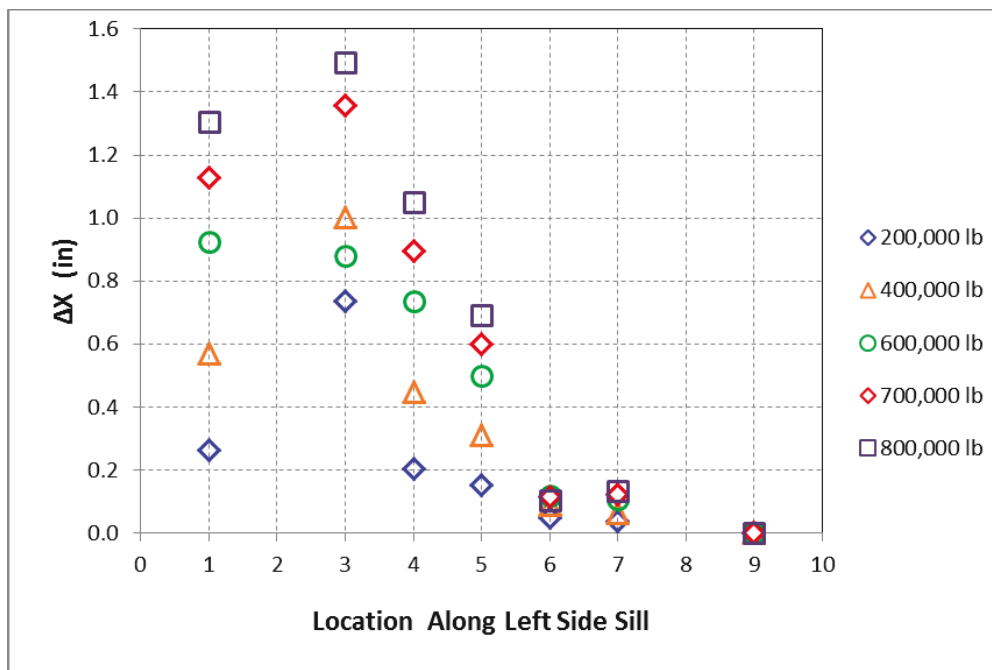


Figure 19. 800,000-pound Load Test Left Side Sill Longitudinal Compression

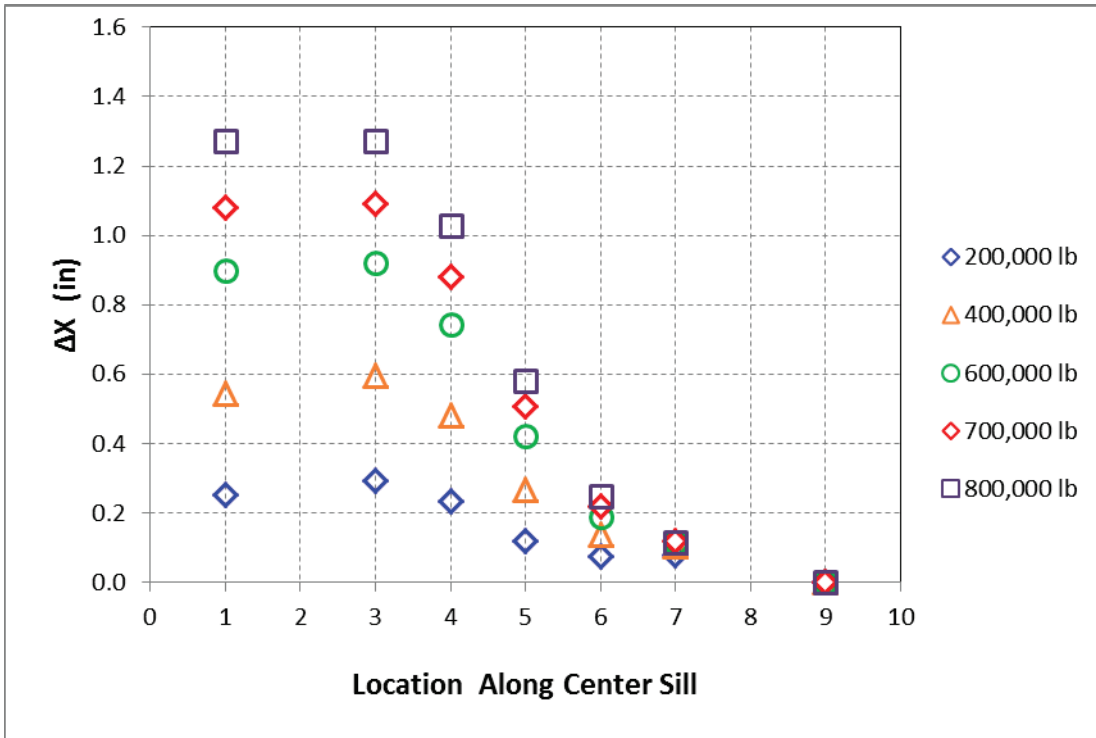


Figure 20. 800,000-pound Load Test Center Sill Longitudinal Compression

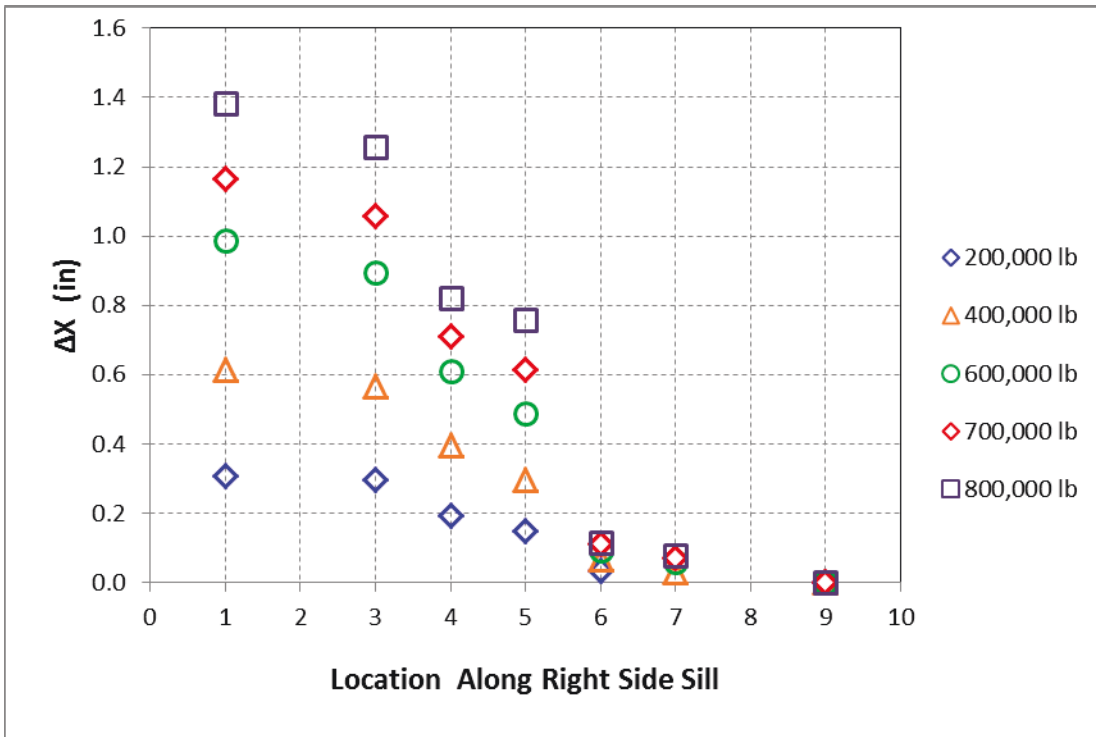


Figure 21. 800,000-pound Load Test Right Side Sill Longitudinal Compression

Aside from some minor bending on the side sills and window rails, the primary structure of Budd M1 Car 9614 suffered no permanent deformation during the 800,000-lb load test. Figure 22 shows the load-deflection curve for the test, which indicates that the car behaved nearly elastically. The permanent compression that resulted from the loads was less than 0.1 inches. As a result, Car 9614 was deemed suitable for the crippling test.

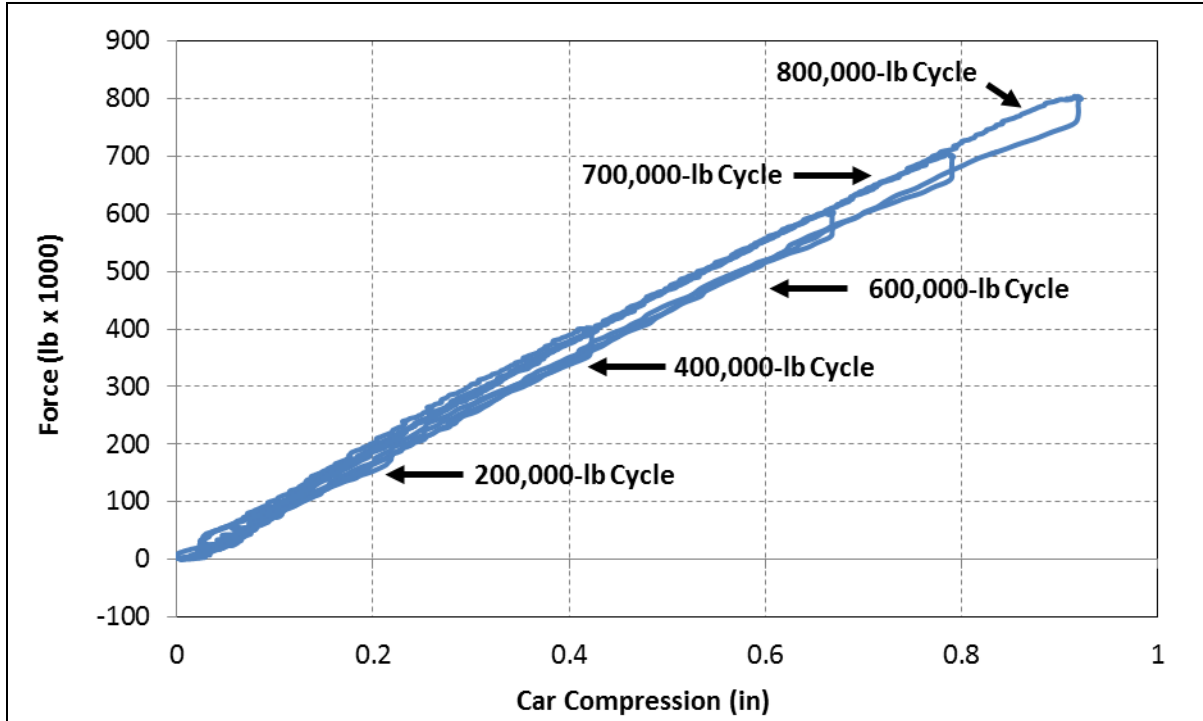


Figure 22. 800,000-pound Load Test Load-Deflection Curve

Figure 23 shows plots of strains for the 800,000-lb load test. The section numbers in the plot titles represent the various instrumentation cross sections along the length of the car. Channel names correspond to those in Table A2, Appendix A.

Arching behavior of the car was observed. All strain gages were in compression, except for those located on the roof (S2R, S4R, S5R, S6R and S8R).

Strain gage S7SSBL shows constant offset of measurement; this strain gage was damaged during the 800,000-lb load test.

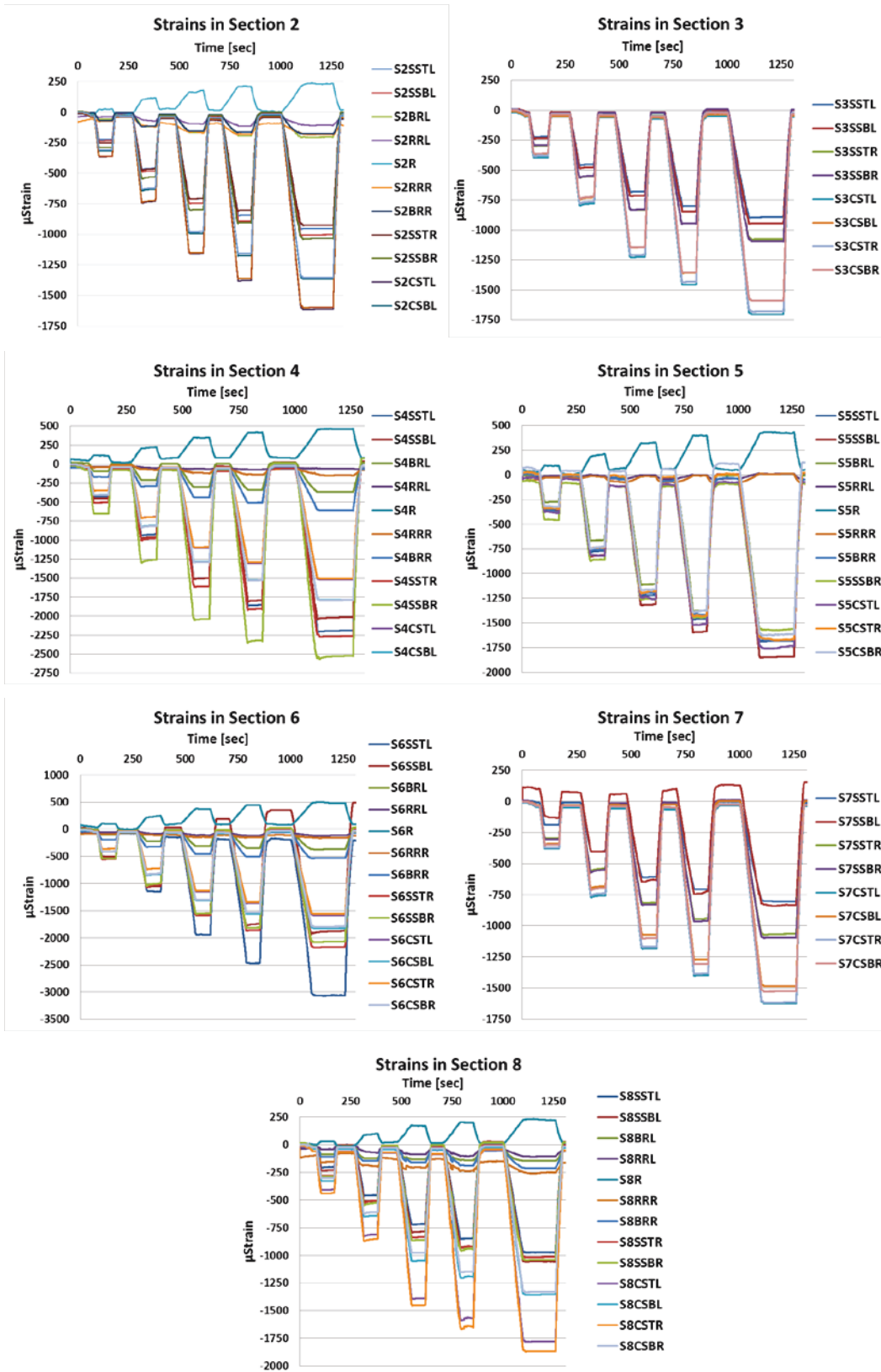


Figure 23. 800,000-pound Load Test Strains

Figure 24 and Figure 25 show that the car incurred minor damage during the 800,000-lb load test. Both side sills had deformations at Cross-Section 6.

Figure 24. Damage on Left Side Sill Following 800,000-pound Load Test

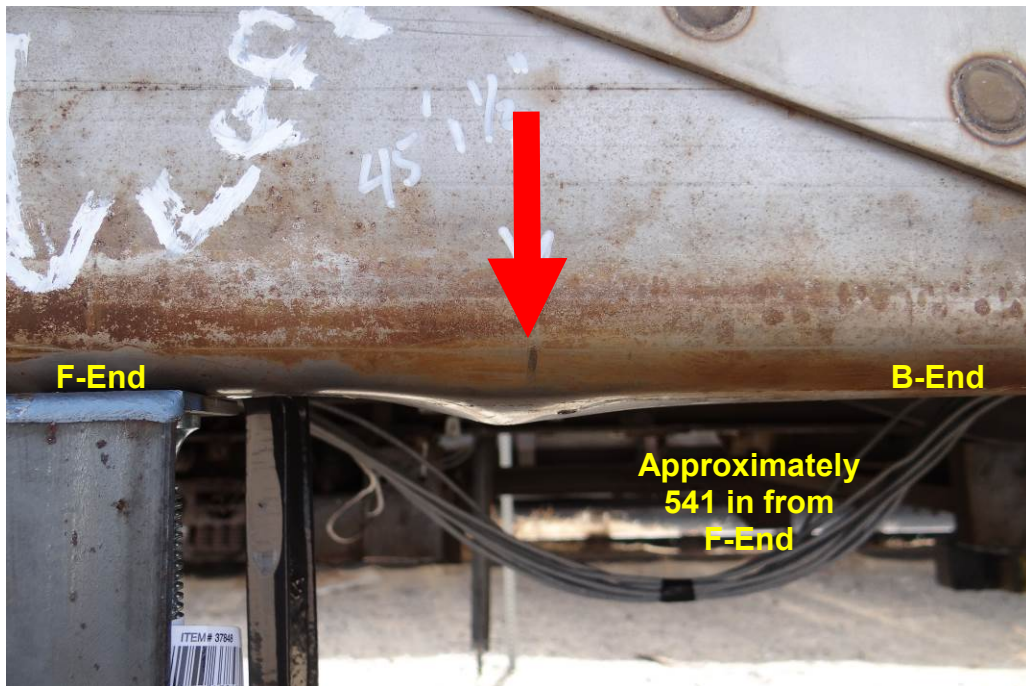


Figure 25. Damage on Left Side Sill Following 800,000-pound Load Test



Figure 26. Damage on Right Side Sill Following 800,000-pound Load Test

4.2 Crippling Load Test Results

Budd M1 Car 9614 was subjected to a crippling load test on July 17, 2013. Loads were applied at all four CEM pockets on the F-end with synchronous stroke control and reacted at all four CEM pockets on the B-end. Buckling first occurred on the roof at approximately 700,000 pounds; complete car crippling occurred at approximately 1,100,000 pounds. The total car length reduction at failure was approximately 3 inches.

4.2.1 Initial Load Application and Slack Removal

Before the test, low-magnitude loads were applied to the car to remove slack in the loading system. Figure 26 and Figure 27 show the initial load offsets for both ends of the car. Once all the slack was removed from the car, the total load applied at the F-end was approximately 8,000 pounds, and all load cells on the reaction end showed nonzero readings. With the slack removed, all the instrumentation was zeroed, and the test began.

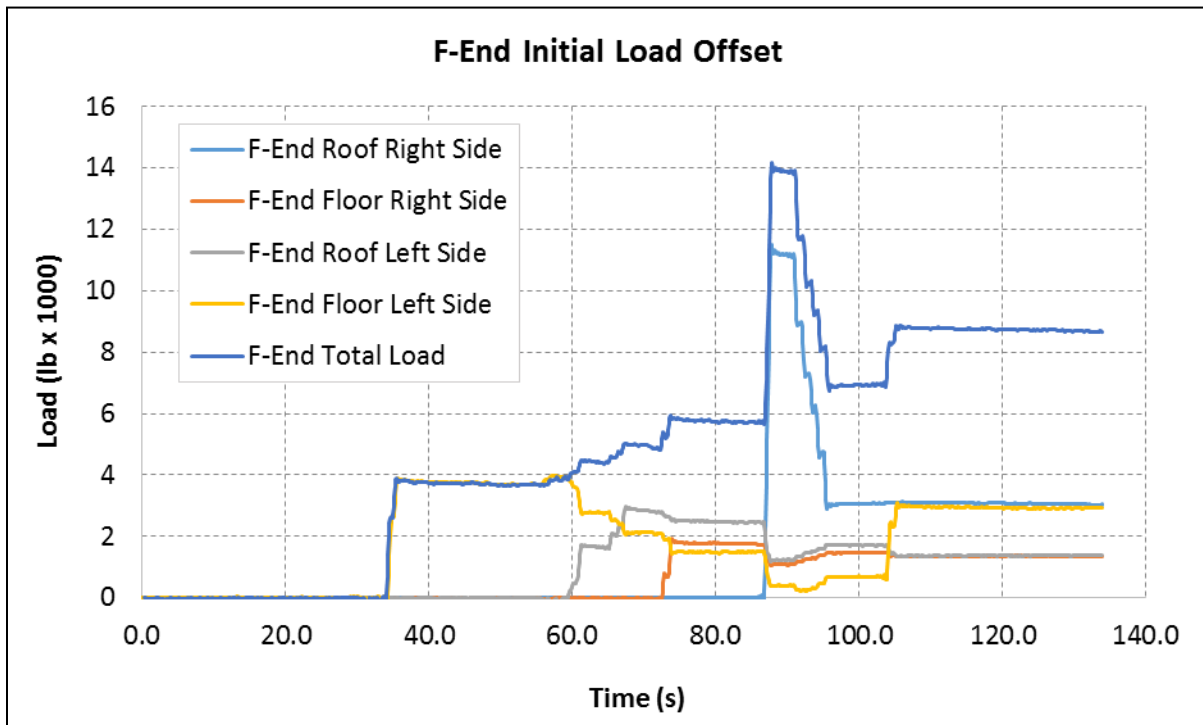


Figure 27. F-End Initial Load Offset

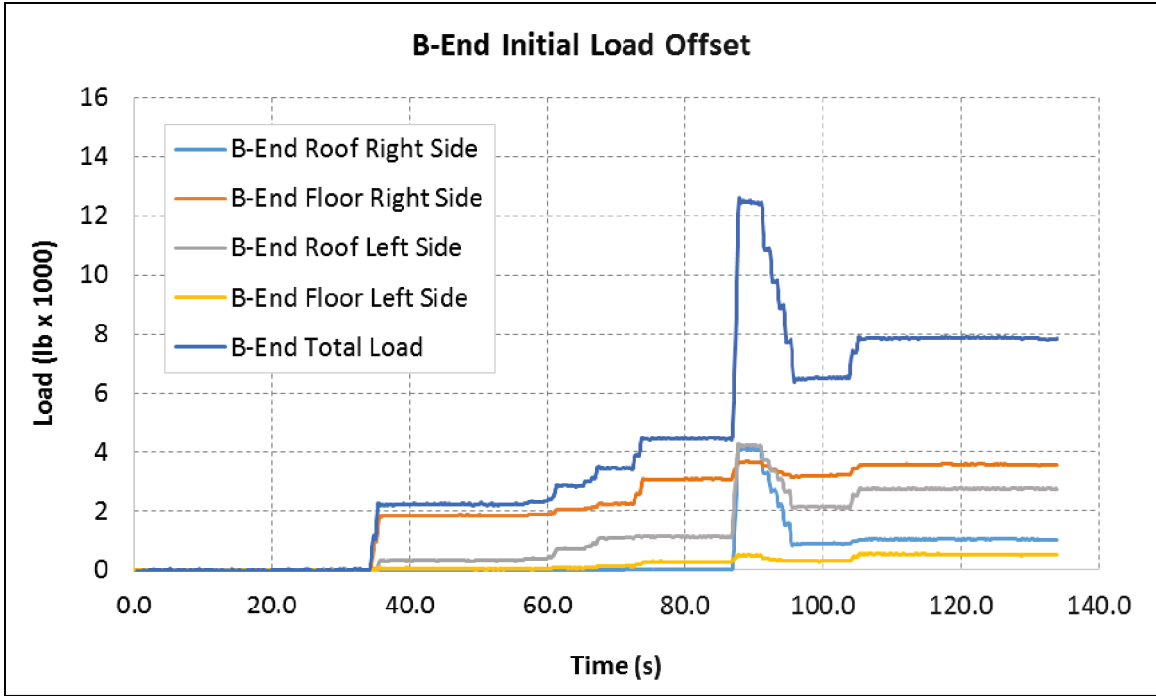


Figure 28. B-End Initial Load Offset

4.2.2 Results

Figure 28 shows the load history for the test. No significant deformations resulted from the 200,000-, 400,000-, and 600,000-lb load cycles.

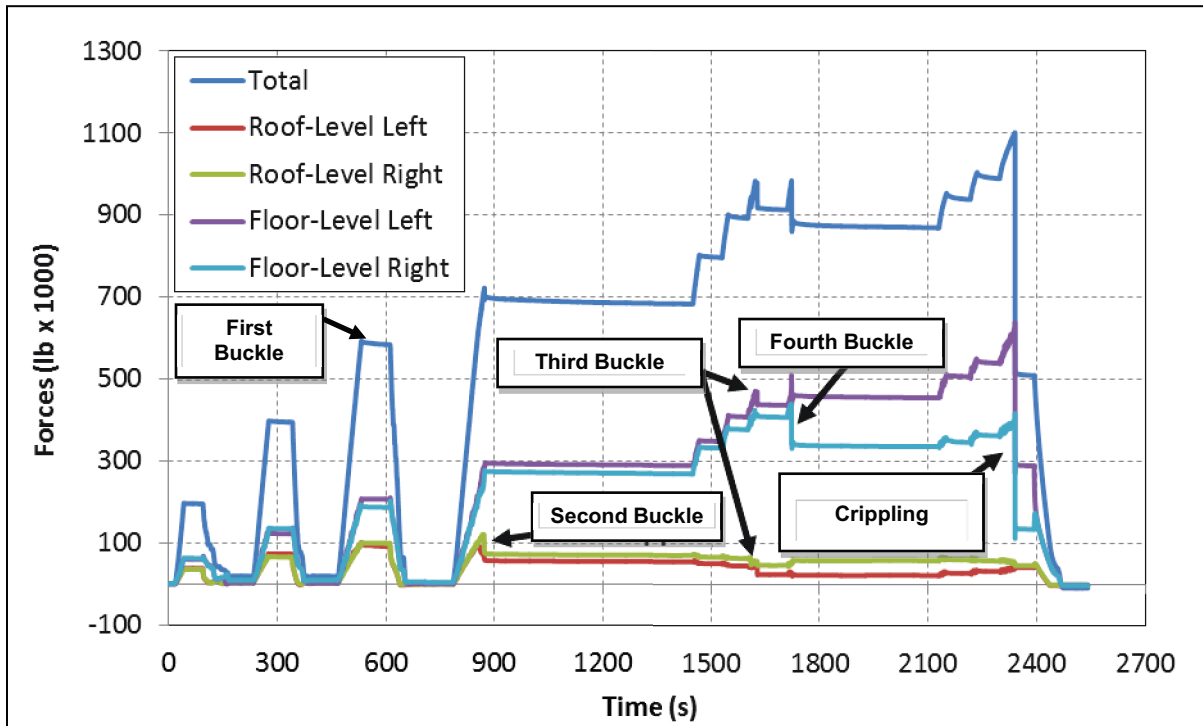


Figure 29. Load History for Crippling Load Test

Through examination of the strain gage data, it appears the roof rail at Cross-Section 2 (closest to the F-end) began to buckle locally just as the total load reached 600,000 pounds. Because the load was held at 600,000 pounds, no reduction in force is apparent due to this buckling. However, the strains experience a near-instantaneous transition from compression to tension, as seen in Figure 29.

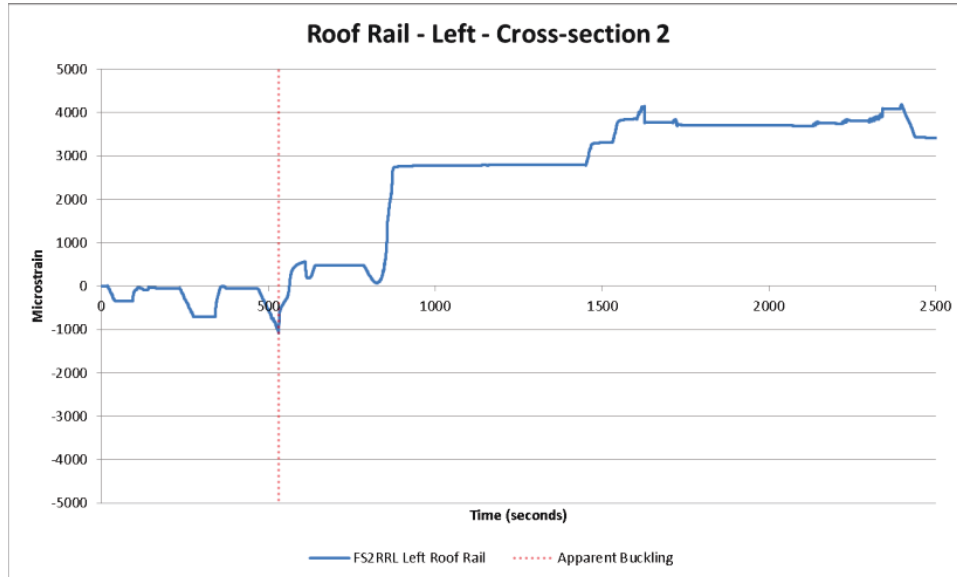


Figure 30. Strain versus Time for Strain Gage on Left Roof Rail, Cross-Section 2

Post-test examination of this area revealed buckling occurred in both the window and roof rails at this location. Prior to the crippling test, an area of pre-existing damage was noted on the window rail in the approximate area that buckled during the test. The two buckled areas are circled in Figure 30. The area of pre-existing damage is outlined with a dashed rectangle in this figure.

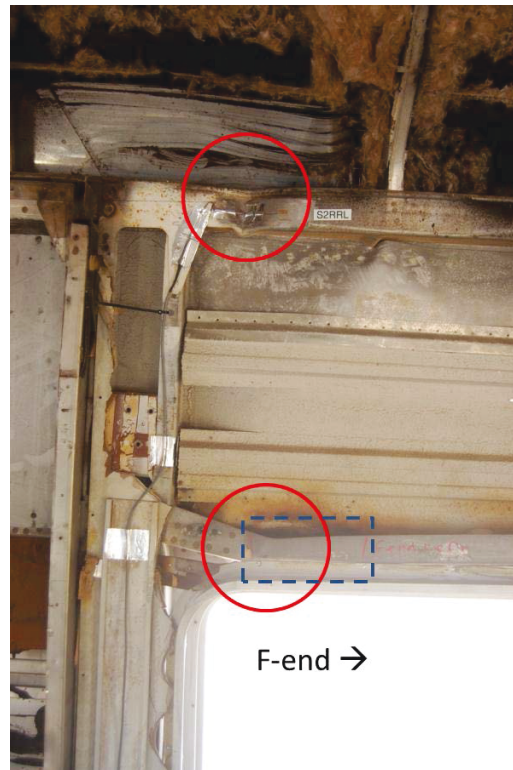


Figure 31. Buckled Areas of Left Roof Rail and Window Rail at Cross-Section 2

During the 800,000-lb load cycle, the car began to buckle on the roof near the F-end doors, as Figure 31 shows. Buckling began at approximately 700,000 pounds. The left side of this figure shows the exterior of the car and the right side of this figure shows the interior right-side wall at Cross-Section 2. The damage to the window rail and roof rail are circled, and an area of pre-test damage to the window rail is outlined with a dashed rectangle.



Figure 32. First Buckle at Approximately 700,000 lbs Exterior (left) and Interior (right)

After the first buckle, loads were increased using 0.25-inch displacement increments rather than increments of applied load. The second buckle occurred on the roof near the B-end doors at approximately 1,000,000 pounds and it was similar to the first buckle. Figure 32 shows the damage resulting from the second buckle. The first two buckling locations were outside of the doors near the ends of the car. The second buckle was located close to the instrumentation Cross-Section 8.

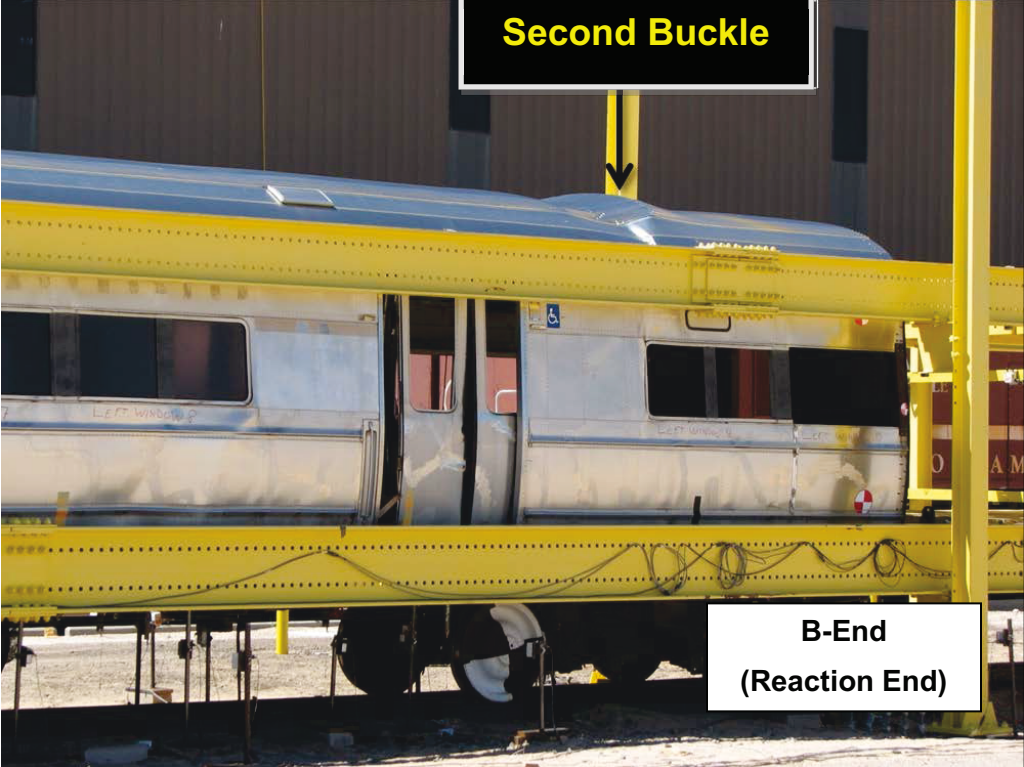


Figure 33. Second Buckle at 1,000,000 lb

During the fourth quarter-inch increment, buckling was observed on the right-side sill near Cross-Section 4 and on the left side sill near Cross-Section 6. Figure 33 shows the buckle on the right-side sill near Cross-Section 4, and Figure 34 shows the buckle on the left side sill near Cross-Section 6. After the 800,000-lb load test, the left side sill was slightly bent at Cross-Section 6. The string potentiometer VLL near the defect was moved 19-inches toward the F-end to avoid losing data at this location. The left side still buckled at that location during the crippling test.



Figure 34. Section 4 Right Side Sill Buckle



Figure 35. Section 6 Left Side Sill Buckle

After six quarter-inch increments, the applied load on the test car was increased until the car could sustain no further load. At approximately 1,100,000 pounds of total load, the car experienced crippling of the center and side sills. The post-test damage to the side sill and the strain-time history from the buckled location at Cross-Section 4 are both shown in Figure 35. The post-test damage to the center sill and the strain-time history from the buckled location at Cross-Section 4 are both shown in Figure 36.

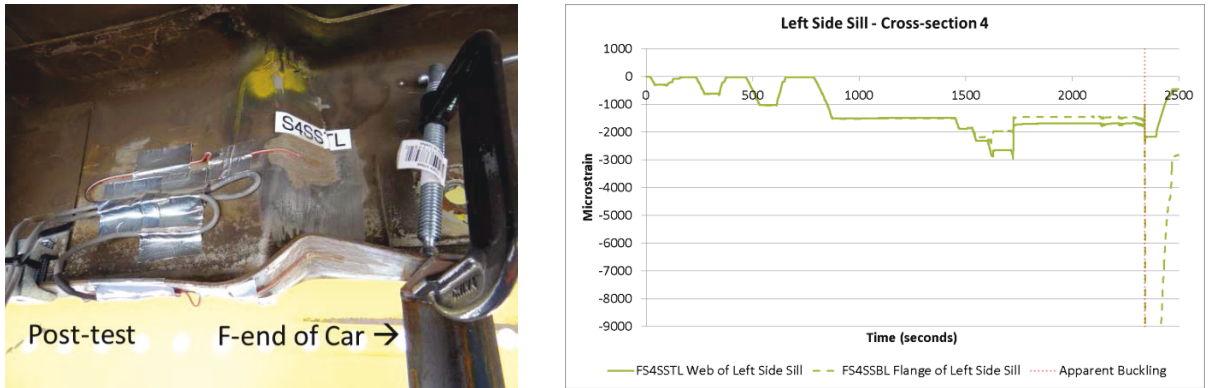


Figure 36. Buckled Left Side Sill at Cross-Section 4 (left) and Strain-time History (right)

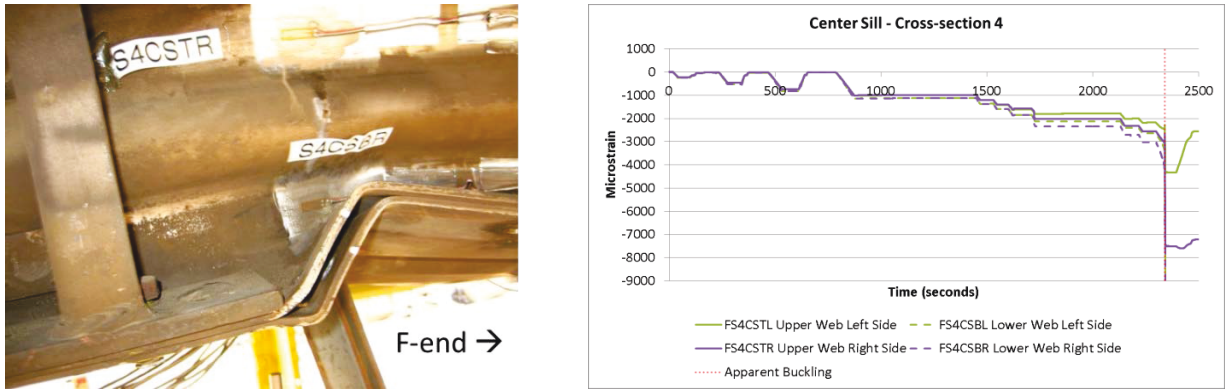


Figure 37. Buckled Center Sill at Cross-Section 4 (left) and Strain-time History (right)

Figure 37 and Figure 38 show load-deflection curves for the crippling test. Figures B7 through B23 in Appendix B depict more of the damage incurred by the car during the crippling load test.

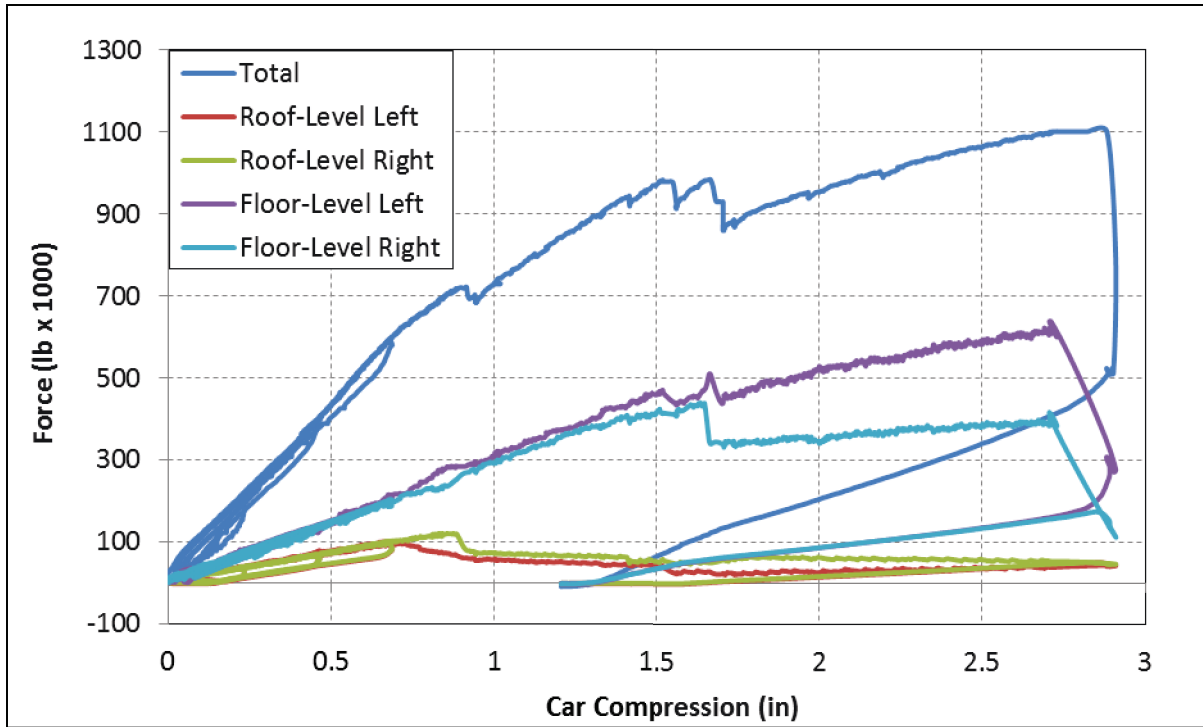


Figure 38. Crippling Load Test – Load Deflection Curves

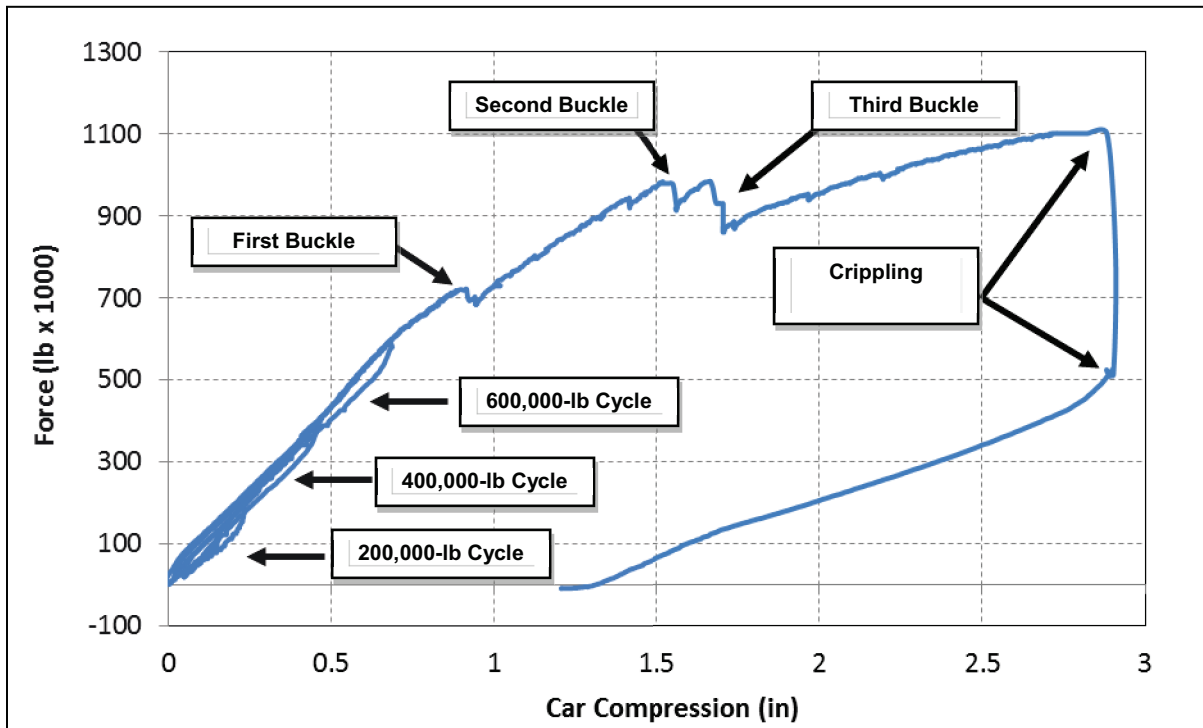


Figure 39. Crippling Load Test - Total Load-Deflection Curve Only

Figure 39 plots the longitudinal displacement of the left side sill throughout the crippling load test. At loads above 800,000 pounds, left side sill displacements at Cross-Sections 1 through 6 increased significantly. However, the displacements at Sections 7 and 8 did not increase under

the same loads, which indicate crippling between Cross-Sections 6 and 7. Figure 34 shows the resulting buckle at Cross-Section 6.

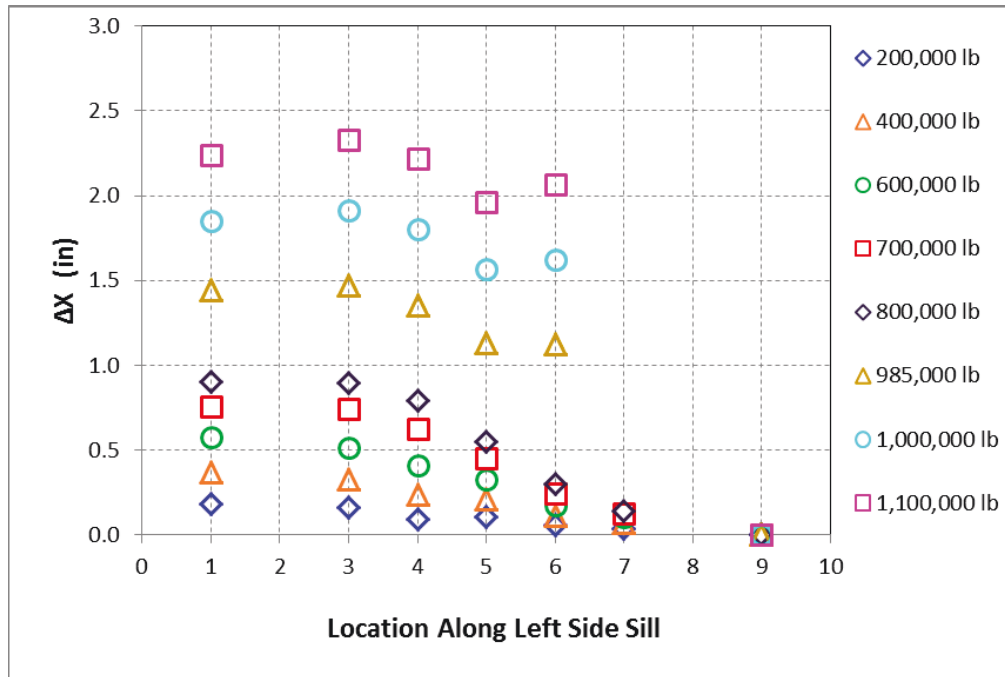


Figure 40. Crippling Load Test Left Side Sill Longitudinal Compression

Center sill displacements show a similar trend in Figure 40. Displacements between Cross-Sections 4 and 6 dropped sharply at higher loads, suggesting possible buckling in the vicinity.

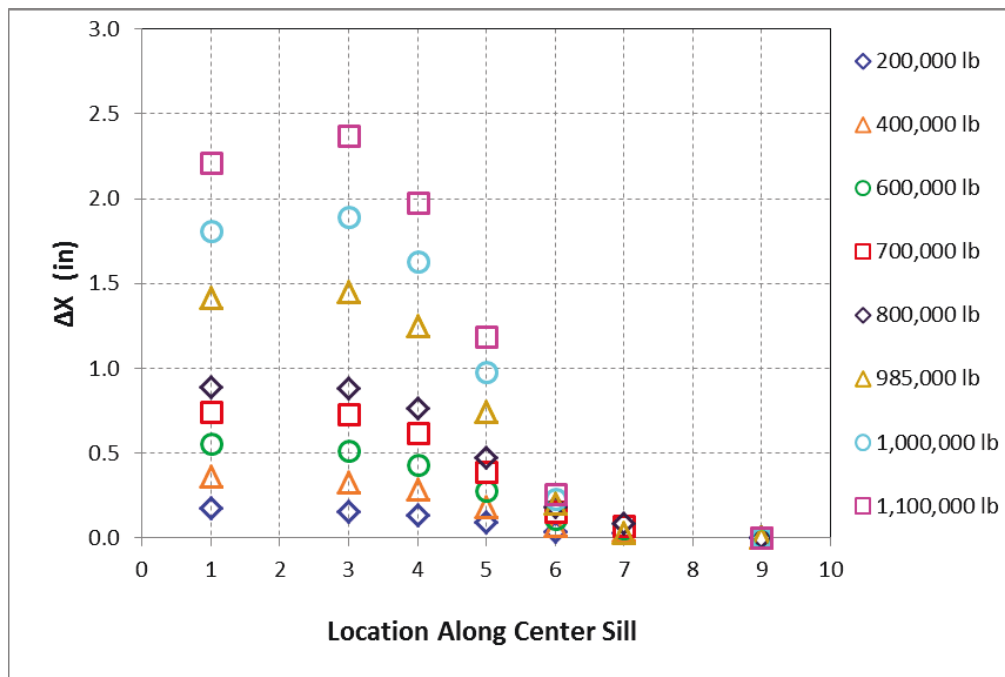


Figure 41. Crippling Load Test Center Sill Longitudinal Compression

Similarly, right side sill displacements at Sections 1 and 3 increased drastically at loads above 800,000 pounds, as seen in Figure 41. Displacements elsewhere on the side sill increased considerably less under the same loads, suggesting there was buckling between Sections 3 and 4. Figure 33 shows the resulting buckle.

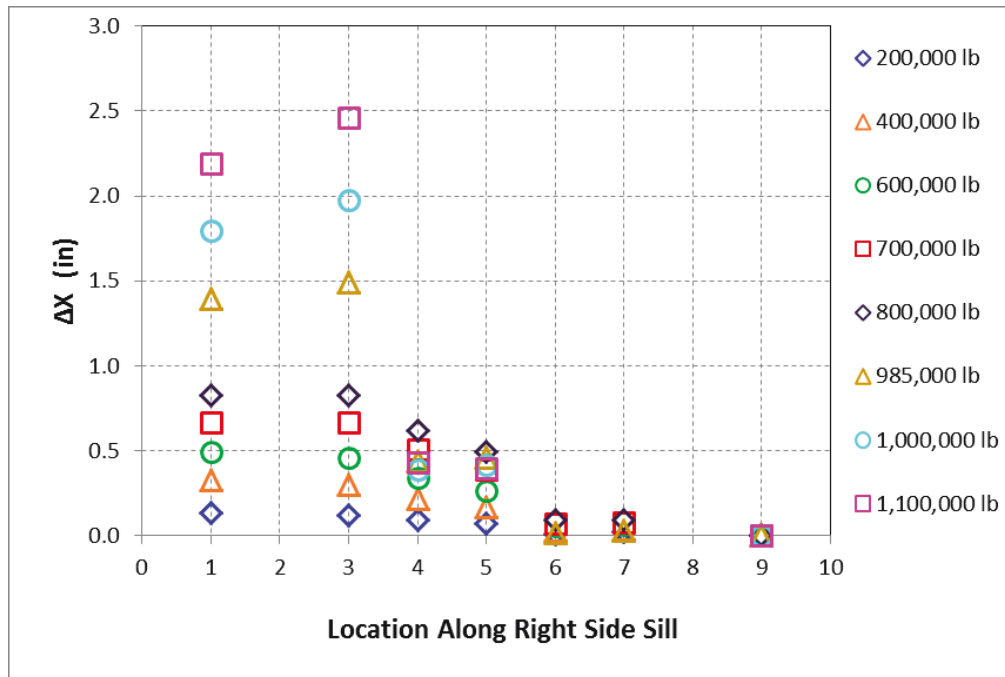


Figure 42. Crippling Load Test Right Side Sill Longitudinal Compression

Figure 42 shows plots of strains for the crippling load test. The section numbers in the plot titles represent the various instrumentation Cross-Sections along the length of the car. Channel names correspond to those in Appendix A (see Table A2). Several strain gages were placed at or very close to the buckling locations, as documented on the post-test photos in Appendix B. Therefore, significant change in strains was observed when buckling occurred. Single strain gage S7SSBL measured unrealistic strains and was considered as damaged.

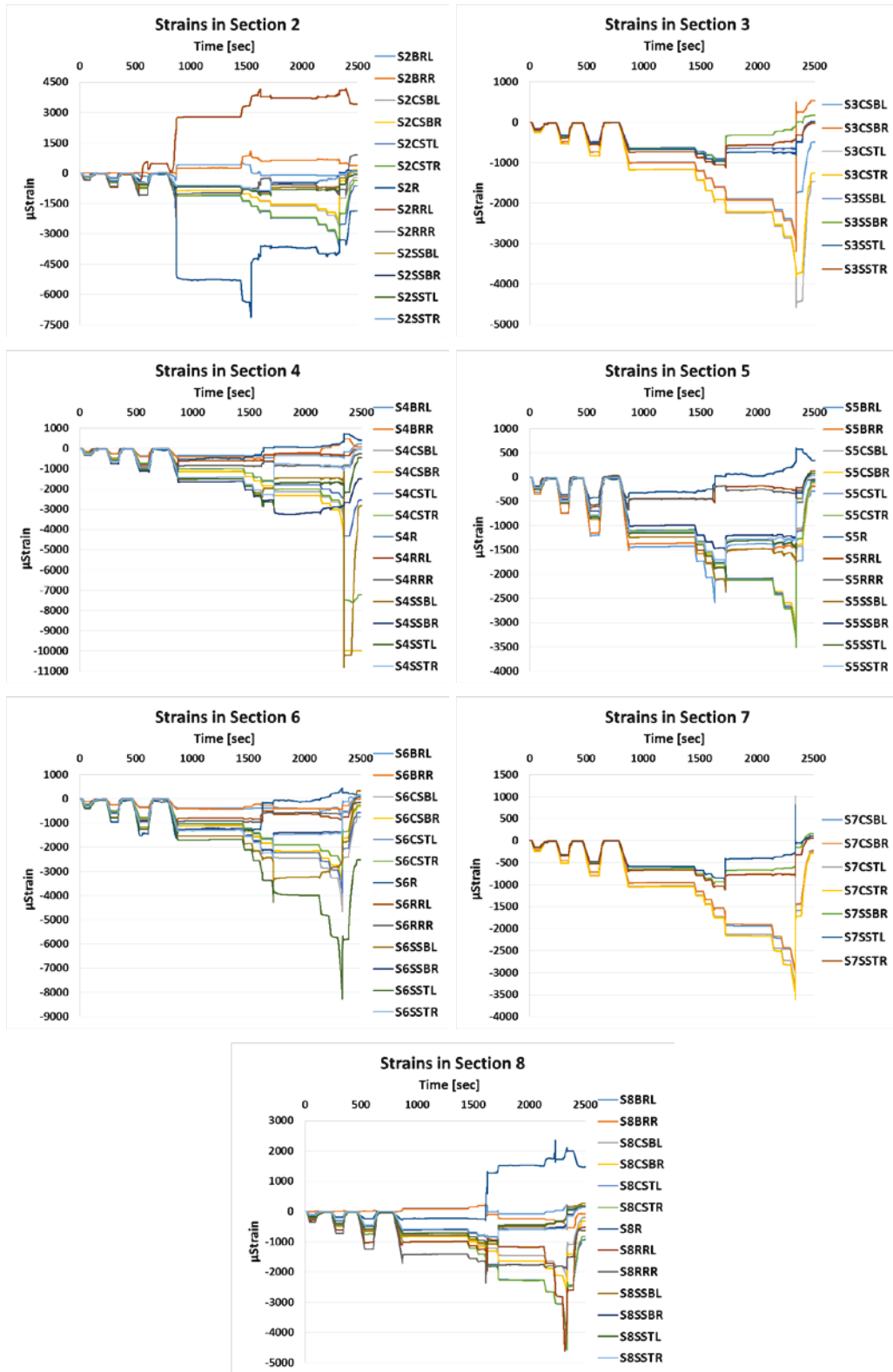


Figure 43. Crippling Load Test — Strains

5. Analysis Overview - Arup

5.1 Finite Element Model in LS-DYNA

Figure 43 shows Arup's FE model. The model includes approximately 700,000 shell and beam elements. The analysis was carried out using the commercially available LS-DYNA FE software.

Spot welds and bolted connections are generally modeled using beam elements and linear welds modeled as tied contacts.

A rigid representation of the loading bars from the test is used to apply the load to the railcar through a contact definition.

See Appendix C for additional details on the model and analysis setup.

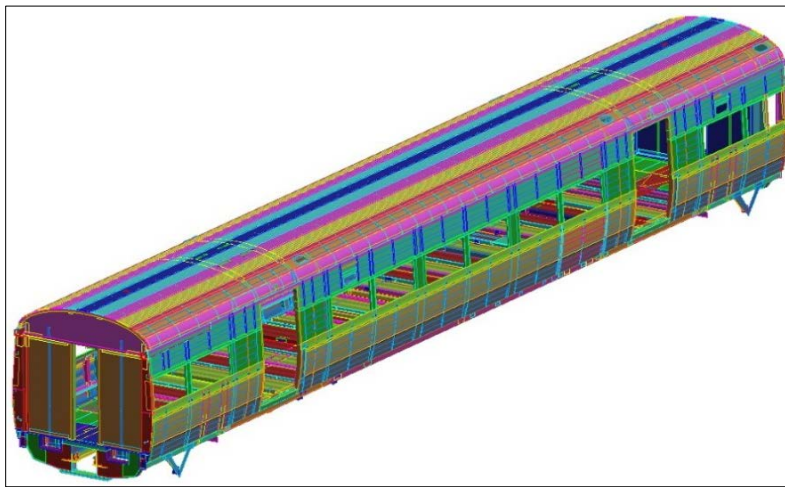


Figure 44. Finite Element Model of the Budd M1 Railcar

5.2 Materials

Materials available from the results of the physical coupon test were modeled in LS-DYNA as nonlinear plastic. Where such coupon tests were not available, bilinear material formulations were used based on codified minimum values. Figure 44 illustrates typical nonlinear (right side) and bilinear (left side) formulations. See Appendix D for additional details.

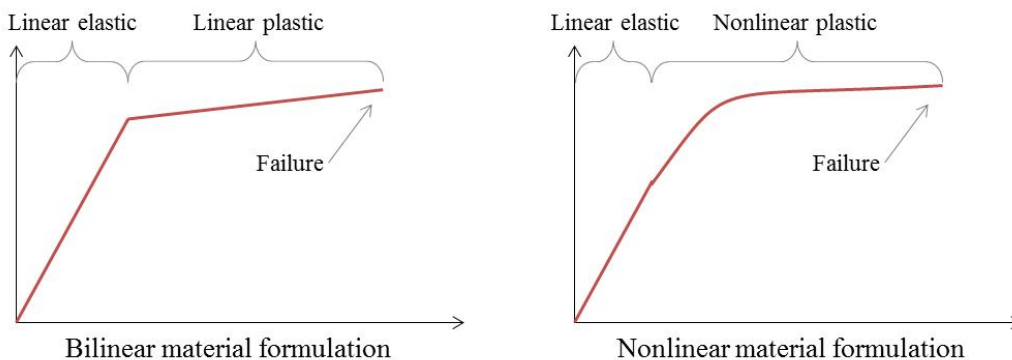


Figure 45. Bilinear and Nonlinear Material Formulations

5.3 Model Verification

The verification studies for the 800,000-lb load analysis looked at force transfer through the model, examined the energy balance of the analysis, and determined if the effect of element formulation was within the guidelines given in [2].

See Appendix F for additional details.

5.4 Post-Processing of Test Results

The analysis and physical test results were adjusted to disaggregate rigid body motion from railcar deformations in both tests.

See Appendix I for additional details.

5.5 Calibration of the Model to the 800,000-Pound Load Test

The 800,000-lb load analysis was calibrated to the results of the physical test. Boundary conditions and spot weld stiffness were the parameters that were considered and tested for calibration. In the end, truck spring stiffness was the only calibration adjustment that had a significant impact on the results. Reducing the spring stiffness from 17,000 lbs/in to 2,000 lbs/in increased the vertical deflection of the railcar by around 13 percent, bringing it in line with the physical test results. It should be noted that the original stiffness was selected to reduce the amount the car settled as gravity was applied to the model, while the new stiffness was based on advice on typical stiffnesses of railcar truck springs.

All the other calibrations that were investigated had a minimal effect on the results.

Figure 45 compares test and analysis force-displacement results for several locations on the car. The results from the final calibrated 800,000-lb load analysis correlated well with the physical test for displacements and for strain history in general. Some differences in the level of strain were observed, particularly where local buckling occurred.

See Appendix E for additional details.

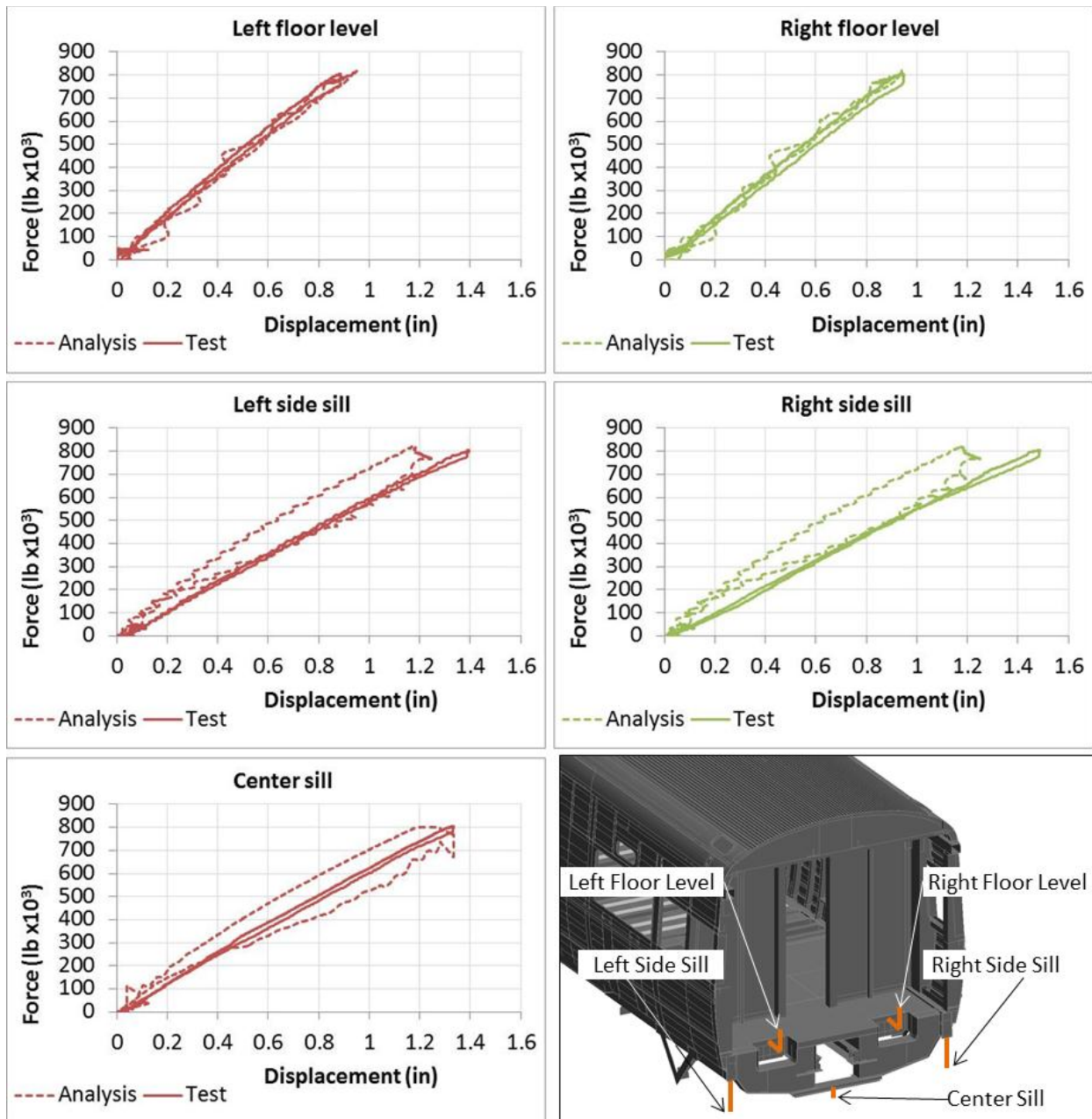


Figure 46. Force-displacement Curves for the 800,000-pound Load Test and Analysis

5.6 Comparison of Arup’s FE Analyses with Crippling Load Test Results

For the crippling load test, the railcar was resting on its trucks. The load was applied with hydraulic jacks to the F-end of the car at the two upper CEM pockets located on the roof and the two floor-level CEM attachment locations. This load was resisted at the B-end of the car at the same four locations by a set of restraining bars (see Appendix C for more details). The jacks were displacement controlled so that all four load points displaced at the same rate.

Following calibration (see subsection 5.5), the results of the 800,000-lb load analysis correlated well with the results of the actual (physical) test. This calibrated model was used to make predictions for the crippling load test. The predictions (made prior to the test) and the crippling load test results are compared in this section of the report.

See Appendix G for additional results.

5.6.1 Carbody Damage and Force-displacement Results

Figure 46 contains maps of the failure locations for the crippling load analysis (top) and the crippling load test (bottom). The locations are numbered in order of failure.

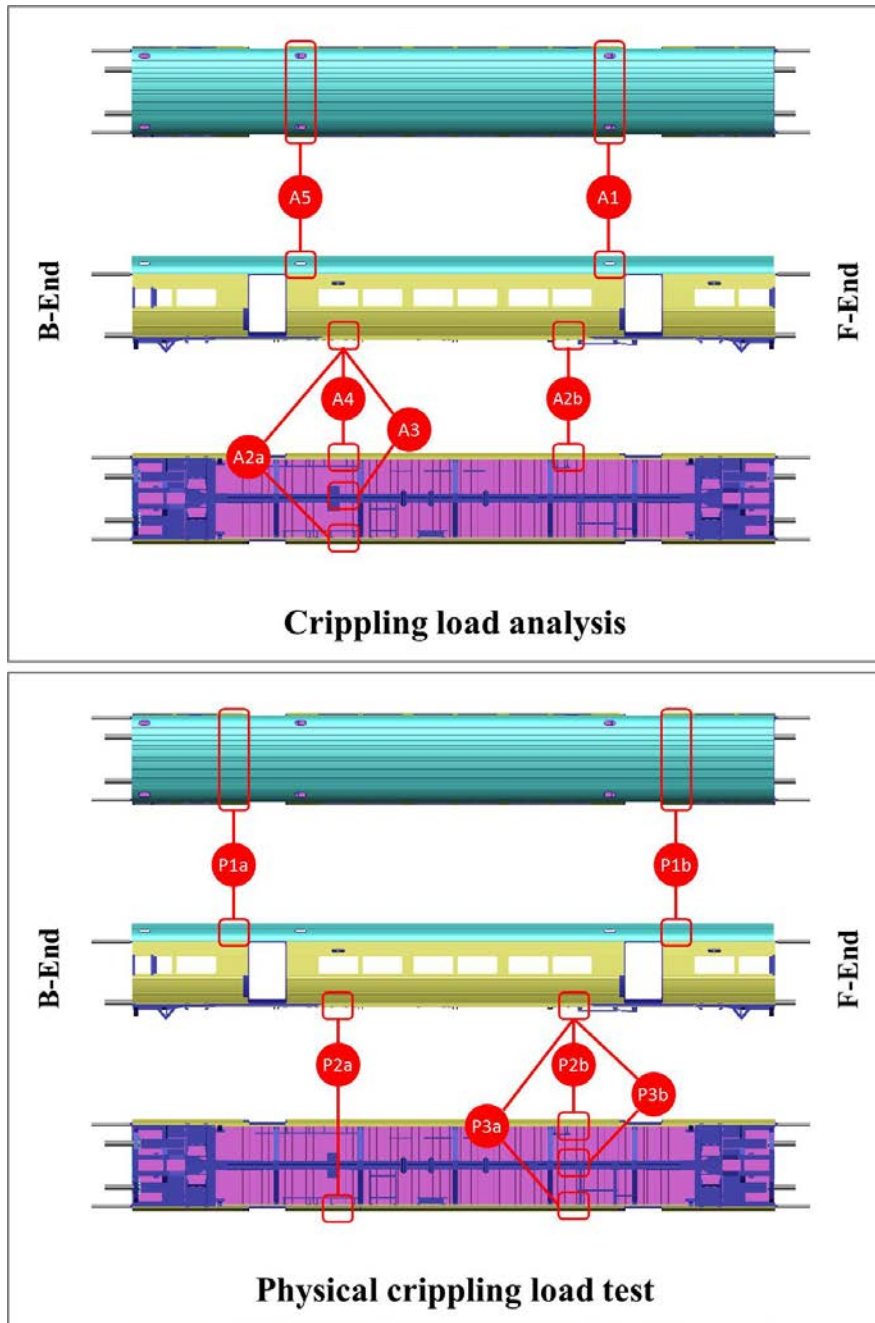


Figure 47. Maps of Failure Points in Crippling Test (bottom) and Analysis (top)

By comparing the crippling load analysis results (solid lines) to the crippling load test results (dashed lines), Figure 47 shows that reasonable correlation was achieved up to the first failure point (in the roof at about 0.8-inch displacement). During this phase, the analysis generally overstates the stiffness of the car floor; whereas, at roof level, the analysis and the crippling load test results match very closely.

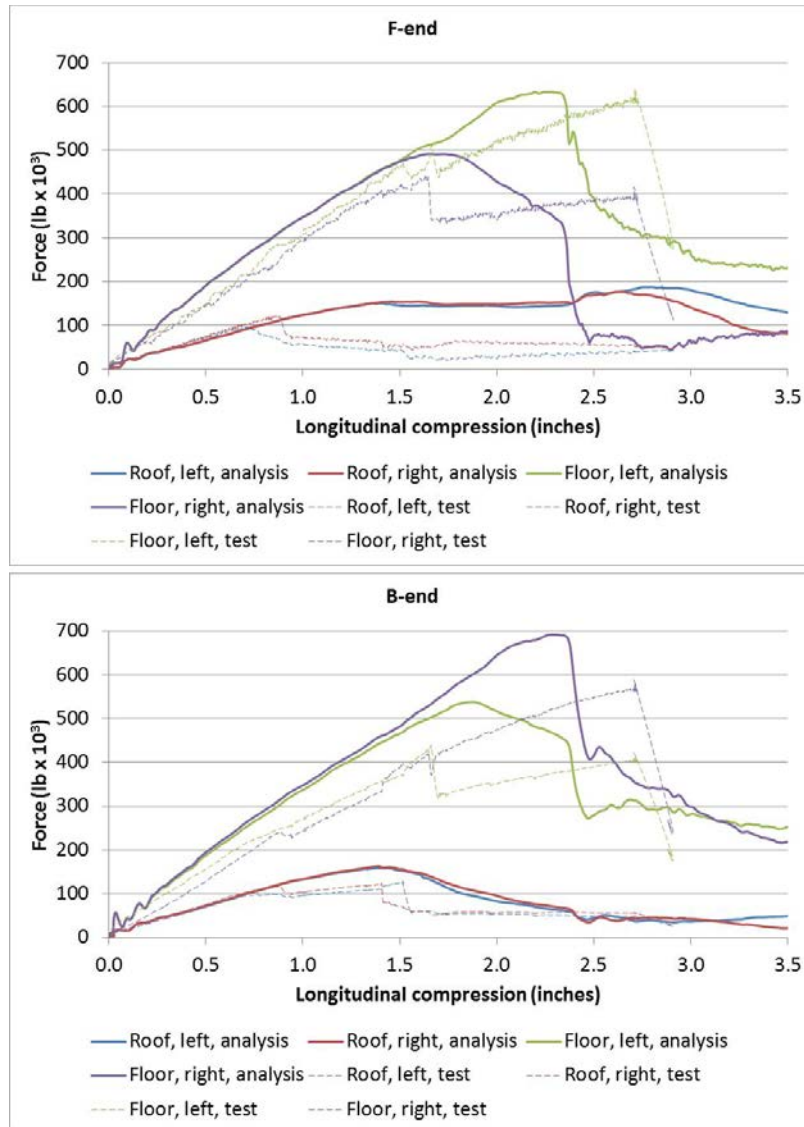


Figure 48. Force-Displacement Curves for the Crippling Analysis and Crippling Load Test Results at Roof and Floor, Left and Right

In both the crippling load test and the corresponding analysis, the distribution of loads between the four loading points at each end differs between the F- and B-end. This occurs when consecutive failure shifts the load paths as failed components lose stiffness. For instance, in the crippling load test, the roof failed at the F-end first. This causes the load in the top loading points at the F-end to drop off and transfer to the bottom loading points, while the load at the B-end, where the roof still has its original stiffness, continues to be more evenly distributed between the top and the bottom loading points as the compression continues to increase.

The main difference between the performances of the simulated and physical railcars is the point at which the roof buckled and the effect this had on the subsequent resistance history. Also, the analysis and the crippling load test results differed in terms of the side sills' post-buckle behavior.

Figure 48 shows that there is a marked difference in the resulting overall strength of the railcars in the test and the analysis. The physical railcar lost a large percentage of the resistance from each component as it failed, while the simulated railcar tended to have a more gradual decline in resistance. As a result, each local buckle had a much larger impact on the overall resistance of the physical railcar than the simulated railcar, and the prediction for overall maximum load was around 21 percent larger than that recorded in the crippling load test.

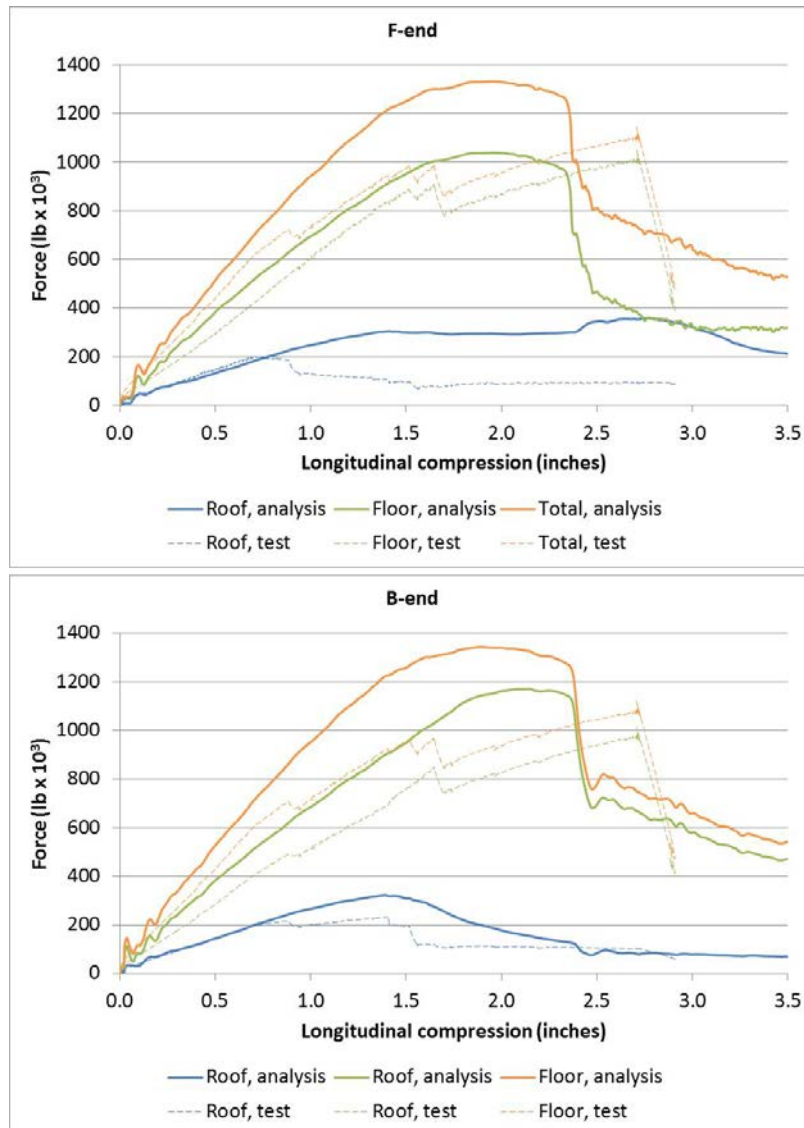


Figure 49. Force-displacement for the Crippling Load Analysis and Test Results at Roof and Floor, and for Total Overall Load

5.6.2 Roof buckling

Figure 49 shows the predicted and actual locations of the roof buckling failures. The simulation predicted that the roof would fail just inboard of the doorways (locations A1 and A5 in Figure 46). This is a location which would have an abrupt change in stiffness due to the reinforcement around the doorway, and reduced strength because of the vents penetrating the roof structure.

In the crippling load test, the failure occurred outboard of the doors (locations P1a and P1b in Figure 46). The difference in the location is may be due to additional structural elements (longitudinal stringers and duct work) within the roof structure that were not in the available drawings, but were revealed during asbestos abatement when some of the ceiling panels were removed. The additional structures may have prevented the buckling deformation of the roof that was predicted by the analysis. Instead, the buckling occurred in an unstiffened area that was outboard of the doors.

There was also a difference in the nature of the failure in the analysis and the test. The failure was ductile in the analysis, with the wave-like deformations increasing gradually without significant loss of resistance. The physical crippling test, by contrast, showed a sudden failure of the roof as the corrugations folded abruptly with significant loss of resistance.

The gradual versus abrupt failures of the roof may account for much of the difference in post-failure stiffness profiles shown in subsection 5.6.1.

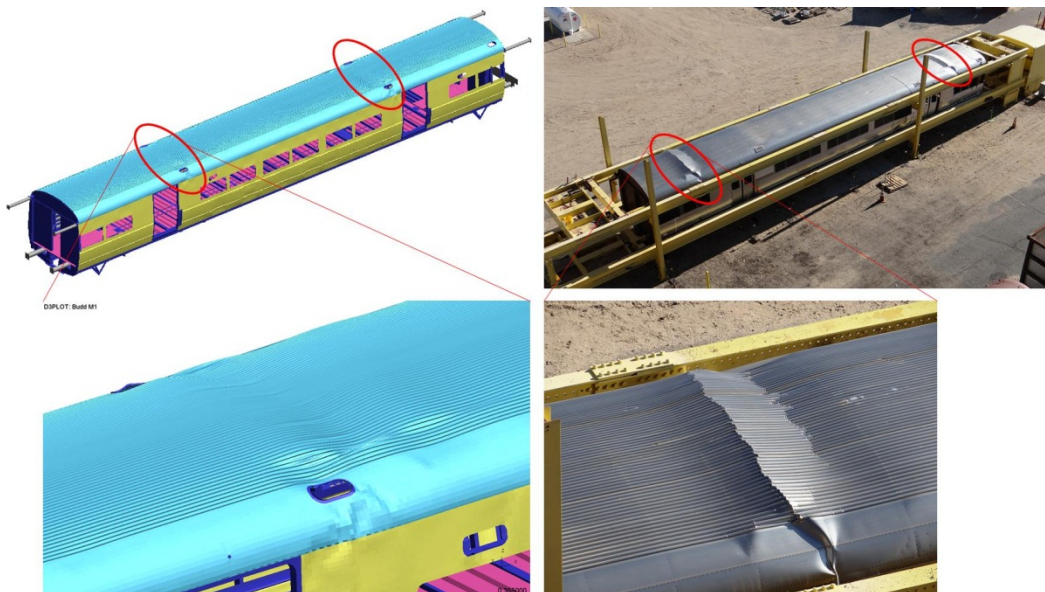


Figure 50. Roof Failure in the Simulated and Physical Railcars

5.6.3 Side Sill and Center Sill Failures

Failures in the side and center sills occurred at approximately the same locations in the analysis and the crippling load test. In some cases, the failure modes were very similar. In others, there are important differences.

Figure 50 shows that in the crippling load test and the analysis, the side sill underwent buckling at the repaired location (locations A2b and P2b).

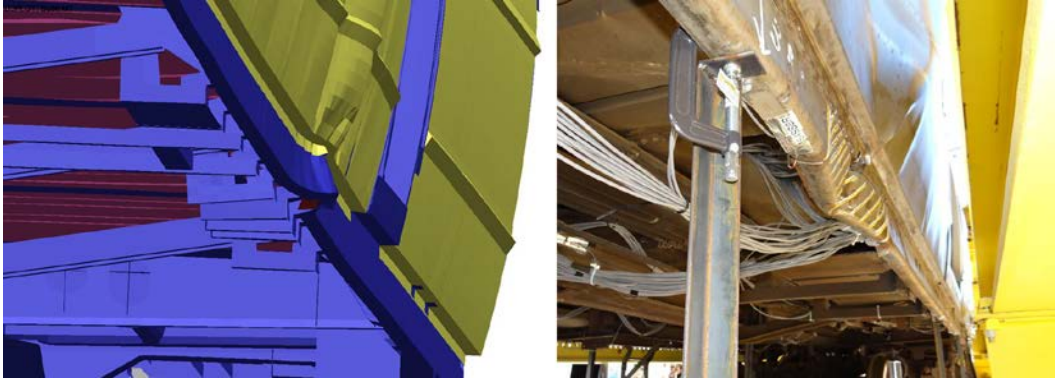


Figure 51. Buckling at the Repair Location in the Crippling Load Analysis (left) and Test (right)

In the test, the side sill also buckled on the opposite side of the repair, in the same longitudinal location (P3a in Figure). This buckle included a folding of the side sill in conjunction with delamination of the layered components and tearing at a spot weld.

In the diagonally opposite location, the analysis model underwent a similar failure (A4 in Figure). The side sill folded in the same way and delamination started to occur. However, because the spot weld definitions in the analysis did not include failure, the tearing was not simulated and the delamination was limited. Figure 51 compares these buckles on the model and the physical railcar.

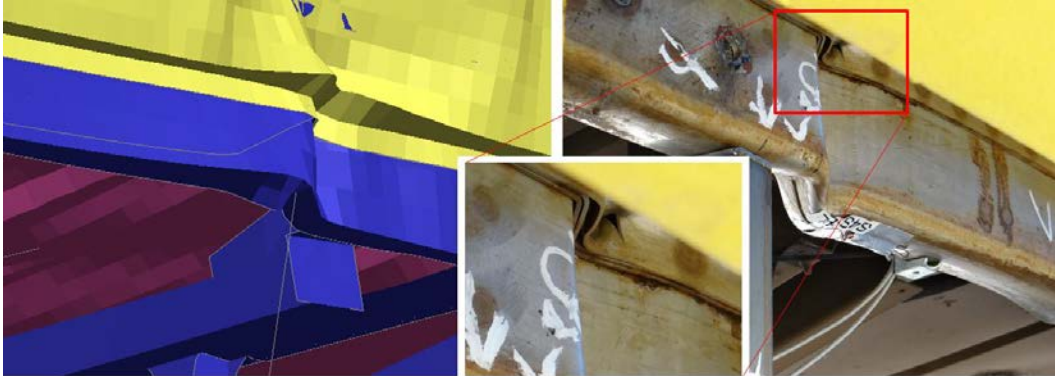


Figure 52. Similar Side Sill Buckles in the Crippling Load Analysis (left) and Test (right)

This same phenomenon occurred in other locations on the side sills and center sill. In the analysis, ductile failure occurred as the buckles gradually increased in magnitude. During the crippling load test, the failure was more sudden and the tearing of the parent material near spot welds may have been a factor in this. Figure 52 shows two examples.

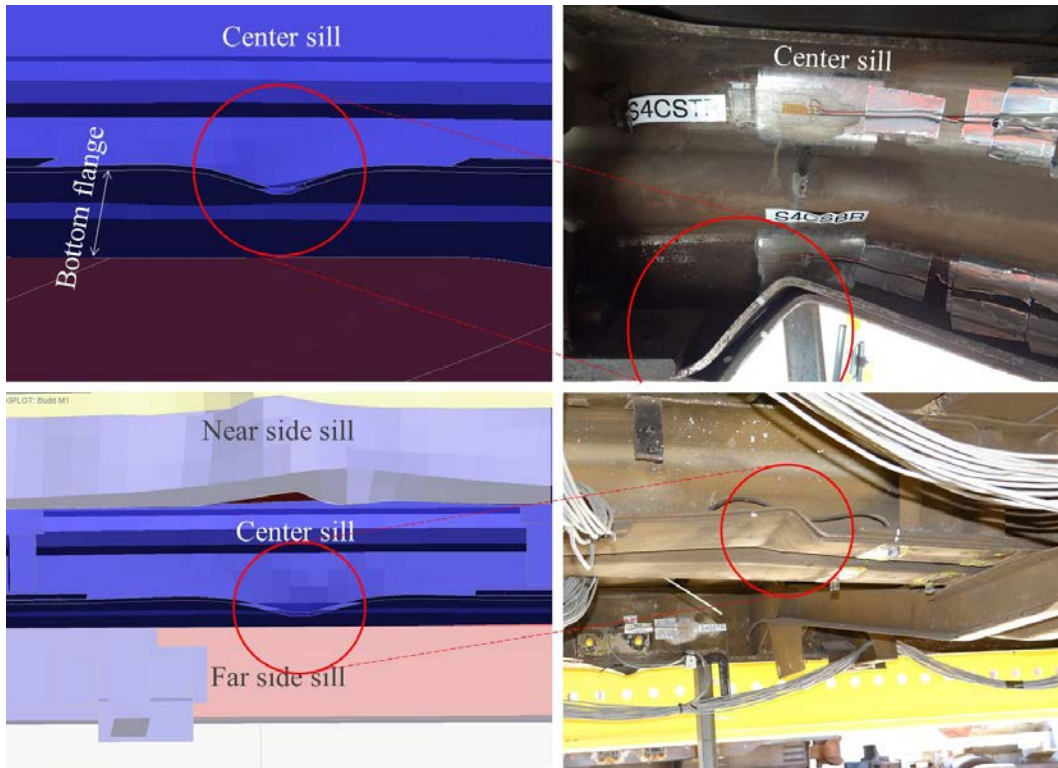


Figure 53. Comparison of Buckles in the Center Sill (top — A3, P3b)

6. Analysis Overview – Volpe

6.1 Finite Element Model in Abaqus/Explicit

The Volpe FE model was pre-processed using Abaqus/CAE and executed using the Abaqus/Explicit solver [5]. Abaqus/Explicit is a commercially-available non-linear dynamic explicit finite element solver. While both the 800,000-pound and crippling load tests were executed at a quasi-static speed, an explicit FE solver was used to ensure that the model adequately captured the non-linear effects of the crippling test. While the 800,000-lb load test did not result in any significant non-linearities or large displacements, Volpe chose Abaqus/Explicit to simulate this test so it could ensure consistency of results between the model used to simulate the 800,000-lb test and the crippling test.

Volpe's FE model is shown in Figure 53. This model is based on a half-symmetric FE model of a CEM-equipped Budd M-1 car used in the CEM train-to-train test [3]. That model featured a highly-refined representation of the crush zone at the F-end of the car with a more coarsely-meshed occupant volume. To make the previous model a better fit for current occupant volume integrity research, Volpe removed the CEM elements from the ends of the model, replaced many beam elements throughout the occupant volume with shell element representations of the structural members, and modeled the left- and right-sides of the car. The final FE model featured approximately 750,000 nodes and approximately 760,000 elements.

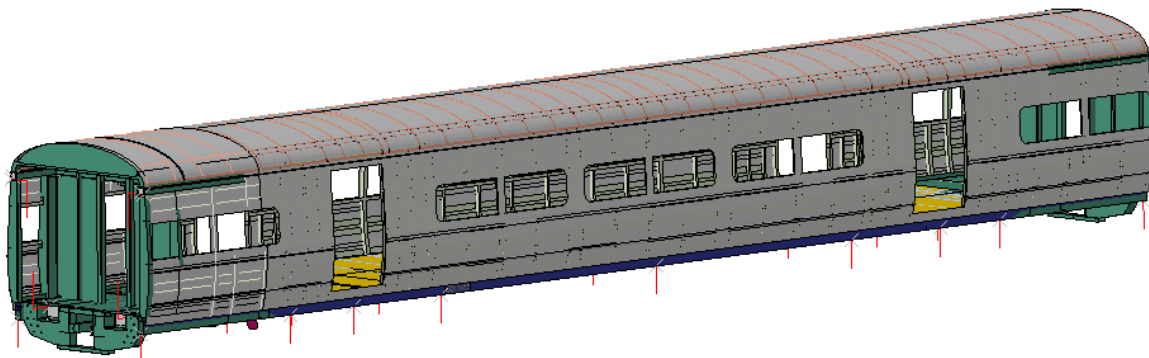


Figure 54. Volpe FE Model of M1 Passenger Car

Further details on Volpe's FE model can be found in Appendix J.

6.2 Materials

Prior to the tests, material samples of various structural components were removed from a companion M1 railcar. Coupons were taken from the sidewall post, cross bearer, floor panel, roof carline, external wall, center sill, and side sill. A minimum of three samples were taken from each location. For the majority of locations, six samples were tested. These data were used to create bi-linear representations of the materials making up the occupant volume of the M1 railcar.

Discussion of the material properties in the Volpe FE model, including the distribution of materials throughout the model, is provided in Appendix K.

6.3 Model Verification

Because a dynamic FE solver was used to simulate both the 800,000-lb test and the crippling test, care had to be taken to ensure that for each model the loading was applied sufficiently slowly to avoid introducing any dynamic effects into the results. Following the guidelines provided in the ETF's criteria and procedures report, both the 800,000 pound and crippling models were evaluated [2]. The ETF provided two criteria for establishing that a model may be considered quasi-static; only one of the criteria must be met. In this research program, both criteria were applied to each of Volpe's models.

The 800,000-lb model was found to have some initial dynamic effects that subsided prior to reaching the target load of 800,000 pounds. The crippling model was found to have some small initial dynamic effects that subsided well before buckling began to occur in the model.

A full description of the evaluation of the Volpe models and the criteria applied can be found in Appendix M.

6.4 Post-processing of Test Results

The 800,000 pound and crippling test results were both post-processed before being compared with the corresponding FE results. For all channels, the measurements were zeroed to correspond with the approximate time when the car was settled into the test frame. No further post-processing of the strain measurements occurred.

Displacement measurements underwent further post-processing to discriminate vertical, lateral, and longitudinal displacement measurements. While the string potentiometers installed on the car were oriented in the three principal directions, displacement in one direction could register as a change-in-length in an orthogonal string. For example, vertical uplift of a given point will result in an extension of the longitudinally-oriented string potentiometer ("pot"), introducing error into the longitudinal string pot's measurement. By installing VLL arrays of string pots between the underside of the car and ground, the three measurements can be used to resolve the motion of the point on the car into its true vertical, lateral, and longitudinal components. The mathematical relationships used to resolve the string pots can be found in [6].

Most of test displacement results that are compared with Volpe's FE displacement results have undergone this post-processing technique. Because VLL arrays were not installed at the roof-level of the car, this adjustment was not possible for roof-level measurements.

6.5 Comparison of the Model to the 800,000-pound Load Test

Following the 800,000-lb load test, the boundary conditions on the model were modified to replicate the test results. The post-test FE model and the test results themselves were compared so Volpe could establish that the model was successfully capturing the overall behavior of the M1 car during the 800,000-lb test. The global force-displacement behavior, the vertical deformation of the carbody, and the strains throughout the occupied volume were the key results that were compared between the test and the FEA. The complete set of comparisons between the instrumented locations in the 800,000-lb test and Volpe's post-test FE analysis is provided in Appendix L.

To determine the overall shortening of the M1 car during the 800,000-lb test, the rigid body displacement associated with lengthening of the test frame must first be subtracted from the live end displacements. As shown in Figure 15, longitudinal string potentiometers were installed between the car and the ground at the left, center, and right side of both the F-end (Cross-Section 1) and the B-end of the car (Cross-Section 9). The differences between the F-end and B-end measurements were calculated for both test and FE model using the displacements at these locations. Figure 54 shows the force-displacement behavior from both the test and the FEA on the left side sill, center, and right side sill. These figures also feature a $\pm 10\%$ envelope on the test measurements. This envelope is consistent with the ETF's criteria for demonstrating model validation.

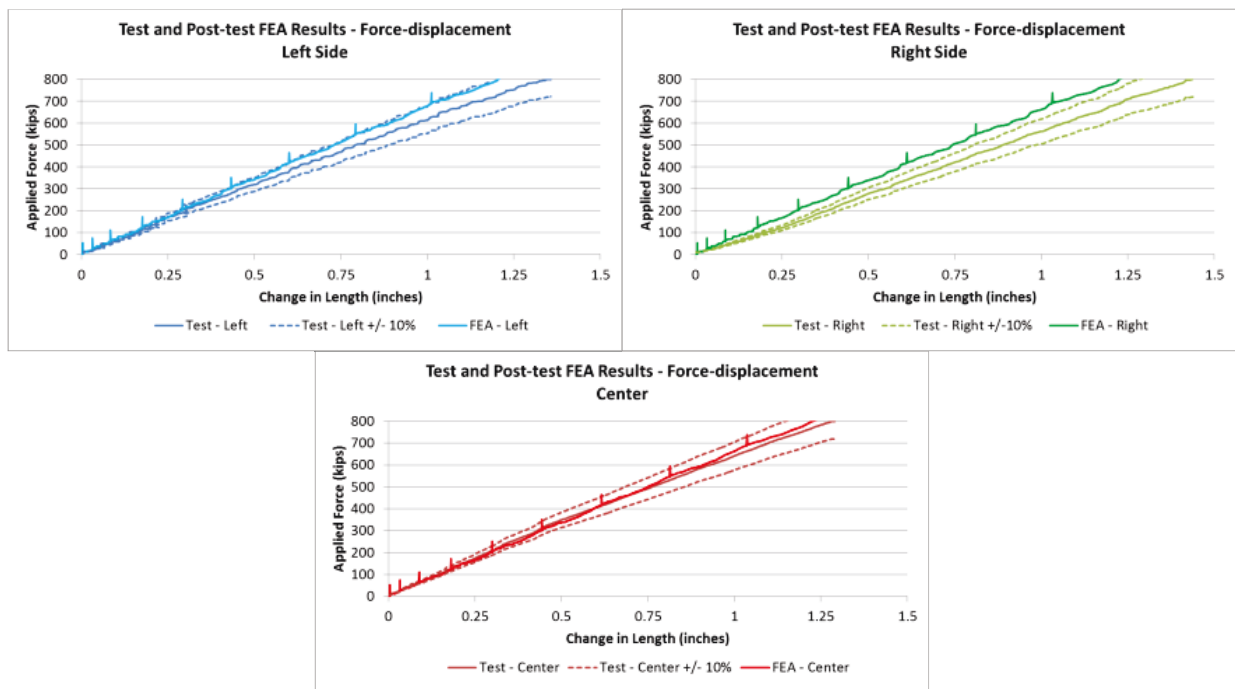


Figure 55. 800,000-pound Test and Volpe FE Force-displacement Results

The test and the FE force-displacement results are within 10 percent of each other for the left-side sill and the center sill. At the right-side sill, the FE model is apparently stiffer than the measured change in length of the M1 car, which results in the analytical force-displacement behavior falling slightly outside of the 10-percent envelope on the test results.

The second global behavior that Volpe compared with the FEA was the vertical deflection of the carbody. After examining the results of the 800,000-lb test, it appeared the carbody exhibited a tendency to roll during the test. At the center of the car, the left side of the carbody lifted up more than either the center or the right side. An attempt was made to replicate this behavior in the post-test FE model by applying vertical and longitudinal displacement of the loading plates (see Appendix J for a description of the loading conditions in the 800,000-lb simulation). Figure 55 shows the vertical displacement profiles of the car on the left side sill, center sill, and right side sill for both the test and the model under an axial load of 800,000 pounds. The horizontal axis represents distance from the F-end of the car (Cross-Section 1).

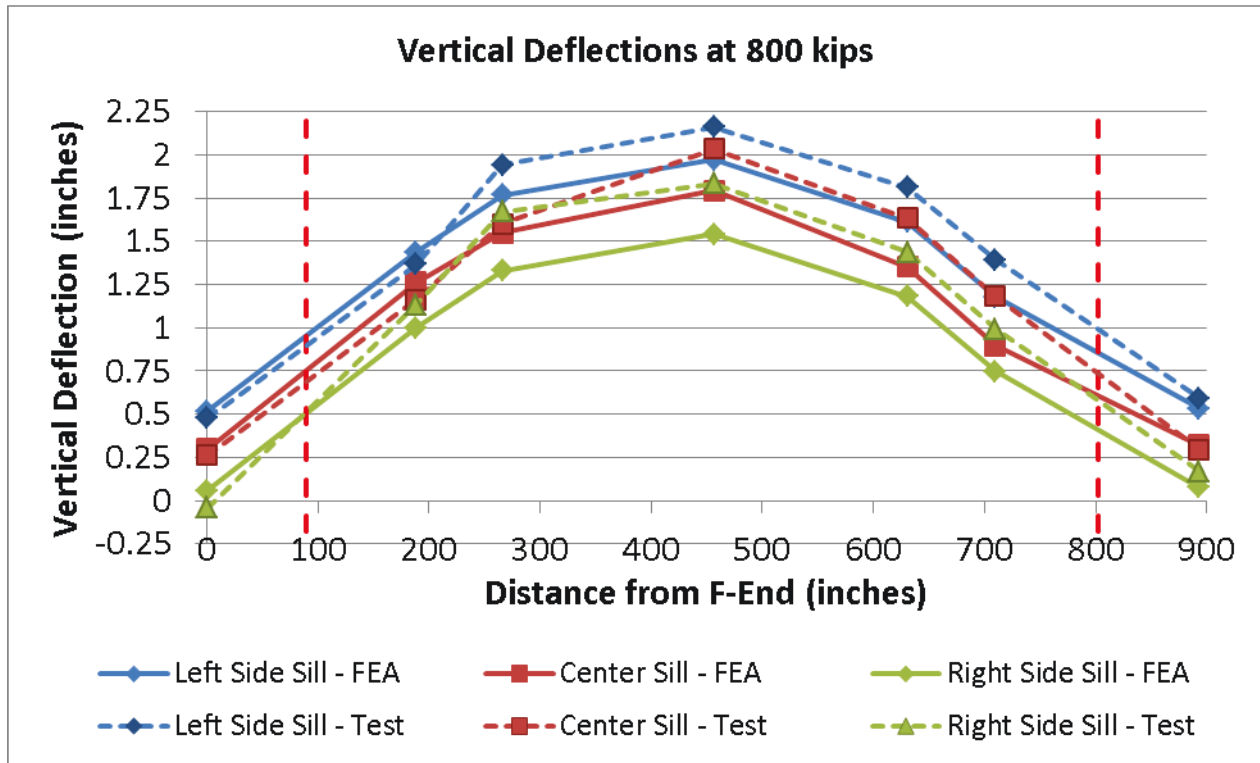


Figure 56. 800,000-pound test and Volpe FE Vertical Displacement Results

The model captured the overall behavior of the car during the test, with the center of the car lifting upwards by approximately 2 feet. In Figure 55, the vertical dashed lines represent the center of the trucks on either end of the car. It is worth noting that in both the test and the FE analysis the carbody lifted upward at all three cross sections at the trucks during the 800,000-lb load test.

Figure 56 features a cross-plot of the strains measured in the test (vertical axis) with the strains calculated at the corresponding locations in the FE model (horizontal axis). This type of plot provides an overall indication of the quality of the correlation between the test and Volpe's post-test FE model. The perfect-correlation line, shown in this figure as a solid line, has a slope of 1. This line indicates the condition where the strain measurement from the test is exactly equal to the strain calculated by the FE model. Additionally, two dashed lines are shown, indicating a $\pm 20\%$ envelope on this perfect-correlation line. This $\pm 20\%$ envelope is consistent with the target correlation value provided by the ETF [2].

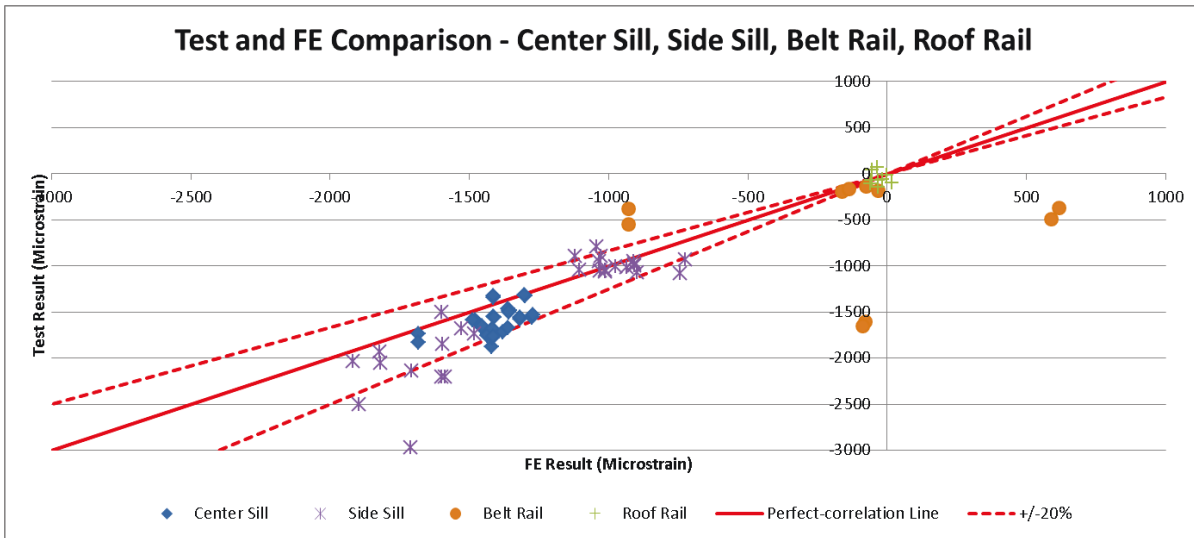


Figure 57. 800,000-pound test and Volpe FE Strain Comparison

While the belt rail and roof rail were instrumented during the test, these members carried relatively little of the 800,000-lb load. Due to the majority of gages on the members of the underframe, the side sill and center sill fell within the $\pm 20\%$ envelope. There were several underframe gages that fell outside of this range. Those gages are listed in Table 3.

Table 3. 800,000-pound Underframe Strain Gage and Volpe FE Results Outside $\pm 20\%$ Envelope

Channel Name	FE Result (Microstrain)	Test Result (Microstrain)	% Difference (Test-Analysis) (Test)
S3SSTL Web of Left Side Sill	-1120.83	-895.08	-25.22
S4SSTL Web of Left Side Sill	-1599.35	-2201.19	27.34
S4SSTR Web of Right Side Sill	-1586.05	-2201.26	27.95
S4SSBR Flange of Right Side Sill	-1895.67	-2504.38	24.31
S5CSBL Lower Web Left Side of Center Sill	-1418.90	-1880.93	24.56
S6SSTL Web of Left Side Sill	-1711.26	-2972.30	42.43
S6SSTR Web of Right Side Sill	-1707.20	-2139.98	20.22
S6CSBL Lower Web Left Side of Center Sill	-1416.48	-1785.94	20.69
S7SSTL Web of Left Side Sill	-1042.46	-797.70	-30.68
S7SSBL Flange of Left Side Sill	-723.46	-933.11	22.47
S7SSBR Flange of Right Side Sill	-744.18	-1085.97	31.47

Based on the comparison between the test results and the post-test FE model, the model simulated the 800,000-lb test of the M1 passenger railcar acceptably.

6.6 Comparison of Volpe’s FE Analysis with Crippling Load Test Results

The Volpe FE model for the 800,000-lb test was slightly modified when it was used for the crippling test. Because the crippling test introduced load into the occupant volume at both the floor- and roof-level energy absorber supports, additional load plates were added into the model at the level of the roof. Volpe’s crippling model was executed prior to the crippling test to help predict the outcome of the test. The results from this pre-test crippling model are presented throughout this section of the report. The full set of results from Volpe’s pre-test crippling analysis is presented in Appendix N.

6.6.1 Carbody Damage and Force-displacement Results

Figure 57 shows a top, side (exterior and interior), and bottom view of Volpe’s FE model in its post-crippling condition. Damage to the roof, sidewall, and underframe (center and side sills) is highlighted in this figure. For comparison, damage to the tested M1 car is mapped out in the bottom half of Figure 46.

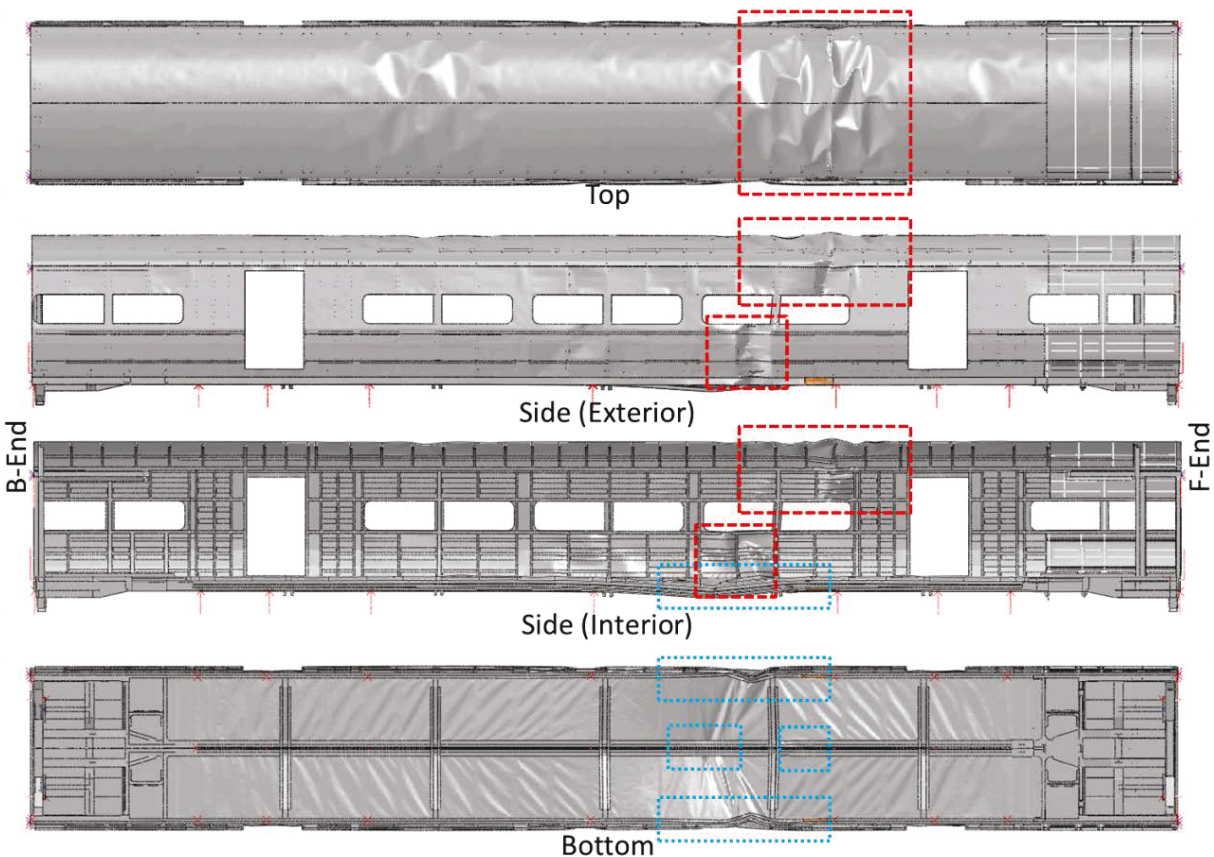


Figure 58. Crippling Load Damage in Volpe FE Model

The longitudinal force-displacement responses were one of the key results that Volpe used to compare the crippling test with the analysis. While the test loads were applied to the F-end of the M1 car using displacement control, this loading technique only ensures the same displacement magnitudes at the four F-end actuators. At the B-end of the car, each reaction location could experience a different longitudinal displacement based on both the magnitude of the load being reacted and the stiffness of the load frame at that location. Different amounts of

car shortening are likely to be calculated based upon the two locations being used in such a calculation.

In Figure 58, the applied force versus change in length are plotted for each of the two floor loading locations for both the test and the model. The change in length for each side (i.e. left and right) of the car was calculated by taking the difference between the longitudinal string pot reading at Cross-Section 1 and Cross-Section 9 on the corresponding side of the car. The force data are taken from the F-end actuators in both the test and the FE model.

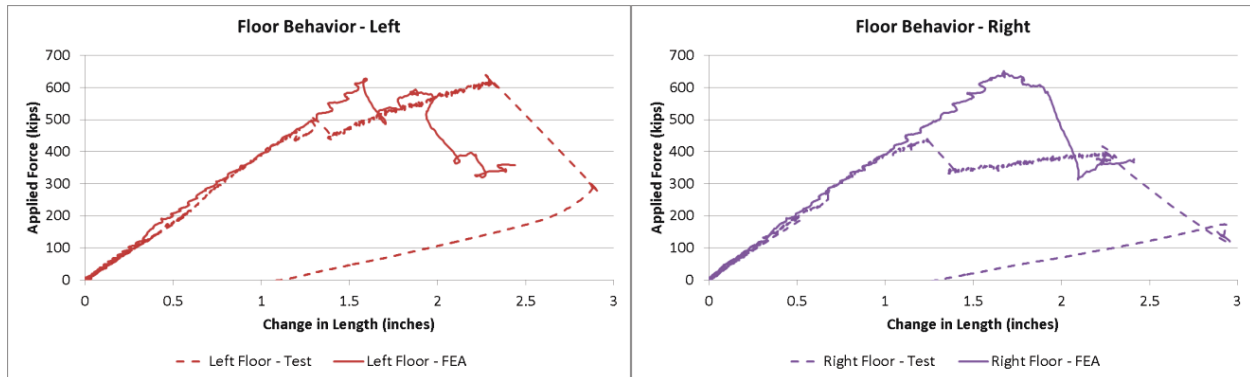


Figure 59. Crippling Test and Volpe FE Floor Force-displacement Results

At the left-side floor location, there was very good agreement between the test and the pre-test FEA up to a load of approximately 500 kips. At that load, the test data experienced a drop in load of approximately 50 kips, while the model continued to carry increasing load up to approximately 600 kips. At that load, the model experienced a 100-kip drop in load. During the test, the right and left side sills experienced buckling coincident with this drop in load. Figure 28 shows this drop in load corresponds to a time of approximately 1,700 seconds and is labeled as the third buckle in this figure. Figure 34 shows the buckled area on the left side sill.

Following the initial drop in load on the left side of the floor, both the test and model results indicate resumed loading along a similar slope, up to a load of approximately 600 kips. At this point on both curves, the car floor has reached its crippling load and the load drops with further reduction in car length.

At the right-side floor location, there was good agreement between the test and the pre-test FEA up to a load of approximately 400 kips. At that load, the measurements indicated a drop in load of approximately 100 kips, while the model continues to carry increasing load up to more than 600 kips. Figure 33 shows the location on the right side sill that appears to have buckled at this load during the test. Following this drop, the test load increased again, albeit at a lower slope than the initial load. However, the load that was introduced into the right-side floor does not climb above the peak load, which occurred just prior to the first drop.

On both sides of the floor, the model and test results exhibit good agreement over the initial portion of the force-displacement characteristic. On both sides, the qualitative behavior predicted by the model was exhibited during the test. However, the loads at which buckling occurred during the test were lower than the loads where buckling was predicted to occur in the model.

Particularly, the largest load carried by the right side of the floor was significantly lower than both the load predicted by the FE model for that side, as well as the measured peak load carried

by the left side of the floor during the test. Because the left side of the floor carried a much higher load than the right side of the floor, it is likely that pre-existing damage to the right side of the car compromised the ability of the underframe on the right side to carry loads. Repair work made to the right side of the car included replacement of a portion of the right sidewall and straightening of a dent on the right side sill (see Section 1.1). Buckling of the right side sill and side wall occurred in the vicinity of these repairs (see Figure 33 and Appendix B).

In Figure 59, the applied force versus change in length results are plotted for the left and right roof loading locations for both the test and the model. String pots were installed from L-brackets attached to each roof loading or reaction location to ground (see Figure 9, Figure 10, and Figure 14). The change in length for each side (i.e. left and right) of the car was calculated by taking the difference between the measurement on the F-end roof-level string pot and the B-end roof-level string pot on the same side. The force data was taken from the F-end actuators in both the test and the FE model.

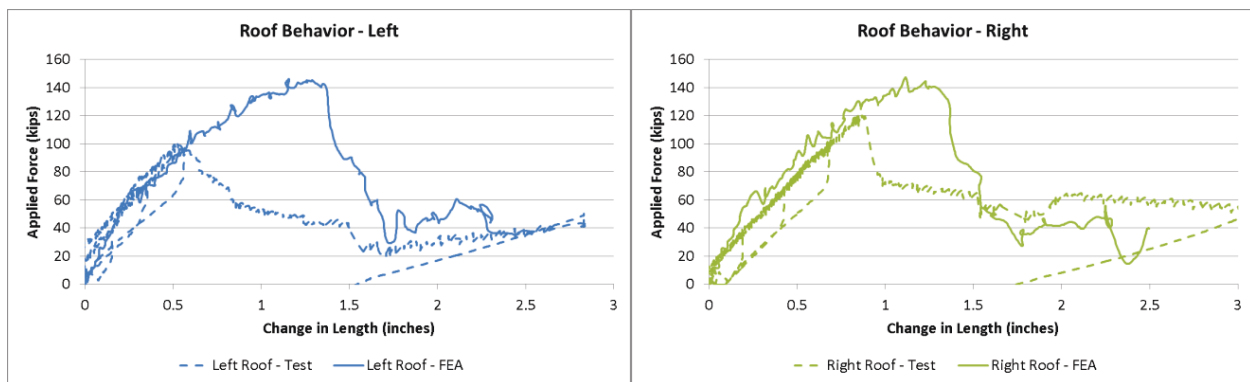


Figure 60. Crippling Test and Volpe FE Roof Force-displacement Results

At the left side of the roof, there is agreement between the test results and the pre-test FEA up to approximately 100 kips. From examination of the test data, there appears to be a considerable hysteresis apparent during the initial loading and unloading cycles. At a total load of approximately 100 kips, the measured force began to drop. The FE model continues to increase in its load-carrying ability up to approximately 140 kips.

At the right side of the roof, the test data exhibited less hysteresis than on the left side. There is agreement between the test and the pre-test FEA up to approximately 120 kips after which the test measurement experiences a sudden drop. The FE model continued to increase in its load-carrying ability up to approximately 140 kips.

As described in Appendix J, Volpe’s FE model represented the roof structure without its corrugations. It was expected that this approximation would lead to the FE model under-predicting the buckling loads at the roof, as the corrugations would add to the stability of the roof in the tested car. At both the left and right sides of the roof, however, the model predicted a higher buckling load than was measured during the test.

The lower roof buckling loads that were measured during the test may have happened due to areas of pre-existing damage in the superstructure of the car. Prior to the start of the crippling test, several areas of damage were noted throughout the occupant volume of the M1 car. After the test was completed, an inspection of the car revealed that several of these areas had

undergone further damage during the test. This indicated that the areas of pre-existing damage likely served as initiation sites for further damage.

Figure 60 contains a plot of the total applied load from the four F-end loading locations versus the change in car length for both the test and the pre-test FEA. For both the test and the FEA, the change in length was calculated on the left side sill, center sill, and right side sill. Generally, the model and the test results qualitatively agree with one another. As described above, the tested car experienced buckling at lower force levels than the FE model. It is apparent in this figure that the tested car experienced a lower crippling load at a larger displacement than was predicted by the FE.

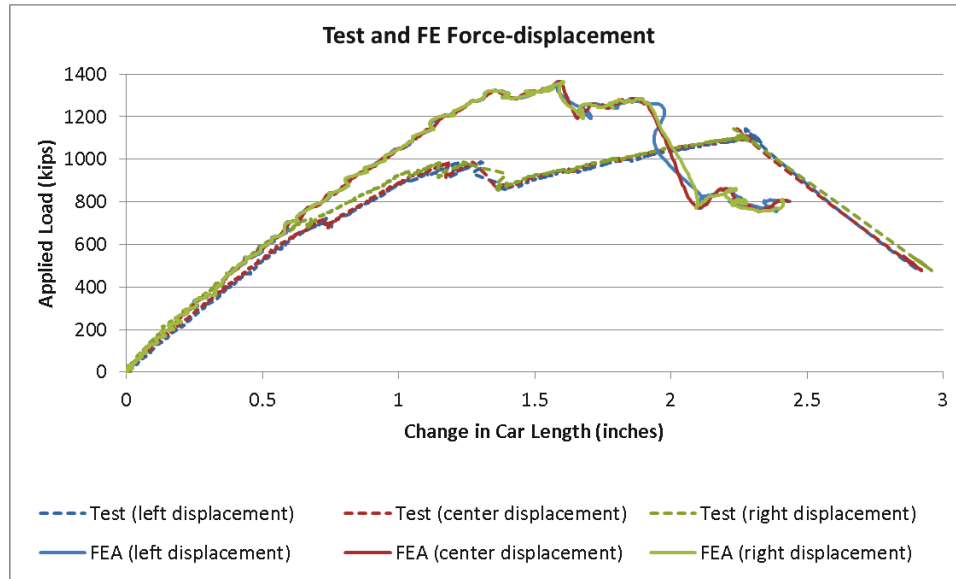


Figure 61. Crippling Test and Volpe's Pre-test FEA Force-displacement Results

6.6.2 Roof Buckling

Figure 61 displays the deformed shape of Volpe's FE model following the crippling simulation. The inset image within this figure shows an interior view of the roof and sidewall damage in the model. The model predicted roof buckling at the F-end of the car, in the vicinity of the first window inboard of the door. While it is apparent from the exterior of the car that the roof sheet has buckled, the interior view reveals that the roof rail and upper window rail have also buckled at approximately the same location as the roof itself.

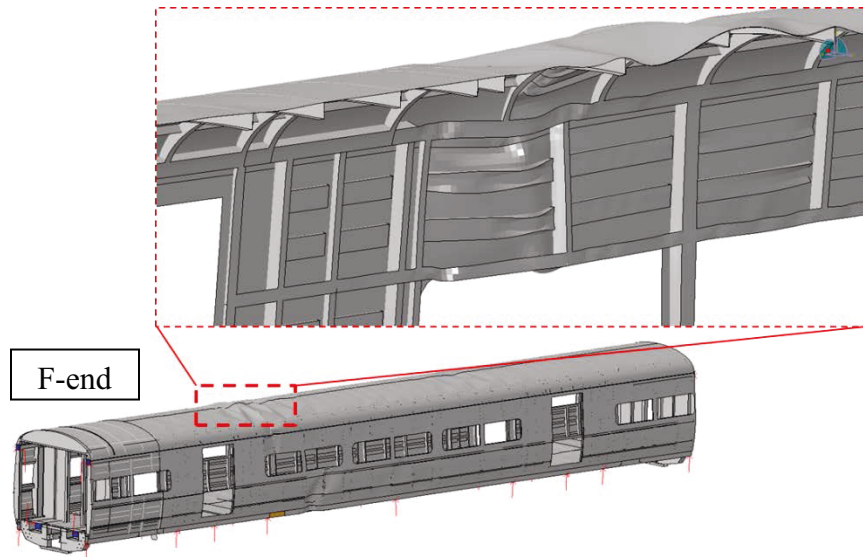


Figure 62. Roof Buckling in Volpe Crippling FE Model with Inset Showing Interior

In the actual test, roof buckling occurred in two locations at opposite ends of the car. On both the F-end and the B-end, the tested car buckled above the first window outboard of the door on the respective end (see Figure 31 and Figure 32). Figure 62 shows the left and right sides of the interior of the car at Cross-Section 2 (nearest the F-end), where the roof buckled. These images indicate the areas of buckling on the structural members of the roof and sidewall with solid circles, and areas where damage had been noted prior to the test with dashed rectangles. On both the left and right sides, damage had been observed in approximately the same area of the upper window rail. Following the test, it was apparent that further damage had occurred in these areas.

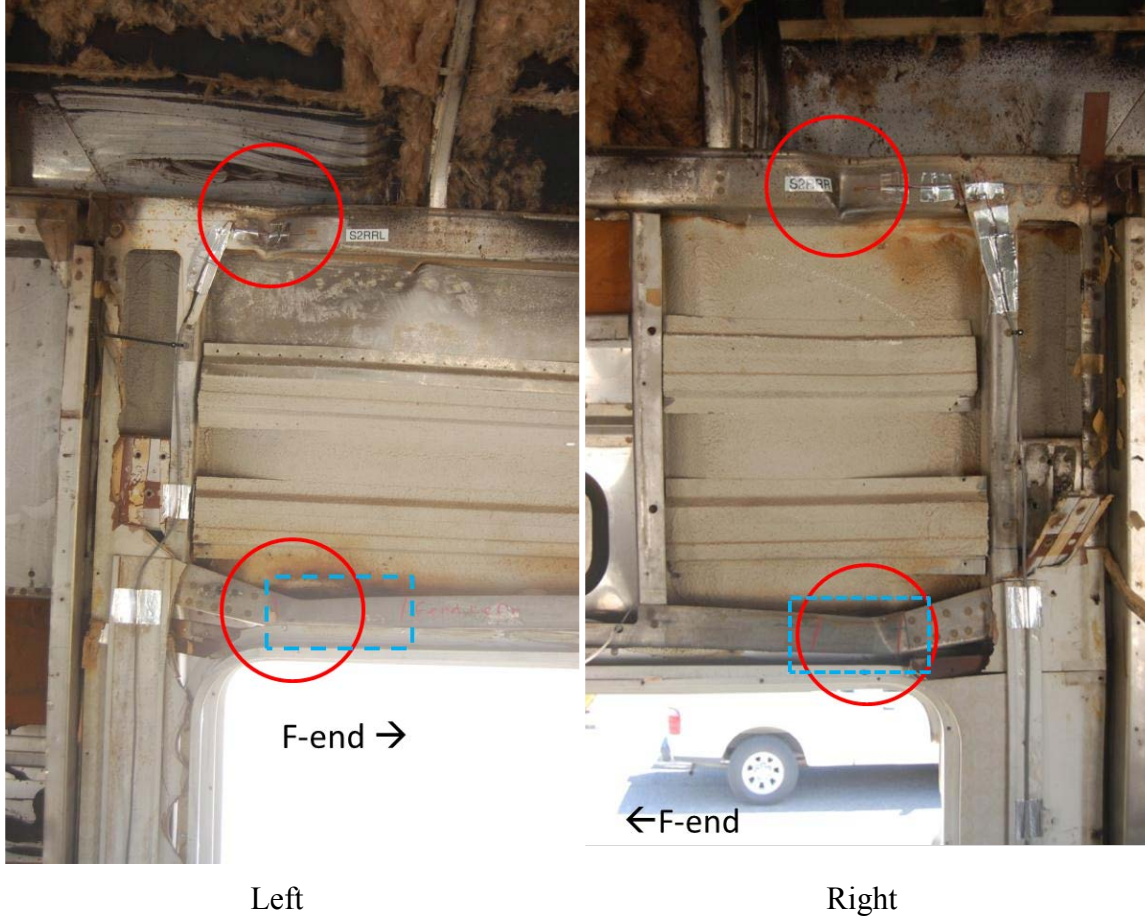


Figure 63. Buckling in F-end Roof at Cross-Section 2 with Pre-existing Damage Noted

Figure 63 shows the inside of the left and right sides of the M1 car at Cross-Section 8 (near the B-end) after the test. This cross-section of the car corresponds to the area of roof buckling on the B-end. These images indicate the areas of buckling on the structural members of the roof and sidewall with solid circles, and areas where damage had been noted prior to the test with dashed rectangles. On both the left and right sides, damage had been observed in approximately the same area of the upper window rail. Following the test, it was apparent that further damage had occurred in these areas.

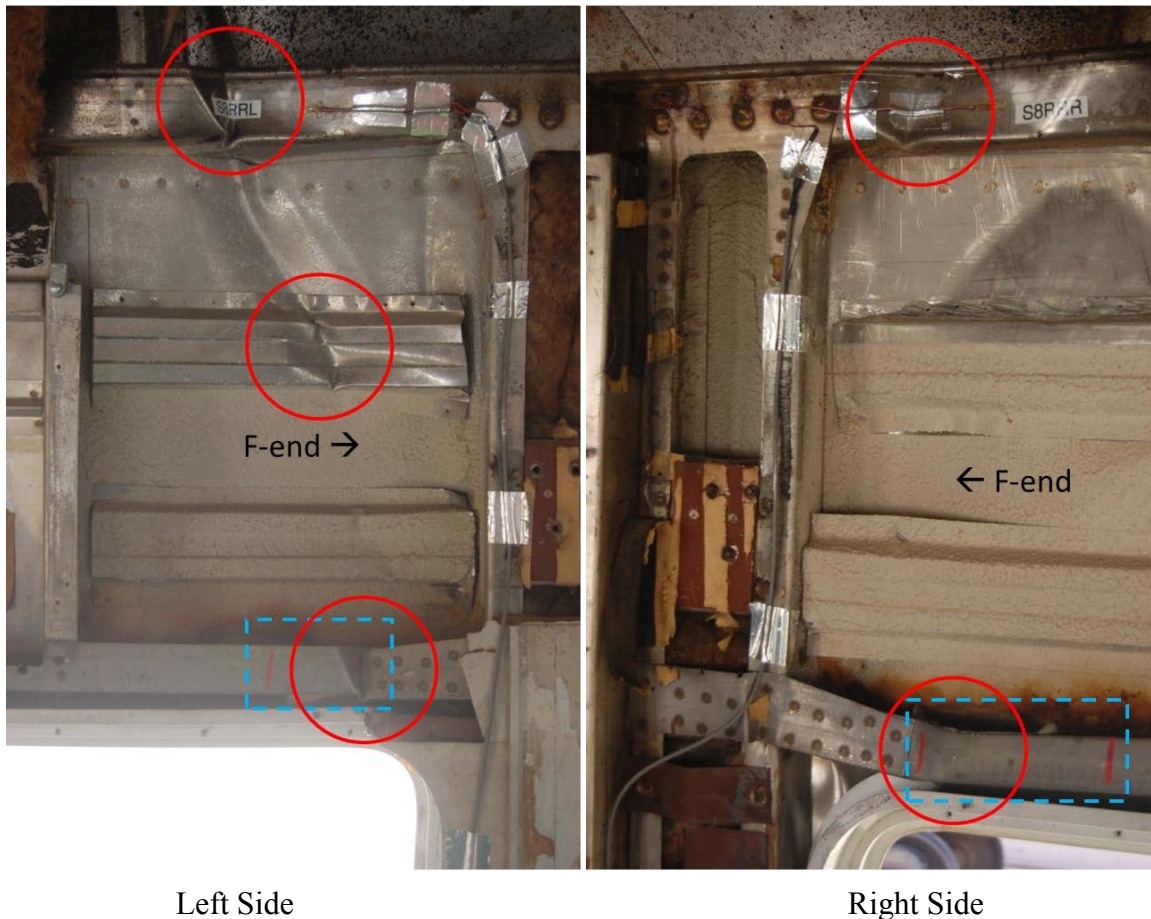


Figure 64. Buckling in B-end Roof at Cross-Section 8 with pre-existing Damage Noted

Given the existence of damage on both the left- and right-side upper window rails on both the F-end and B-end of the car at the approximate location of roof buckling, it is likely that this pre-existing damage served to influence the location of roof buckling. It is likely that this damage occurred during the CEM train-to-train test when collision loads were transmitted into the roof structure during activation of the energy-absorbing elements on both ends of the car.

6.6.3 Side Sill and Center Sill Failure

Figure 64 is a zoomed-in view of the buckling damage to the underframe in Volpe's pre-test crippling FE model. This figure highlights two areas of buckling to the center sill, buckling to the left side sill, and buckling to the right side sill. During the test of the M1 car, the center sill buckled at approximately the same location as the buckle in the model shown closer to the F-end. The side sills of the tested car buckled adjacent to the side sill patches (areas of repaired

damage), whereas the modeled side sills buckled further from the patches, toward the B-end of the car.

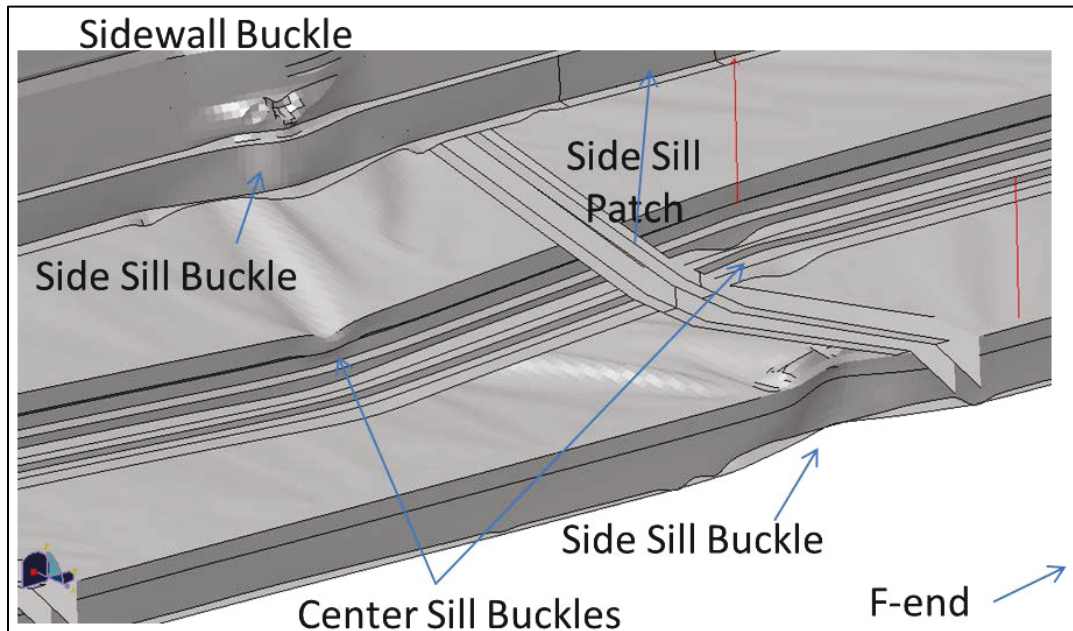


Figure 65. Damage to Underframe in Volpe Pre-test Crippling Model

Figure 65 shows the damaged center sill from the crippling test on the top, and the damaged center sill from the pre-test FE model on the bottom. In both images, areas of buckling have been indicated with dashed rectangles. In both the test and the FE model, different types of buckling were observed. On the near side of the cross-member, buckling of the bottom flange was observed in both the test and the analysis. On the far side of the cross-member, buckling of the top of the center sill occurred in both the test and the analysis.

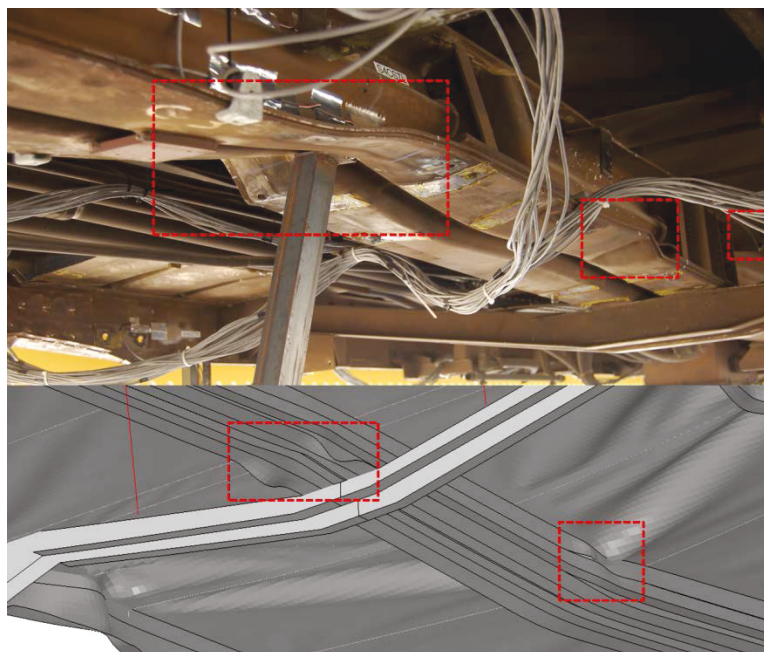


Figure 66. Center Sill Buckling in Crippling Test (top) and Volpe FE Model (bottom)

Figure 66 shows the damaged right side sill from the crippling test on the top, and the damaged right side sill from the FE model on the bottom. Similar buckling modes occurred in both the test and the analysis. In the test, the side sill buckled in the area where the patch had been installed. This area is indicated by a hatch pattern in the top photograph. In the FE model, the side sill buckled behind (that is, toward the B-end) the patched portion of the side sill. The patched area of the FE model is visible in the bottom figure to the right of the buckled area.

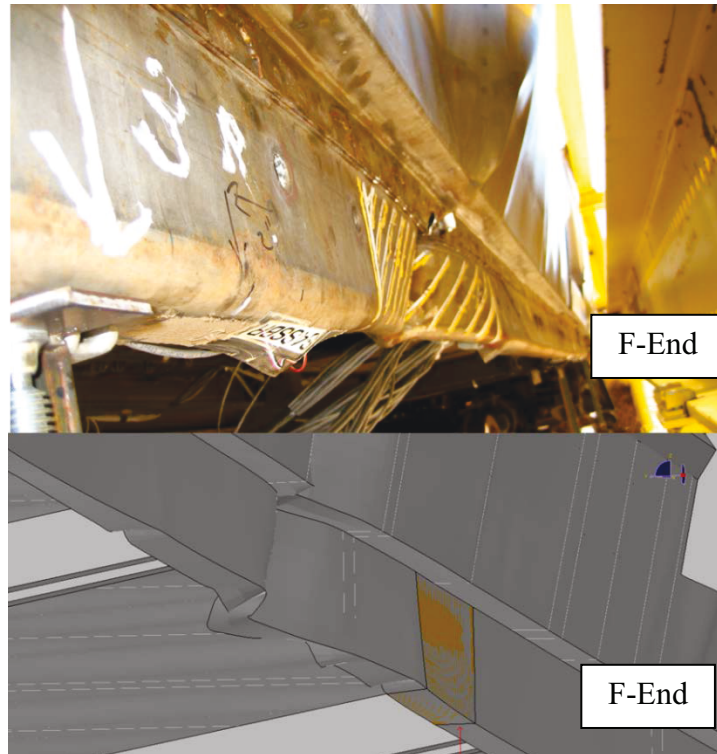


Figure 67. Side Sill Buckling in Crippling Test (top) and Volpe FE Model (bottom)

The underframe of the tested car experienced several additional buckles. Particularly, the left side sill buckled toward the B-end of the car, at Cross-Section 6. No corresponding damage occurred in the FE model. However, this area of side sill exhibited pre-existing damage prior to the crippling test. Following the test, it was apparent that the damage in this area had expanded. Figure 67 shows a pre-test (left) and post-test (right) comparison of the damage to the left side sill at Cross-Section 6.



Figure 68. Pre- (left) and Post- (right) Test Photographs of Left Side Sill, Cross-Section 6

7. Test Observations

TTCI conducted an 800,000-lb load test on Budd M1 Car 9614 to ensure that the car was suitable for a crippling load test. Loads were applied at the two-floor level CEM pockets on the F-end and reacted at the two-floor level CEM pockets on the B-end. Except for some minor bending on the side sills, the car suffered no significant permanent compression during the 800,000-lb load test. Car 9614 was deemed suitable for the crippling load test.

While the 800,000-lb test did not strictly meet the requirements of 49 CFR § 238.203, the 800,000-lb test was successful in providing data for model validation and establishing that M1 car 9614 possessed sufficient structural integrity for crippling testing. Following this test, examination of the test data revealed several carbody behaviors that warrant further discussion.

From examination of the vertical displacement data, it appeared that the car experienced roll during this test, with one side of the car lifting up more than the other. There are several possible reasons for this behavior. The carbody could have been out-of-square with respect to the test frame, the carbody could have been at an initial angle due to the suspension, or loads may have been introduced into the car at a slight angle. While the results of the 800,000-lb test were suitable for demonstration of the carbody's integrity and calibration of the FE models, caution must be exercised when using this type of test for model validation as a part of a program of compliance demonstration.

Introducing loads and restraining the car at multiple locations introduces potential complications compared with performing the conventional 800,000-lb line-of-draft test. In the conventional test, the carbody is loaded and restrained along the line-of-draft. Depending on the specific loading and reaction devices, the car may be thought of as experiencing a single point load at the F-end and a single point load at the B-end. This type of loading setup is unlikely to result in carbody roll, as the load is being applied and reacted along the centerline of the car. Further, if the loading and reaction mechanisms are unable to transmit moments into the carbody, the longitudinal loads would be unlikely to develop the type of moment necessary to roll the carbody.

After some initial survey measurements to measure the position of the car in the test fixture, TTCI conducted a crippling load test on Car 9614. Loads were applied in synchronous stroke control at all four CEM pockets on the F-end and were reacted at all four CEM pockets on the B-end. Crippling first occurred on the roof at approximately 700,000 pounds, and complete car crippling occurred at approximately 1,100,000 pounds. Crippling occurred on the side sills, center sill, belt rails, roof rails, side walls, and roof near the doors. The total car length after the test was reduced by approximately 3 inches.

The behavior of the carbody in the crippling test was largely as-expected based on the pre-test FE modeling. The most significant differences involved the crippling load experienced during the test as well as the vertical uplift of the carbody following buckling of the roof members. The carbody initially experienced very little vertical uplift, likely due to the presence of longitudinal loads at the roof and floor whose moments partially cancelled out. Once the roof failed and no longer carried significant loads, the loading was similar to the loading arrangement used in the conventional 800,000-lb buff test. This led to the tendency of the carbody to bow upwards at its center under the floor loads.

8. Discussion

One of this research program's initial goals was to provide an example of model validation using an elastic test and successful prediction of the crippling behavior of a passenger railcar that could be used by the rail industry as a template. While the previous Budd Pioneer testing program (sponsored by FRA) established a technical basis for the ETF's adopted crippling load criteria of 1.2 million pounds and demonstrated that an FE model could successfully capture the crippling behavior of a passenger railcar, the program described in this report sought to provide further guidance in successfully conducting a program of model validation and simulation.

The test railcar chosen for this program was Budd M1 9614. This car had been previously modified to include CEM features on both its F-end and B-end. The car was then involved in a high-energy dynamic impact test. This impact test resulted in some areas of permanent deformation to the structure of the railcar. While the most seriously-damaged areas underwent repair or replacement prior to the beginning of this program, there were some areas of damage that remained. Following completion of the crippling test, it is apparent that the pre-existing damage served both as initiation sites for several buckling events and may have lowered the ultimate load capacity of the car.

Obviously, some of the difficulties encountered during this research program are unique to the research program. In an industrial setting, where a new carbody would be developed and tested, some of the difficulties encountered during this program would not present themselves. However, some of the lessons learned, in spite of being unique to the research program, have some relevant implications to the industrial application of the ETF's criteria and procedures.

8.1 Material Characterization

One of the key inputs for a structural FE model of a railcar is the behavior of the materials making up the carbody. While samples were removed from a Budd M1 passenger car similar to car 9614, it was not practical to test samples from every component within the carbody. This is one challenge that was unique to the research program. Since these cars were donated to FRA, there was limited information available on the materials used throughout the carbody. This is in contrast with a newly-designed railcar undergoing evaluation, for which the designers would specify the materials of construction based on the desired strength. When evaluating a new carbody design, material properties for all components in the carbody would be based upon manufacturers' material specifications, at a minimum.

One of the significant differences between the ETF's Occupied Volume Integrity (OVI) criteria and the existing 800,000-lb buff strength requirement involves the ability of the structure undergoing evaluation to experience permanent deformation. Under the current regulation at 49 CFR § 238.203, the carbody must experience no permanent deformation. Therefore, in generating a FE model of the structure for evaluation against the existing requirement, the material behavior must only include elastic behavior and some representation of material yielding. At its simplest, a model could simulate the conventional 800,000-lb test using only elastic materials. If no stresses were found in the model that exceeded the minimum yield strength given for each material used in its construction, a test could be conducted with reasonable confidence that the carbody would pass.

In the ETF's criteria, one of the options for demonstrating OVI is to show that the carbody possesses a crippling strength of at least 1.2 million pounds. Because the crippling strength is defined as the ultimate longitudinal load the carbody can support, the material characterization in a crippling model must be more sophisticated than that in an elastic model. In a crippling model, the plastic behavior of the construction materials take on a new level of importance, as the carbody can experience plastic deformation before it reaches its crippling load. If the material properties are not appropriately modeled, the simulation may predict crippling loads in excess of what the physical carbody can sustain. Because a crippling test would probably not be performed during an industrial application of the ETF's procedures, the simulation must provide a conservative estimate of the crippling load. Critical steps in the process of developing a model to evaluate OVI include 1) properly establishing both the elastic and plastic behaviors of the construction materials and 2) using this information to appropriately characterize the material properties in the FE model.

In both the current program and the previous Budd Pioneer crippling test program [6], the railcars under evaluation have been primarily constructed from stainless steel and carbon steel. The ETF's criteria and procedures were written in such a way as to be highly design-neutral, which will permit a wide variety of carbody designs to be evaluated. Since steel is not the only material from which an occupant volume may be constructed, more complex forms of material characterization may be necessary as appropriate to a particular design. For example, modeling a carbody constructed from extruded aluminum with a high-level of confidence may require additional material characterization data compared to modeling railcars made of conventional steel.

8.2 Loading Boundary Conditions

One of the challenges encountered during this testing and analysis program was simulating the boundary conditions on the model appropriately. Ideally, the boundary conditions on a model would represent the physical constraints on the tested car without introducing any unnecessary restraint or alternative load paths. During the tests performed in this program, initially the carbody was vertically supported on its own trucks. Longitudinal constraint was introduced through contact between the load plates and the energy-absorber supports. While the F-end loading plates were used to introduce forces into the car, through friction these plates are capable of providing both lateral constraint and introducing non-longitudinal loads into the structure.

During the 800,000-lb load test, the vertical displacement measurements indicated several non-ideal modes of deformation. While the carbody was resting on its trucks, examination of the data indicated that the carbody apparently lifted upward and off its trucks during the course of the test (see Figure 55). Examination of these same data also shows that the carbody experienced a rolling motion during the test, where the left side of the car apparently experienced a larger uplift than the right side of the car.

These two behaviors indicate a need to fully understand the boundary conditions acting on a physical car during a test. While this particular car was tested on its original trucks, it is likely that for an evaluation of a newly-designed railcar, vertical support would be provided by another means. This vertical support could be provided by a set of stands at the truck locations, a set of "dummy" trucks lacking suspension components, or a more complicated support structure in the case of a railcar with features such as an articulation. APTA SS-C&S-034 provides guidance on

vertical support, stating that “[d]uring the compression test, the car body shall be supported on trucks, or a simulation thereof, to allow longitudinal movement” [4].

Regardless of the support mechanism chosen, the boundary conditions placed on the model should be chosen to appropriately represent the constraint introduced to the carbody. Based on the results of the 800,000-lb test, Volpe and Arup each made modifications to their respective FE models to better represent the support conditions of the test. Following the test, Arup modified its FE model to reduce the stiffness of the suspension springs, which would allow the carbody to experience more vertical uplift. Volpe’s FE model did not include any vertical boundary conditions at the suspension springs, permitting free uplift of the car. Volpe’s post-test model attempted to replicate the rolling experienced by the car by applying both vertical and longitudinal loads to the floor-level loading locations.

8.3 Weld Characterization

Volpe’s FE model did not explicitly characterize welds (i.e. whether they build up composite sections or attach structural components to one another). Volpe’s approach to modeling the crippling behavior of the railcar assumed that the overall crippling strength of the railcar would be determined by the buckling strength of the center sill and side sills. This assumption is based upon the observed behaviors during two previous crippling tests of Budd Pioneer railcars [6] as well as the requirement given at 49 CFR § 238.203(c):

When overloaded in compression, the body structure of passenger equipment shall be designed, to the maximum extent possible, to fail by buckling or crushing, or both, of structural members rather than by fracture of structural members or failure of structural connections [1].

Arup’s FE model of the crippling test modeled the spot welds and other connections within the carbody structure explicitly. Additionally, Arup performed post-test studies on the effects of different spot weld modeling techniques.

When the ETF’s criteria and procedures are used to evaluate the OVI of an alternatively-designed railcar, it is critical that the FE model(s) used produce results that are conservative compared to the results that would be obtained through a crippling test. While the regulation cited above calls for the structural members to fail before the connection fails, welds or other connections may play critical roles in establishing the crippling strength of the railcar. If that is the case, it is important that the model can adequately capture the limited strength of the connections to prevent over-prediction of the crippling strength of the physical car. A carbody manufacturer may need to perform additional small-scale or component-level tests to ensure that critical connections are modeled appropriately.

Also, engineering judgment must be exercised when choosing the appropriate level of connection detail to include in a model. Different types of welds or other connections may require different levels of detail to be adequately modeled.

8.4 Pre-existing Damage

Prior to this research program, M1 Car 9614 had been modified to include CEM components and was used in a dynamic impact testing program [3]. As a result of this previous testing program, the car was known to have some areas of damage at the start of the current research program. While the car underwent repairs, including patches on damaged areas of the side sills and

replacement of a portion of the sidewall structure, other areas of minor damage remained on the structural members throughout the car. During the 800,000-lb test, several areas of additional damage appear to have occurred (see Section 4.1). Prior to the crippling test, areas of damage to the side sill and the sidewall members were documented. Following the test, several of these areas were found to have acted as initiation sites for further damage. It is likely that these areas of pre-existing damage reduced the maximum load the particular member could carry, thus decreasing the apparent crippling strength of the car.

In an actual application of the ETF's criteria and procedures to evaluate a newly-designed railcar, a manufacturer would test a pristine specimen free from any pre-existing damage. While the lessons learned from testing a railcar with pre-existing damage in this program are not directly applicable to a manufacturer who is evaluating on a new, pristine car structure, the lessons may be applicable to cars that have been involved in a slight to moderate accident and are intended to be repaired and returned to service.

With CEM passenger equipment, the railcar is designed to experience permanent deformation in a controlled area [7]. This permanent deformation is meant to be limited to the dedicated energy-absorbing components for collisions up to the designed capacity of the CEM system. For the CEM components to function properly, the occupant volume must be designed to have a crippling load that is higher than the peak load experienced by the CEM system. If the occupant volume possesses sufficient strength, the energy-absorbing components will crush before the occupant volume is crippled. If, however, the occupant volume begins to crush before the CEM system has reached its full energy-absorbing capacity, the occupant volume will be compromised and survival space for passengers may be lost prior to exhaustion of the CEM components.

For a new railcar design, the parameters of the CEM system (e.g., stroke length, maximum force, target energy-absorbing capacity) are characteristics of the railcar that the designer can establish within reasonable limits. The occupant volume of the railcar should also be designed with these CEM parameters in consideration in order to ensure a compatibility of strength between the CEM components and the occupant volume.

An advantage offered by CEM railcars is the ability to repair the damage to the car following a minor to moderate collision, where CEM components have been deformed but not exhausted. Designs have been developed in which components trigger in a sequential manner, thus limiting the damage to CEM components based on the severity of the particular accident [7]. While this approach allows a railcar to undergo repair (e.g., replacement of crushed energy-absorbing components) and re-enter service, it is critical to ensure that after an accident, the occupant volume of the railcar maintains the level of integrity that the designers intended. As this research program has shown, areas of repaired damage within the occupant volume may serve as initiation sites for further damage. Since the damaged areas have already buckled, the effective buckling load of the damaged component is lower than the buckling load of the pristine component. Depending on the severity and location of any damage to the occupant volume, the maximum compression load necessary to cause loss of occupant volume may be dramatically lower than that established by the manufacturer for a pristine car. This, in turn, may greatly decrease the amount of energy that can be absorbed by a CEM system before loss of occupant volume, as the occupant volume would begin to crush prior to exhaustion of the CEM system. In effect, the CEM system would no longer function as designed if the occupant volume were unable to support the necessary longitudinal loads to prevent its own crush.

9. Conclusion

FRA conducted a research program in which the ETF's OVI criteria and procedures have been applied to a CEM-equipped passenger railcar. In support of this program, FRA contracted with TTCI to perform a series of full-scale tests and FEA on Budd M1 Car 9614. One goal of this program was to provide a case study for manufacturers seeking to qualify alternatively designed railcars through the process adopted by the ETF.

This particular railcar, the Budd M1 Car 9614, had been previously modified to include CEM components on both ends. The tests performed in this program included the following:

- 800,000-Pound Load Test: 800,000-pound quasi-static end-load test using loads applied through the floor level of CEM pockets. This test was conducted on March 13, 2013.
- Crippling Load Test: Quasi-static end-load test to determine the ultimate strength of the car using loads applied through the floor and roof level of CEM pockets. This test was conducted on July 17, 2013.

Arup recommends that the confidence and accuracy of FEA should be increased in this application through further work. Strict guidelines on acceptable modeling methodology, with a demonstration of comparability to physical testing of materials and connections, should also be developed. If these steps are not taken, FEA calibrated to elastic tests could over predict the performance of railcars and allow nonconforming railcars into usage.

Arup, in collaboration with TTCI, developed a detailed FE model of the test car and provided predictions before each test. Exclusive of TTCI's contract with FRA and independent of Arup's FEA, FRA also directed Volpe to perform another FEA of the same test car in parallel to Arup's analysis. This parallel modeling effort was intended to demonstrate that two different modelers, utilizing different approaches (e.g., different modeling techniques, different software packages, etc.) could yield comparable results that paralleled the measurements from the tests.

The 800,000-lb load test was conducted to provide data for FE model validation as well as to ensure that Car 9614 was suitable for use in a crippling test. Computational work performed by Arup and Volpe provided predictions of the railcar's response for test planning. Based upon the results of the 800,000-lb test, both models were modified post-test and provided appropriate comparisons with the test measurements. These models were then both used to predict the behavior of the car during the crippling test. Both FE models predicted a maximum crippling load of approximately 1.3 million pounds. During the actual test, the maximum crippling load was measured to be approximately 1.1 million pounds.

10. References

1. Code of Federal Regulations, Title 49, Transportation, Volume 2, Subtitle B (Parts 200-299) Federal Railroad Administration, Department of Transportation.
2. Carolan, Michael et al. (2011 October). “Technical Criteria and Procedures for Evaluating the Crashworthiness and Occupant Protection Performance of Alternatively Designed Passenger Rail Equipment for Use in Tier I Service,” DOT/FRA/ORD-11/22. Available at: <http://www.fra.dot.gov/eLib/Details/L01292>.
3. Tyrell, D., Jacobsen, K., Martinez, E. (2006 November). “A Train-to-Train Impact Test of Crash Energy Management Passenger Rail Equipment: Structural Results,” American Society of Mechanical Engineers, Paper No. IMECE2006-13597. Available at: <http://ntlsearch.bts.gov/tris/record/ntl/43084.html>.
4. American Passenger Transportation Association. (2006, June 15). “APTA SS-C&S-034-99, Rev. 2. Standard for the Design and Construction of Passenger Railroad Rolling Stock.”
5. Abaqus Version 6.12. (2012). Dassault Systems Simulia Corp. Providence, RI.
6. Carolan, M., Perlman, B., and Tyrell, D. (2013 October). “Alternative Occupied Volume Integrity (OVI) Tests and Analyses,” U.S. Department of Transportation, DOT/FRA/ORD-13/46. Available at: <http://ntlsearch.bts.gov/tris/record/ntl/48366.html>.
7. Strang, J., Hynes, R., Peacock, T., Lydon, B., Woodbury, C.A., Stastny, J., Tyrell, D. (2007 January). “Development of a Crash Energy Management Specification for Passenger Rail Equipment,” Compendium of Papers, 86th Annual Meeting, Transportation Research Board, Paper No. 07-0080. Available at: http://ntl.bts.gov/lib/43000/43000/43077/Tyrell_DevelopmentCrash_Energy.pdf.

Appendix A – Instrumentation Locations and Technical Specifications

Table A1. Load Measuring Channels

Channel Name/Comments	Transducer Type	Measurement
ACTUATOR END OF CAR (F)		
LCLRRL ¹ 0- to 300,000-pound range	500,000-pound Load Cell	F-end Roof Left Side
LCLRRL ¹ 0- to 300,000-pound range	500,000-pound Load Cell	F-end Roof Right Side
LCLFL 0- to 700,000-pound range	1,000,000-pound Load Cell	F-end Floor Left Side
LCLFR 0- to 700,000-pound range	1,000,000-pound Load Cell	F-end Floor Right Side
LCLT	Synthetic Channel	Sum of all F-end Applied
REACTION END OF CAR (B)		
LCRRL ¹ 0- to 300,000-pound range	500,000-pound Load Cell	B-end Roof Left Side
LCRRL ¹ 0- to 300,000-pound range	500,000-pound Load Cell	B-end Roof Right Side
LCRFL 0- to 700,000-pound range	1,000,000-pound Load Cell	B-end Floor Left Side
LCRFR 0- to 700,000-pound range	1,000,000-pound Load Cell	B-end Floor Right Side
LCRT	Synthetic Channel	Sum of all B-end Applied

¹Used only on crippling load test

Table A2. Strain Gage Locations

Channel Name	Longitudinal Distance from F-end Bolster (in)	Location of Strain Gages
S2SSTL	43	Web of left side sill
S3SSTL	99	Web of left side sill
S4SSTL	214	Web of left side sill
S5SSTL	368	Web of left side sill
S6SSTL	535.5	Web of left side sill
S7SSTL	620.5	Web of left side sill
S8SSTL	675	Web of left side sill
S2SSBL	43	Flange of left side sill
S3SSBL	101	Flange of left side sill
S4SSBL	214	Flange of left side sill
S5SSBL	368	Flange of left side sill
S6SSBL	535.5	Flange of left side sill
S7SSBL	620.5	Flange of left side sill
S8SSBL	675	Flange of left side sill
S2SSTR	44	Web of right side sill
S3SSTR	101	Web of right side sill
S4SSTR	218	Web of right side sill
S5SSTR	368	Web of right side sill
S6SSTR	539	Web of right side sill

Channel Name	Longitudinal Distance from F-end Bolster (in)	Location of Strain Gages
S7SSTR	617.5	Web of right side sill
S8SSTR	673.5	Web of right side sill
S2SSBR	44	Flange of right side sill
S3SSBR	101	Flange of right side sill
S4SSBR	215	Flange of right side sill
S5SSBR	368	Flange of right side sill
S6SSBR	539	Flange of right side sill
S7SSBR	622.5	Flange of right side sill
S8SSBR	673.5	Flange of right side sill
S2CSBL	49	Lower web, Left side of center sill
S3CSBL	94	Lower web, Left side of center sill
S4CSBL	177	Lower web, Left side of center sill
S5CSBL	368	Lower web, Left side of center sill
S6CSBL	541.5	Lower web, Left side of center sill
S7CSBL	620.5	Lower web, Left side of center sill
S8CSBL	664.5	Lower web, Left side of center sill
S2CSTL	49	Upper web, Left side of center sill
S3CSTL	94	Upper web, Left side of center sill
S4CSTL	177	Upper web, Left side of center sill
S5CSTL	368	Upper web, Left side of center sill
S6CSTL	541.5	Upper web, Left side of center sill
S7CSTL	620.5	Upper web, Left side of center sill
S8CSTL	664.5	Upper web, Left side of center sill
S2CSBR	49	Lower web, Right side of center sill
S3CSBR	94	Lower web, Right side of center sill
S4CSBR	177	Lower web, Right side of center sill
S5CSBR	368	Lower web, Right side of center sill
S6CSBR	541.5	Lower web, Right side of center sill
S7CSBR	620.5	Lower web, Right side of center sill
S8CSBR	664.5	Lower web, Right side of center sill
S2CSTR	49	Upper web, Right side of center sill
S3CSTR	94	Upper web, Right side of center sill
S4CSTR	177	Upper web, Right side of center sill
S5CSTR	368	Upper web, Right side of center sill
S6CSTR	541.5	Upper web, Right side of center sill
S7CSTR	620.5	Upper web, Right side of center sill
S8CSTR	664.5	Upper web, Right side of center sill
S2BRL	43	Left belt rail
S4BRL	177	Left belt rail

Channel Name	Longitudinal Distance from F-end Bolster (in)	Location of Strain Gages
S5BRL	368	Left belt rail
S6BRL	541.5	Left belt rail
S8BRL	674.5	Left belt rail
S2RRL	22	Left roof rail
S4RRL	177	Left roof rail
S5RRL	368	Left roof rail
S6RRL	541.5	Left roof rail
S8RRL	696	Left roof rail
S2BRR	43	Right belt rail
S4BRR	177	Right belt rail
S5BRR	368	Right belt rail
S6BRR	541.5	Right belt rail
S8BRR	674.5	Right belt rail
S2RRR	22	Right roof rail
S4RRR	177	Right roof rail
S5RRR	368	Right roof rail
S6RRR	541.5	Right roof rail
S8RRR	696	Right roof rail
S2R	43	Roof
S4R	177	Roof
S5R	368	Roof
S6R	541.5	Roof
S8R	674.5	Roof

Table A3. 800,000-pound Load Test String Potentiometer Locations

Channel Name	Longitudinal Distance from F-end Bolster (in)	Location of String Potentiometers
DFRLX	-90	Roof-level, Left side of F-end of Car
DFFLX	-90	Floor-level, Left side of F-end of Car
DFRRX	-90	Roof-level, Right side of F-end of Car
DFFRX	-90	Floor-level, Right side of F-end of Car
D1LX	-90	Left side sill
D1LY	-90	Left side sill
D1LZ	-90	Left side sill
D1CX	-90	Center sill
D1CY	-90	Center sill
D1CZ	-90	Center sill
D1RX	-90	Right side sill
D1RY	-90	Right side sill
D1RZ	-90	Right side sill
D3LX	101	Left side sill
D3LY	101	Left side sill
D3LZ	101	Left side sill
D3CX	101	Center sill
D3CY	101	Center sill
D3CZ	101	Center sill
D3RX	101	Right side sill
D3RY	101	Right side sill
D3RZ	101	Right side sill
D4LX	211	Left side sill
D4LY	211	Left side sill
D4LZ	211	Left side sill
D4CX	177	Center sill
D4CY	177	Center sill
D4CZ	177	Center sill
D4RX	219	Right side sill
D4RY	219	Right side sill
D4RZ	219	Right side sill
D5LX	355	Left side sill
D5LY	355	Left side sill
D5LZ	355	Left side sill
D5CX	370	Center sill
D5CY	370	Center sill

Channel Name	Longitudinal Distance from F-end Bolster (in)	Location of String Potentiometers
D5CZ	370	Center sill
D5RX	370	Right side sill
D5RY	370	Right side sill
D5RZ	370	Right side sill
D6LX	542	Left side sill
D6LY	542	Left side sill
D6LZ	542	Left side sill
D6CX	542	Center sill
D6CY	542	Center sill
D6CZ	542	Center sill
D6RX	542	Right side sill
D6RY	542	Right side sill
D6RZ	542	Right side sill
D7LX	626	Left side sill
D7LY	626	Left side sill
D7LZ	626	Left side sill
D7CX	624	Center sill
D7CY	624	Center sill
D7CZ	624	Center sill
D7RX	626	Right side sill
D7RY	626	Right side sill
D7RZ	626	Right side sill
D9LX	803	Left side sill
D9LY	803	Left side sill
D9LZ	803	Left side sill
D9CX	803	Center sill
D9CY	803	Center sill
D9CZ	803	Center sill
D9RX	803	Right side sill
D9RY	803	Right side sill
D9RZ	803	Right side sill
DBRLX	803	Roof-level, Left side of B-end of Car
DBFLX	803	Floor-level, Left side of B-end of Car
DBRRX	803	Roof-level, Right side of B-end of Car
DBFRX	803	Floor-level, Right side of B-end of Car

Table A4. Crippling Load Test String Potentiometer Locations

Channel Name	Longitudinal Distance from F-end Bolster (in)	Location of String Potentiometers
DFRLX	-113	Roof-level, Left side of F-end of Car
DFFLX	-104	Floor-level, Left side of F-end of Car
DFRRX	-112	Roof-level, Right side of F-end of Car
DFFRX	-104	Floor-level, Right side of F-end of Car
D1LX	-90	Left side sill
D1LY	-90	Left side sill
D1LZ	-90	Left side sill
D1CX	-105	Center sill
D1CY	-105	Center sill
D1CZ	-105	Center sill
D1RX	-90	Right side sill
D1RY	-90	Right side sill
D1RZ	-90	Right side sill
D3LX	101	Left side sill
D3LY	101	Left side sill
D3LZ	101	Left side sill
D3CX	101	Center sill
D3CY	101	Center sill
D3CZ	101	Center sill
D3RX	101	Right side sill
D3RY	101	Right side sill
D3RZ	101	Right side sill
D4LX	211	Left side sill
D4LY	211	Left side sill
D4LZ	211	Left side sill
D4CX	177	Center sill
D4CY	177	Center sill
D4CZ	177	Center sill
D4RX	219	Right side sill
D4RY	219	Right side sill
D4RZ	219	Right side sill
D5LX	360	Left side sill
D5LY	360	Left side sill
D5LZ	360	Left side sill
D5CX	370	Center sill
D5CY	370	Center sill

Channel Name	Longitudinal Distance from F-end Bolster (in)	Location of String Potentiometers
D5CZ	370	Center sill
D5RX	370	Right side sill
D5RY	370	Right side sill
D5RZ	370	Right side sill
D6LX	523	Left side sill
D6LY	523	Left side sill
D6LZ	523	Left side sill
D6CX	542	Center sill
D6CY	542	Center sill
D6CZ	542	Center sill
D6RX	542	Right side sill
D6RY	542	Right side sill
D6RZ	542	Right side sill
D7LX	626	Left side sill
D7LY	626	Left side sill
D7LZ	626	Left side sill
D7CX	624	Center sill
D7CY	624	Center sill
D7CZ	624	Center sill
D7RX	626	Right side sill
D7RY	626	Right side sill
D7RZ	626	Right side sill
D9LX	803	Left side sill
D9LY	803	Left side sill
D9LZ	803	Left side sill
D9CX	814	Center sill
D9CY	814	Center sill
D9CZ	814	Center sill
D9RX	803	Right side sill
D9RY	803	Right side sill
D9RZ	803	Right side sill
DBRLX	824	Roof-level, Left side of B-end of Car
DBFLX	810	Floor-level, Left side of B-end of Car
DBRRX	824	Roof-level, Right side of B-end of Car
DBFRX	810	Floor-level, Right side of B-end of Car

Hydraulic Actuator and Load Cell Specifications

Floor Level Actuators

Manufacturer – Enerpac

General Description – Double acting with imbedded displacement transducer

Extend Capacity –1,133,000 lbs at 10,000 psi.

Retract Capacity –385,800 lbs at 10,000 psi.

Stroke – 11.81 inches

Collapsed Length – 26.24 inches

Roof Level Actuators

Manufacturer – Enerpac

General Description - Double acting with imbedded displacement transducer

Extend Capacity –411,600 lbs at 10,000 psi.

Retract Capacity –196,800 lbs at 10,000 psi.

Stroke – 11.81 inches

Collapsed Length – 18.20 inches

Floor Level Load Cells

Manufacturer – Futek

Model No. – FSH01905

Rated Capacity – 1,000,000 lbs. (453.6 metric tons)

Rated Output – 3 mV per volt of excitation

Excitation Voltage – 20 volts DC max.

Bridge Resistance – 350 ohms nominal

Working Length – 8.00 inches

Nominal Diameter – 6.0 inches

Roof Level Load Cells

Manufacturer – Futek

Model No. – FSH01903

Rated Capacity – 500,000 lbs (226.8 metric tons)

Rated Output – 2 mV per volt of excitation

Excitation Voltage – 20 volts DC max.

Bridge Resistance – 350 ohms nominal

Working Length – 8.00 inches

Nominal Diameter – 6.0 inches

Appendix B – Crippling Test Photos

Pre-test Photos

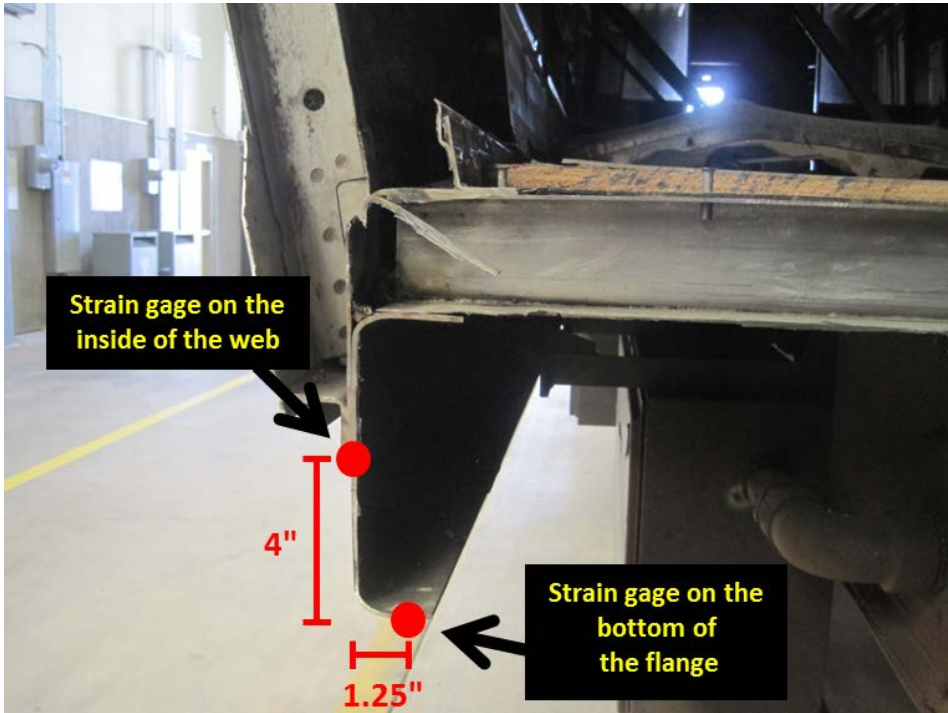


Figure B1. Strain Gage Locations on Side Sill

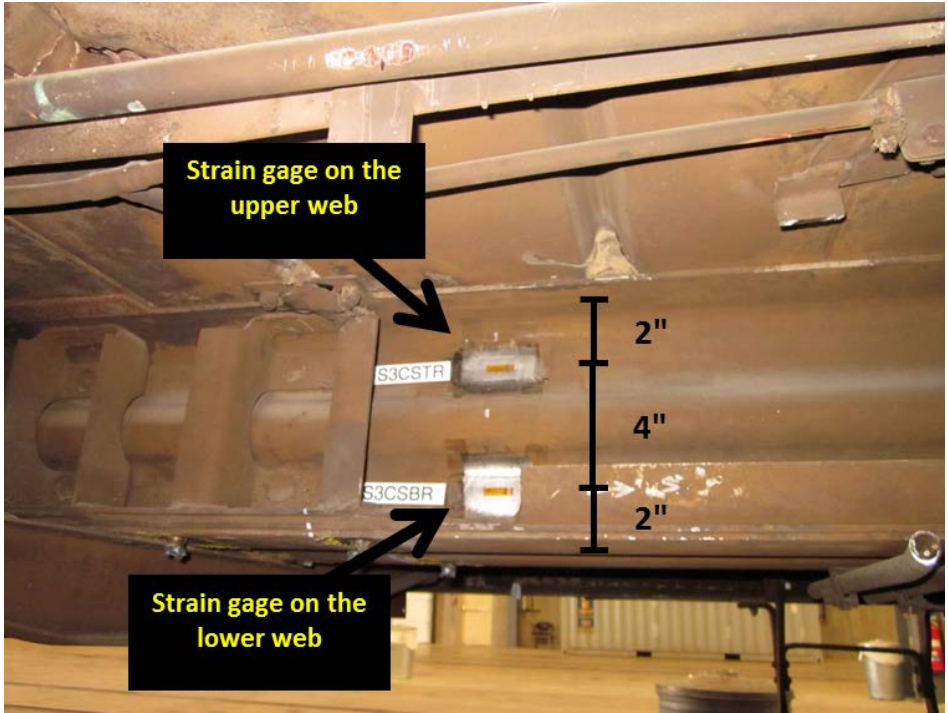


Figure B2. Strain — Gage on Center Sill



Figure B3. Strain Gage Locations near the Side Sill Patch

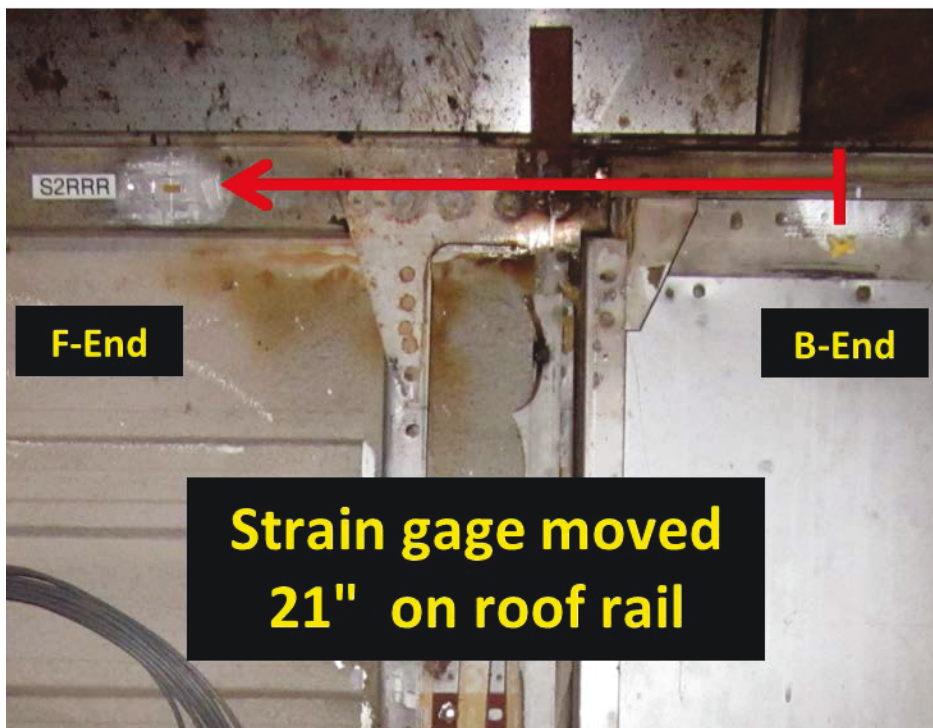


Figure B4. Strain Gages on Roof Rails Moved to Avoid Obstructions



Figure B5. Strain Gage on Belt Rail

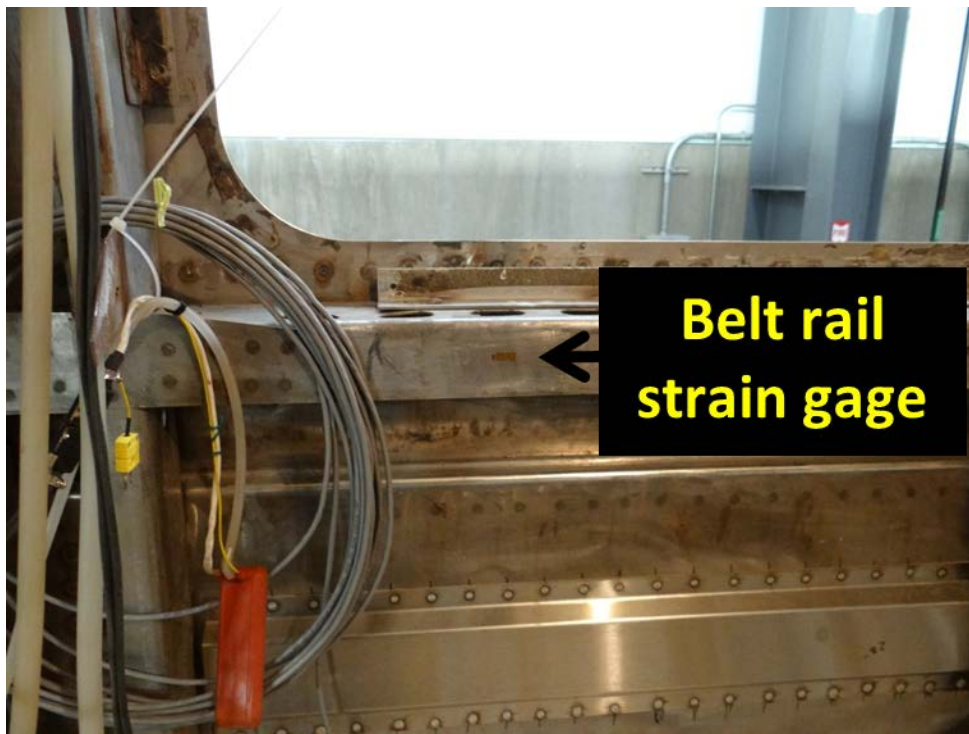


Figure B6. Typical Strain Gage Location on Belt Rail

Post-test Photos

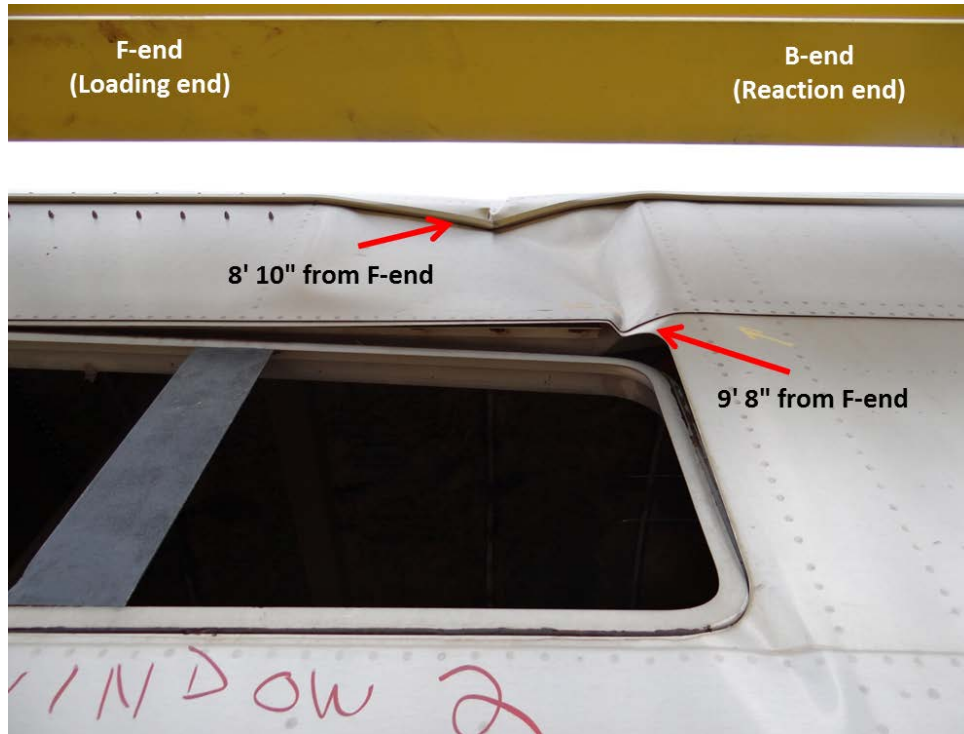


Figure B7. Post-test — Deformation at Section 2 on Left Side of Car



Figure B8. Post-test — Deformation at Section 2 on Right Side of Car



Figure B9. Post-test — Roof Buckle near Section 2



Figure B10. Post-test — Left Roof Rail Buckle at Section 2



Figure B11. Post-test — Right Roof Rail Buckle at Section 2

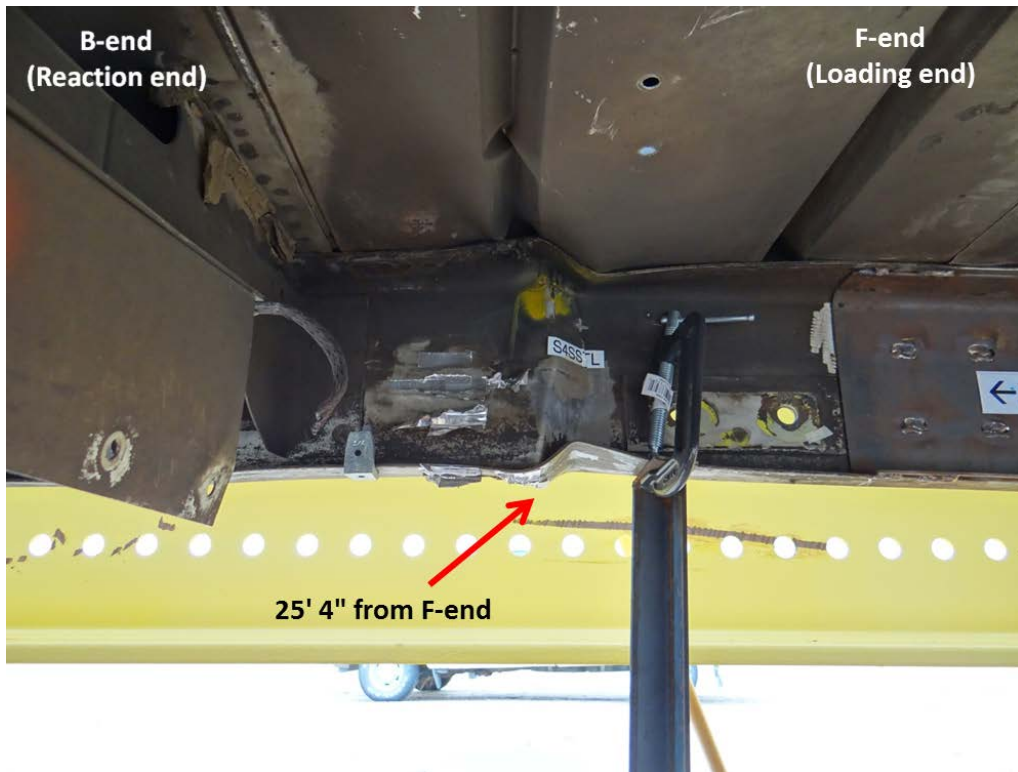


Figure B12. Post-test — Left Side Sill Buckle at Section 4 near Patch

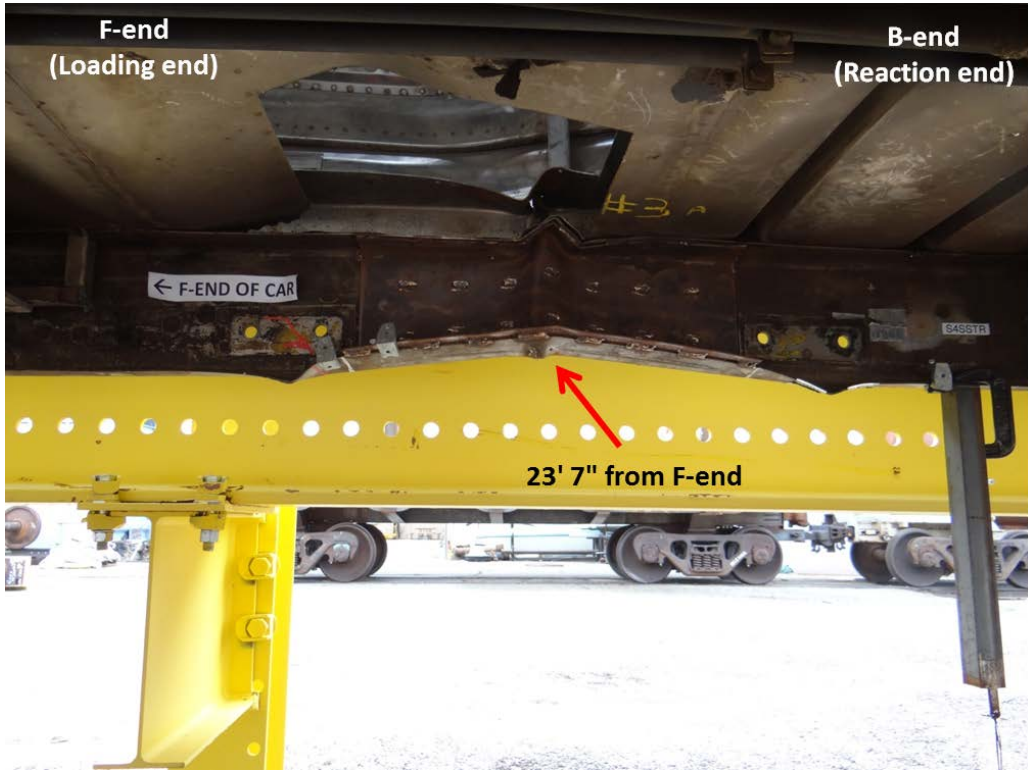


Figure B13. Post-test — Right Side Sill Buckle at Section 4 near Patch

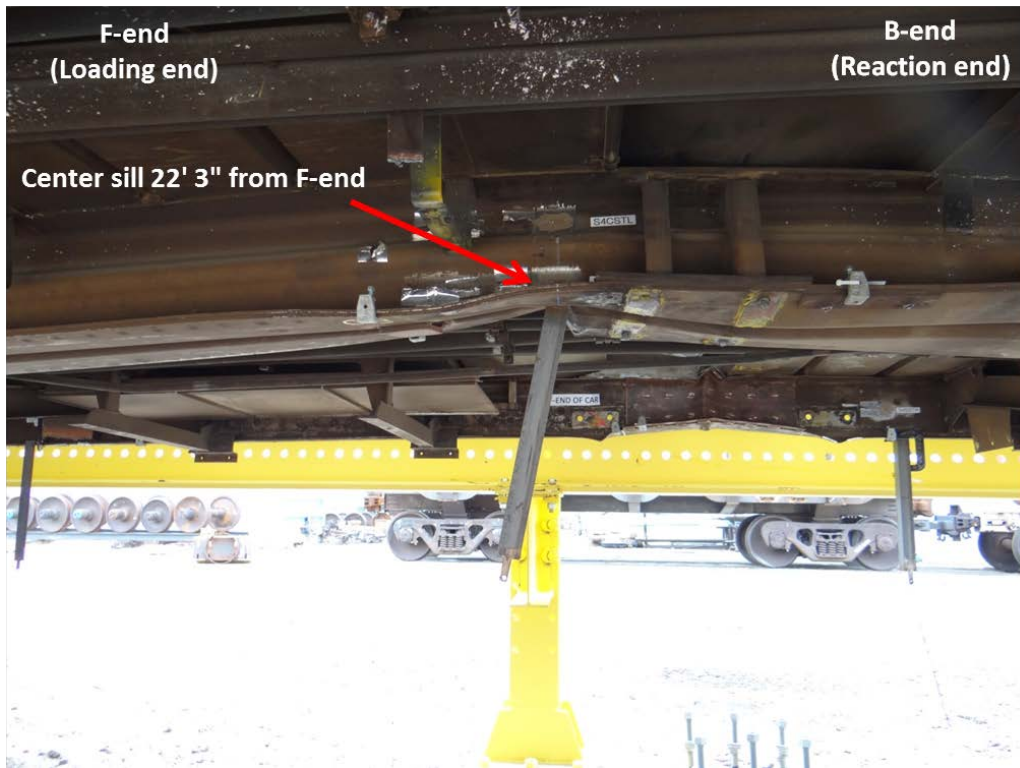


Figure B14. Post-test — Center Sill Buckle at Section 4

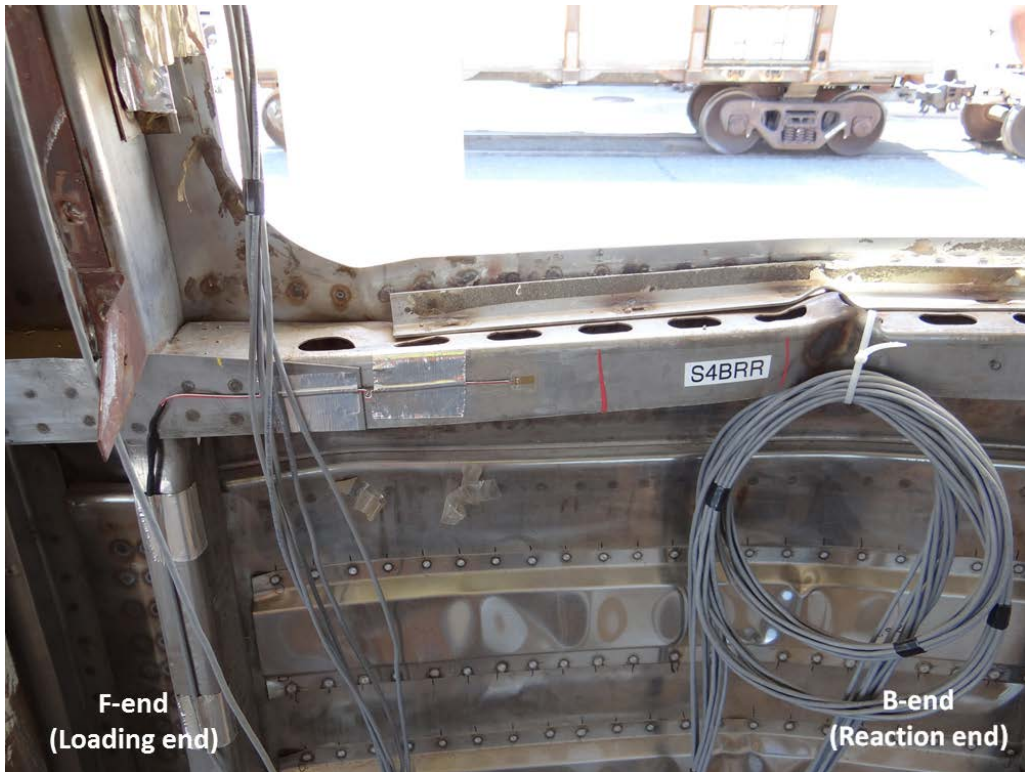


Figure B15. Post-test — Right Belt Rail Buckle near Section 4

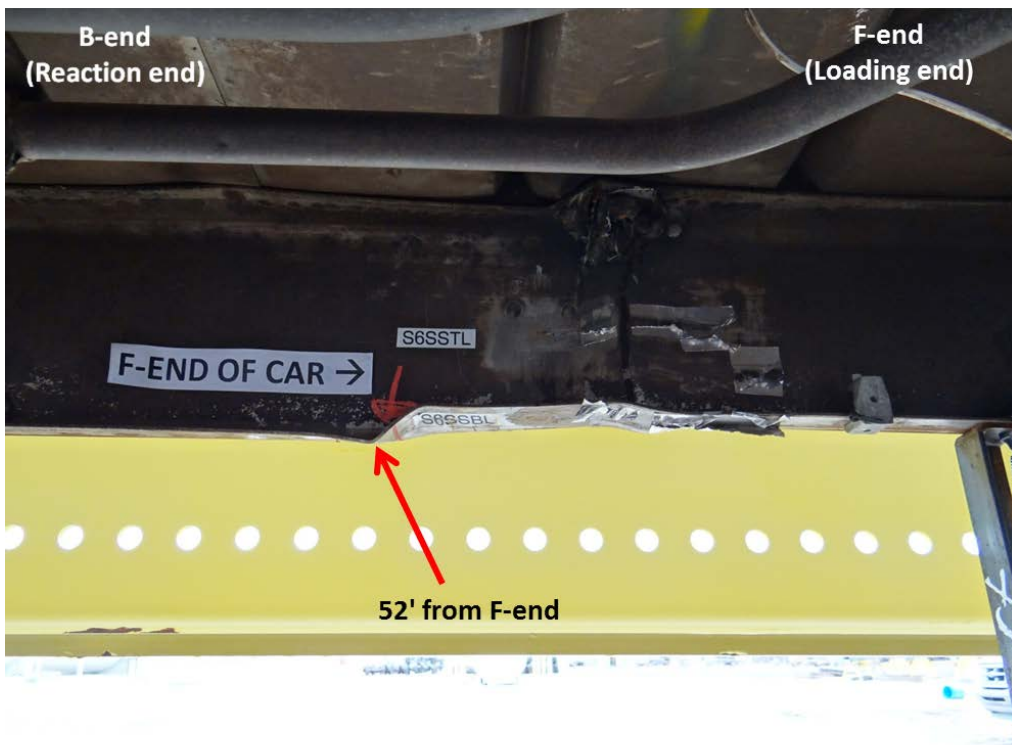


Figure B16. Post-test — Left Side Sill Buckle at Section 6

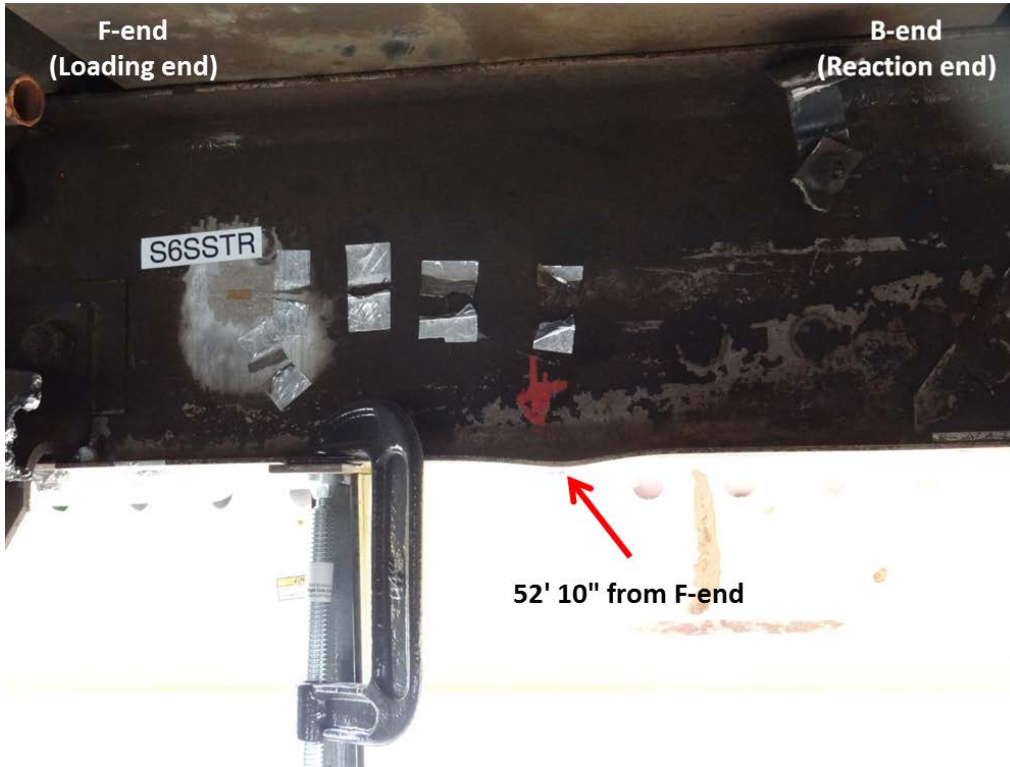


Figure B17. Post-test — Right Side Sill Buckle at Section 6



Figure B18. Post-test — Left Belt Rail Deformation near Section 6

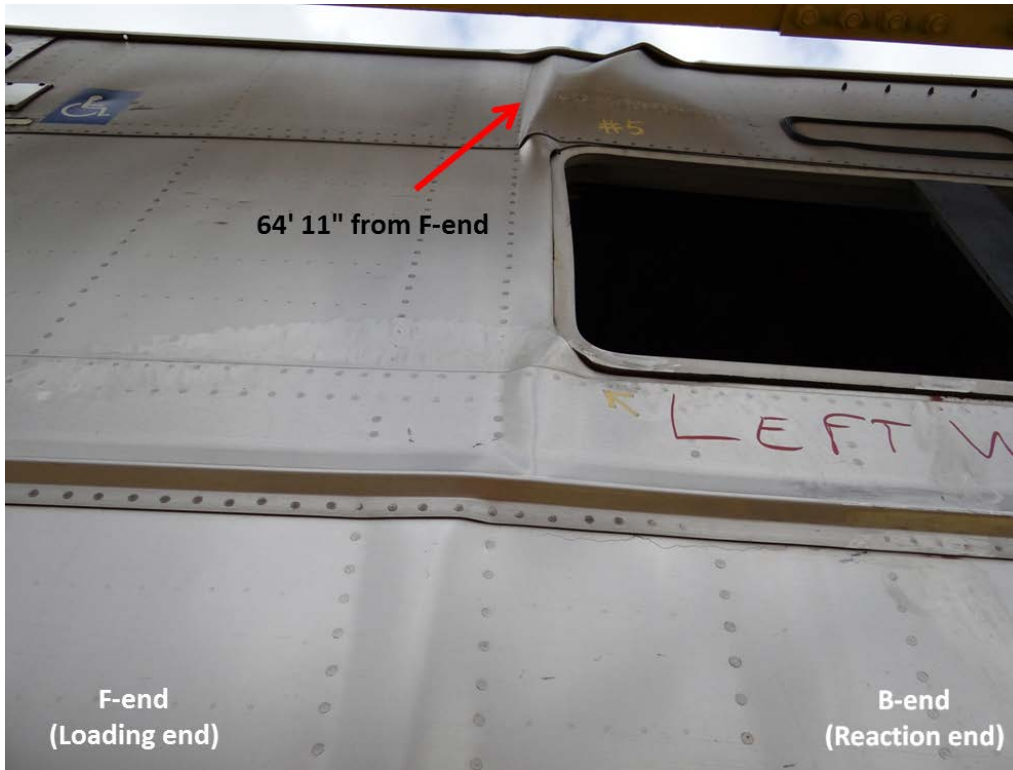


Figure B19. Post-test — Deformation at Section 8 on Left Side of Car

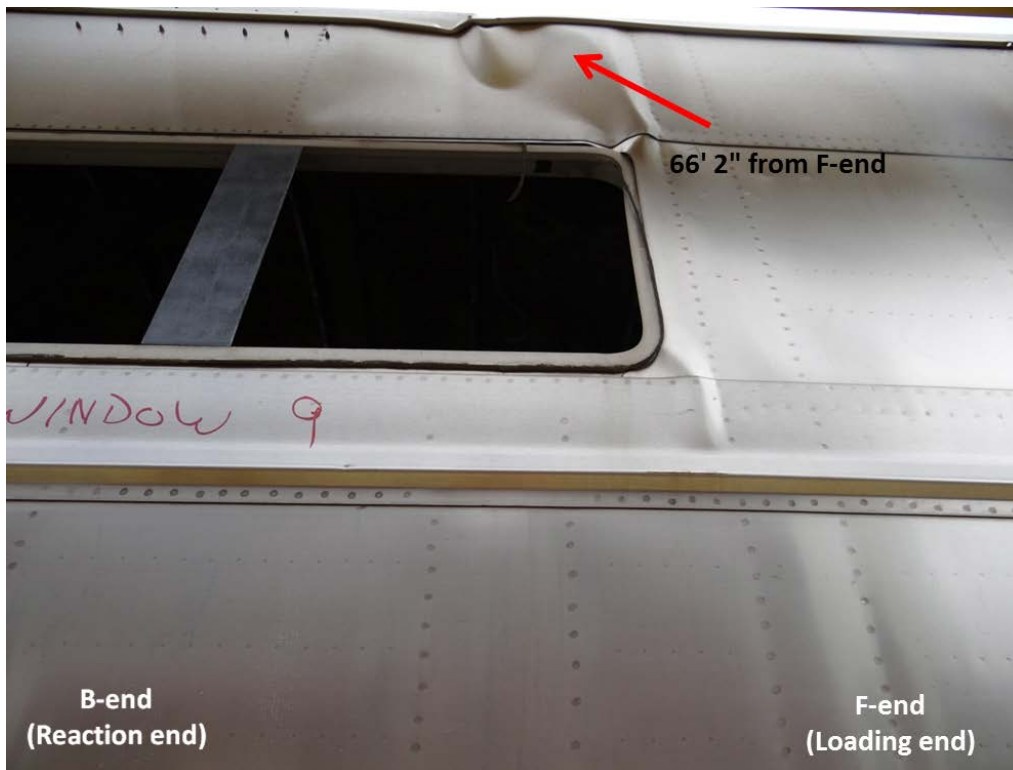


Figure B20. Post-test — Deformation at Section 8 on Right Side of Car



Figure B21. Post-test — Roof Buckle near Section 8



Figure B22. Post-test — Left Roof Rail Buckle at Section 8



Figure B23. Post-test — Right Roof Rail Buckle at Section 8

Appendix C – Model and Analysis Setup (Arup FE Model)

Analysis software

The end load simulations were analyzed using the LS-DYNA finite element (FE) software package, which is commercially available.

Description of the model

The Budd M1 railcar has no planes of symmetry so the FE model includes the full length and full width of the railcar. The trucks have not been modeled explicitly.

The model includes a total of approximately 700,000 elements (Figure C1).

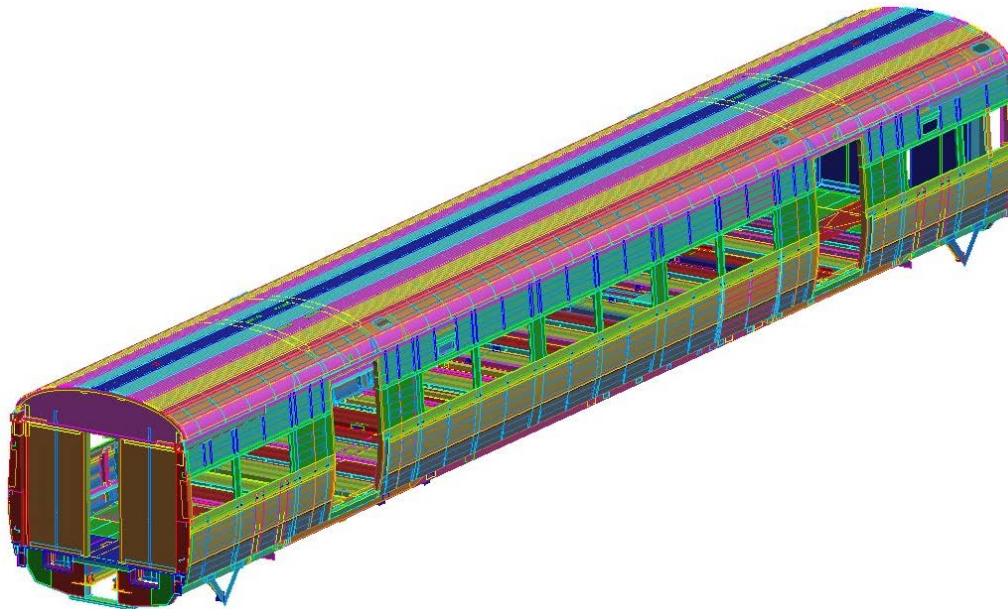


Figure C1. LS-DYNA Model of Budd M1 Railcar

Element type and size

The structure, including brackets and ancillary parts, is modeled using 2-dimensional shell elements. In general, each element has a single integration location in-plane and two integration points through the thickness at this location. The side sills are modeled with fully integrated shells, because they undergo greater deformations than other parts of the railcar.

Spot welds and bolts are modeled using 1-dimensional beam elements. The connection between the beam elements and the corresponding shell elements is achieved using a tied contact or rigid “spider.”

The shell elements have a typical minimum length of between 1/2 and 2 inches.

Connections

Each of the structural components of the railcar has been explicitly modeled using shell elements. The connections between these components have been simulated in one of four ways:

- (1) *Continuous mesh* - In some instances in which two pieces of steel are connected edge-to-edge forming, in essence, one part, they have been modeled as a single component.
- (2) *Tied contact* - Linear welds between the edge of one steel plate and the face of another have been modeled as tied contacts between the nodes and the surface of the respective plates.
- (3) *Discrete connections* - Discrete connections, such as spot welds, puddle welds, bolts and screws, have been modeled as beam elements. The welds have tied contacts to the corresponding components. The screws and bolts are connected using rigid spiders to represent the bolt heads.
- (4) *Rigid connections* - In a very few instances, where the other three connection types were not possible, individual pairs of nodes have been connected using rigid elements.

Boundary conditions and applied loads

Trucks

The support provided by the trucks is represented by a total of four springs—one per bolster spring pocket, as Figure C2 shows. The springs have a stiffness of 2,000 lbs/in in the global vertical direction only, which is based on a typical in-service car mass of 80,000 pounds and a target frequency of 1 Hz.

The springs have no stiffness in the horizontal plane and no rotational stiffness.

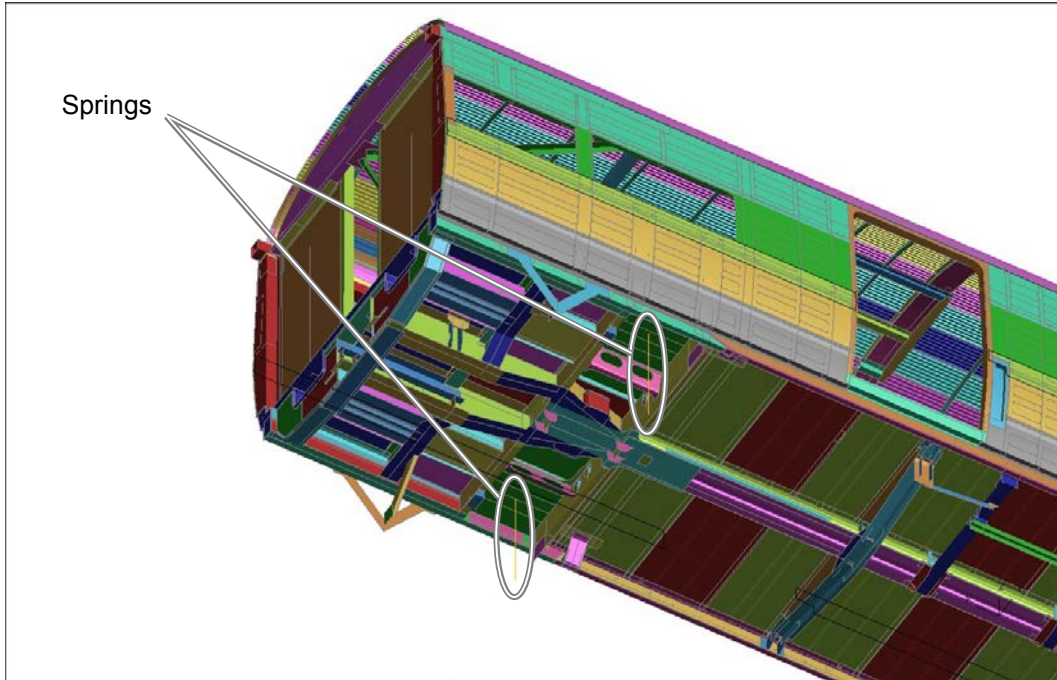


Figure C2. Vertical-Only Springs Representing Trucks

Loading Points

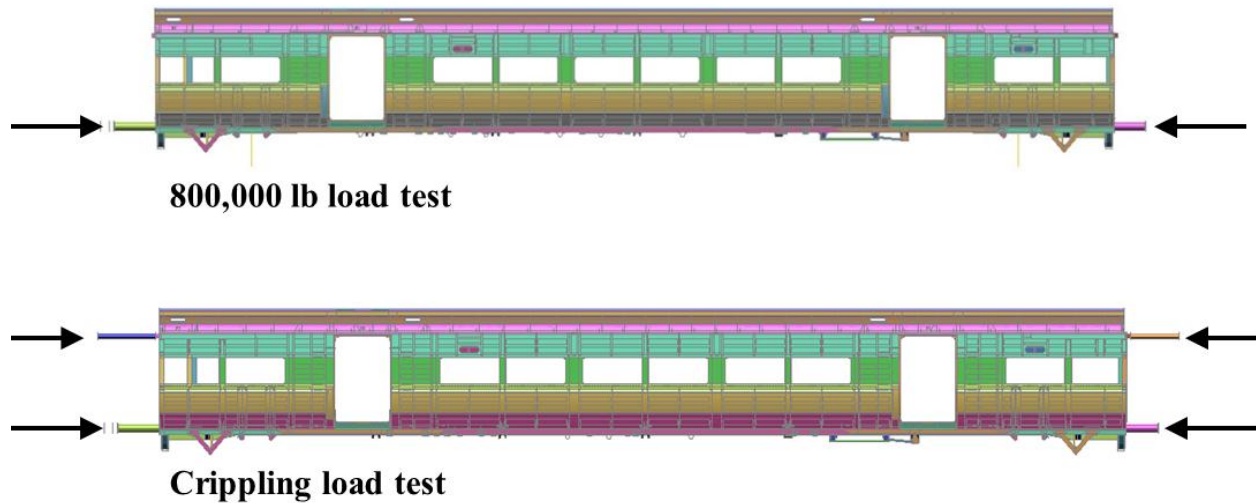


Figure C3. Load Application Points

For the 800,000-lb load test, loading and longitudinal constraints are applied at the lower CEM pockets only. During the crippling load test, loading and longitudinal constraints are at the lower and upper CEM pockets. Figure C3 illustrates the loading locations.

The loading bars have been modeled explicitly as rigid bodies. The interfaces with the railcar CEM pockets use contact definitions. At the fixed end, the ends of the bars furthest from the

railcar are pinned to the ground; i.e. fully restrained translationally and unrestrained rotationally. Figure C4 and Figure C5 show the fixed end constraints for the 800,000-lb load test and crippling load test, respectively.

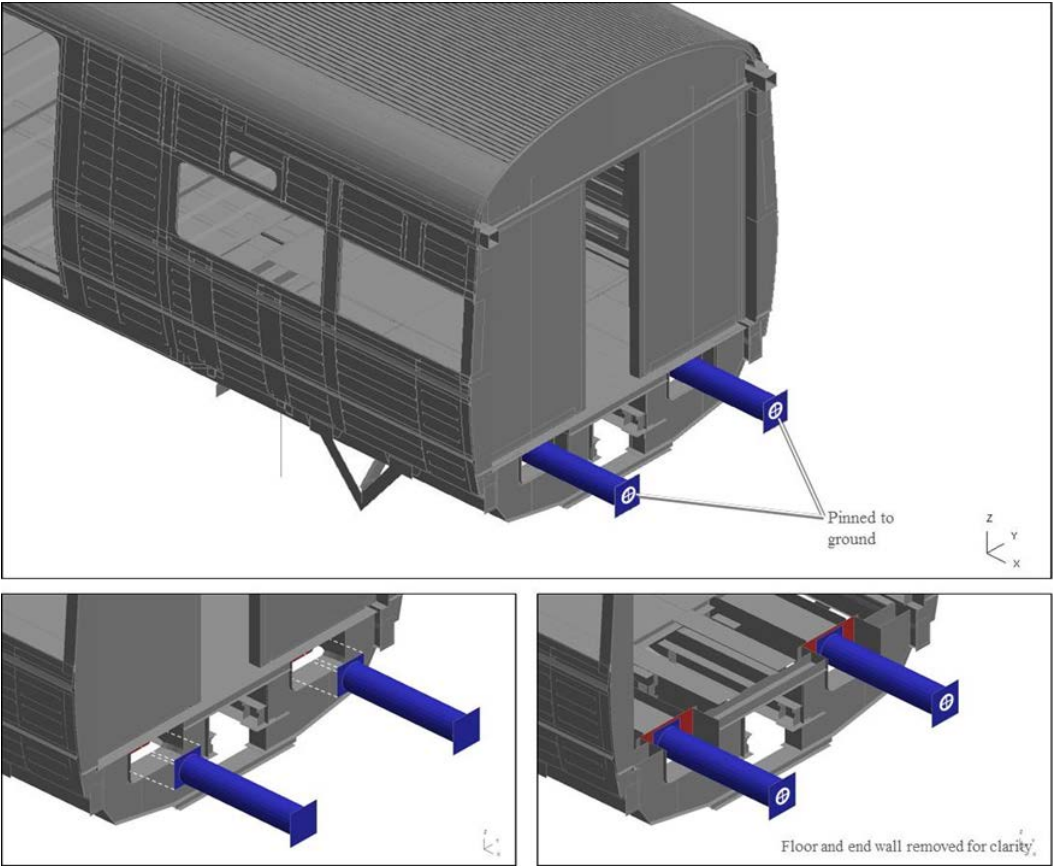


Figure C4. Loading Bars (blue) and Contact to Lower CEM Pockets (red) at the Fixed End for the 800,000-pound Load Test

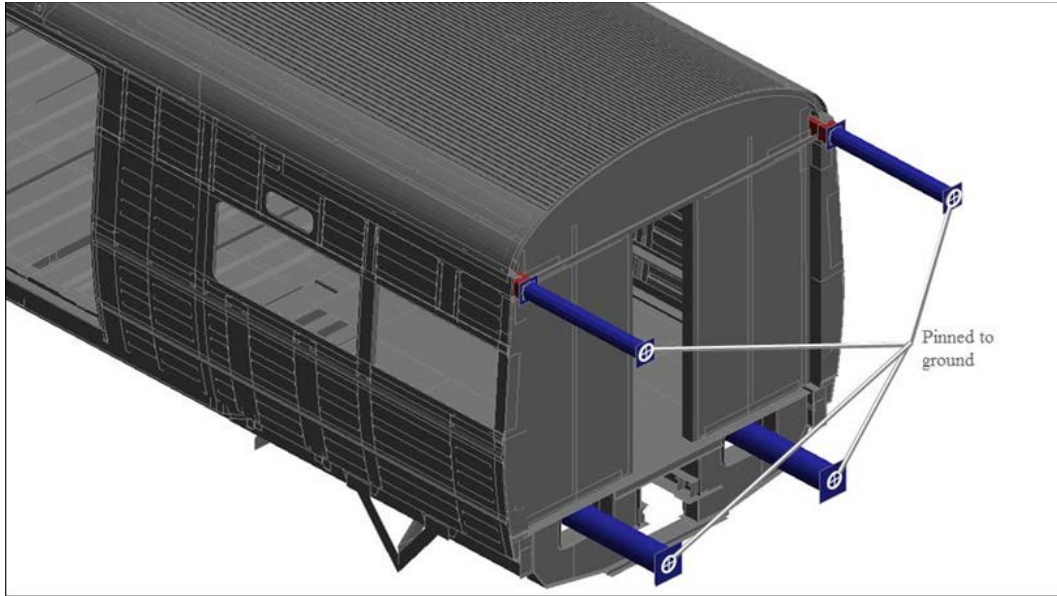


Figure C5. Loading Bars (blue) and Contact to CEM Pockets (red) at the Fixed End for the Crippling Load Analysis

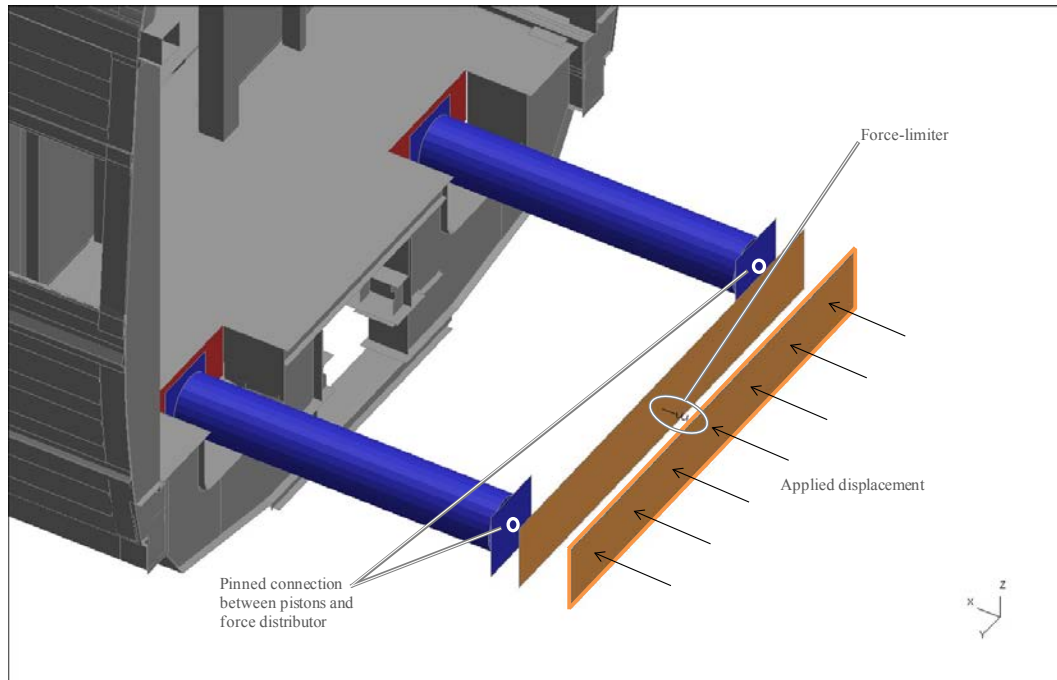


Figure C6. Mechanism for Applying Longitudinal Load in the 800,000-pound Load Test

In the 800,000-lb load test, the force was applied to the actuated loading bars by an equal-displacement, force-limiting mechanism, as Figure C6 illustrates. This mechanism is subjected to an applied displacement, which it transfers to the loading bars, up to a maximum of 800,000 pounds. The displacements of the two loading bars are equal.

During the crippling load analysis, the force limiter is unnecessary so an equal increasing displacement is applied to each of the loading bars.

The full model is subjected to gravity loading.

Material properties

Materials have been modeled using two methods: (1) nonlinear, using an explicitly defined stress-strain curve and (2) bilinear elastic-plastic.

Materials are referred to by the names used in the construction drawings provided by Budd.

Nonlinear materials

Nonlinear material definitions were based upon coupon tests. Coupons were taken for the following materials:

- Steel LT (side-wall post sample)
- Steel MT (floor-beam sample)
- Steel ST (roof car-line sample)
- Steel HT (floor-panel and center-sill samples)
- Deadlite (external side-panel sample)

Appendix D shows the distribution of the materials through the car.

The procedure adopted was:

By TTCI:

1. Physical testing of specimens from a sister railcar.
2. Modification of results to correct for the effects of the test measurement methodology.

By Arup:

3. Initial estimate of an average stress-strain curve based on the modified lab results.
4. FE tensile test of a coupon for comparison to physical test results.
5. Iterative adjustment of the stress-strain definition to achieve good correlation between FE test results and laboratory test results.
6. The linear elastic region was defined by a Young's modulus and a yield stress; the nonlinear plastic region was defined using an explicit stress-strain curve.

Appendix D contains the modified test results, the stress-strain curves used in the analysis, and the results of the coupon tests for the stress-strain curve. Appendix D also describes development of the material curves for the center sill HT and side sill HT materials.

Bilinear materials

All other materials were modeled with bilinear stress-strain curves. For most, material properties were taken using the standards of the American Society of Mechanical Engineers (ASTM) or standards similar to ASTM. Appendix D tabulates the properties for each of these materials.

Appendix D – Material Formulations (Arup FE Model)

Distribution of materials

LT

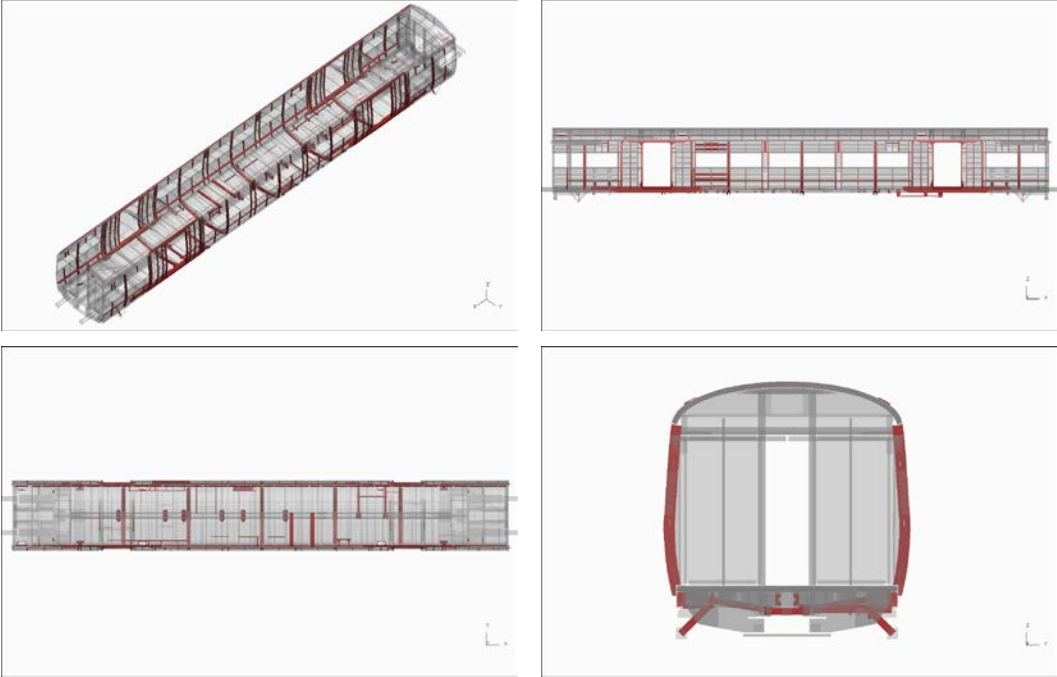


Figure D1. Distribution of LT Material

MT

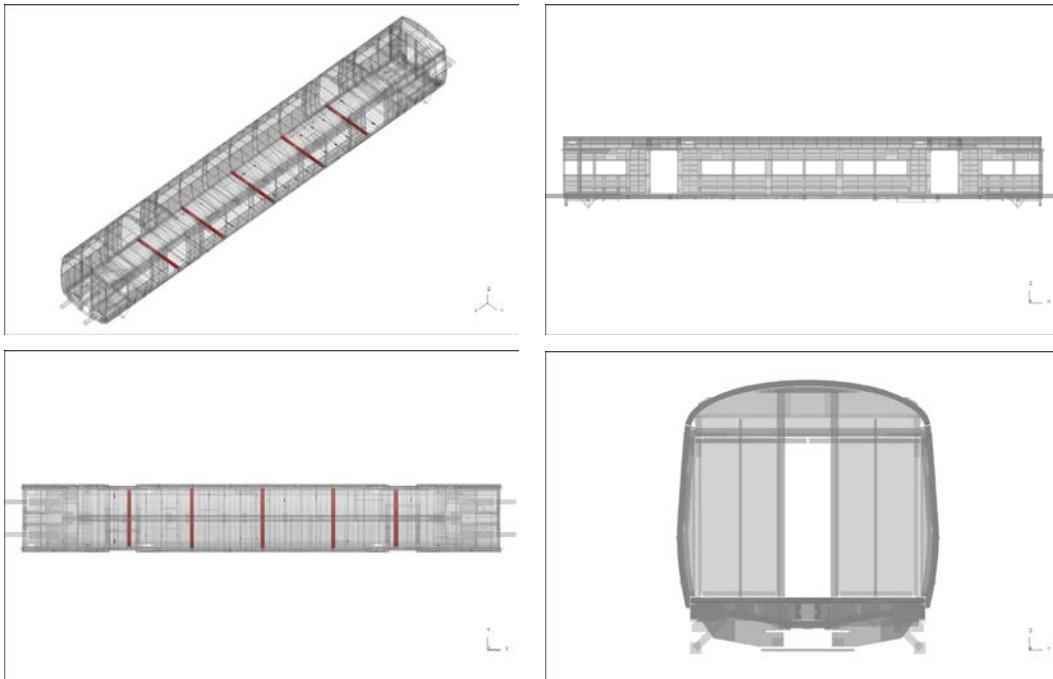


Figure D2. Distribution of MT Material

ST

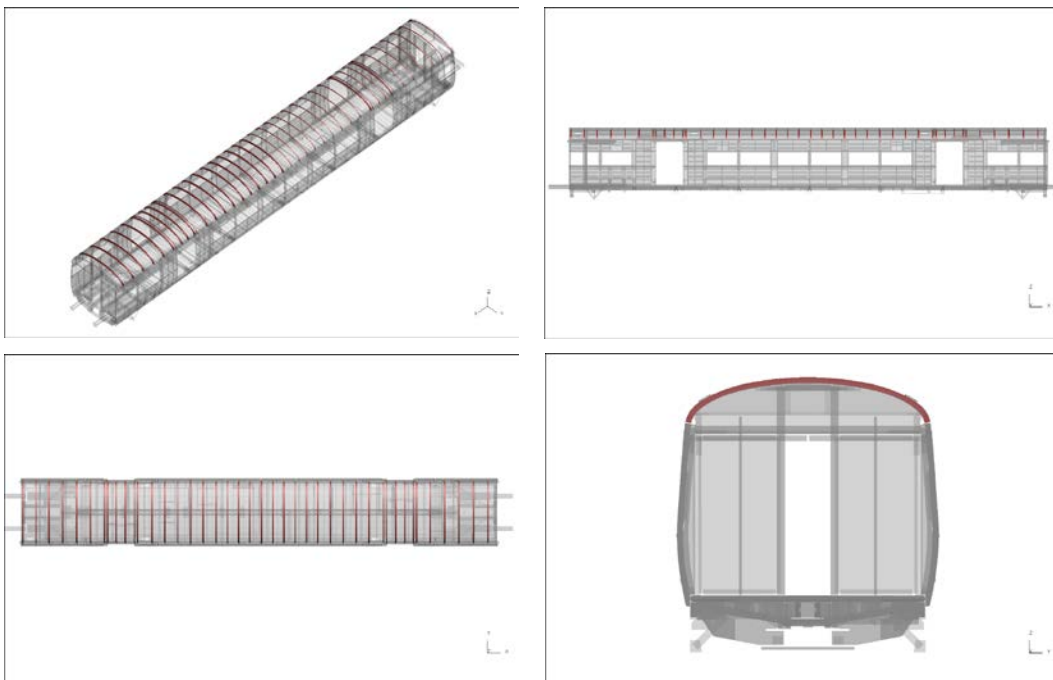


Figure D3. Distribution of ST Material

Deadlite

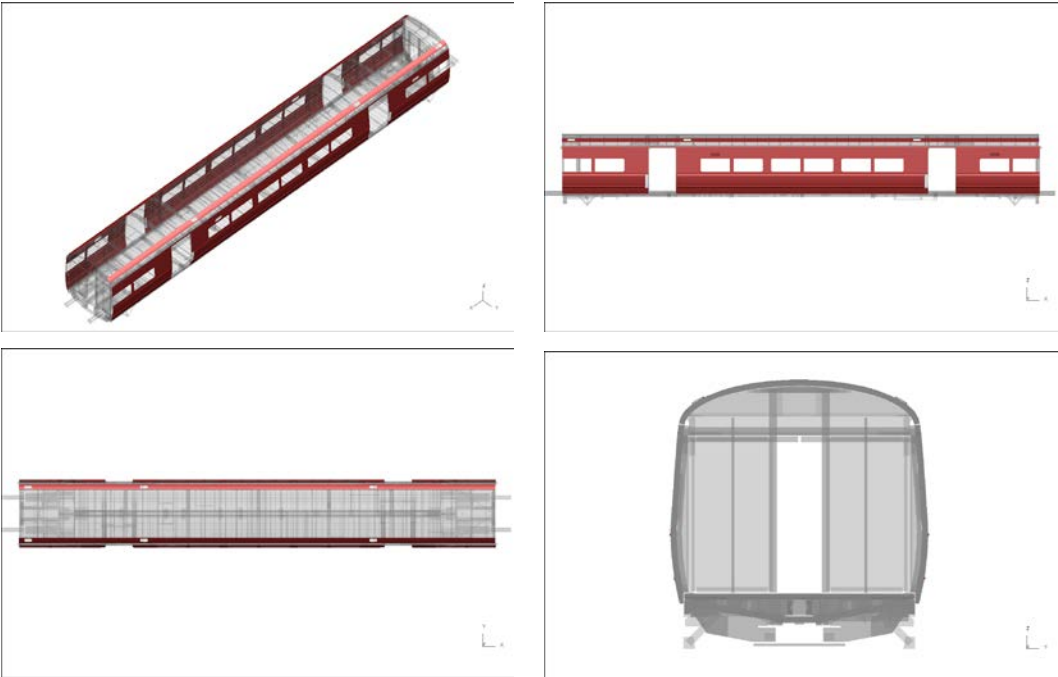


Figure D4. Distribution of Deadlite Material

General HT

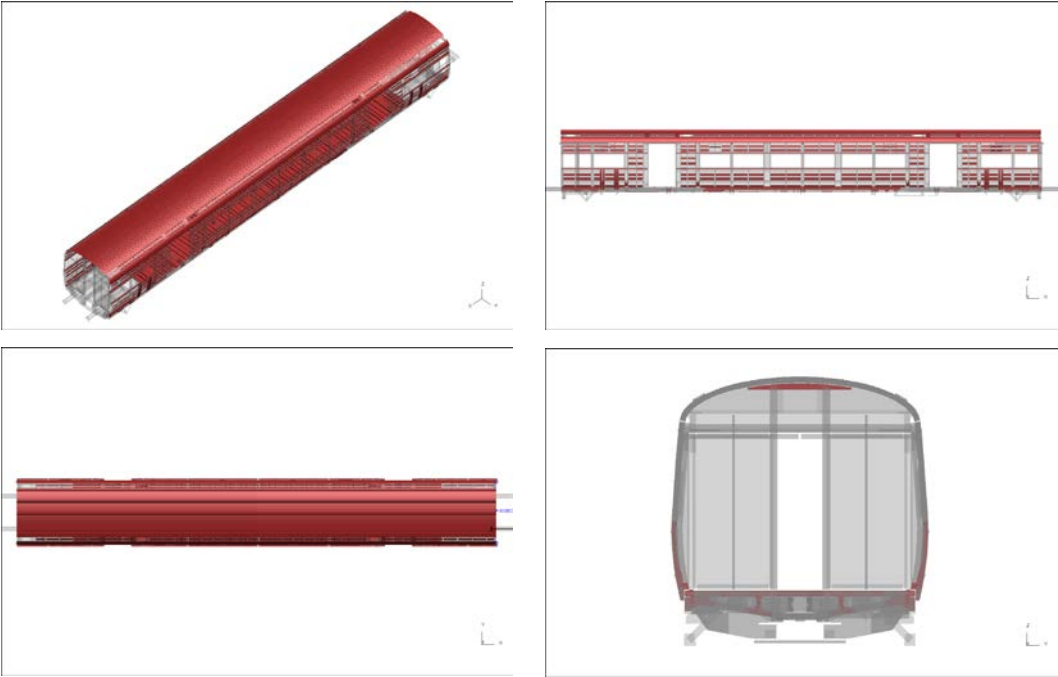


Figure D5. Distribution of General HT Material

Center sill HT

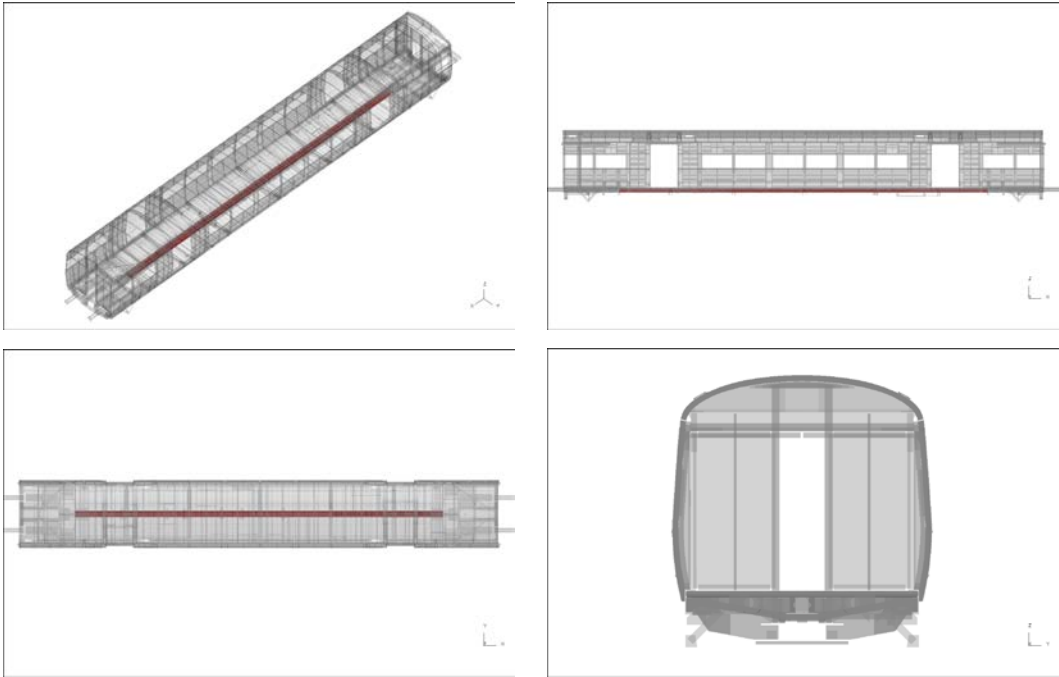


Figure D6. Distribution of Center Sill HT Material

Side sill HT

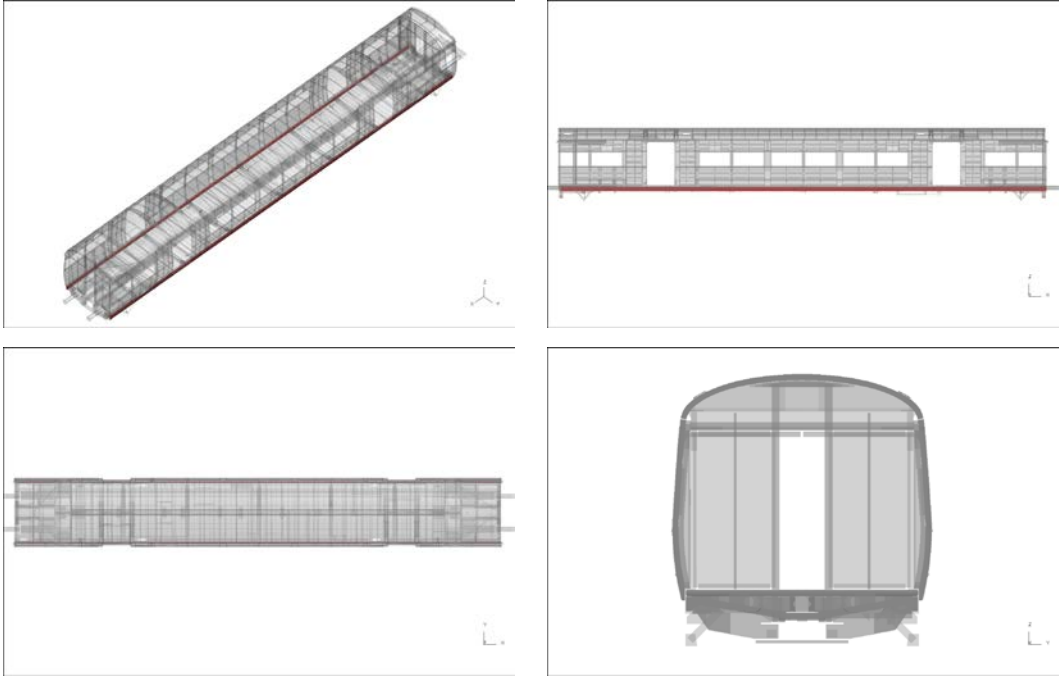


Figure D7. Distribution of Side Sill HT Material

A36

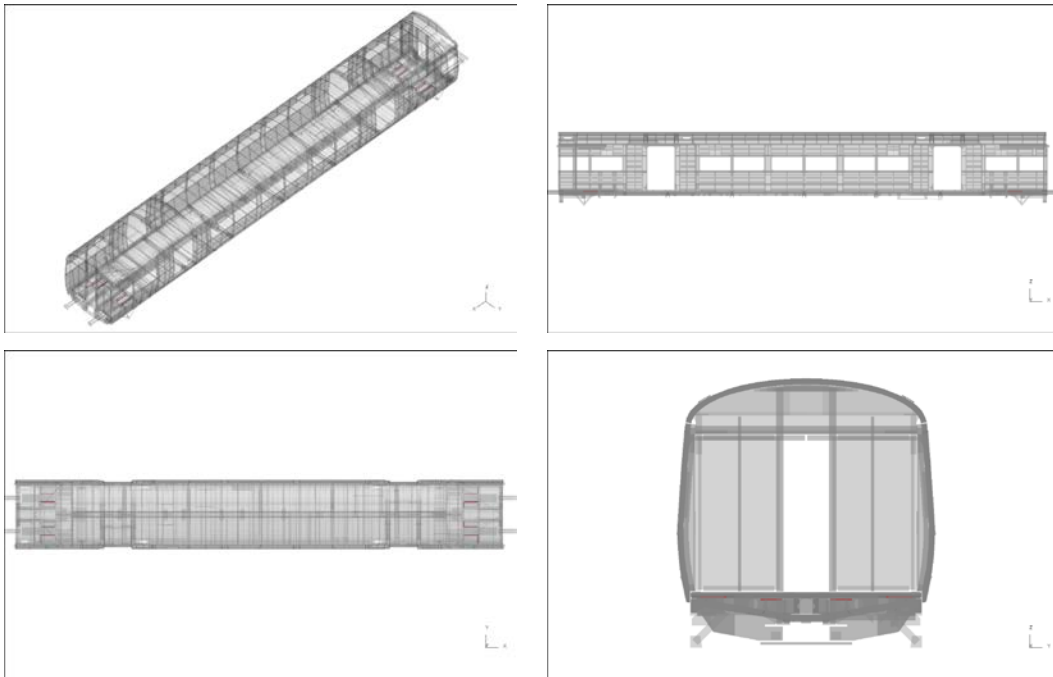


Figure D8. Distribution of A36 Material

A572 Gr50

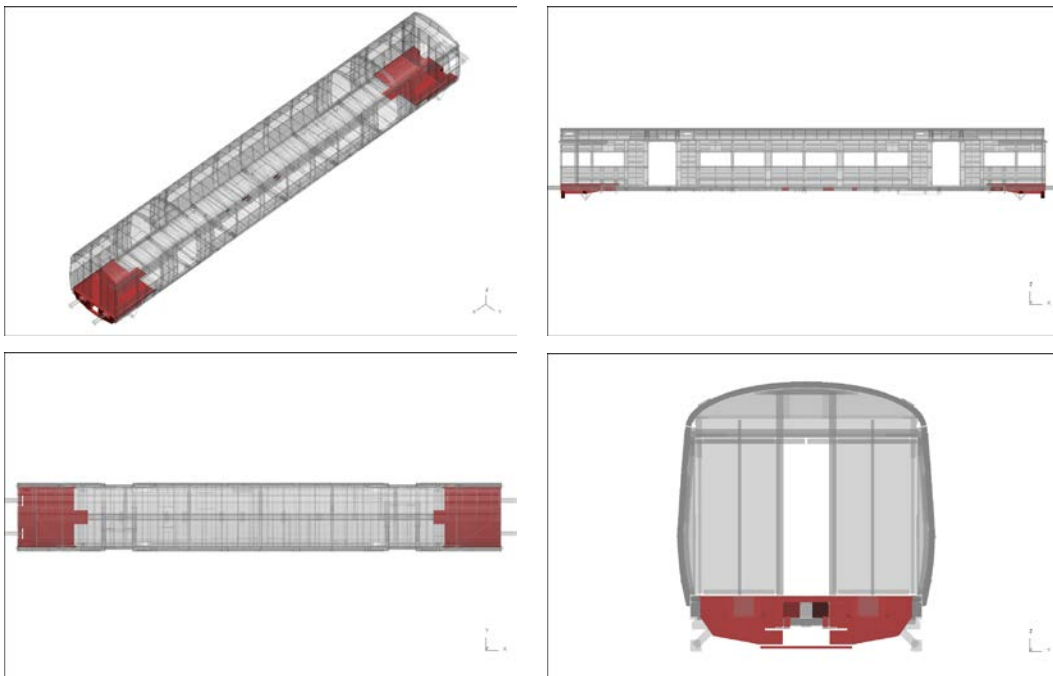


Figure D9. Distribution of A572 Gr50 Material

A710 GrA3

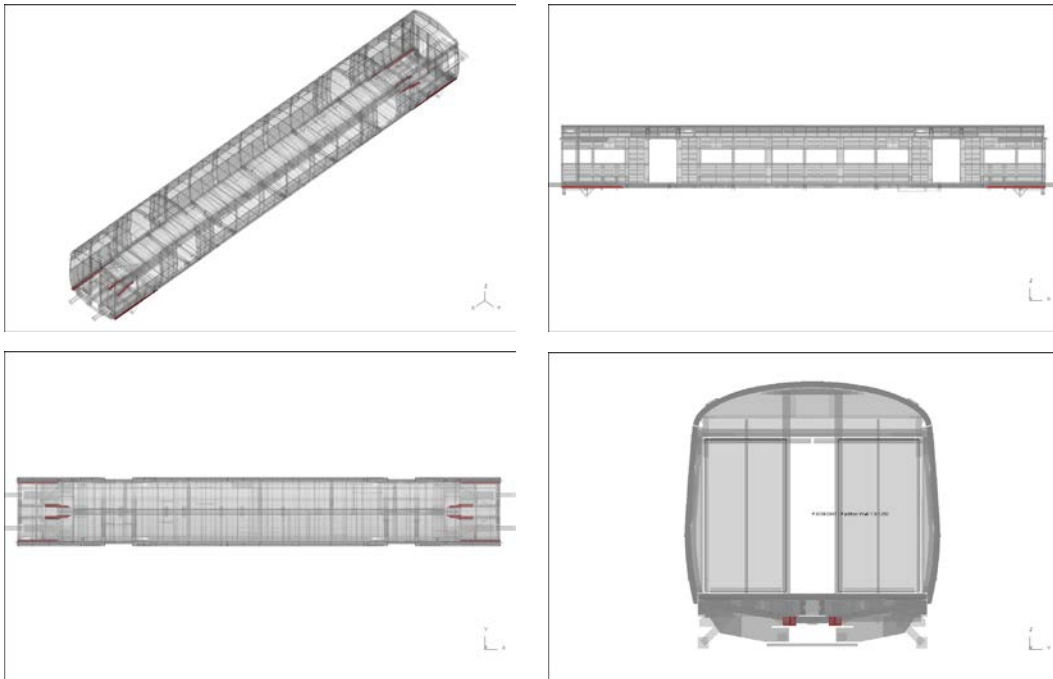


Figure D10. Distribution of A710 GrA3 Material

RY300

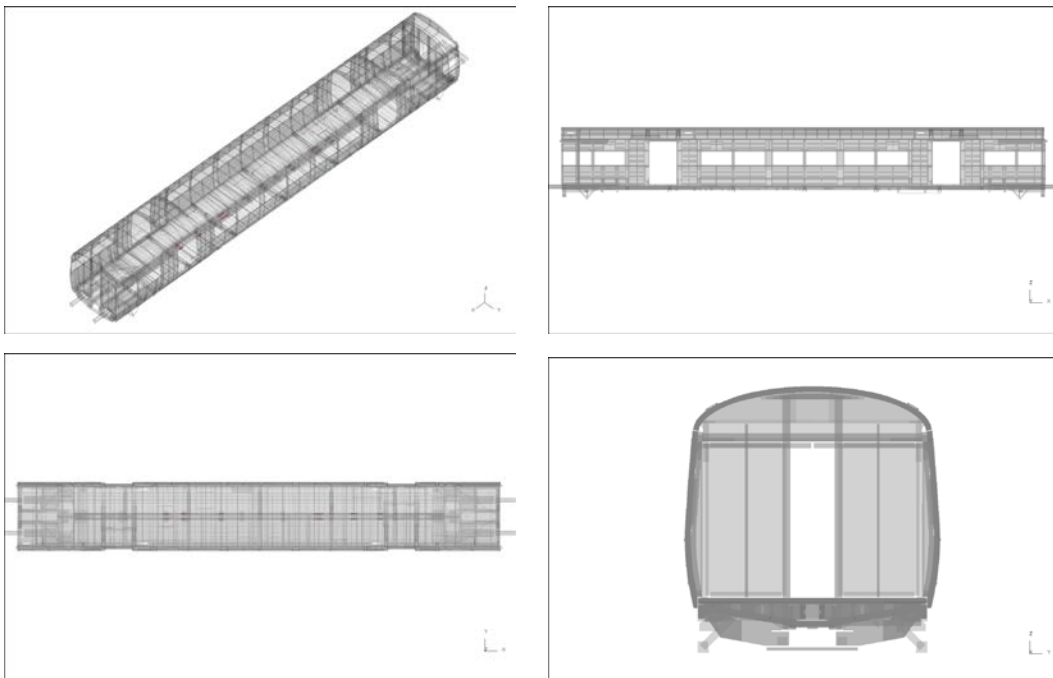


Figure D11. Distribution of RY300 Material

RY306

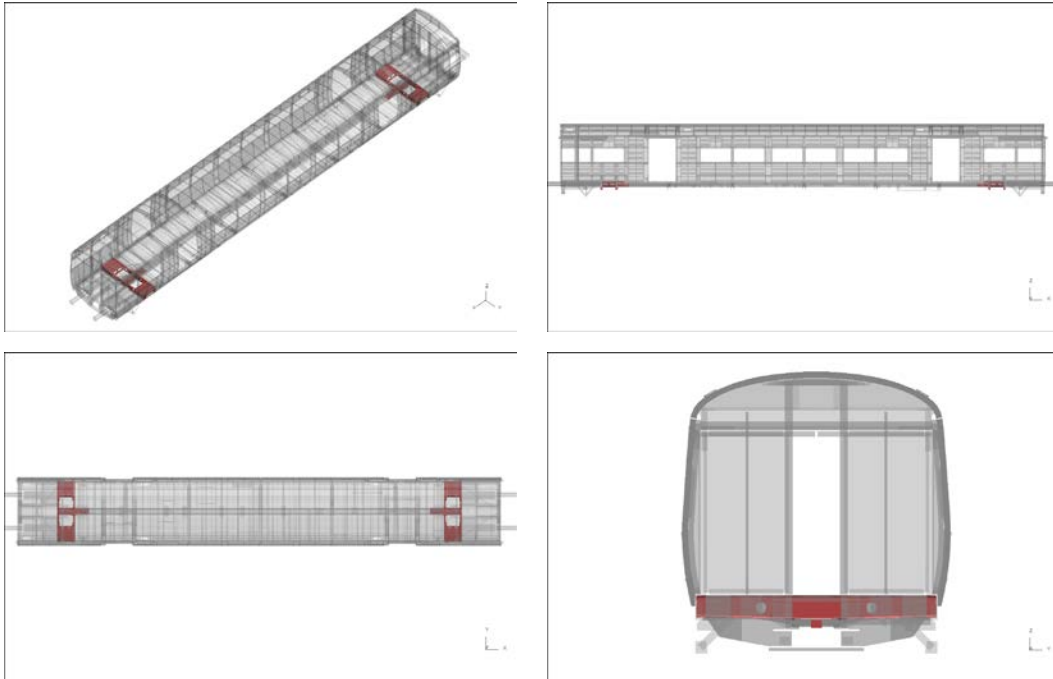


Figure D12. Distribution of RY306 Material

RY400

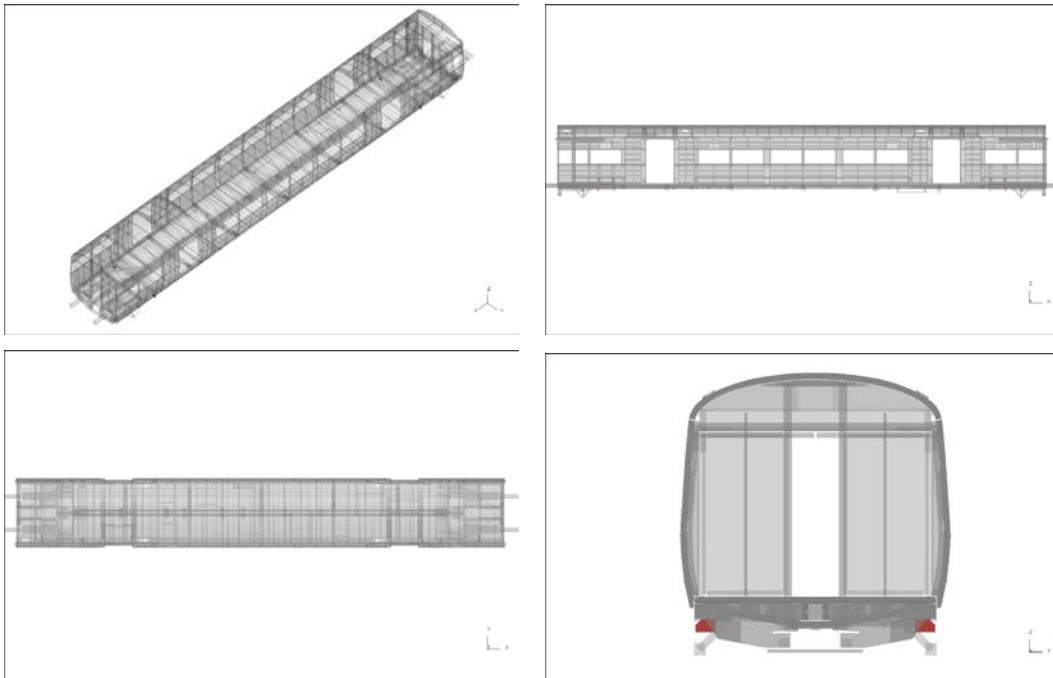


Figure D13. Distribution of Ry400 Material

Deep draw

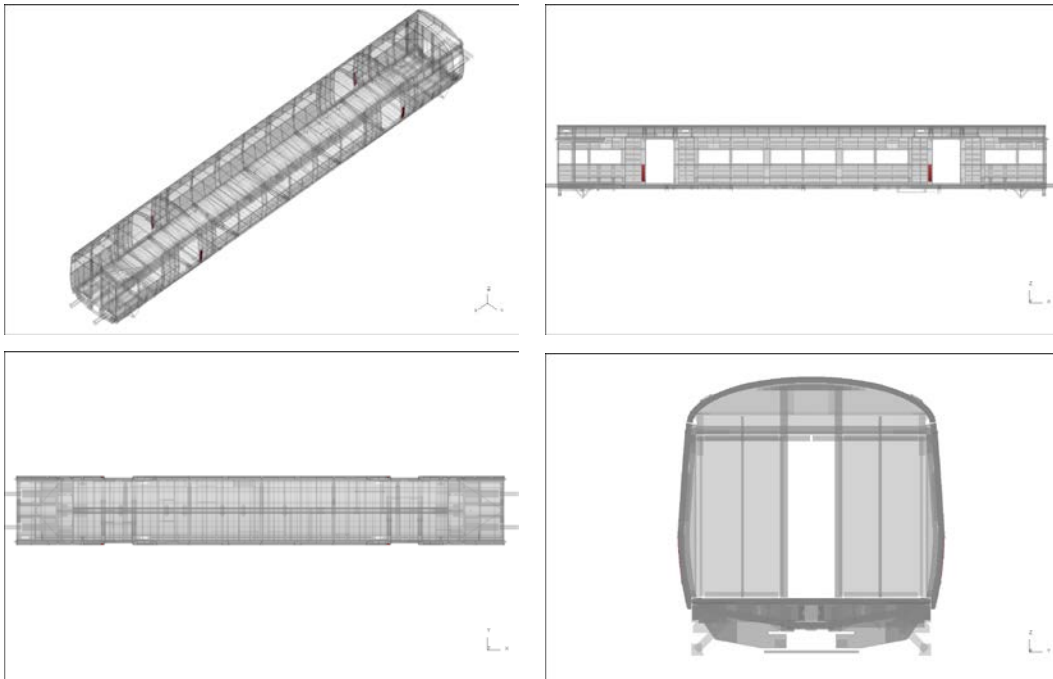


Figure D14. Distribution of Deep Draw Material

CEM material, assumed to be A572 Gr50

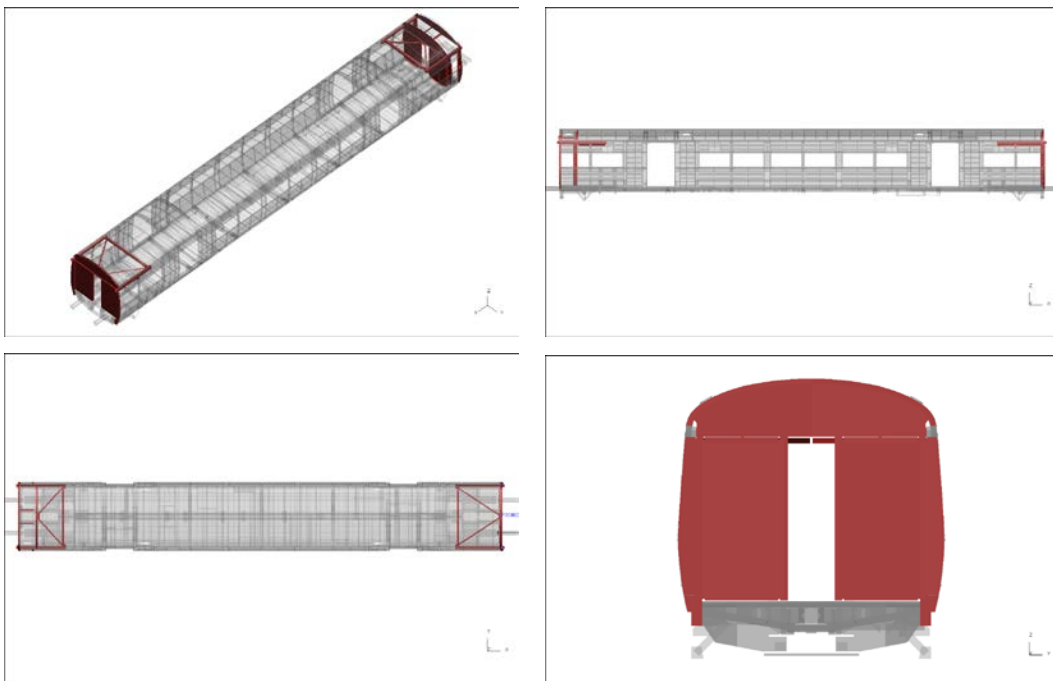


Figure D15. Distribution of CEM Material, Assumed to be A572 Gr50

Nonlinear material properties

TTCI provided results of tensile tests conducted at two laboratories. These results had been cleaned and modified by TTCI to be comparable to each other. Because the lab tests recorded the overall force and the overall extension of the coupons, engineering stresses and strains could be calculated from the results. The conversion to true stresses and strains depends on the deformed shape of the test coupon.

For the end load analyses, the nonlinear material definitions were developed iteratively using the following process:

A true stress-true strain definition was estimated from the results of the lab tests.

- (1) A FE tensile test was conducted with a typical coupon, and the engineering strain and engineering stress were compared to the lab test results.
- (2) The input definition (true stress-strain) was manually adjusted and the coupon retested. This was repeated until a reasonable fit was achieved between the engineering stress-strain characteristics of the analysis and the lab tests.

Figure D16 through Figure D22 show, for each material, the engineering stress and strain from the lab tensile test results (grey), the true stress-strain material definition (blue), and the engineering stress-strain output of the FE coupon analysis (red). Though in some cases the material definitions look like a poor match for the lab results, the coupon analysis output shows that they perform appropriately.

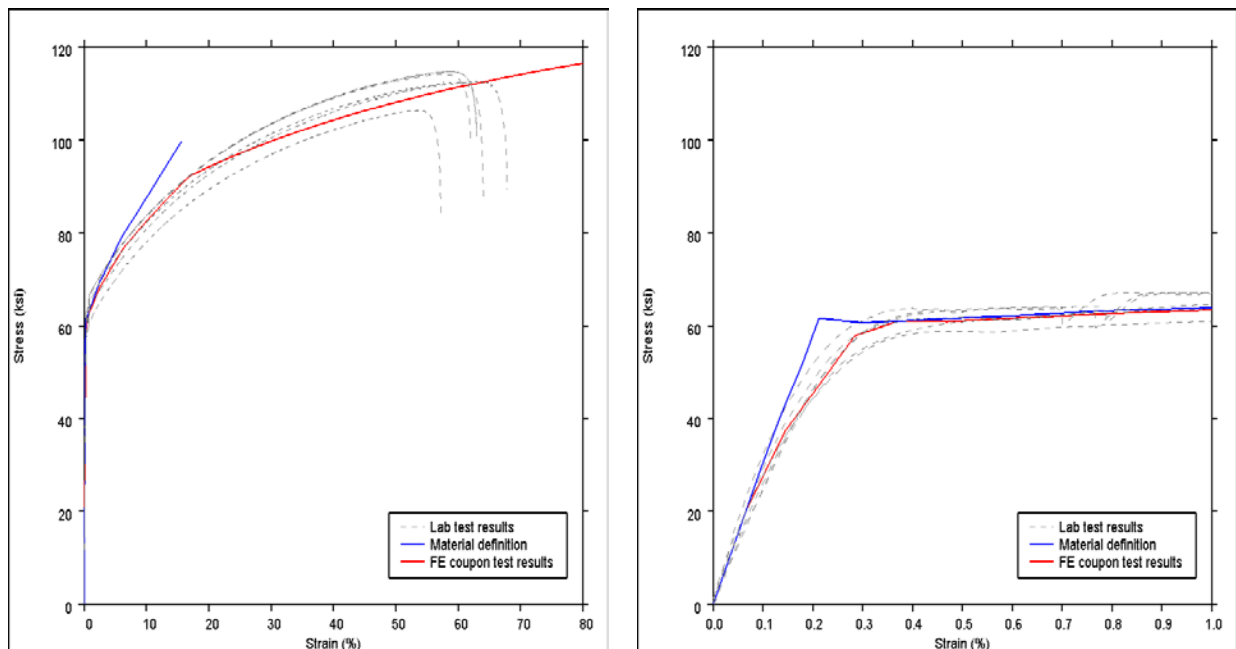


Figure D16. LT: Lab Tensile Test Results, Material Definition, FE Analysis Results

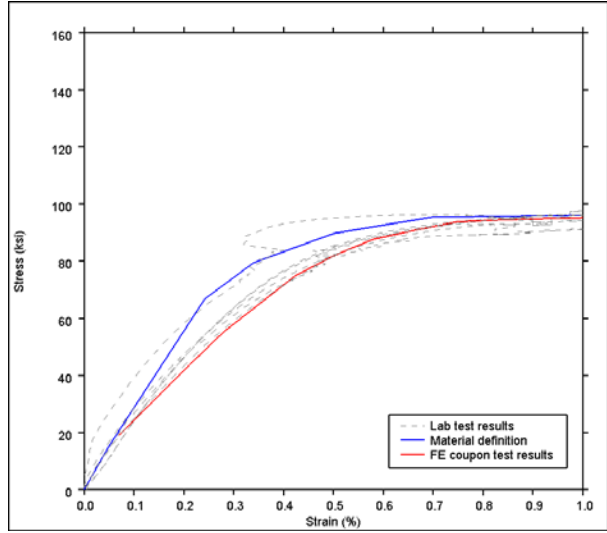
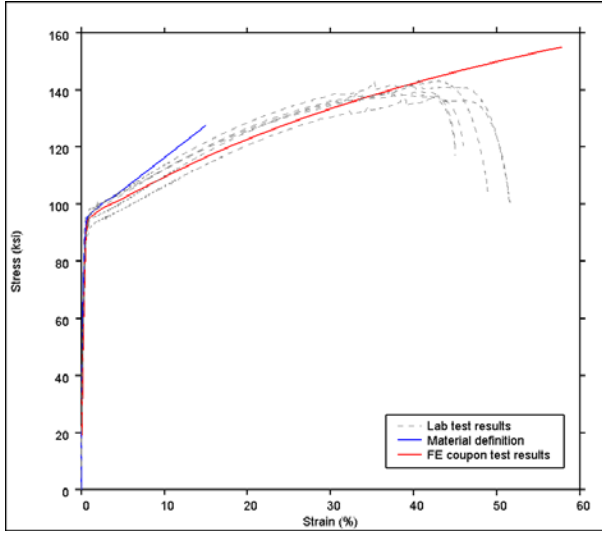


Figure D17. MT: Lab Tensile Test Results, Material Definition, FE Analysis Results

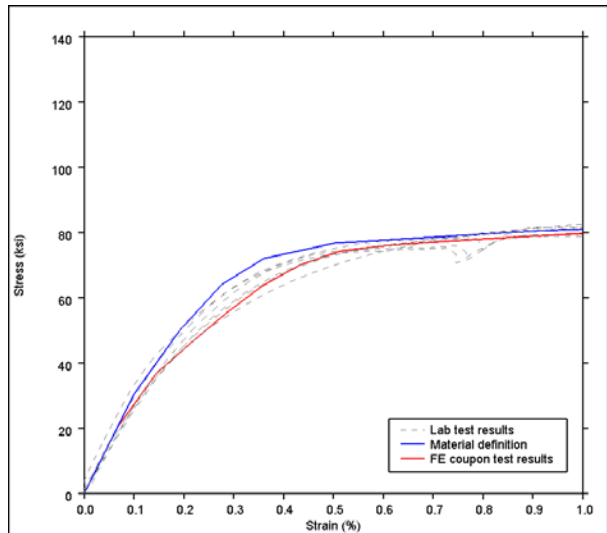
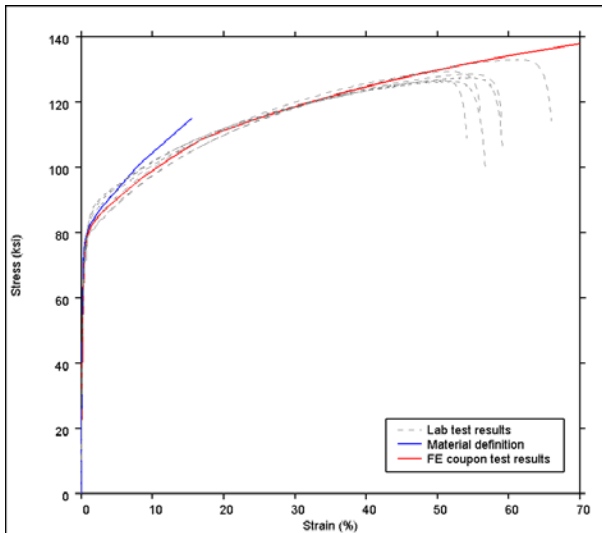


Figure D18. ST: Lab Tensile Test Results, Material Definition, FE Analysis Results

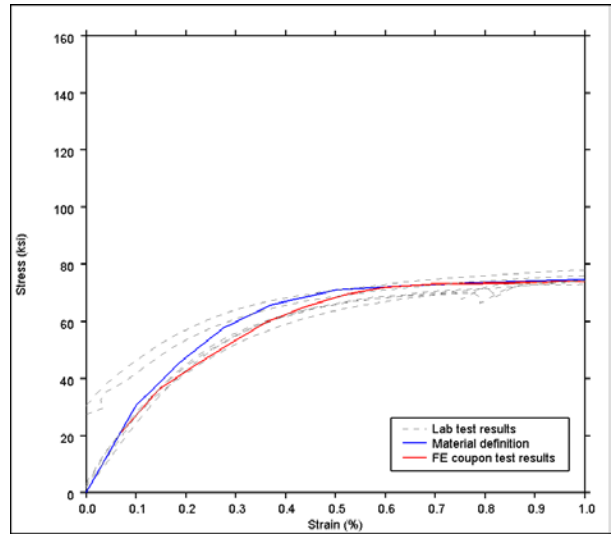
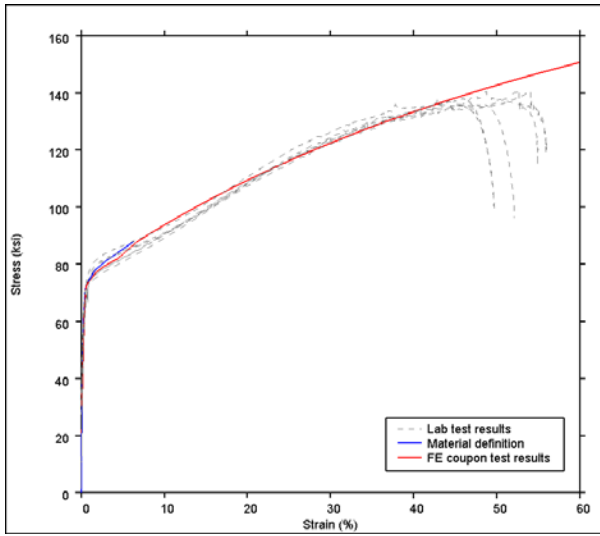


Figure D19. Deadlite: Lab Tensile Test Results, Material Definition, FE Analysis Results

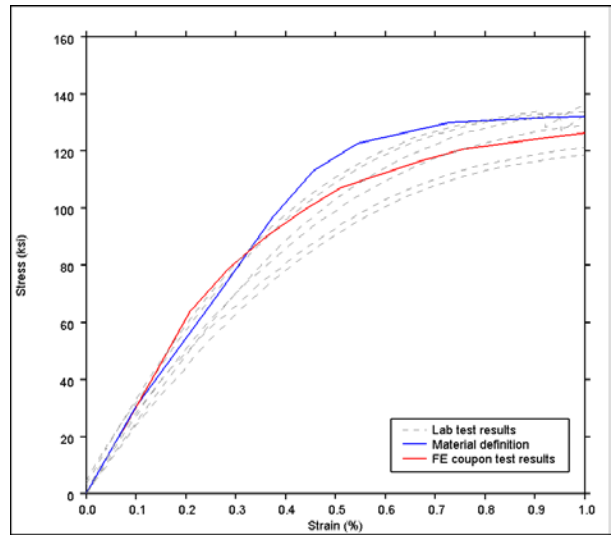
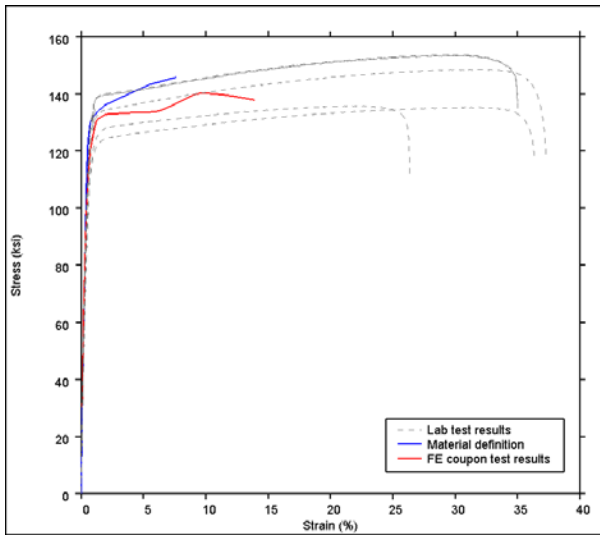


Figure D20. General HT: Lab Tensile Test Results, Material Definition, FE Analysis Results

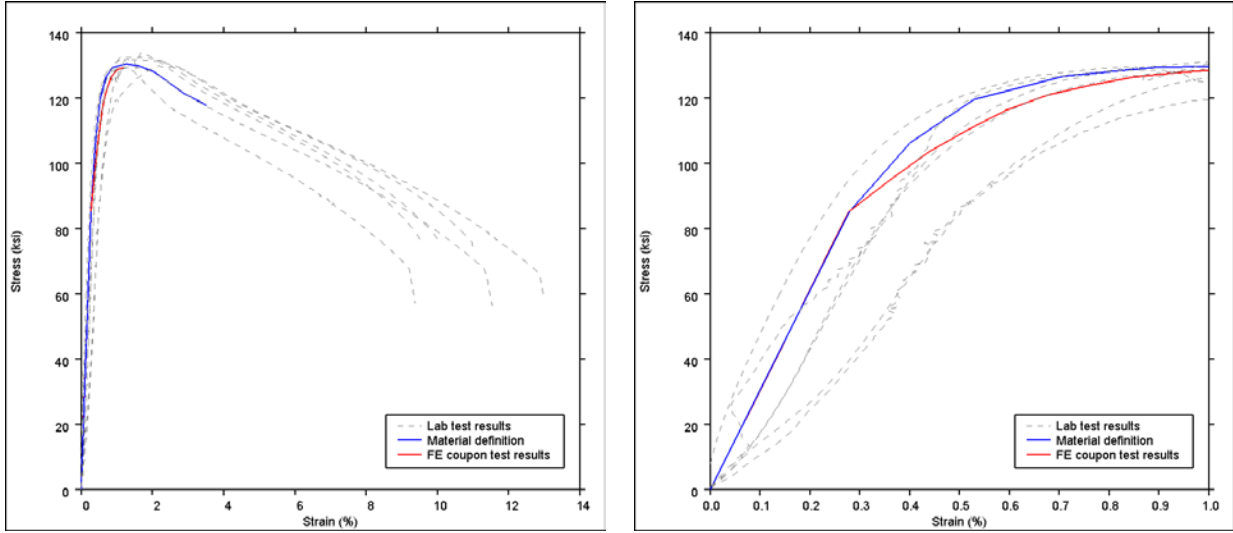


Figure D21. Center Sill HT: Lab Tensile Test Results, Material Definition, FE Analysis Results

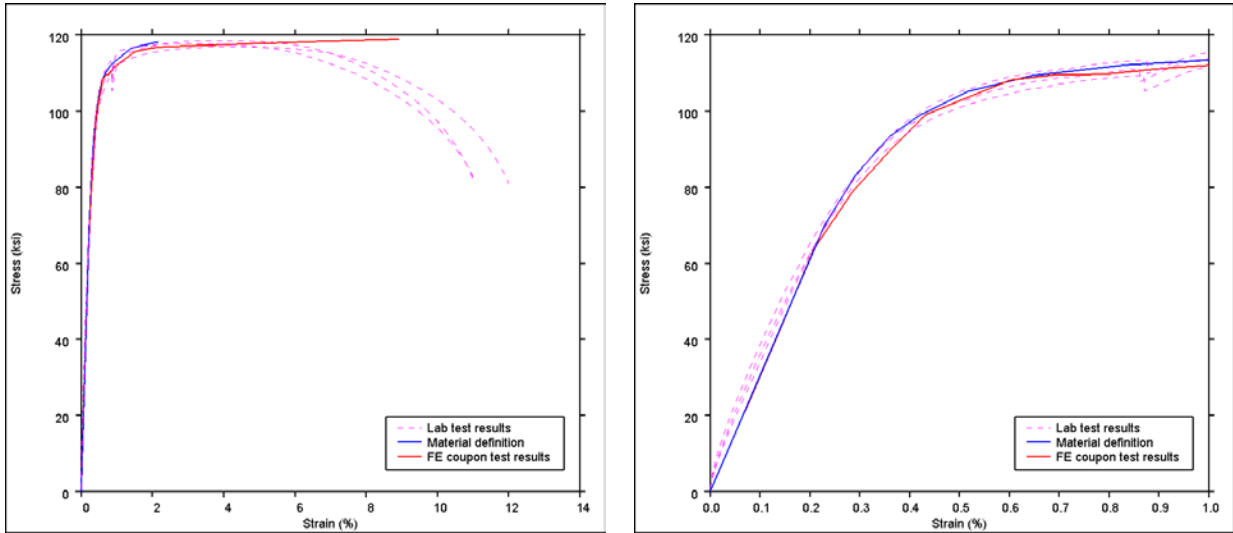


Figure D22. Side Sill HT: Lab Tensile Test Results, Material Definition, FE Analysis Results

Table D1. Bilinear Materials

Material	Yield stress (ksi)*	Tensile strength (ksi)*	Elongation at failure	Source
A36	36.3	58.0	20%	ASTM A36
A572 Gr50	50.0	65.3	21%	ASTM A572
A710 GrA3	74.7	84.9	20%	ASTM A710
RY300	43.5	58.2	20%	Assumed
RY306	43.5	58.2	20%	Assumed
RY400	43.5	58.2	20%	Assumed
Deep draw	43.5	58.2	20%	Assumed
CEM material	50.0	64.7	20%	Assumed to be A572 Gr50

*Stresses were defined in metric units and have been converted to imperial for this report

HT material curves development

The initial analysis showed 0.46 in of residual deformation after unloading from the 800,000-lb load. In the 800,000-lb load test there was no residual strain. Figure D23 shows plastic strain in the center sill and side sills for this condition. There are strains of up to around 0.1 percent along the length of the sills, with some localized higher strains.

For reference, a deformation of 0.46 in over the 680 in between the bolsters corresponds to an average strain of 0.07 percent.

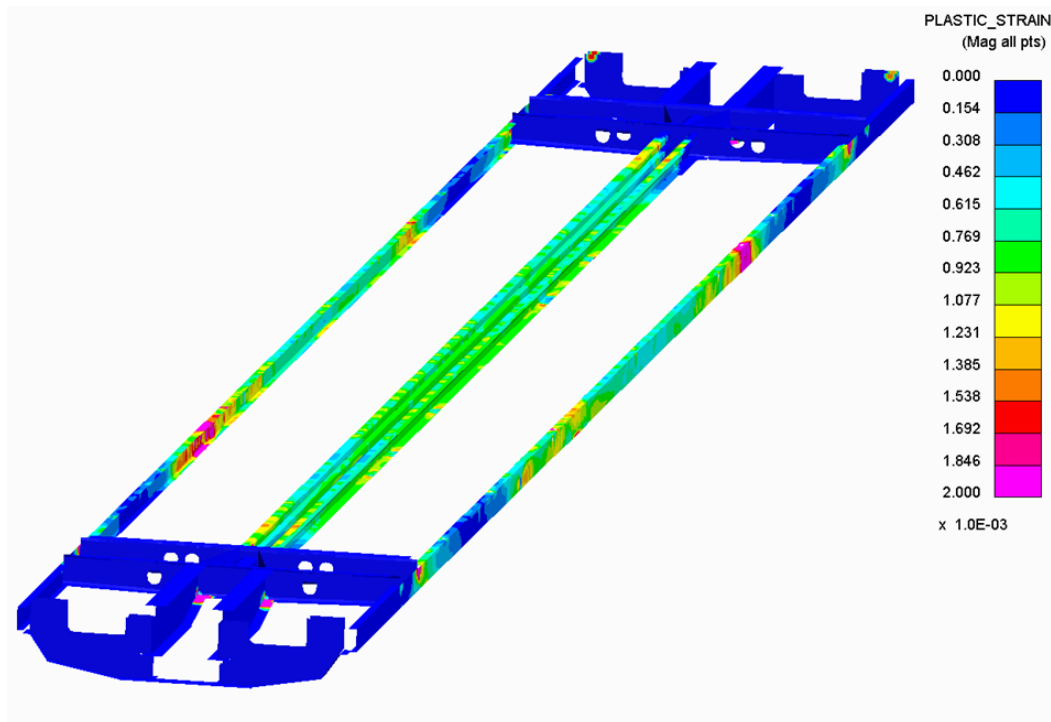


Figure D23. Plastic Strain in the Center and Side Sills following Unload from 800,000 lbs with the Original Material Definitions

Even though these strains were very low, the residual deformation was certainly measurable. Prompted by this, further development on the material definitions for the center sill HT material and the side sill HT material was carried out.

A comparison of the FE coupon analysis results to the lab test results shows a reasonable correlation between the two, when viewed at the 1-percent strain scale. Figure D24 and Figure D25 illustrate this for the center sill material and side sill material, respectively.

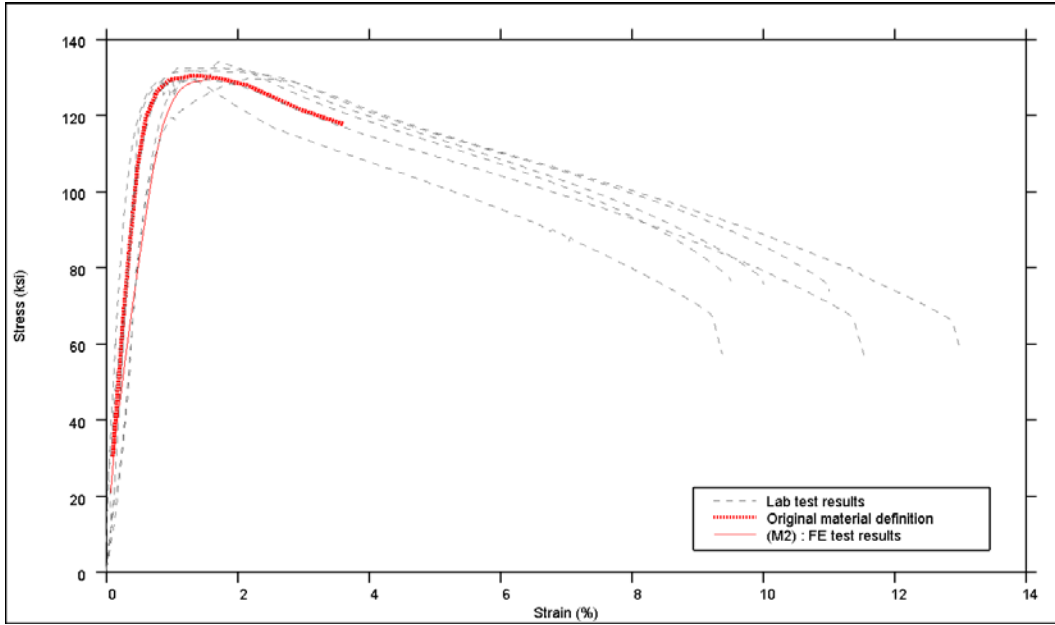


Figure D24. Original Material Definition for the Center Sill HT Material

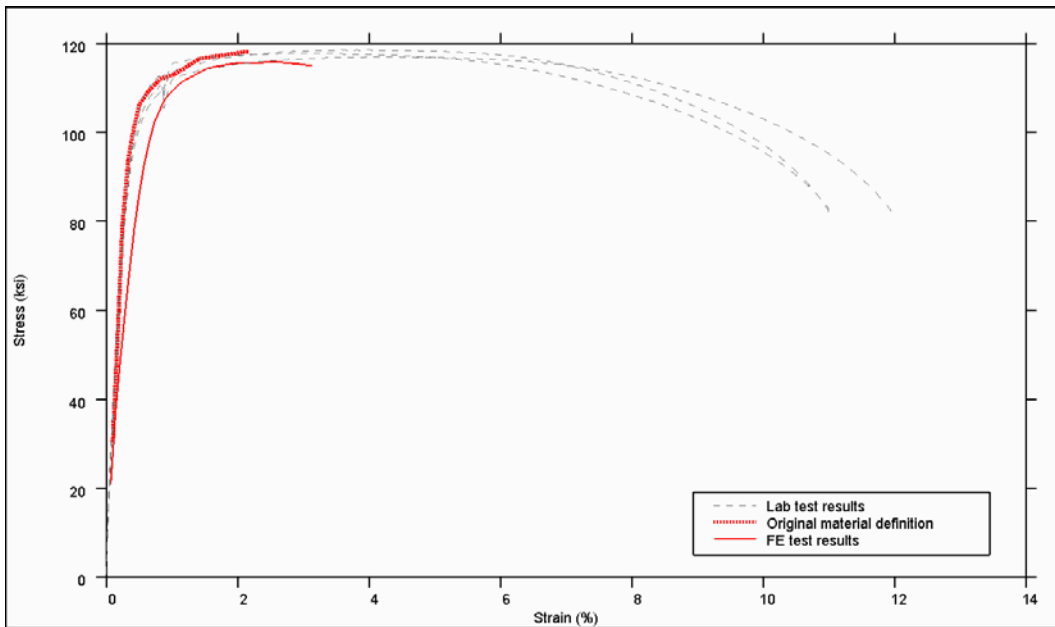


Figure D25. Original Material Definition for the Side Sill HT Material

When strains of less than 0.1 percent affect the results, as in this analysis, the details of the transition from elastic to plastic becomes important. Examination of the sub 1-percent strain region yields the following observations:

- The lab test results for both materials showed a poor match to the theoretical linear elastic curve below yield
- The center sill lab test results showed wide variability
- Between the yield point and 1-percent strain, the FE coupon test results showed lower stiffness than the lab test results
- The FE coupon test results correlated well with the lab test results above 1-percent strain.

Based on these observations, Arup adjusted the material definitions and repeated the analysis. The residual strain dropped to less than 1/16 in and the strain in the center sill and side sill was generally less than 0.03 percent, as Figure D26 shows. Some localized higher strains remained, but they were still below 0.2 percent.

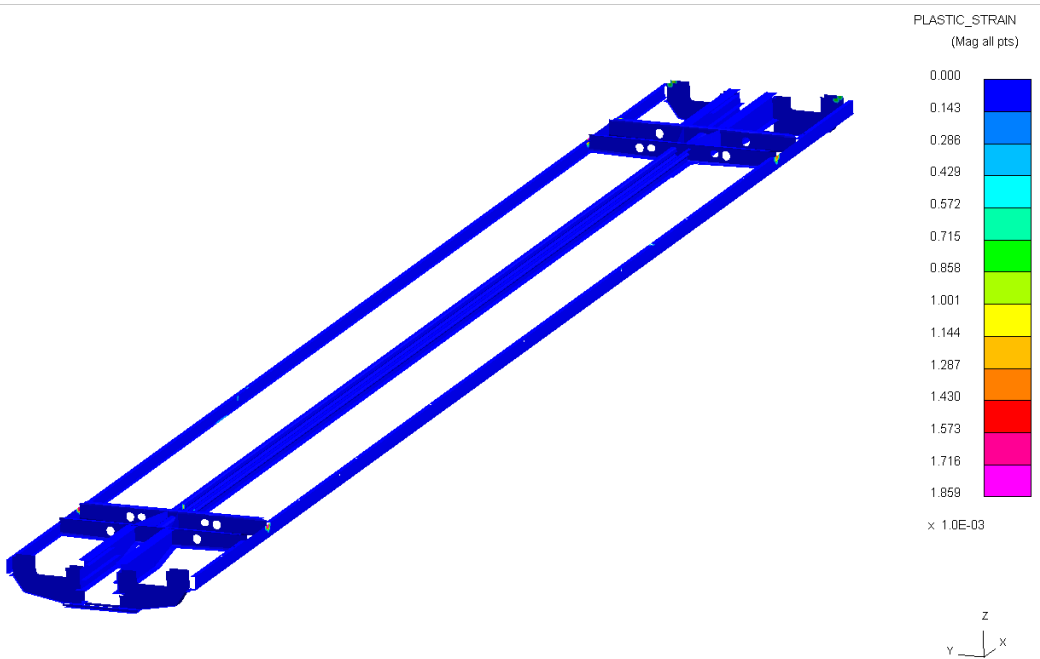


Figure D26. Plastic Strain in the Center and Side Sills following Unloading from 800,000 lbs with the Revised Material Definitions

Figure D27 and Figure D28 compare characteristics of the initial materials and the adjusted materials.

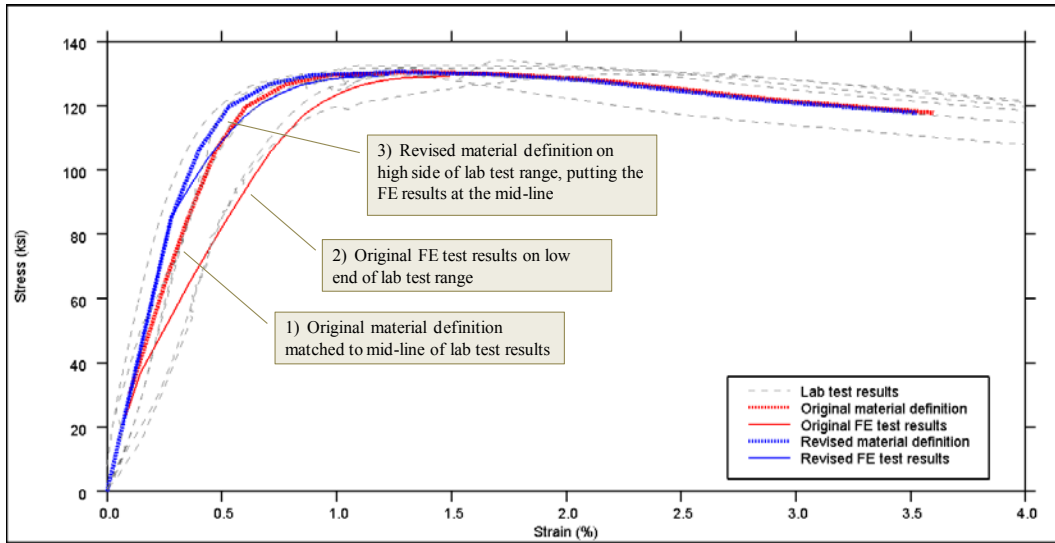


Figure D27. Comparison of Original and Revised Material for Center Sill HT

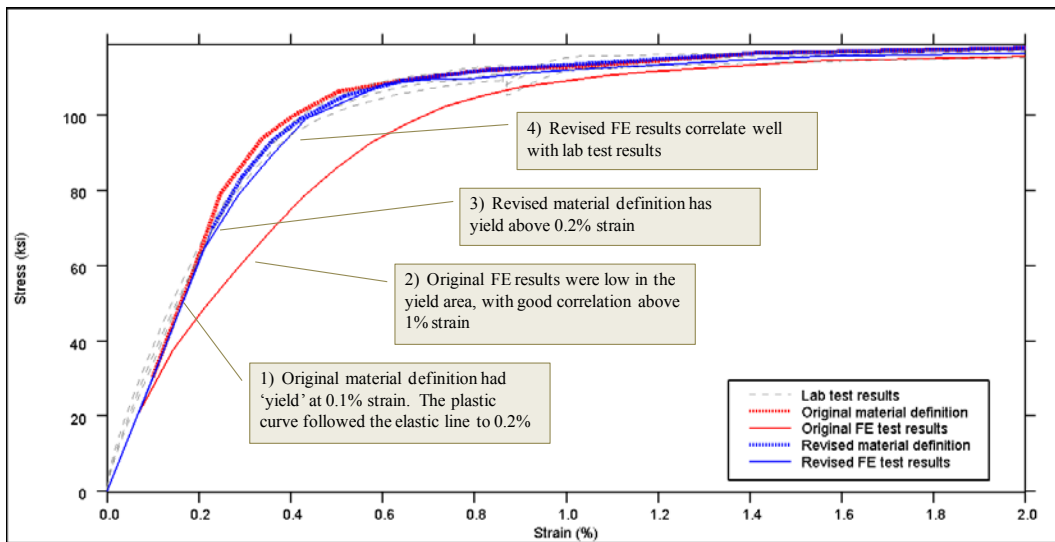


Figure D28. Comparison of Original and Revised Material for Side Sill HT

Appendix E – 800,000-pound Load Analysis and Test Results (Arup FE Model)

800,000-pound Load Analysis Assessment

This analysis has been calibrated to the results of the physical 800,000-lb load test. Calibration has been done frugally, without forcing the results into place by making unjustified modifications to the model, and it has been focused on adjusting global parameters such as boundary conditions.

The base case analysis assumes a perfect test setup. Additional analyses were run to investigate the influence of tolerances in the test rig. These include:

- The angle of the loading bars
- The vertical location of the loading bars relative to the CEM pockets
- Axial offset between loading bars on the left and right sides of the railcar

In general, increasing these tolerances would be expected to result in the railcar displaying reduced stiffness.

For the 800,000-lb load analysis, the influence of initial imperfections in the railcar steelwork has not been investigated. This has been assessed in the crippling analysis, which is described in Appendix H.5 of the report.

In addition to imperfections in the test setup, there are some parameters for which the exact values are not known. The most influential of these that Arup has identified is the stiffness of the truck springs.

Results processing

During the physical test and the analysis, there is some global rotation and translation of the railcar. For better comparability between results, the raw test data have been adjusted to match up the end-to-end alignments of the railcars. Where there is twist from one end to the other, the railcars are oriented such that the angle of the F-end of the car to the horizontal is equal and opposite to the angle of the B-end of the car. On average, the car is horizontal. Appendix I contains a more detailed description.

800,000-pound load base case

The 800,000-lb base case analysis represents a perfect test; i.e., all the pistons engage simultaneously, the car and the loading bars are all aligned, the load is applied centered in the CEM pockets, and there are no initial imperfections in the railcar steelwork.

Compressive stiffness

The overall compressive stiffness of the analytical railcar generally shows good correlation with the test car. Figure E1 shows force-compression curves for the physical test and the analysis. The force, in both cases, is the total applied force. The compressions are the relative movements of the string potentiometer locations at the F-end and B-end. The compressions have been zeroed to ensure that there is zero compression under zero load.

At floor level, there is excellent correlation between the analysis results and the physical test results in terms of the curve gradients, the offsets, and the maximum compressions achieved.

The center sill force-compression curves are also similar, though there is a displacement lag in the analysis results. This is believed to be a result of the damping applied in the analysis. To avoid this, the load could be applied more gradually, though this would increase the analysis runtime significantly. Alternatively, the damping could be reduced. This would result in dynamic overshoot and would overstate the maximum displacements and strains.

This damping-induced lag is also apparent in the side sill curves for the analysis, which additionally show a lower overall compression than the physical test results. It is not fully apparent what is causing this disparity, but it is believed to result from a small difference in the rotation of the string potentiometer bracket, which extends down from the side sill and acts as an amplifying lever-arm.

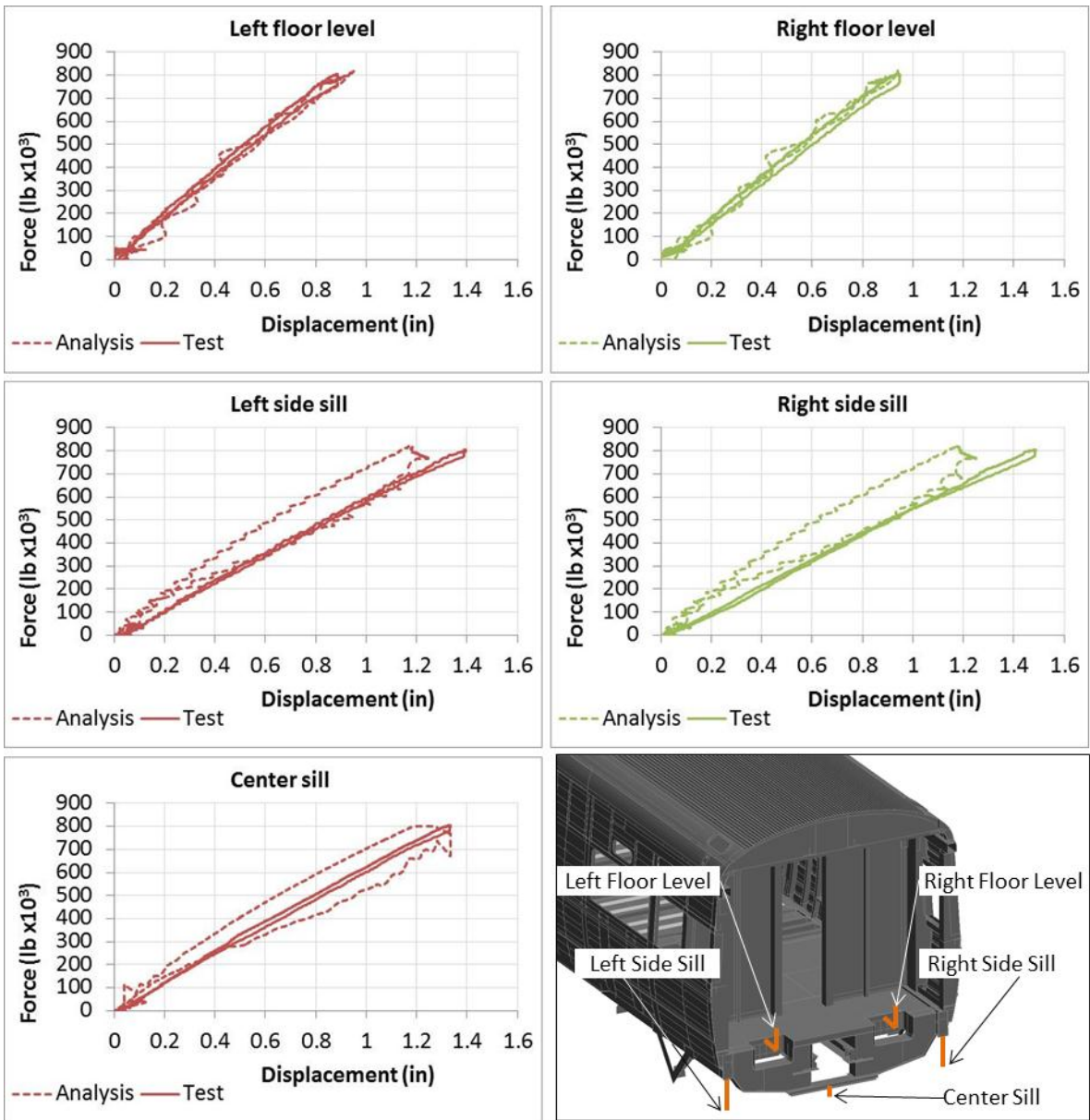


Figure E1. Force-Displacement Curves

Further commentary on damping-induced lag

The damping-induced lag makes it appear that, for a given applied load, there is less deflection in the railcar. For a quasi-static analysis in which the target load is held for a significant duration, this is in no way problematic. Once the analysis reaches a steady state, the stiffness will be correct.

The crippling test, however, is more like a dynamic analysis. There is no target load at which to allow the displacements to settle. Rather, the compression is increased at a constant rate until failure occurs. Damping the crippling analysis, there is a risk of overstating the stiffness of the car and the maximum load that can be carried. On the other hand, insufficient damping would result in greater dynamic behavior of the analysis, which is also undesirable. To balance these risks, the crippling analyses described in Section 5.6 of the report were carried out with reduced damping.

Deflected shape

The deflected shape of the railcar in the 800,000-pound base case analysis shows reasonable correlation with the physical test results. In general, the analysis railcar appears a little stiffer than the physical car and shows more consistent behavior between the left side and the right side.

The analysis shows an average maximum uplift at the middle of the railcar of 1.55 in, compared to 1.68 in in the physical test. This is a difference of 0.13 in or 8 percent.

There is a similar difference in axial displacement of 1.25 in compared to 1.32 in for the analysis and physical test, respectively. This is a difference of 0.07 in or 5 percent.

This paragraph discusses the causes of some of these differences, as well as the greater asymmetry in the response of the physical railcar than the analytical railcar.

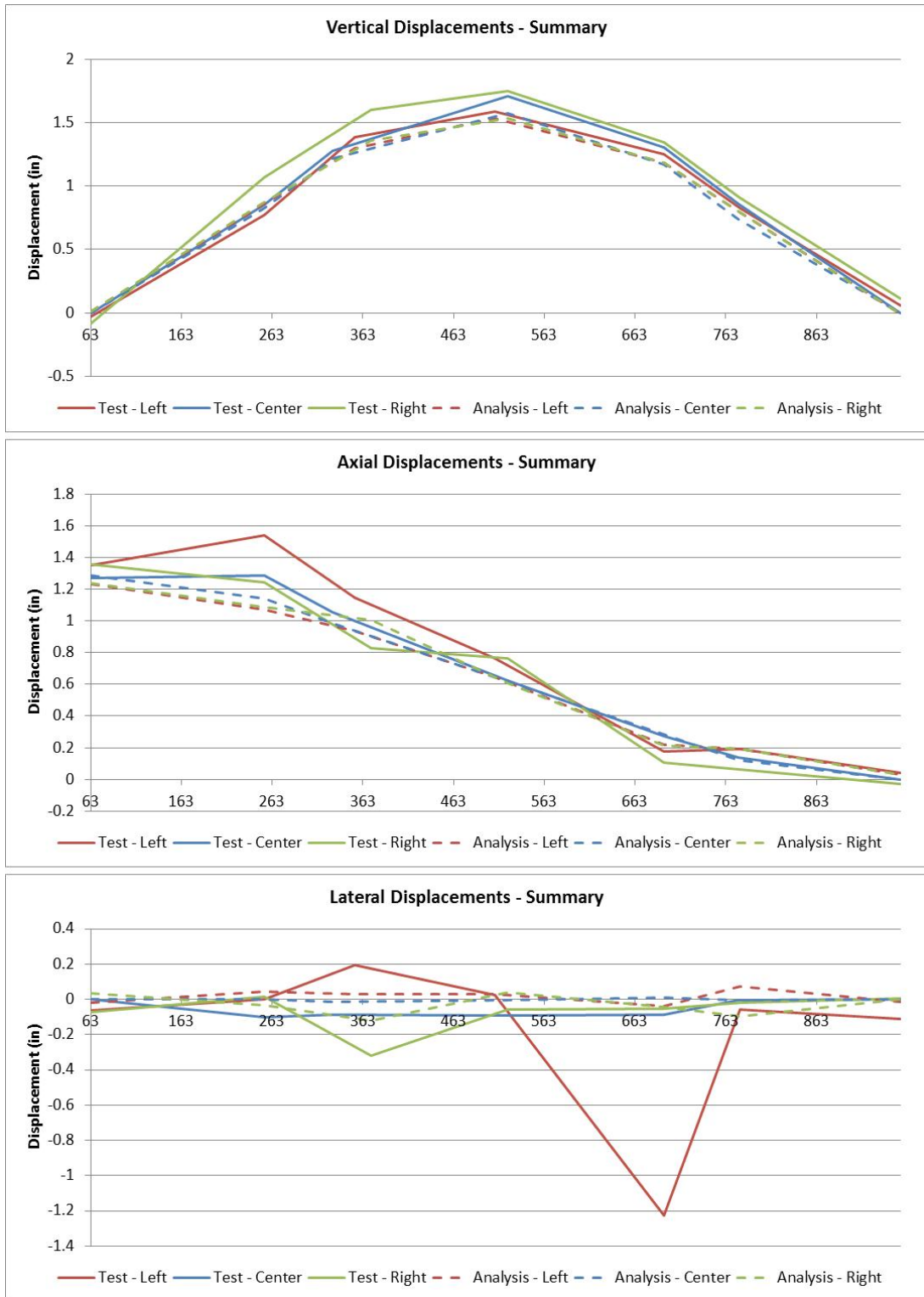


Figure E2. Displacements of the railcars under 800,000-pound Load
 (Each plot shows the left side sill, the center sill, and the right side sill for the 800,000-lb load test and the 800,000-lb load base case analysis. These displacements are adjusted to remove rigid body deflection of the railcar. The F-end of the railcars is on the left-hand side and the B-end is on the right-hand side.)

Strains

In general, the strains predicted in the 800,000-lb load analysis are lower than those measured in the 800,000-lb load test. There is also greater variability in the physical test. TTCI and Arup believed that the increased variability, particularly in the side sills and rails, results from local flange buckling effects.

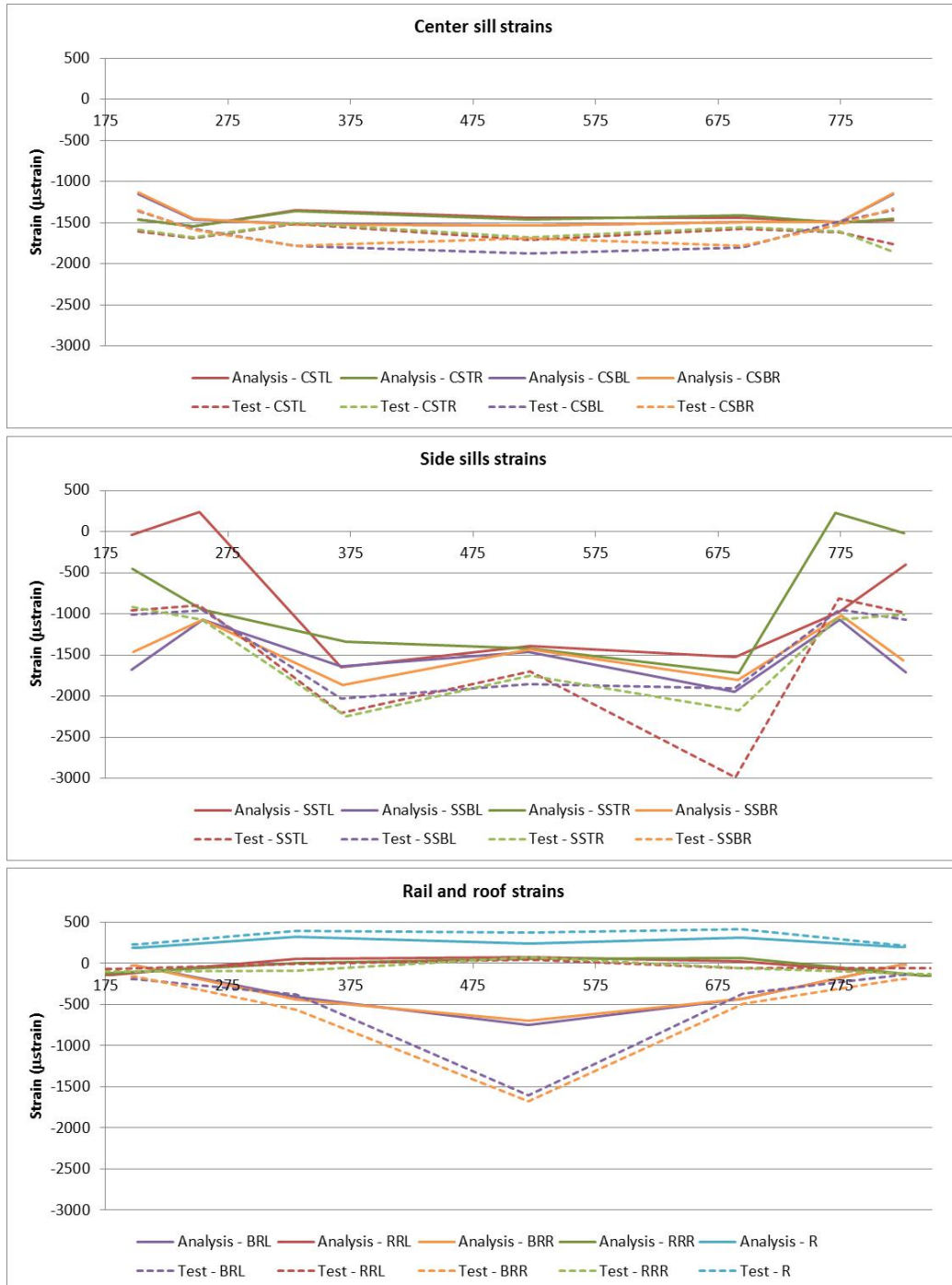


Figure E3. Strains in the Railcar Sills, Rails and Roof under 800,000-pound End Load (The F-end of the railcars is on the left-hand side, and the B-end is on the right-hand side.)

Sensitivity Studies

The 800,000-lb load base-case analysis assumed a perfect test setup. In practice, this will never be the case, and studies have been conducted to investigate the sensitivity of the results to several factors:

- The angle of the loading bars
- The vertical location of the loading bars relative to the CEM pockets
- Truck spring stiffness

Angle of loading bars

The loading bars at the F-end of the railcar were angled downwards at 5 degrees. The contact location was unchanged from the base case and the B-end loading bars were kept horizontal.

An increase in vertical deflections was observed of 12 percent versus the base case. Strains vary a little, generally increasing by a few percent.

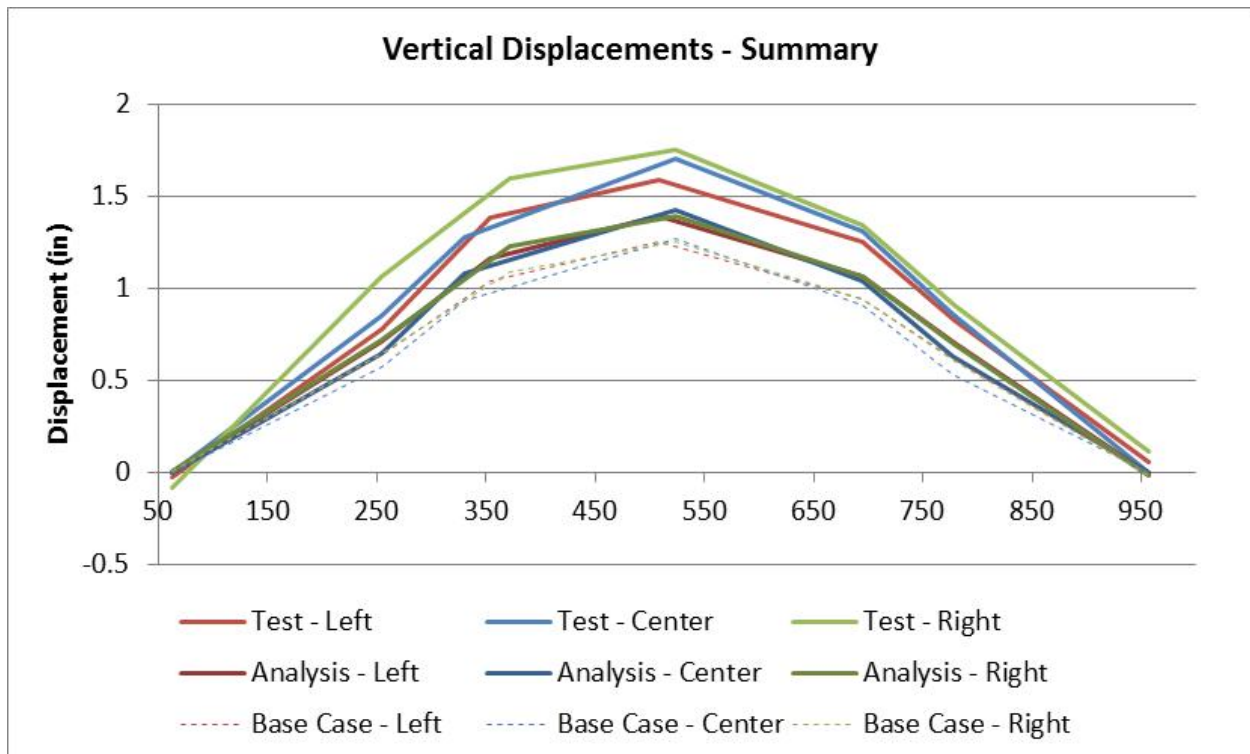
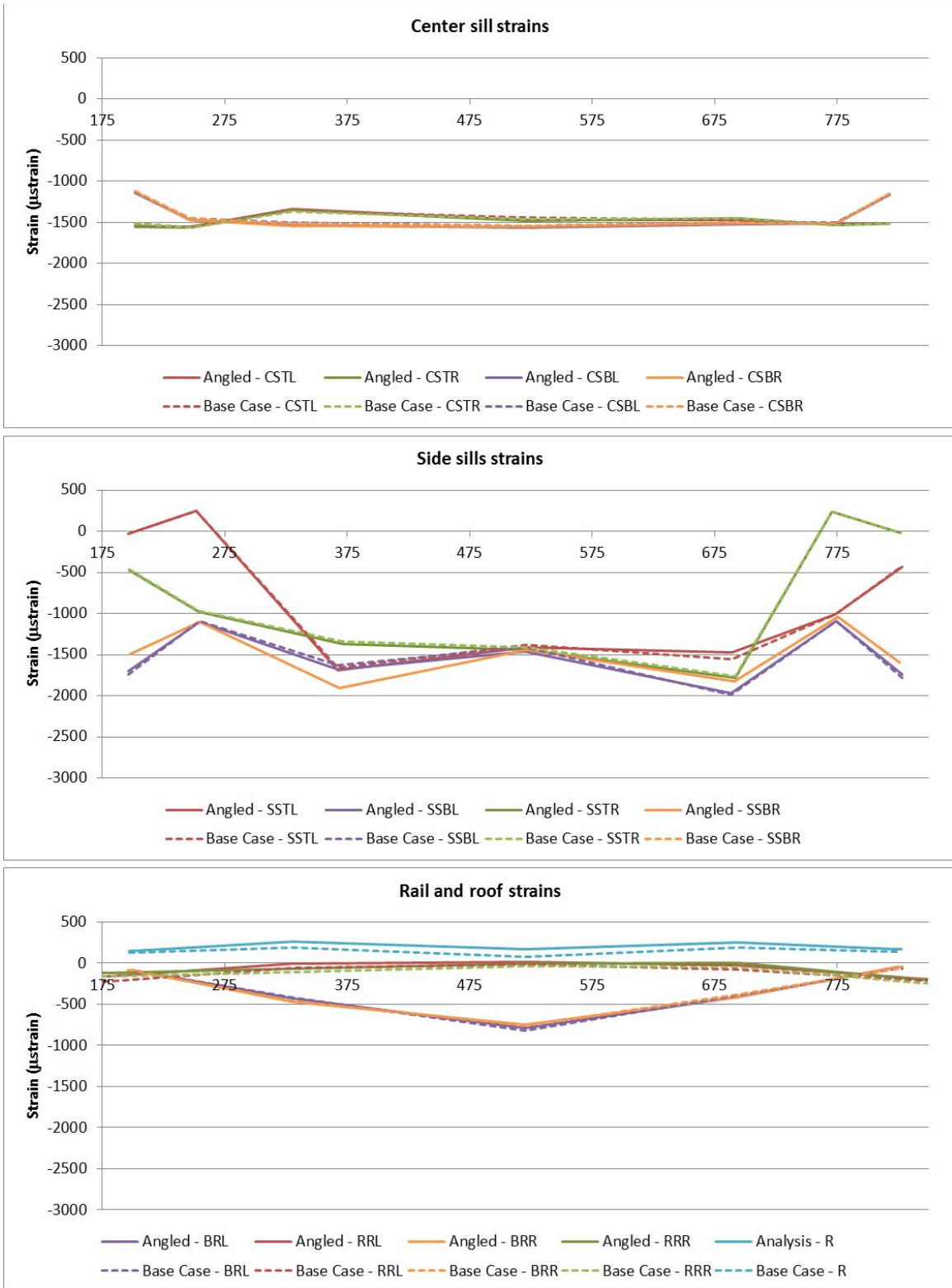


Figure E4. Comparison of Vertical Deflections in the Angled Loading Bars 800,000-pound Load Analysis and the Base Case



**Figure E5. Comparison of Strains in the Angled Loading Bars
800,000-pound Load Analysis and the Base Case**

Loading location

The loading bars at both ends were moved down 0.8 inches. This shifts the loading point further from the neutral axis and was expected to increase bending and the deflected shape.

Figure E6 shows that the shift in loading location causes increased deflections of around 4 percent. There is no significant increase in the asymmetry of the response. The 800,000-lb load test results are shown for reference. There is little impact on the strains.

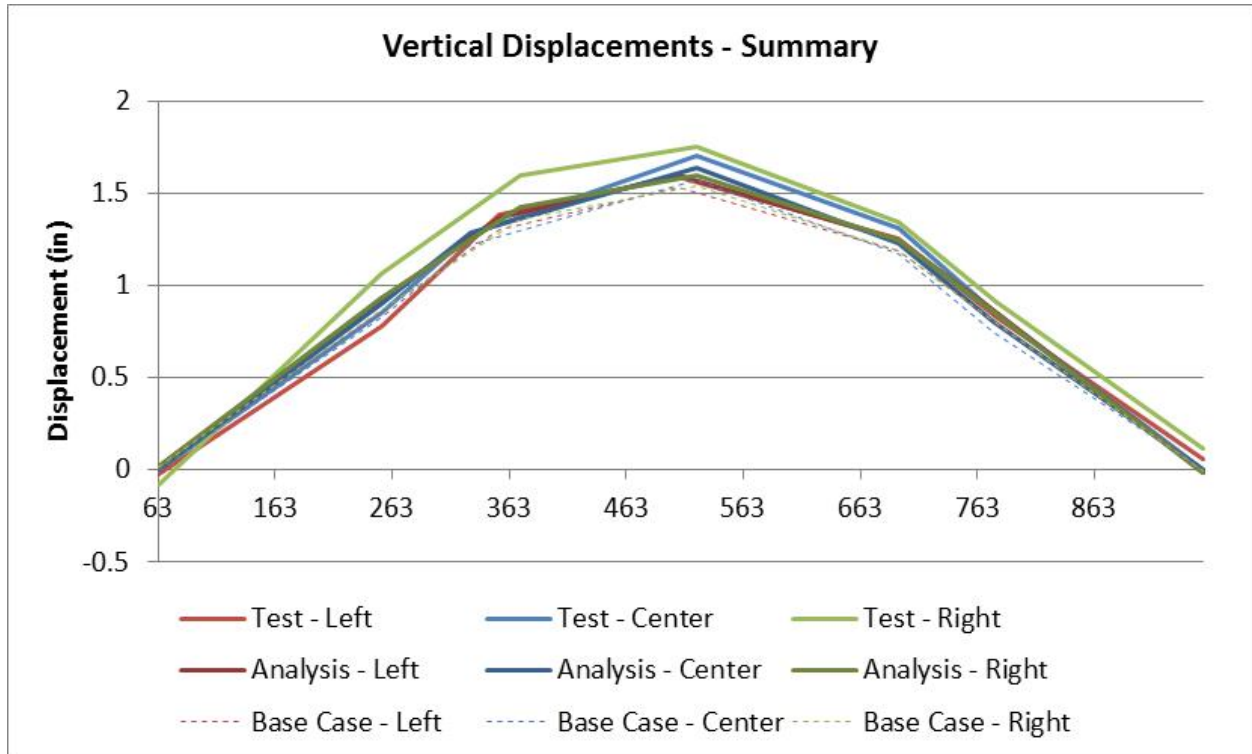


Figure E6. Comparison of Vertical Deflections of the 800,000-pound Load Test and the 800,000-pound Load Analysis with the Loading Points Moved Down 0.8 in, and the Base-Case Analysis

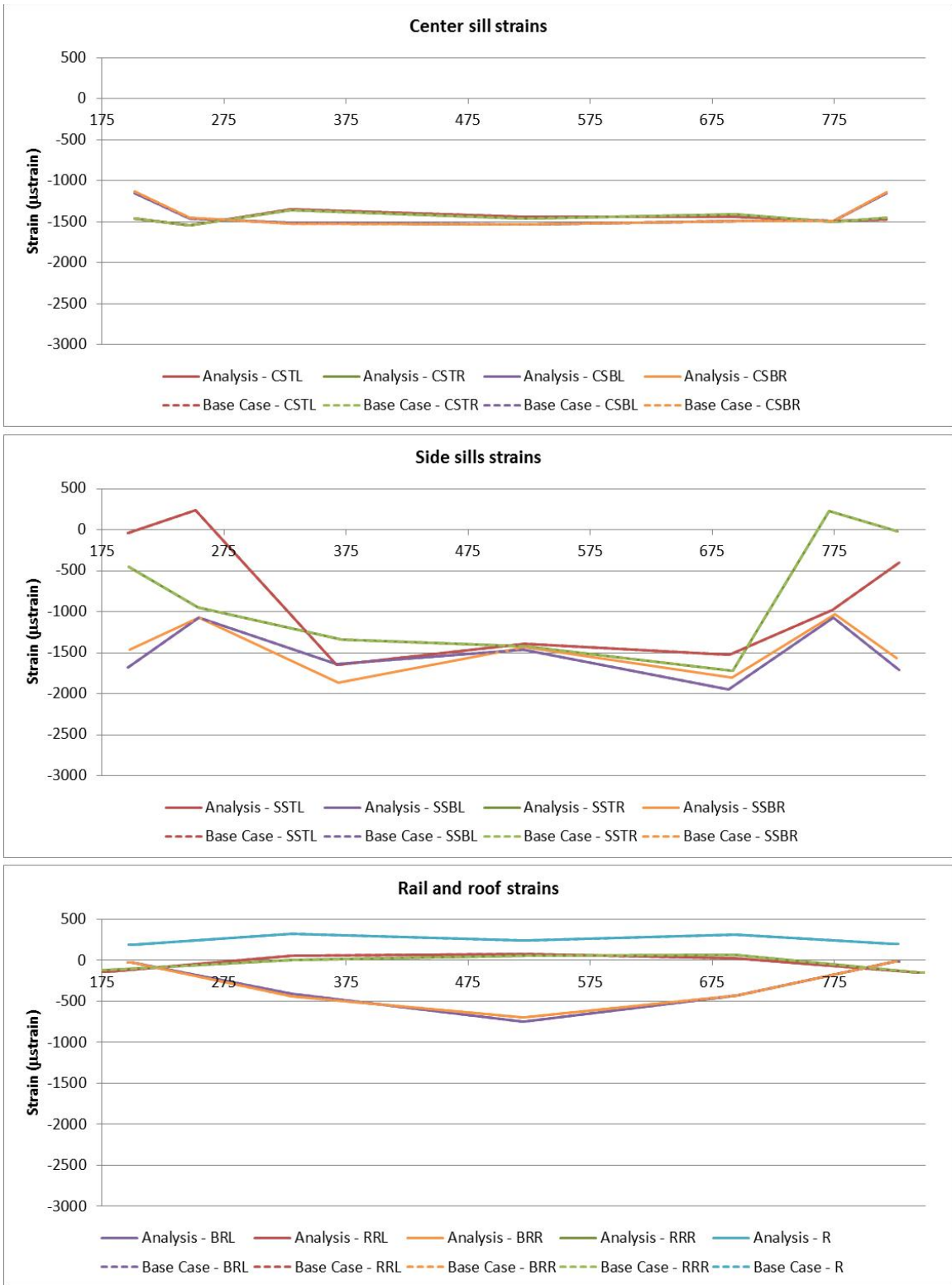


Figure E7. Comparison of Strains for the 800,000-pound Load Analysis with Lower Loading Points and the 800,000-pound Load Base Case Analysis

Truck Spring Stiffness

Initially the truck springs were arbitrarily set to a stiffness of around 17,000 lbs/in. This led to significantly lower deflections than were expected. When the truck spring stiffness was adjusted to 2,000 lbs/in (based on the calculation in Appendix C), the results were much closer to those of the physical test. The influence of truck spring stiffness on the 800,000-lb load analysis is likely to be more significant than for the crippling load analysis because of the loading pattern. In the 800,000-lb load test, the load was applied only at the lower CEM pockets, resulting in increased bending/bowing. However, the crippling load analysis applied the load at the lower and upper CEM pockets, which kept the railcar much straighter. The stiffness of the springs prevented uplift at the location of the trucks, so the effect is most influential when bowing occurs.

Appendix F – Quasi-Static Analysis Verification and Element Formulation Assessment (Arup FE Model)

Criteria

In order for the analysis to be considered quasi-static, the RSAC report requires that either of the following conditions be met:

- (1) The variation between the load recorded at the reaction end and the load recorded at the applied load end shall not exceed ± 5 percent.
- (2) The ratio of kinetic energy to strain energy in the structure shall not exceed 5 percent.

The 800,000-lb load analysis and the crippling load test analysis meet both criteria.

Force transfer

During the 800,000-lb load analysis and the crippling load test analysis, most of the reaction forces were within ± 5 percent of the applied load, as Figure F1 and Figure F2 illustrate. There was some transient dynamic response at the start of the loading period in both analyses, due to the step changes in velocity. However, this does not significantly influence the results.

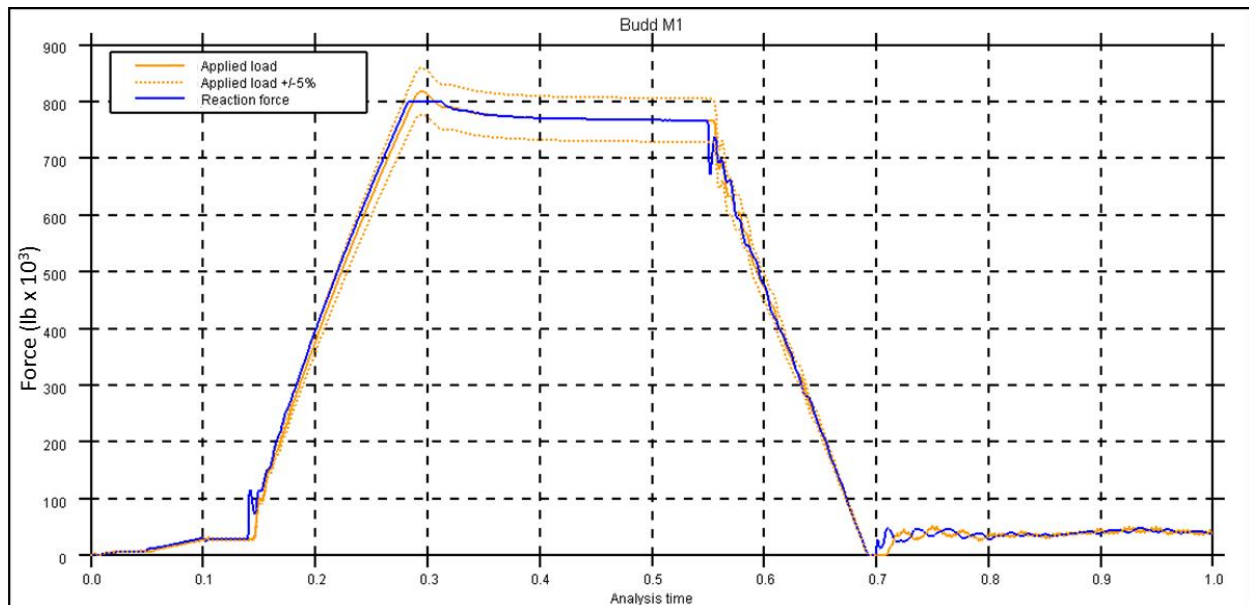


Figure F1. Applied Force and Resulting Reaction Force during the 800,000-pound Load Analysis

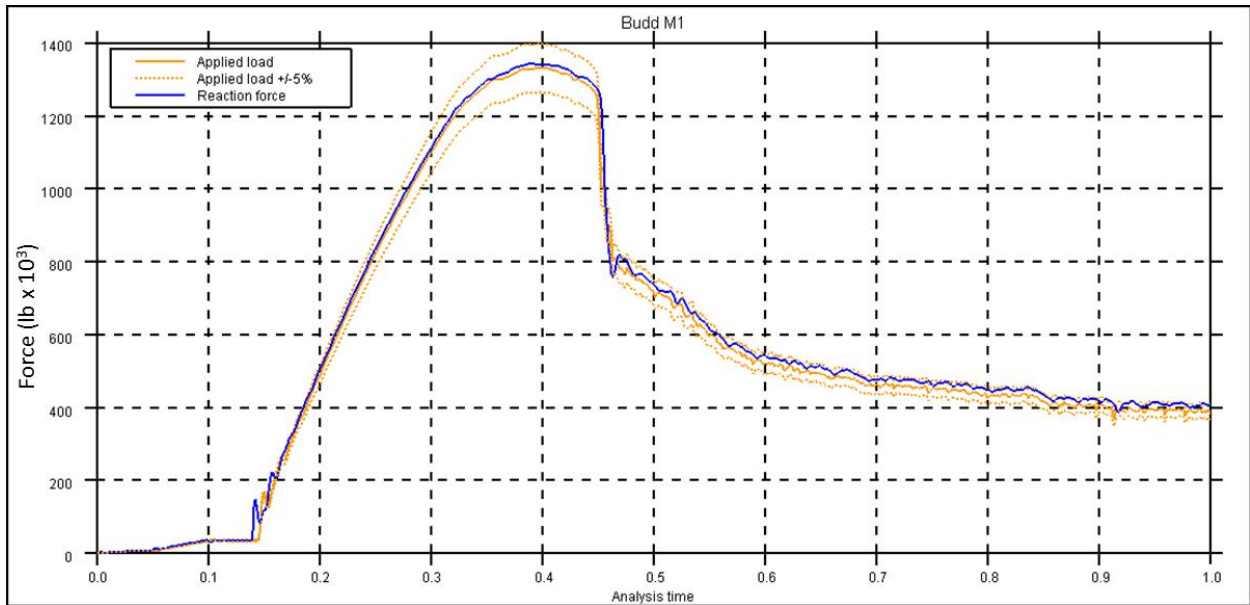


Figure F2. Applied Force and the Resulting Reaction Force during the Crippling Load Analysis

Quasi-static energy characteristics

During most of the 800,000-lb load analysis and the crippling load test analysis, the total kinetic energy was less than 5 percent of the total internal strain energy, as Figure F3 and Figure F4 illustrate, respectively. There was some exceedence at the end of unloading during the 800,000-lb load analysis, which does not affect the results.

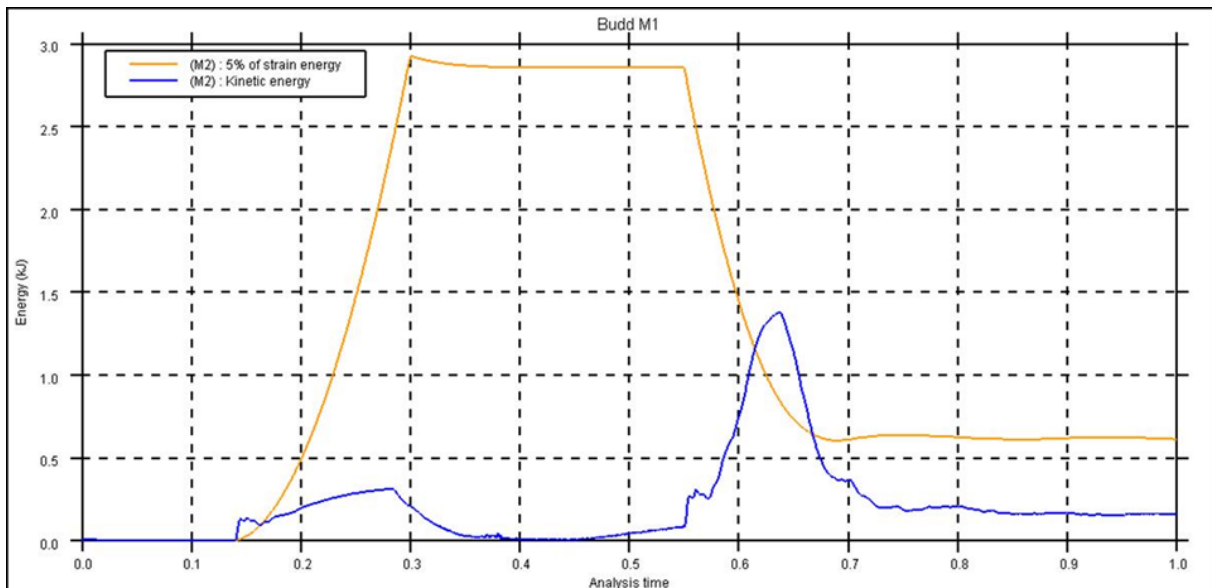


Figure F3. Comparison of Total Kinetic Energy to 5 percent of Total Strain Energy during the 800,000-pound Load Analysis

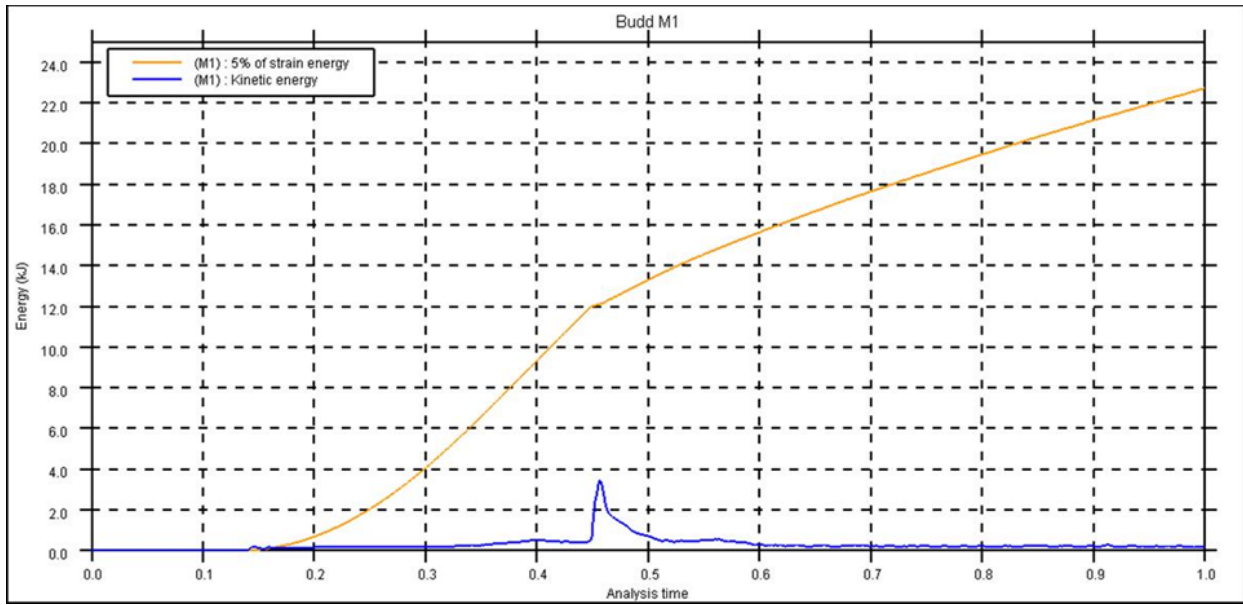


Figure F4. Comparison of Total Kinetic Energy to 5 percent of Total Strain Energy during the Crippling Load Analysis

Finite element formulation

The FE method approximates the behavior of continuous material. Different formulations can be used for the elements, with different approximations being made. The crippling analysis was run with the center sill elements using three different formulations:

- The Basic Formulation, which has one integration point in plan and two through the thickness at each location
- The Fully Integrated Elements, which have four integration points in plan and two through the thickness at each location
- The Through Thickness Formulation, which has one integration point in plan and five through the thickness at each location

Good correlation between the three different formulations is observed for the applied loads (see Figure F5). At the reactions, there is good correlation between all three formulations up to crippling.

At post-buckle, there is slight divergence between the three formulations but within the region of interest — up to 0.45 s — the general behavior is consistent. See Figure F6 for reaction forces. Though the different formulations result in a slight shift in the post-buckle load path, the total force applied and reacted, and the crippling load are consistent between all three analyses, as Figure F7 illustrates.

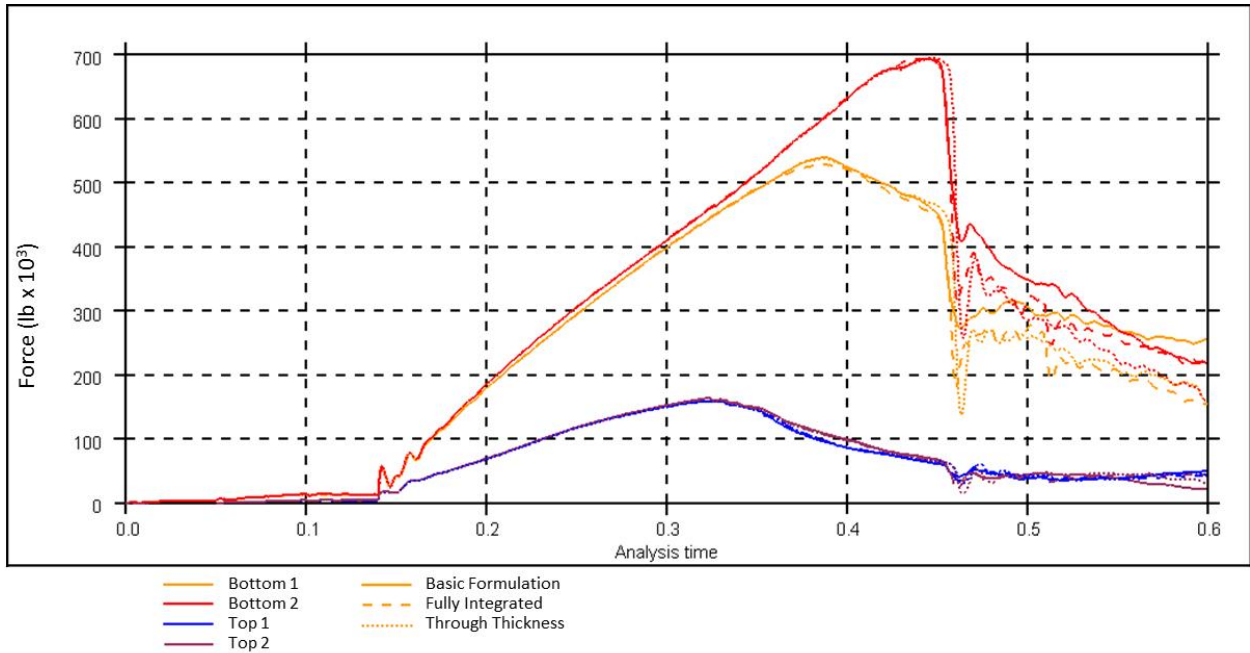


Figure F5. Comparison of Applied Forces during Crippling Load Analysis with Different Element Formulations

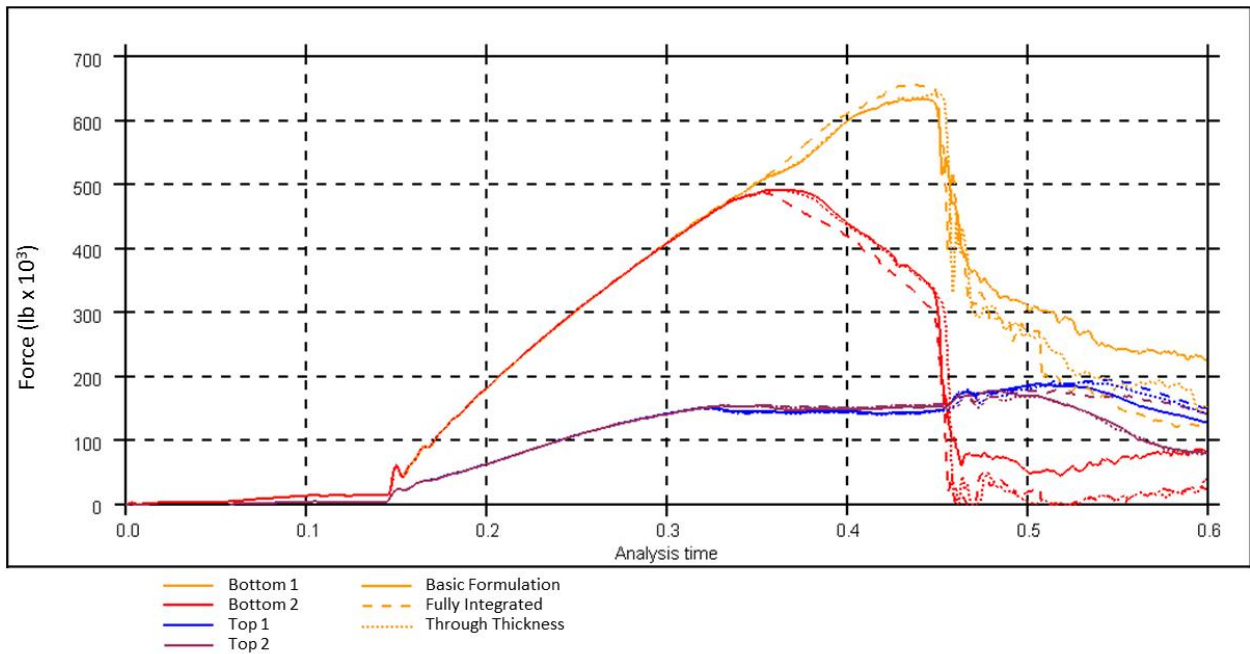


Figure F6. Comparison of Reaction Forces during Crippling Load Analysis with Different Element Formulations

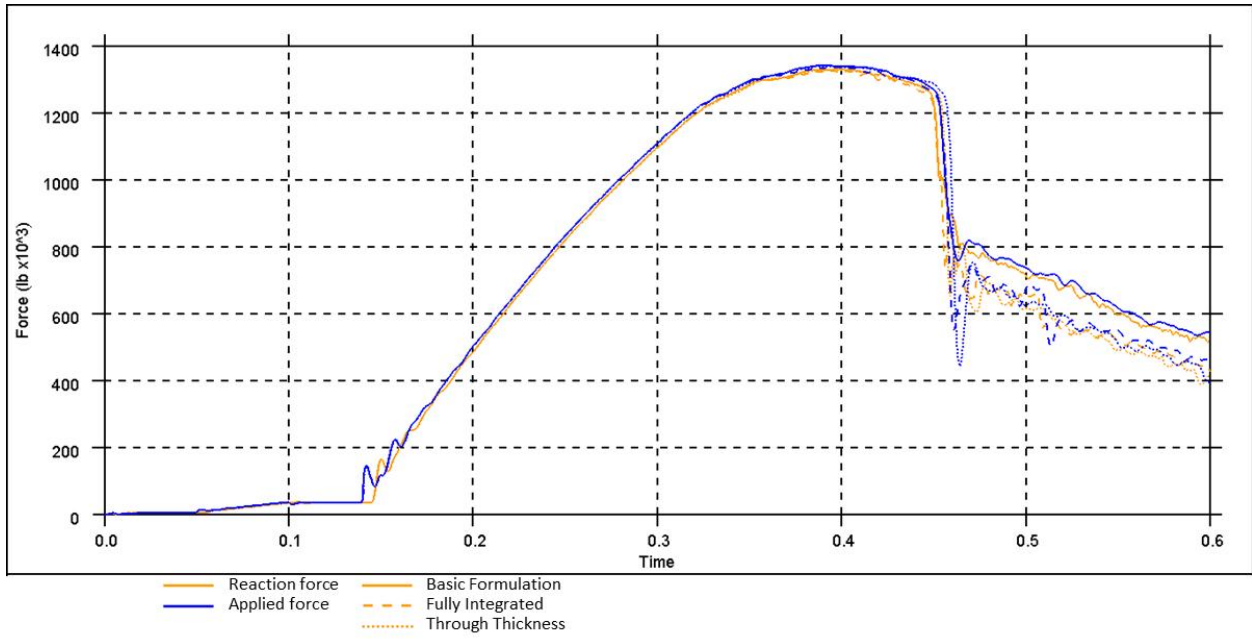


Figure F7. Comparison between Total Applied Forces and Total Reaction Forces During Crippling Load Analysis with Different Element Formulations

Appendix G – Crippling Load Analysis and Test Results (Arup FE Model)

Deflections

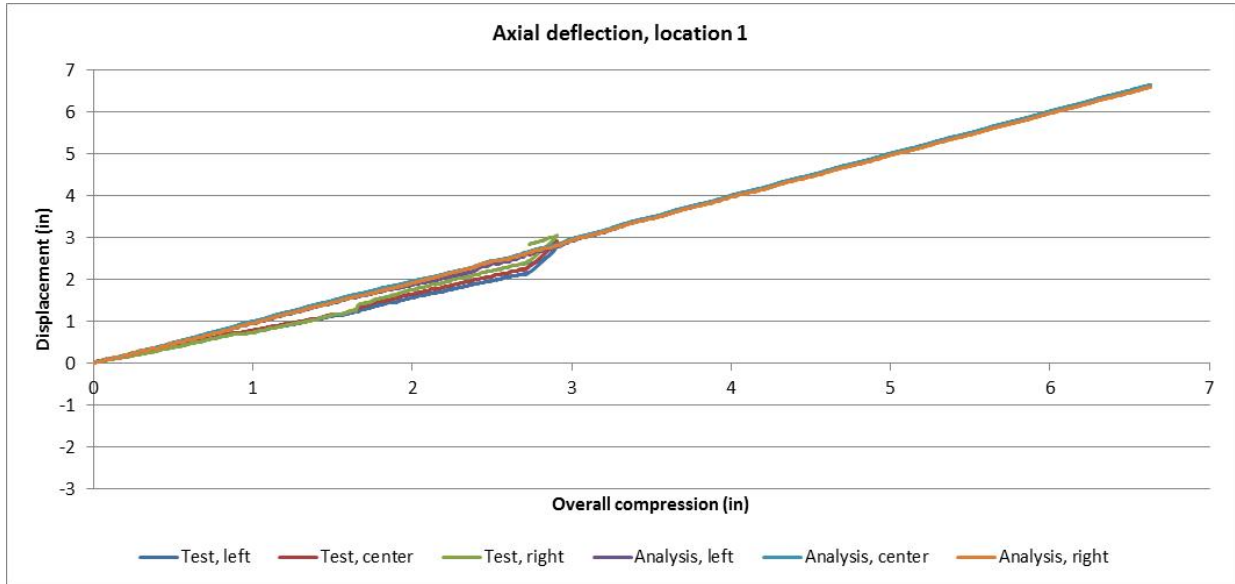


Figure G1. Axial Deflection at Location 1 (F-end)

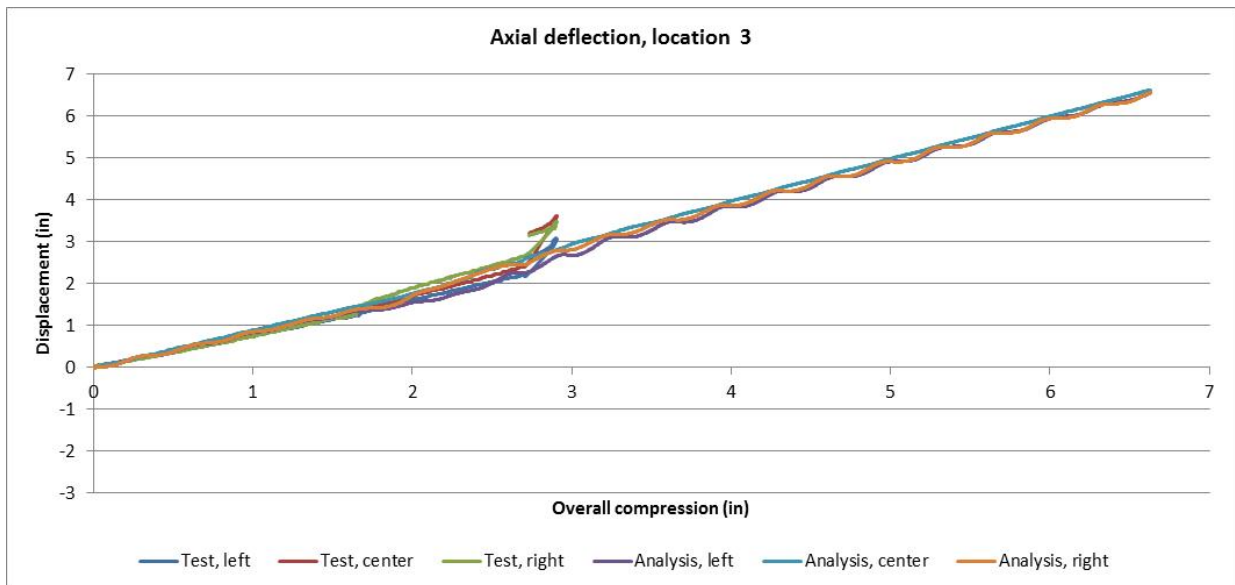


Figure G2. Axial Deflection at Location 3

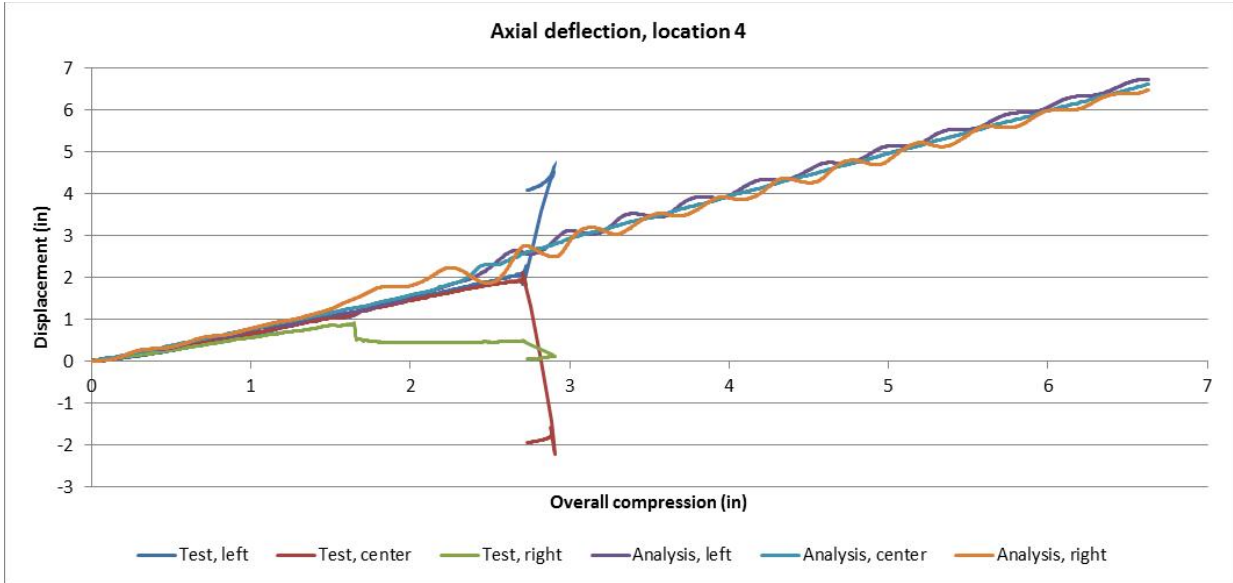


Figure G3. Axial Deflection at Location 4

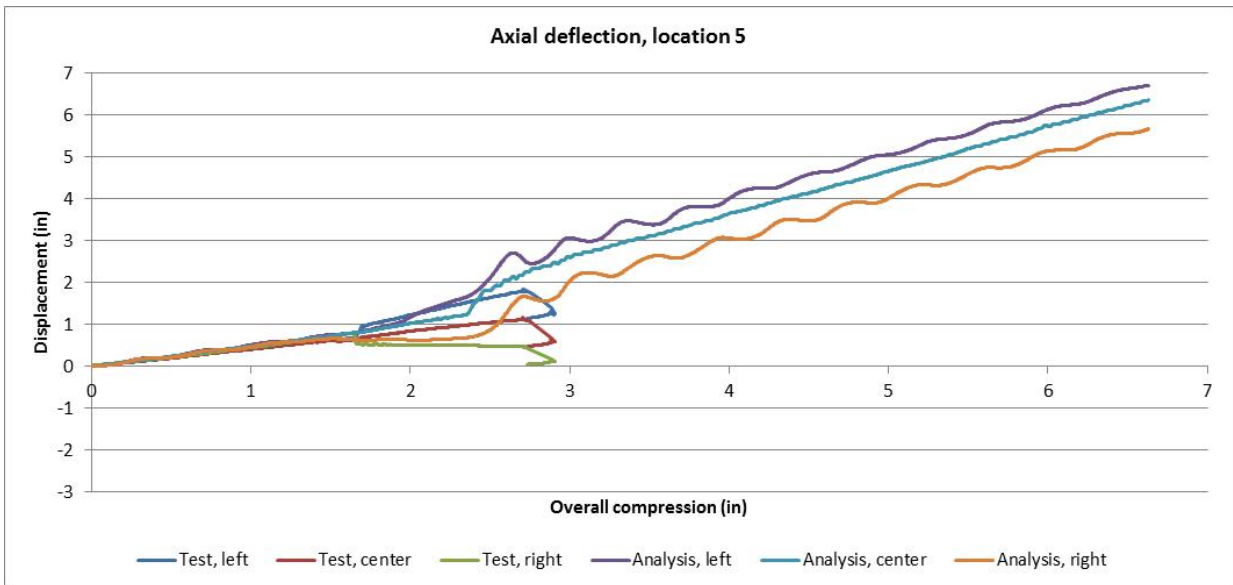


Figure G4. Axial Deflection at Location 5

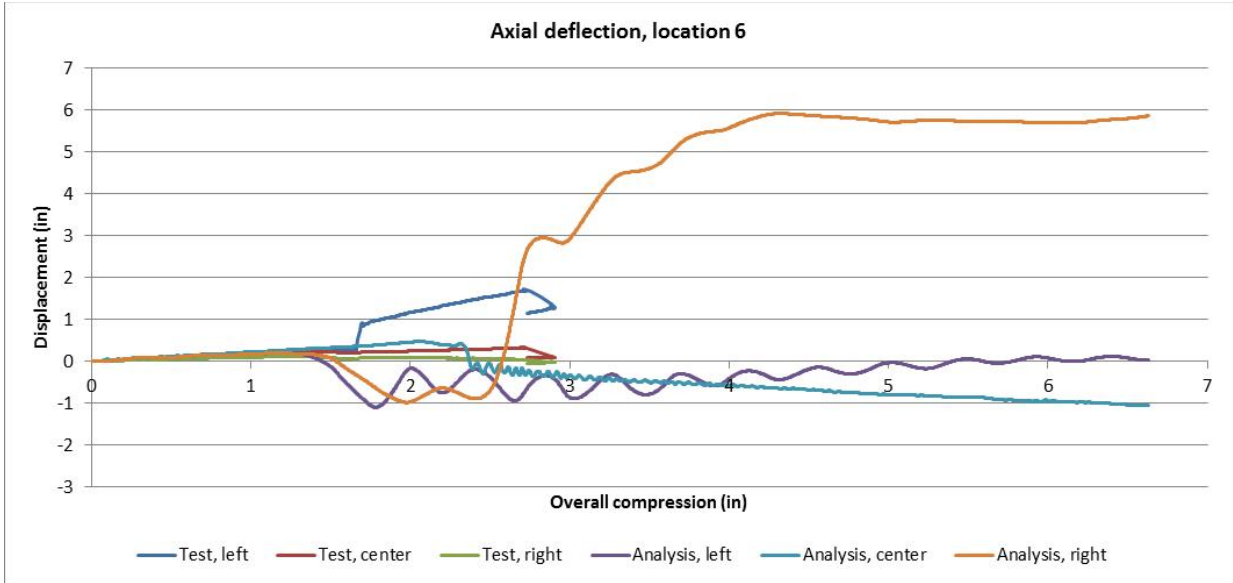


Figure G5. Axial Deflection at Location 6

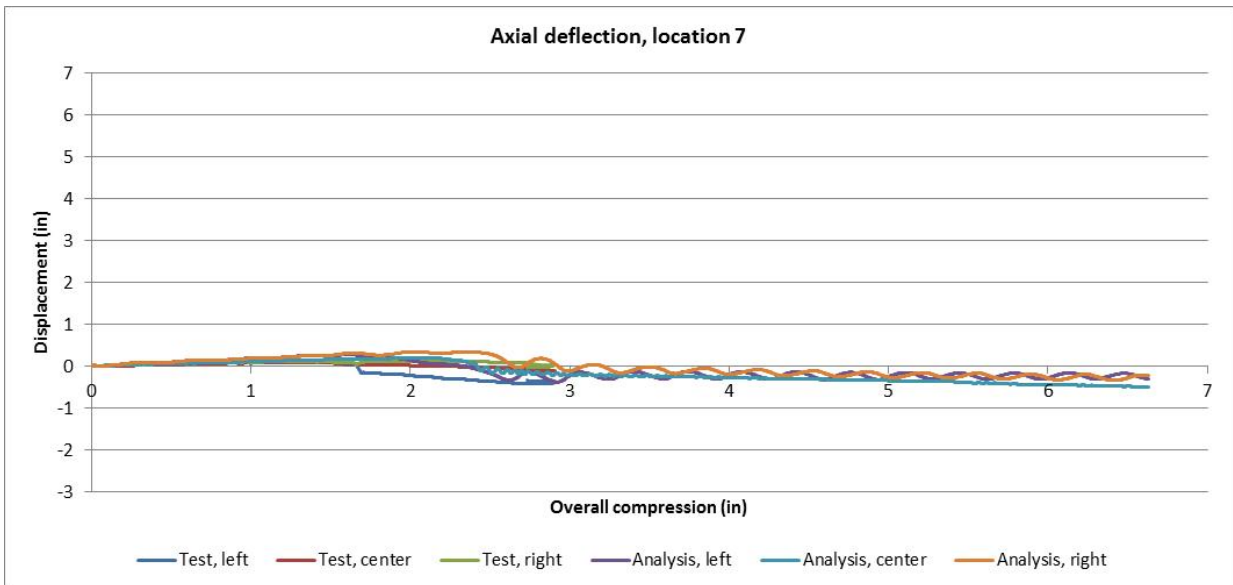


Figure G6. Axial Deflection at Location 7

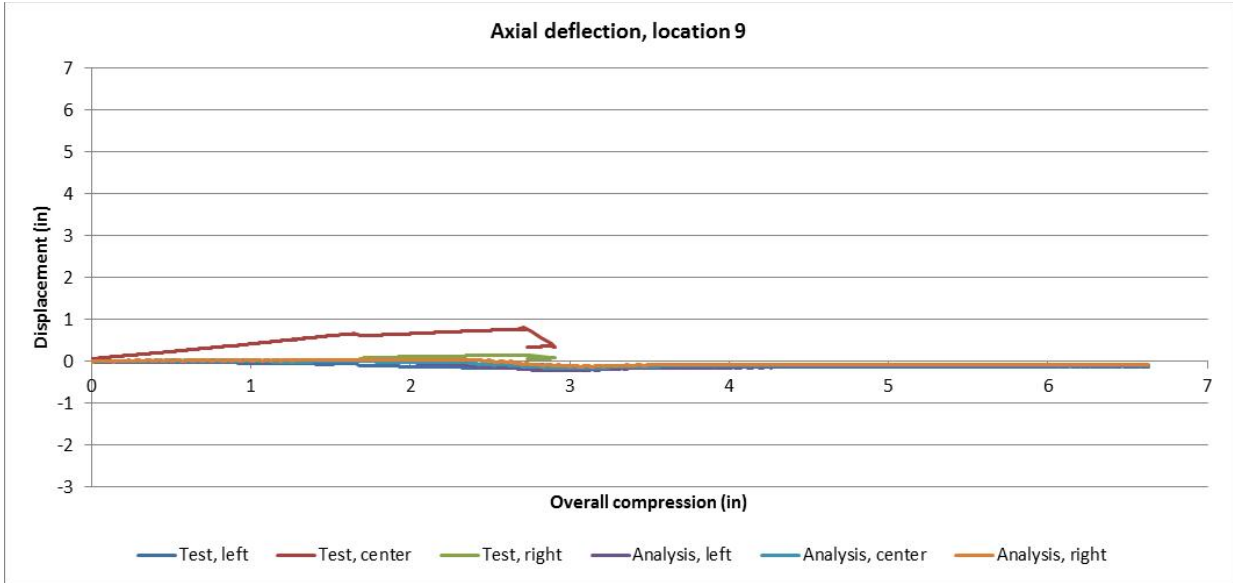


Figure G7. Axial Deflection at Location 9 (B-end)

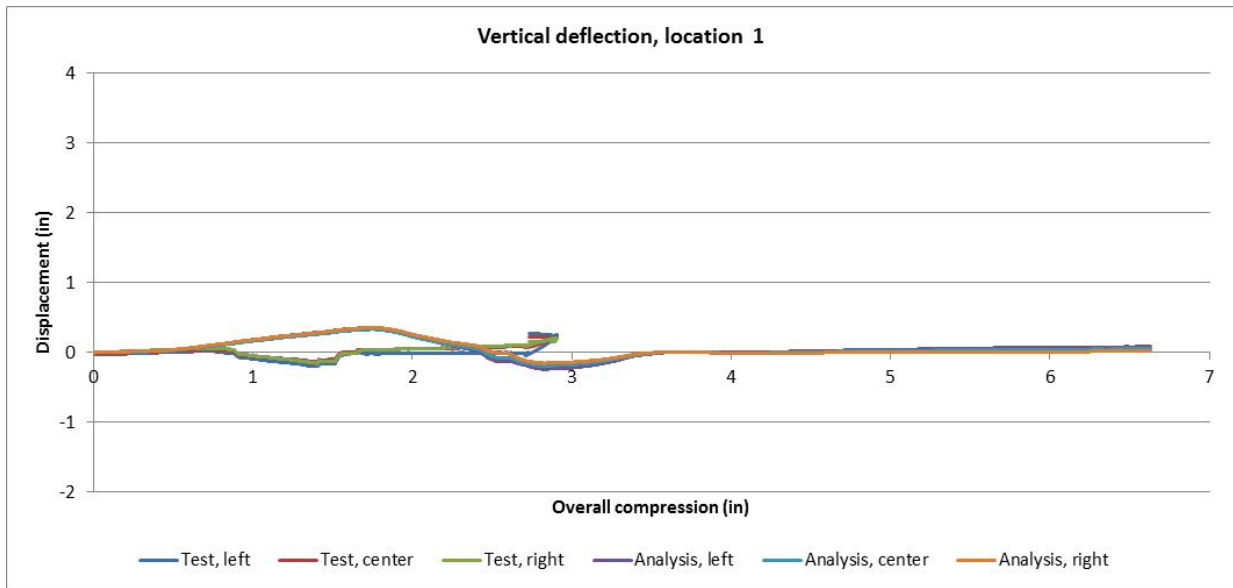


Figure G8. Vertical Deflection at Location 1 (F-end)

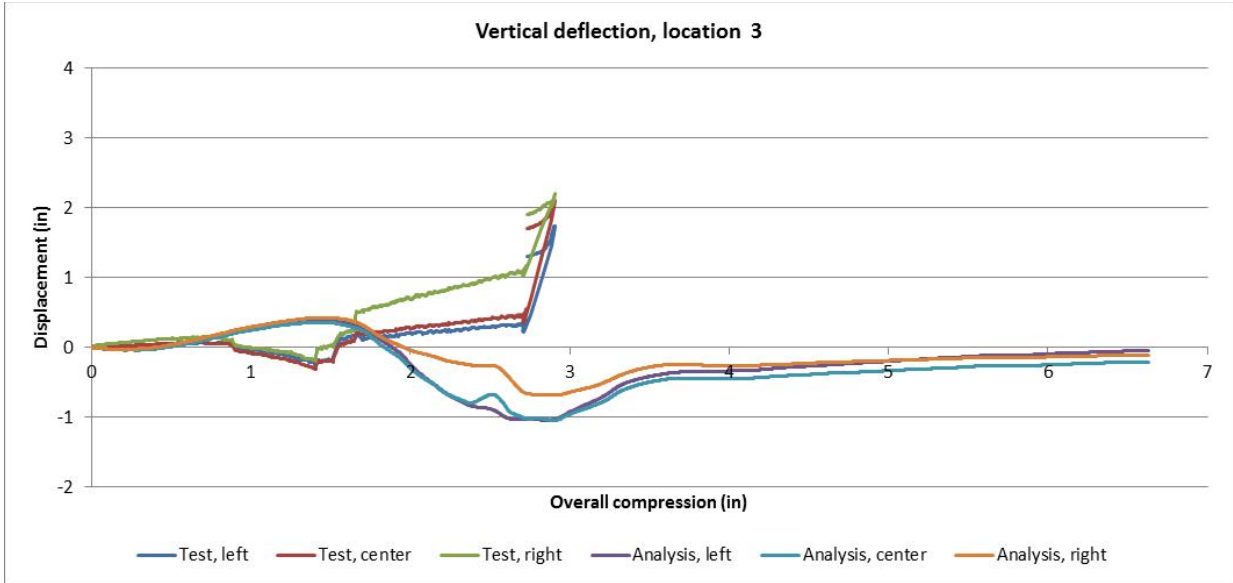


Figure G9. Vertical Deflection at Location 3

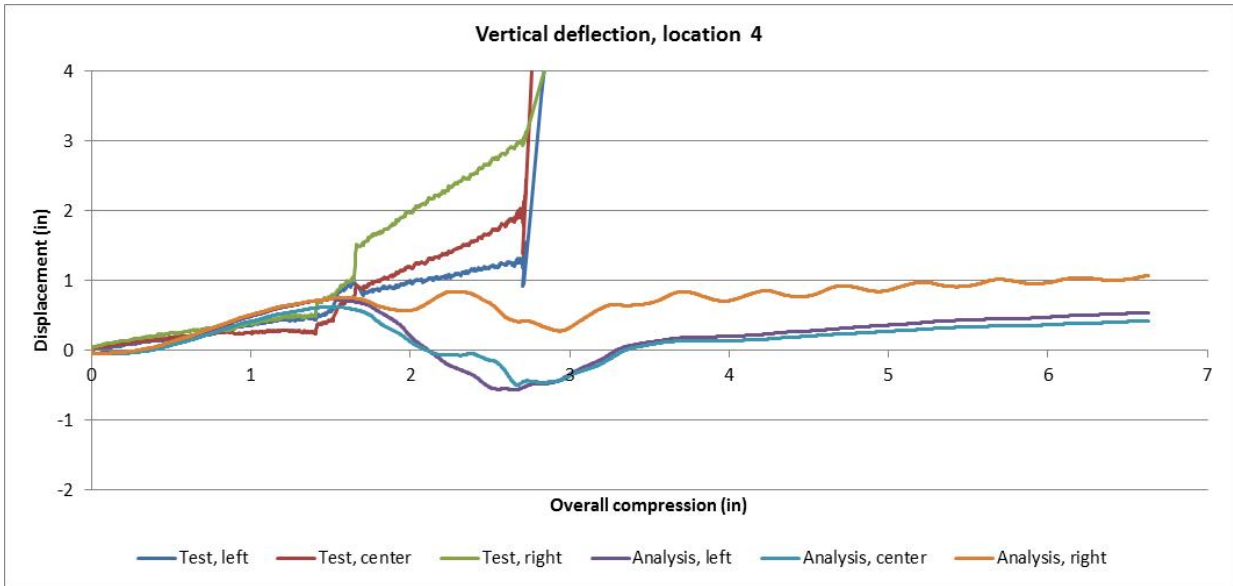


Figure G10. Vertical Deflection at Location 4

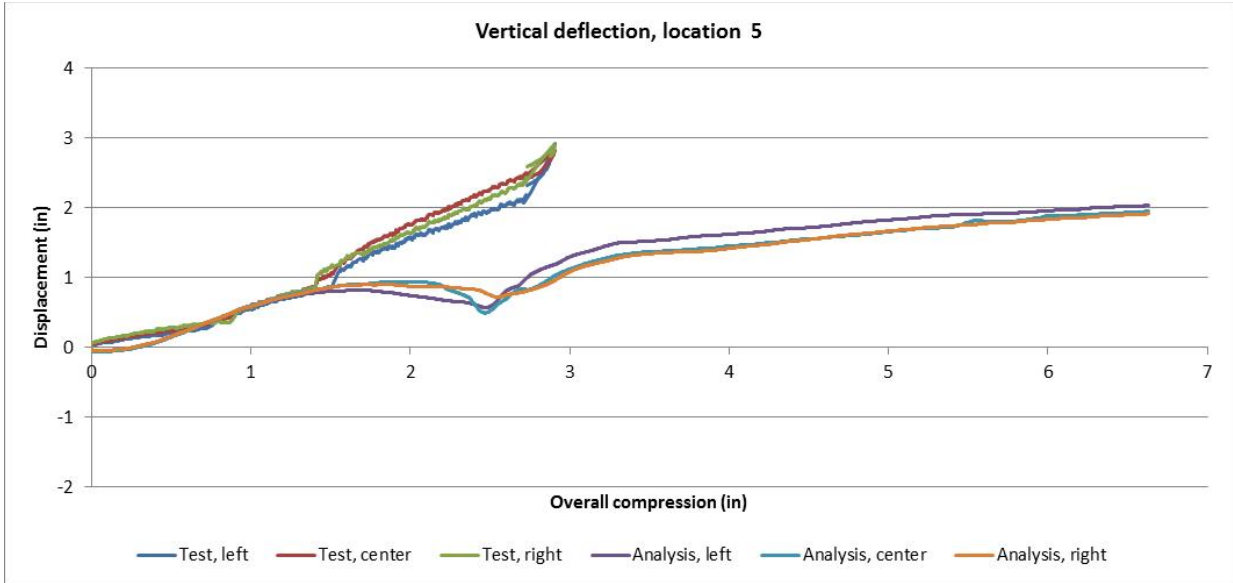


Figure G11. Vertical Deflection at Location 5

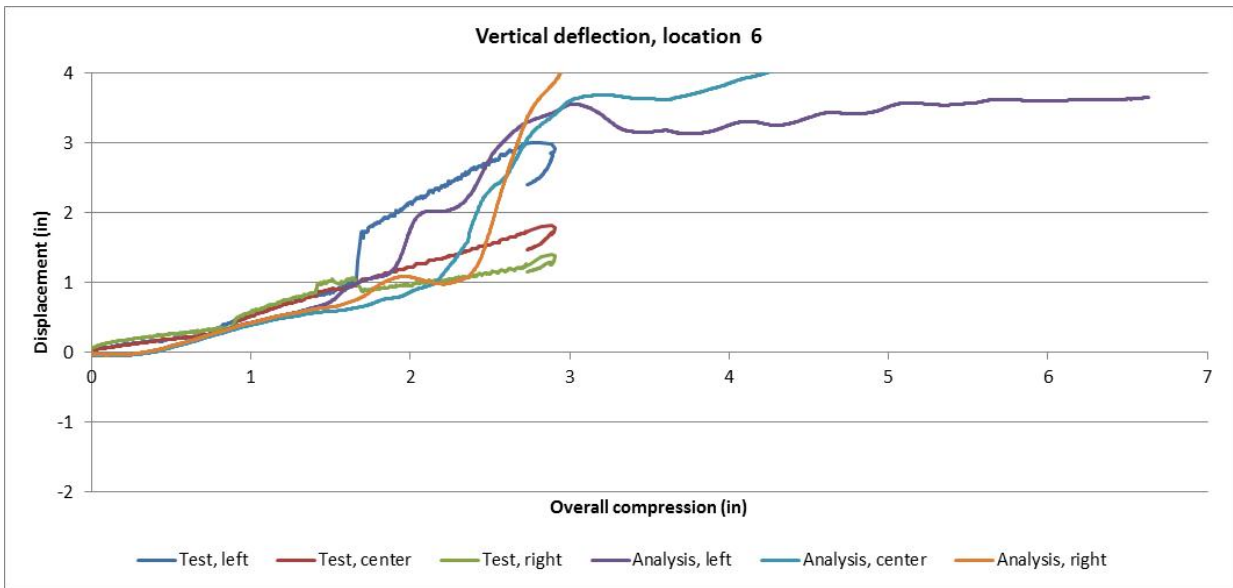


Figure G12. Vertical Deflection at Location 6

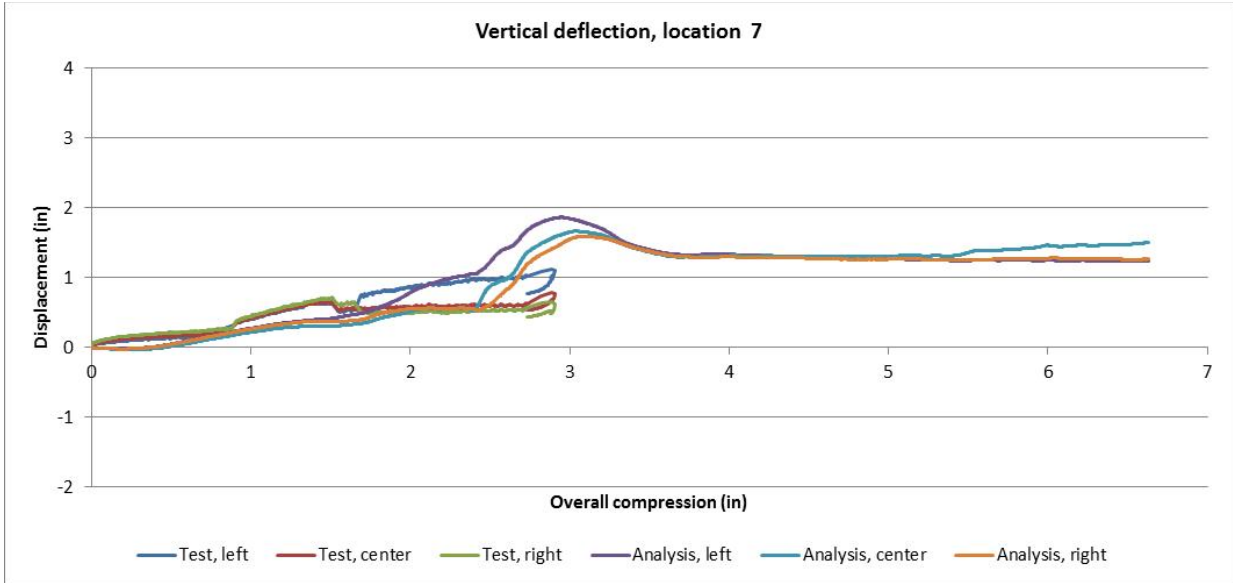


Figure G13. Vertical Deflection at Location 7

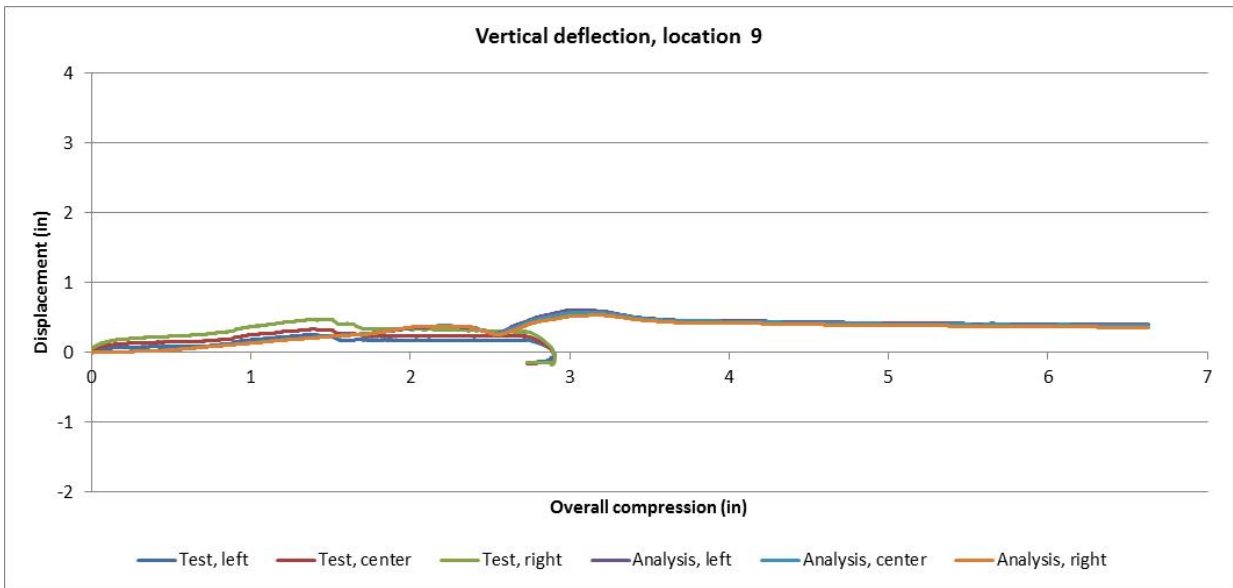


Figure G14. Vertical Deflection at Location 9 (B-end)

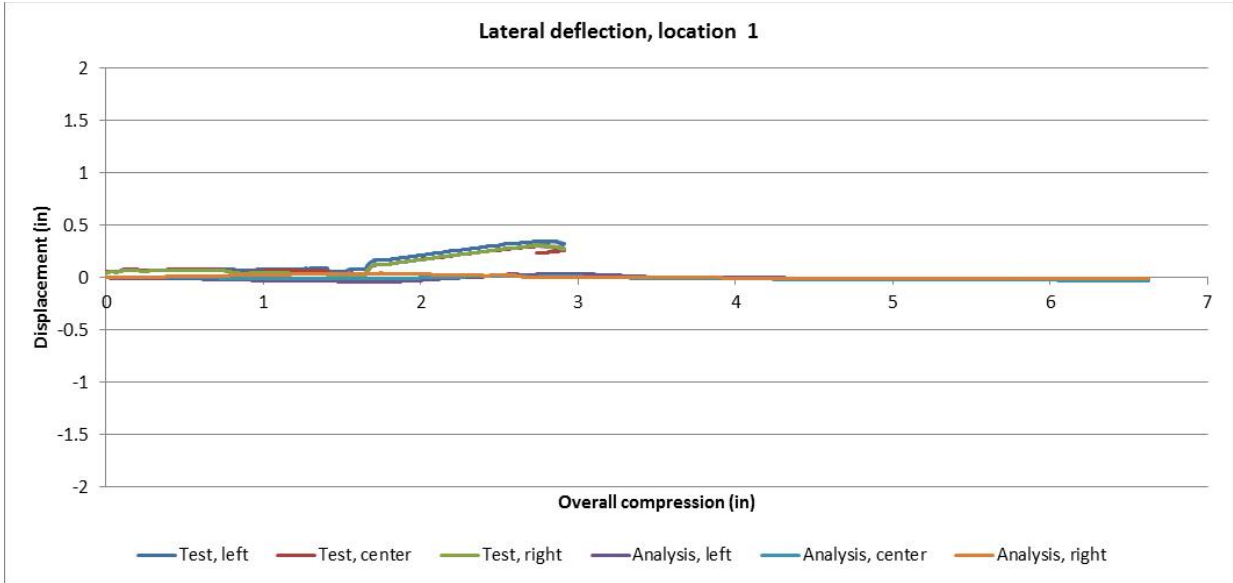


Figure G15. Lateral Deflection at Location 1 (F-end)

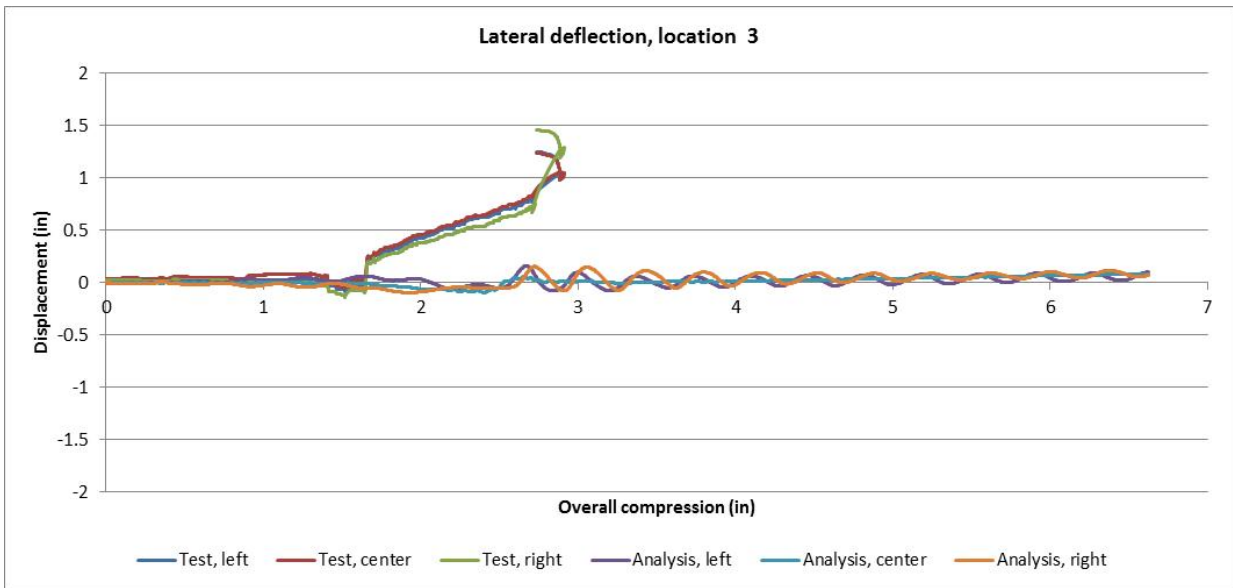


Figure G16. Lateral Deflection at Location 3

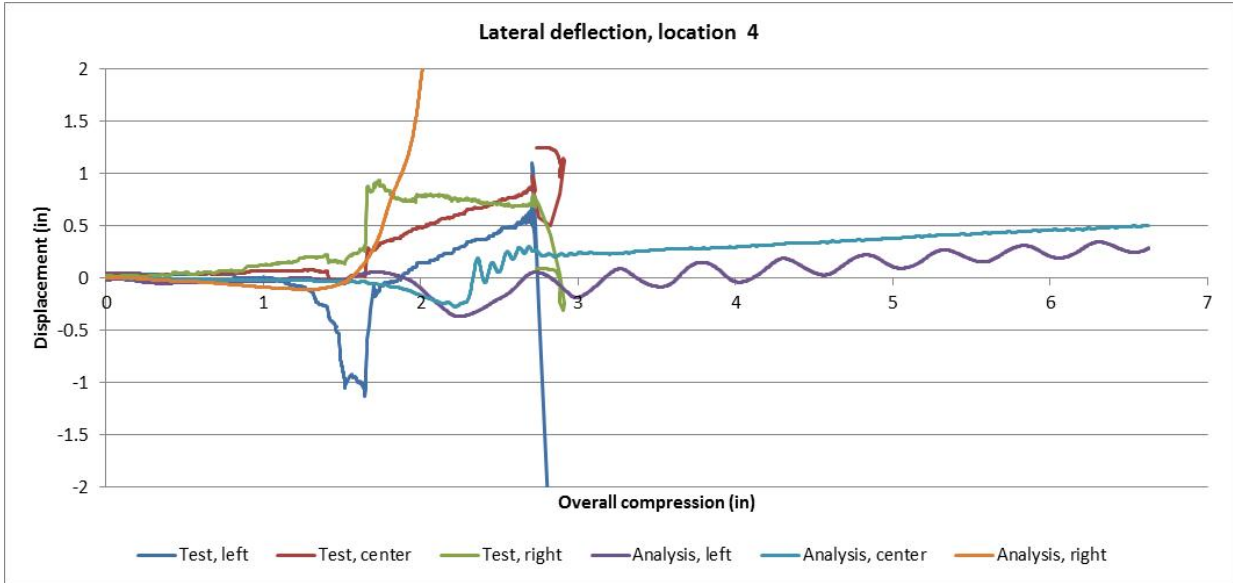


Figure G17. Lateral Deflection at Location 4

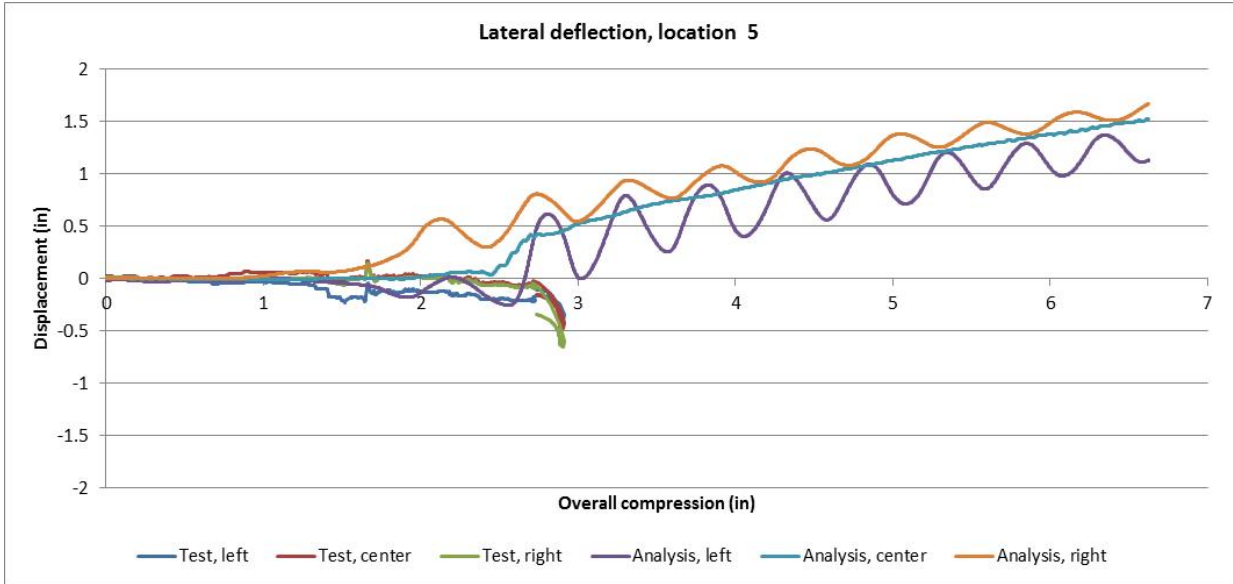


Figure G18. Lateral Deflection at Location 5

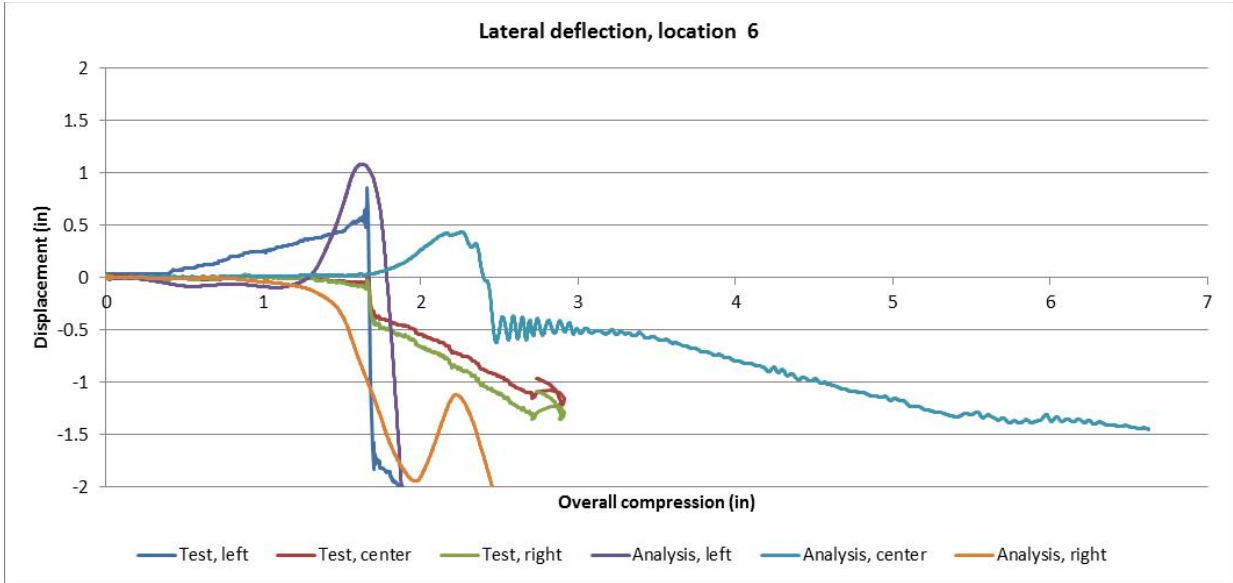


Figure G19. Lateral Deflection at Location 6

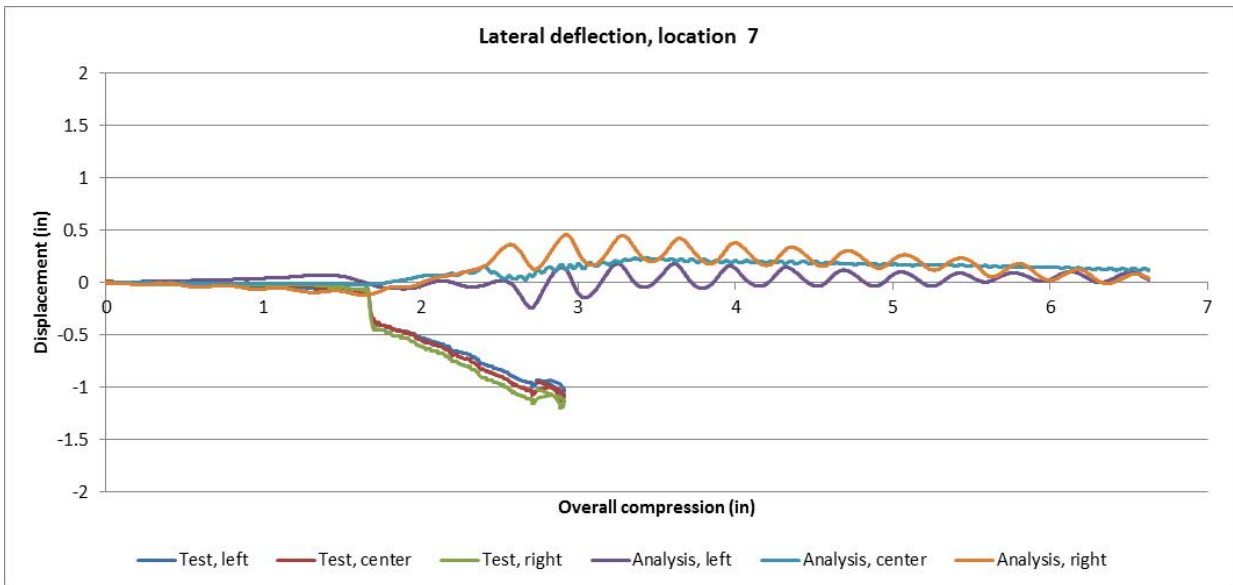


Figure G20. Lateral Deflection at Location 7

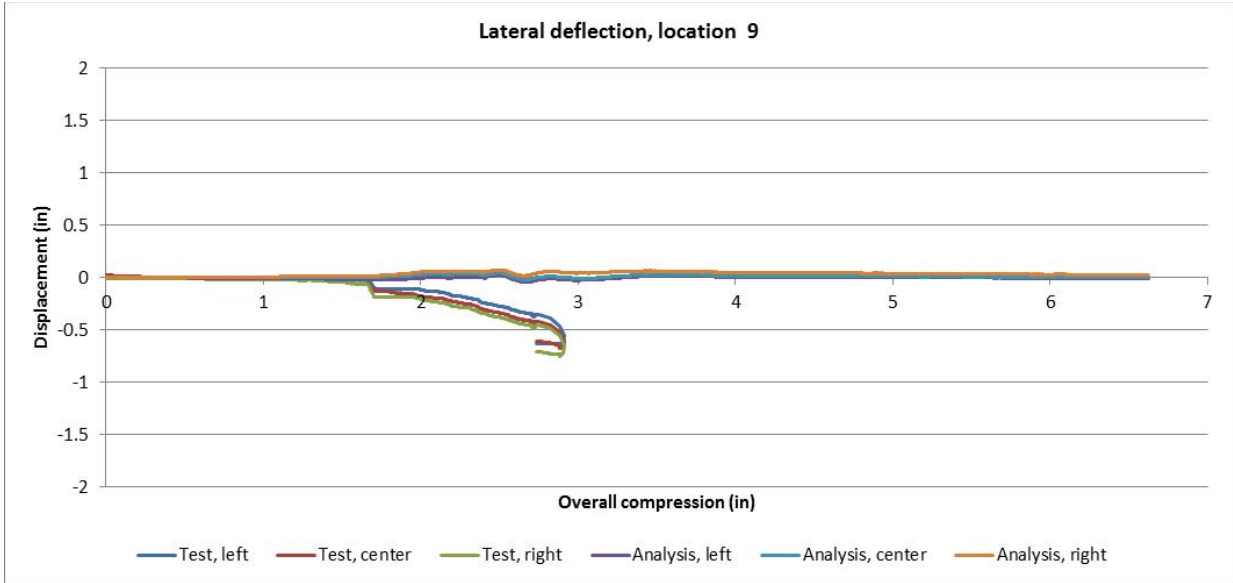


Figure G21. Lateral Deflection at Location 9 (B-end)

Strains

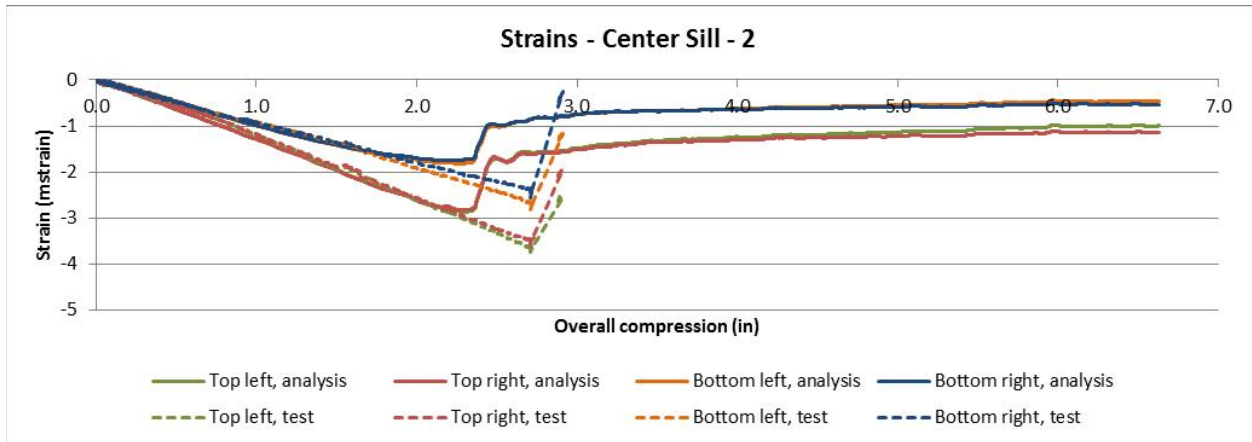


Figure G22. Axial Strains at Location 2 (F-end)

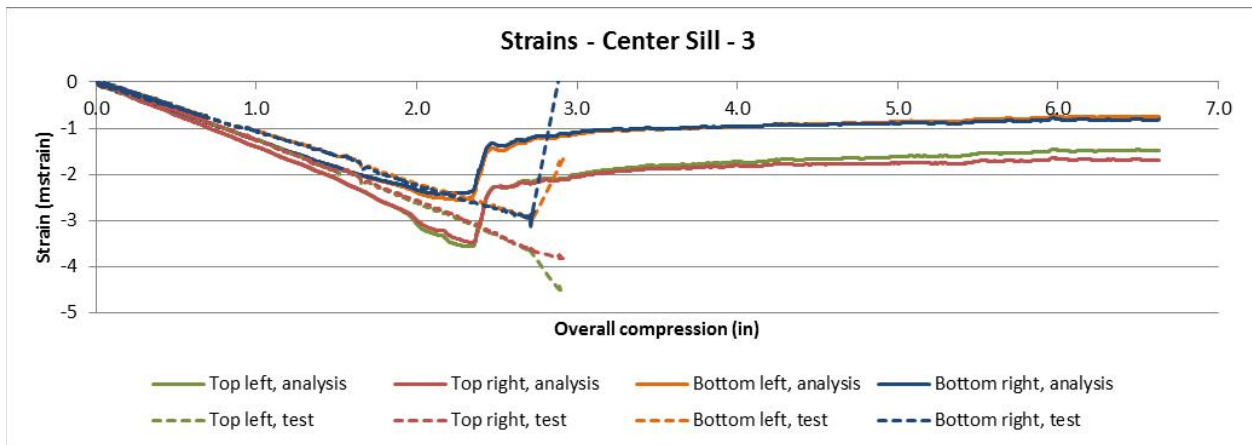


Figure G23. Axial Strains at Location 3

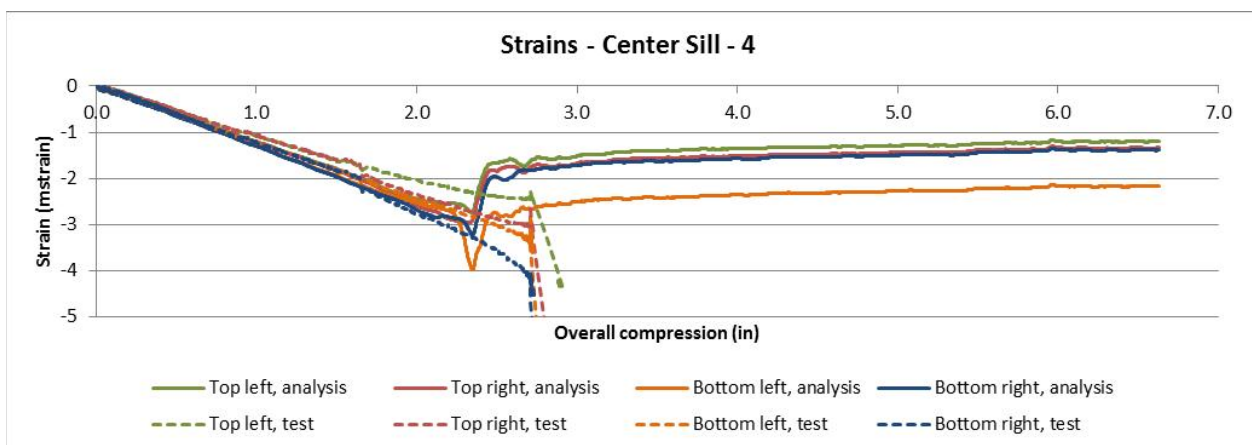


Figure G24. Axial Strains at Location 4

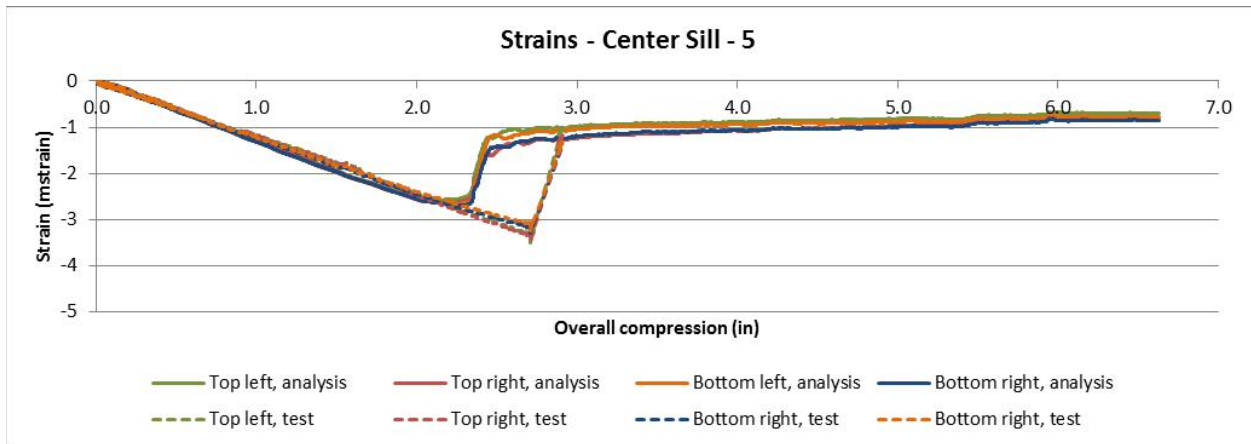


Figure G25. Axial Strains at Location 5

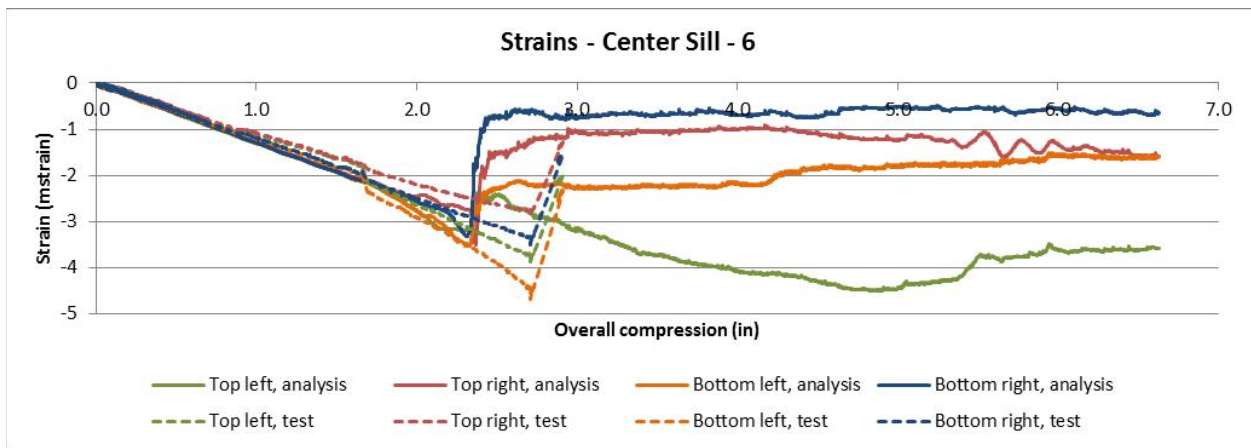


Figure G26. Axial Strains at Location 6

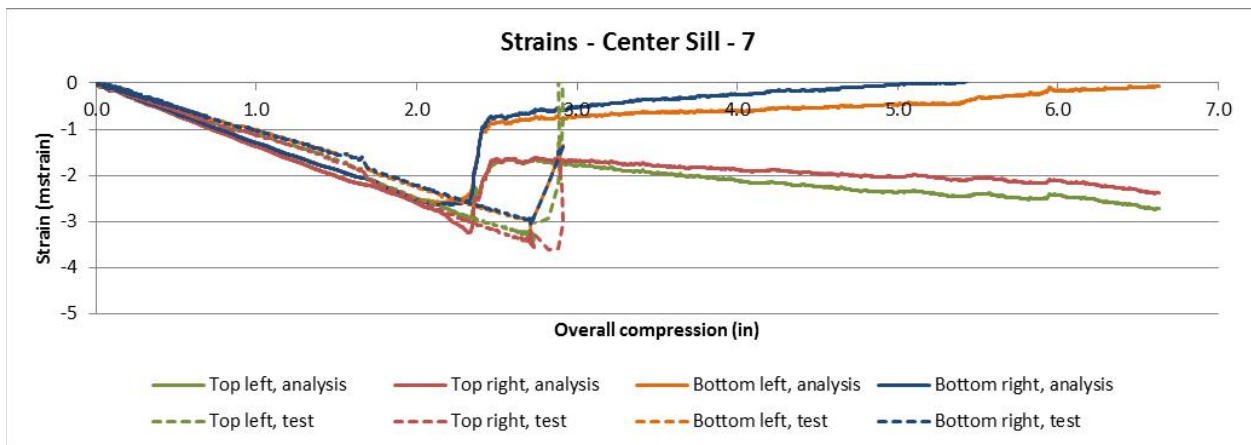


Figure G27. Axial Strains at Location 7

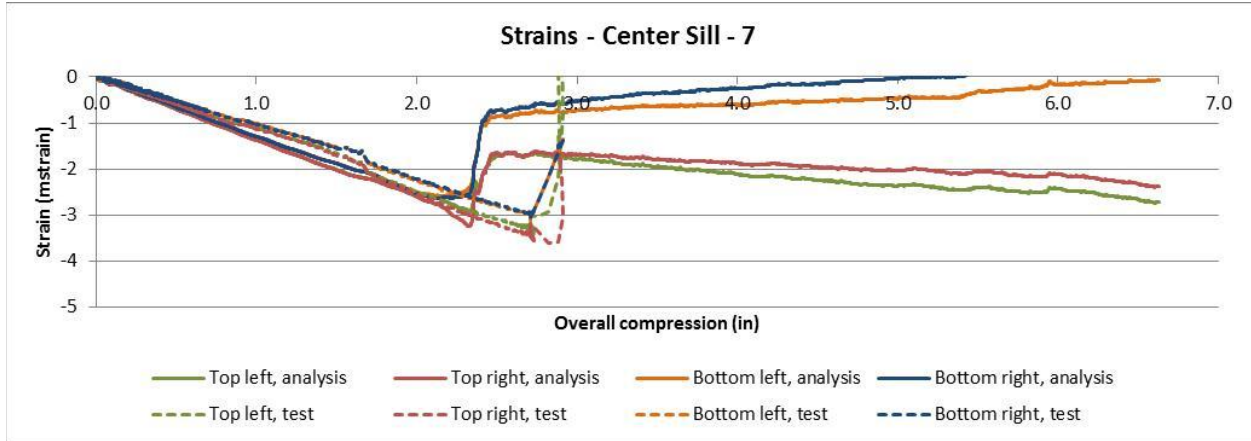


Figure G28. Axial Strains at Location 8 (B-end)

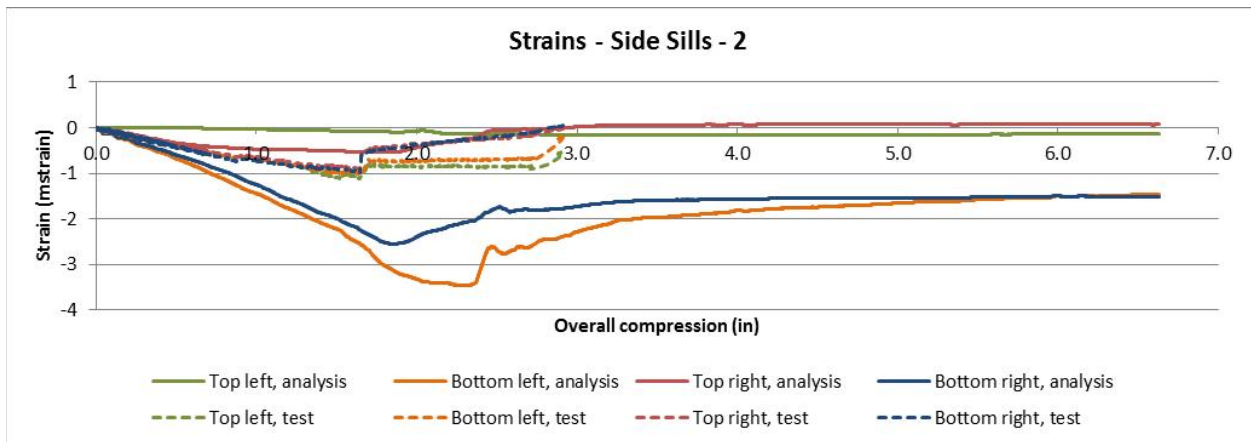


Figure G29. Axial Strains at Location 2 (F-end)

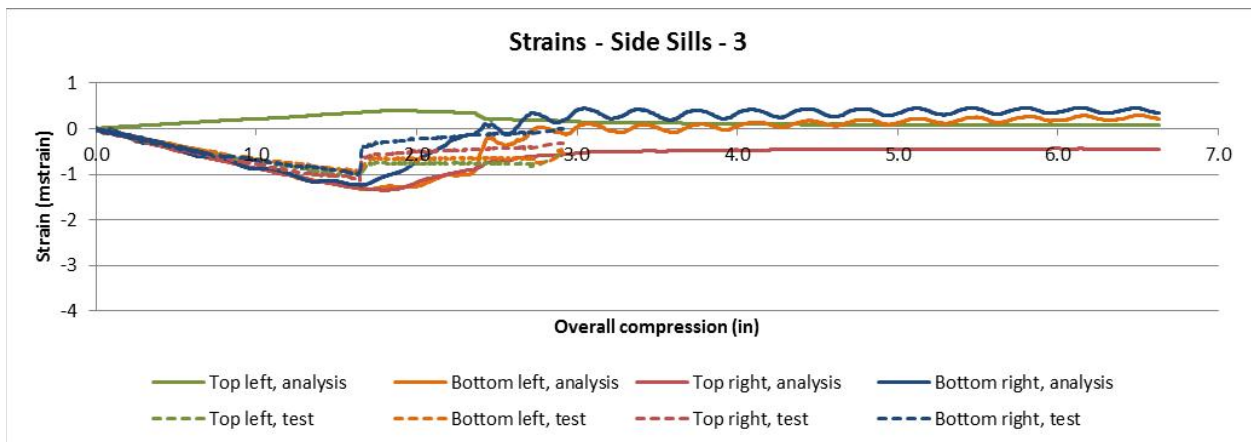


Figure G30. Axial Strains at Location 3

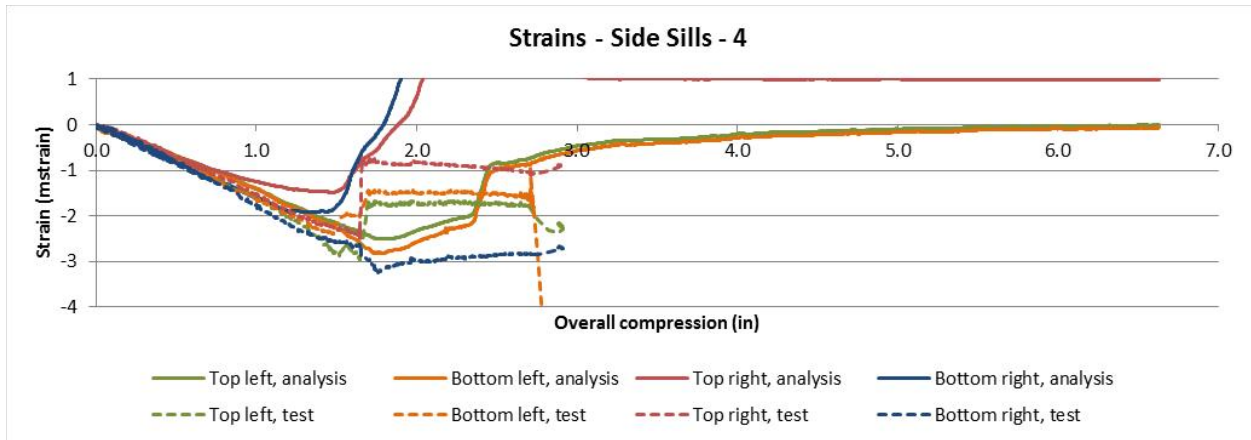


Figure G31. Axial Strains at Location 4

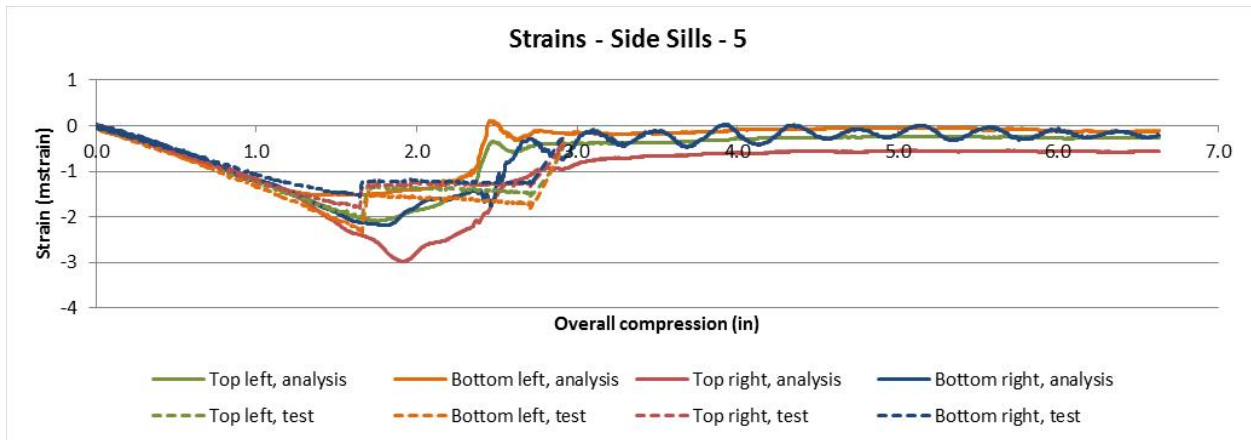


Figure G32. Axial Strains at Location 5

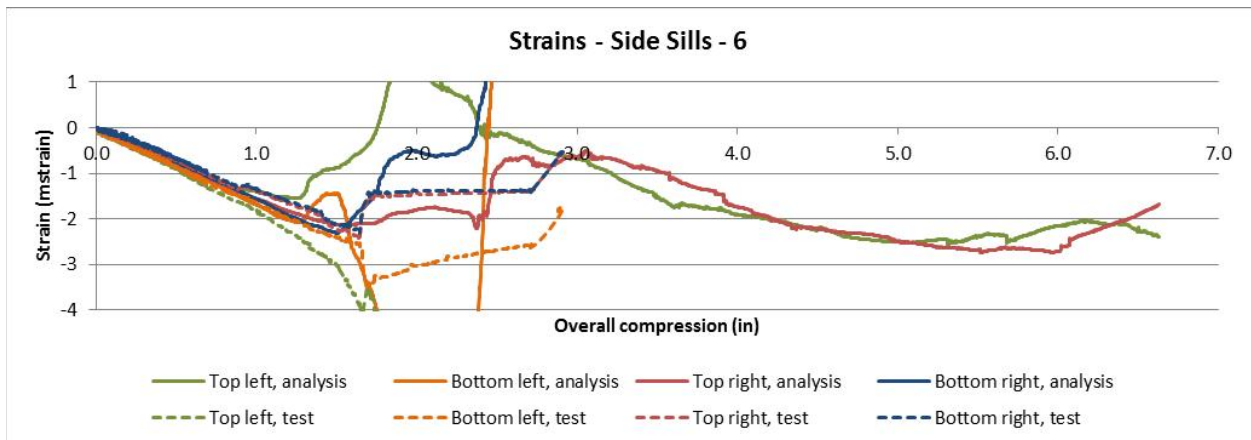


Figure G33. Axial Strains at Location 6

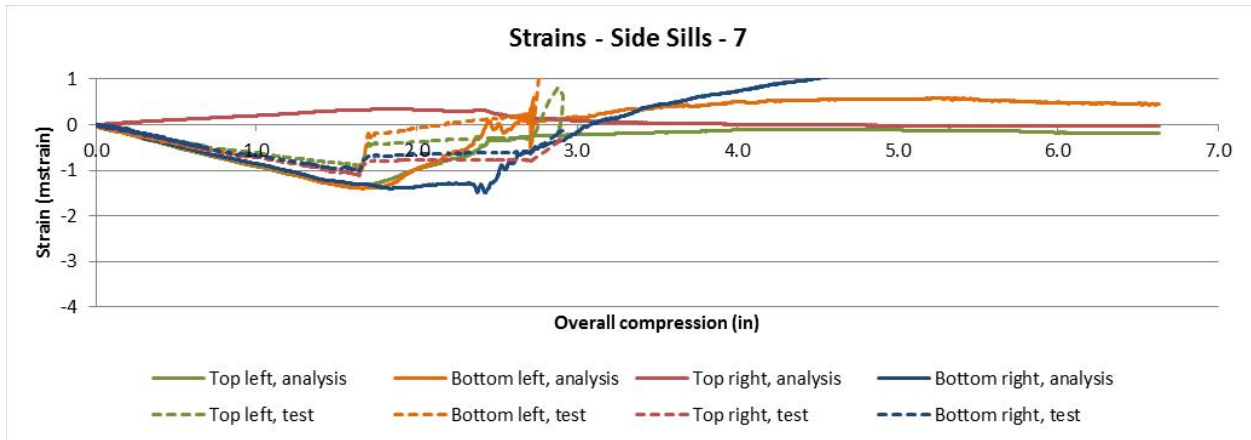


Figure G34. Axial Strains at Location 7

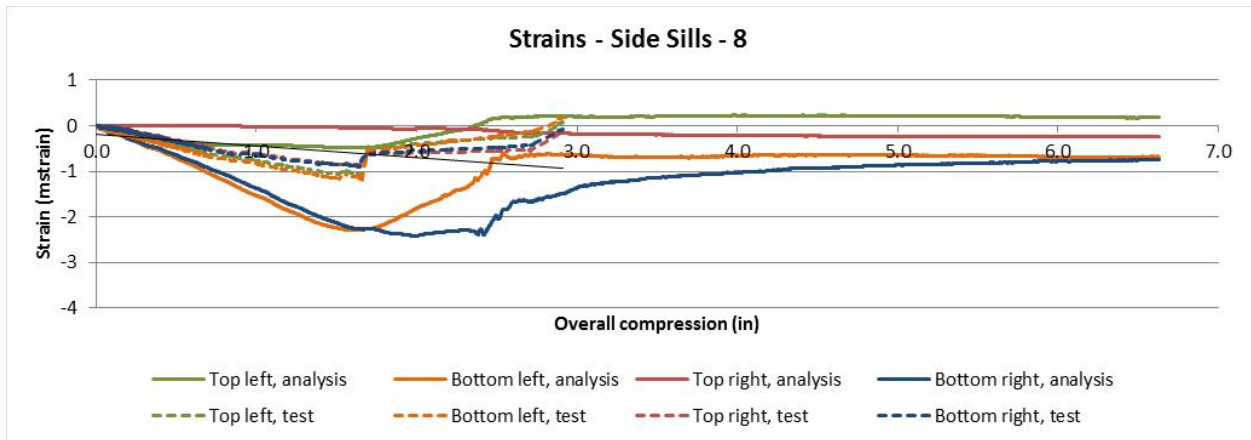


Figure G35. Axial Strains at Location 8 (B-end)

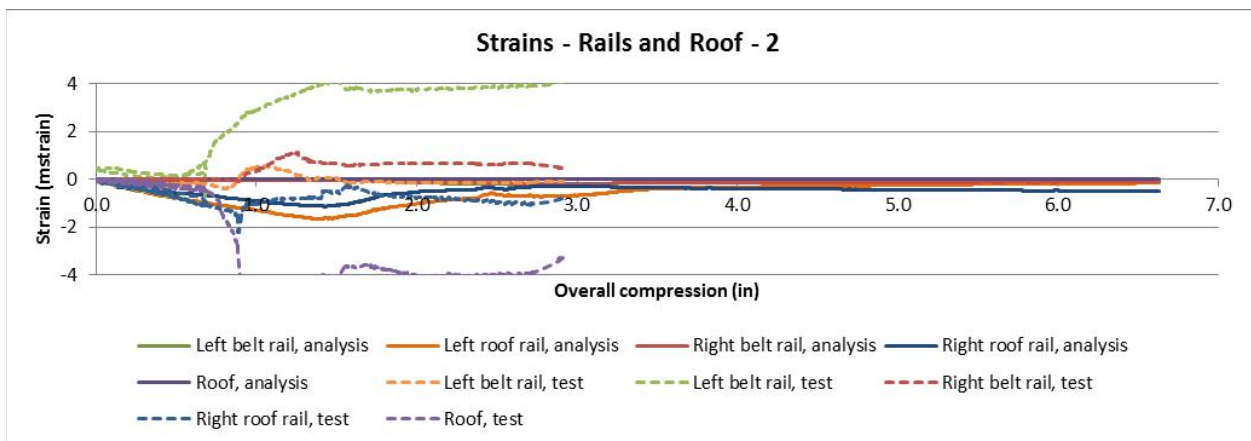


Figure G36. Axial Strains at Location 2 (F-end)

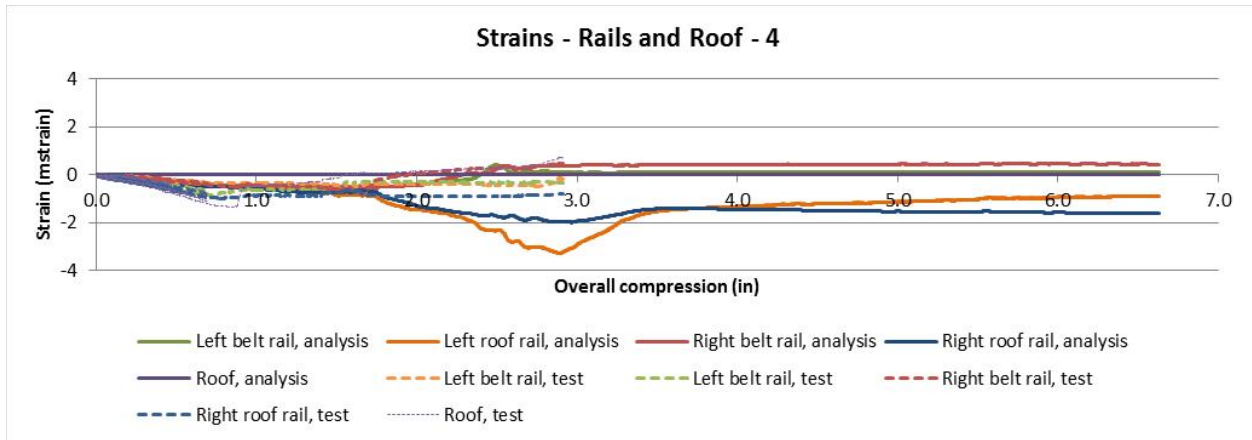


Figure G37. Axial Strains at Location 4

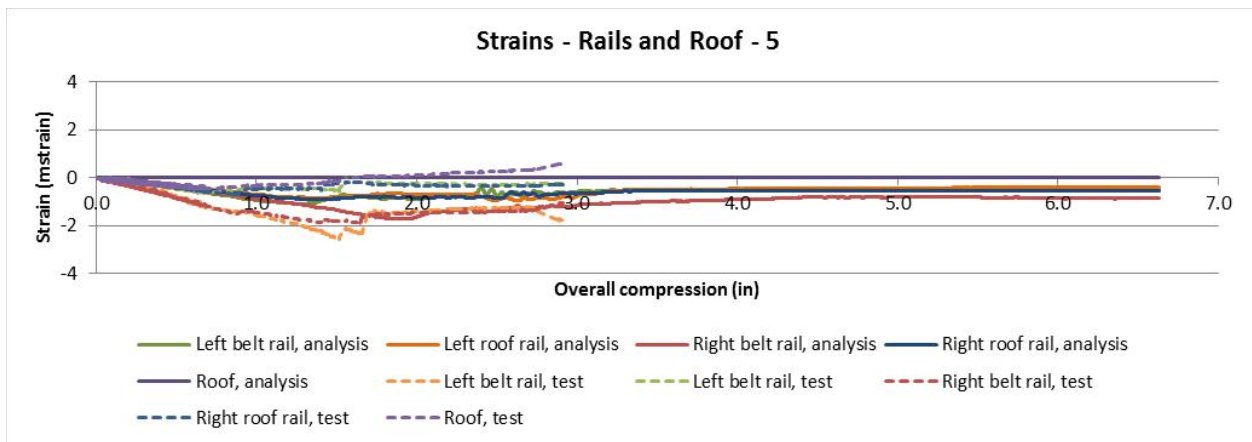


Figure G38. Axial Strains at Location 5

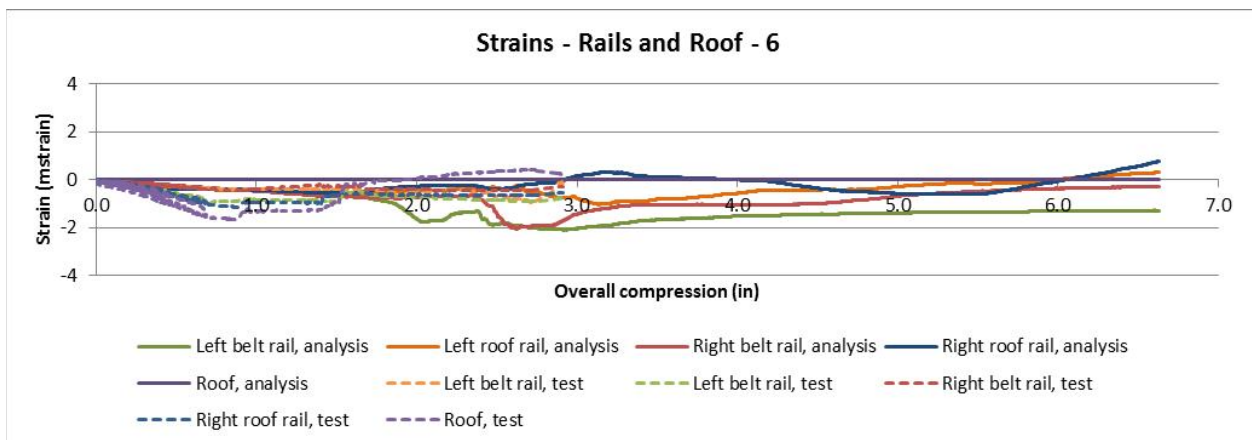


Figure G39. Axial Strains at Location 6

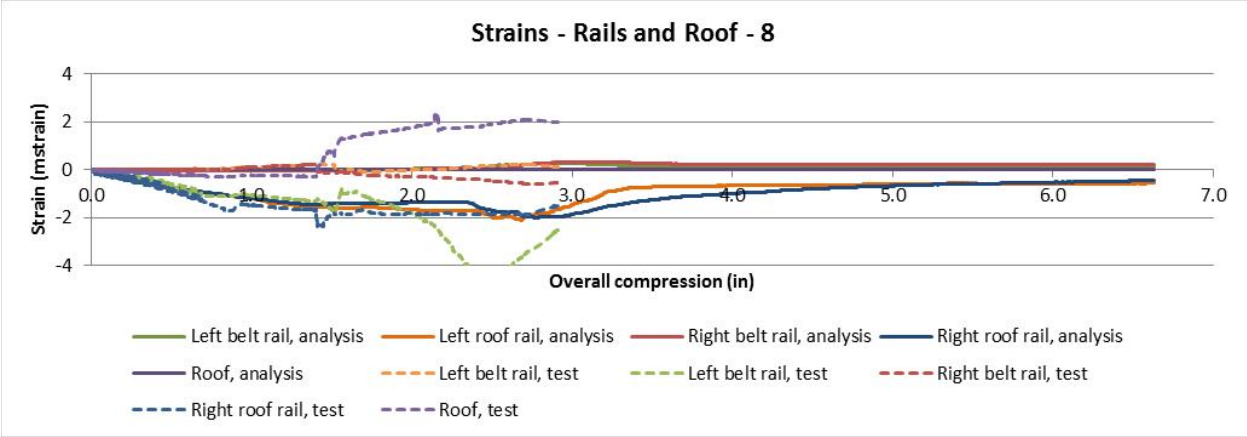


Figure G40. Axial Strains at Location 8 (B-end)

Appendix H – Discussion of Crippling Load Analysis Results (Arup FE Model)

H.1 General Discussion

The results presented in Section 5 show that the analysis displayed similar behavior to the crippling load test in many respects. Nonetheless, there were several differences, which caused the analysis to overstate the strength of the railcar by more than 20 percent.

If FEA will be used to certify railcars, it is critical to understand why the differences occurred and develop modeling validation procedures that ensure adequately reliable results would be obtained within an industry setting.

The major difference between the analysis and the crippling load test is the post-buckling behavior. Failure in the analysis occurred with gradually increasing buckles, which maintained much of their resistance as deformation increased further. During the crippling load test, on the other hand, most failures occurred abruptly, as a result of spot weld failure, tearing, and delamination. In the case of the roof, the abrupt failure occurred as the corrugations folded sharply.

To adequately represent the strength of a railcar, these failure mechanisms must be accurately captured, including the post-peak resistance behavior.

H.2 Roof Buckling — Failure of Corrugated Panels

The corrugations in the roof were modeled using a single element per facet, with a characteristic length of around 0.5 inches. As noted in subsection 5.6.2, this model did not capture the actual failure mechanism of the physical roof — sudden folding of the corrugations.

Arup conducted a study to investigate the sensitivity of corrugated sheets to model characteristics. Four test pieces were analyzed, representing corrugated or un-corrugated sheets with a constant curvature and fixed at the ends. These do not directly relate to the railcar roof structure.

- No corrugations, 0.5-inch mesh
- No corrugations, 0.1-inch mesh
- Corrugations, 0.5-inch mesh
- Corrugations, 0.1-inch mesh

The element thicknesses were set so that all four versions had the same cross-sectional area (i.e., the same axial stiffness) and all were loaded and restrained in the same manner, with equal displacement. Figure H1 shows the force-displacement curves.

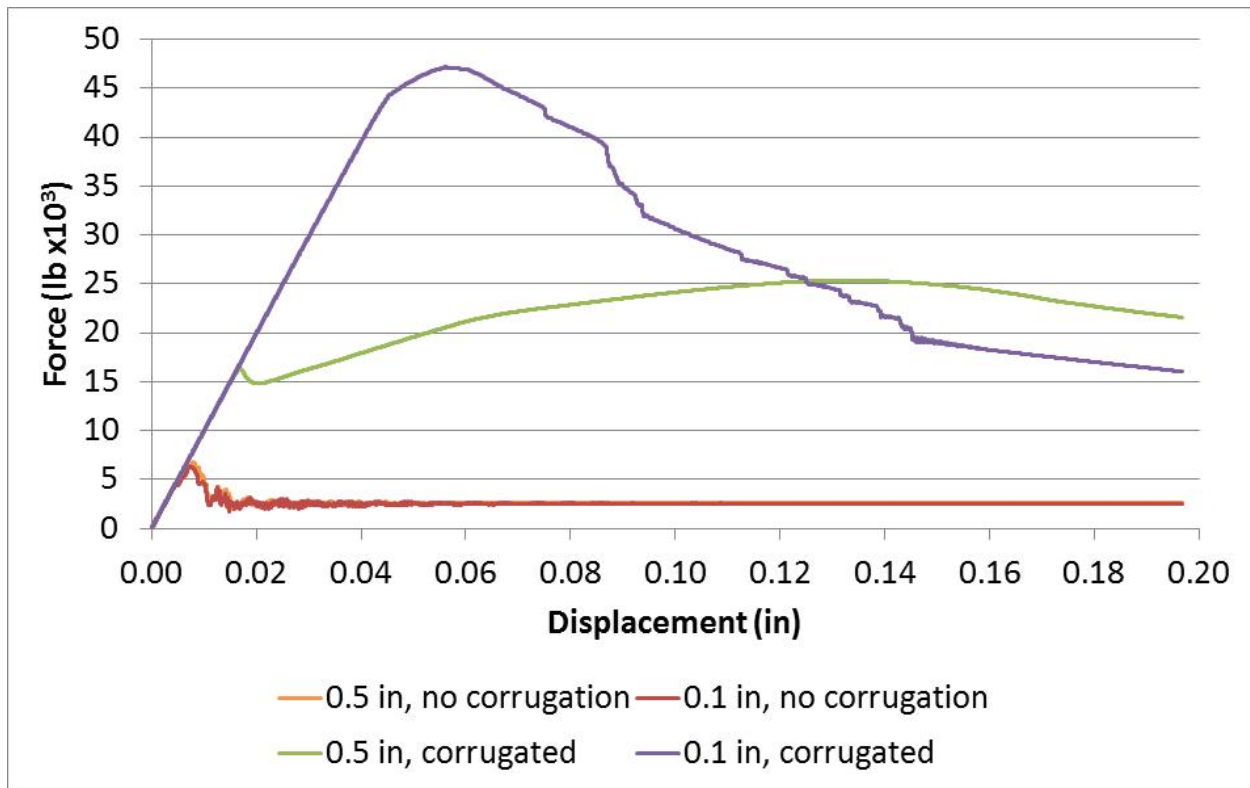
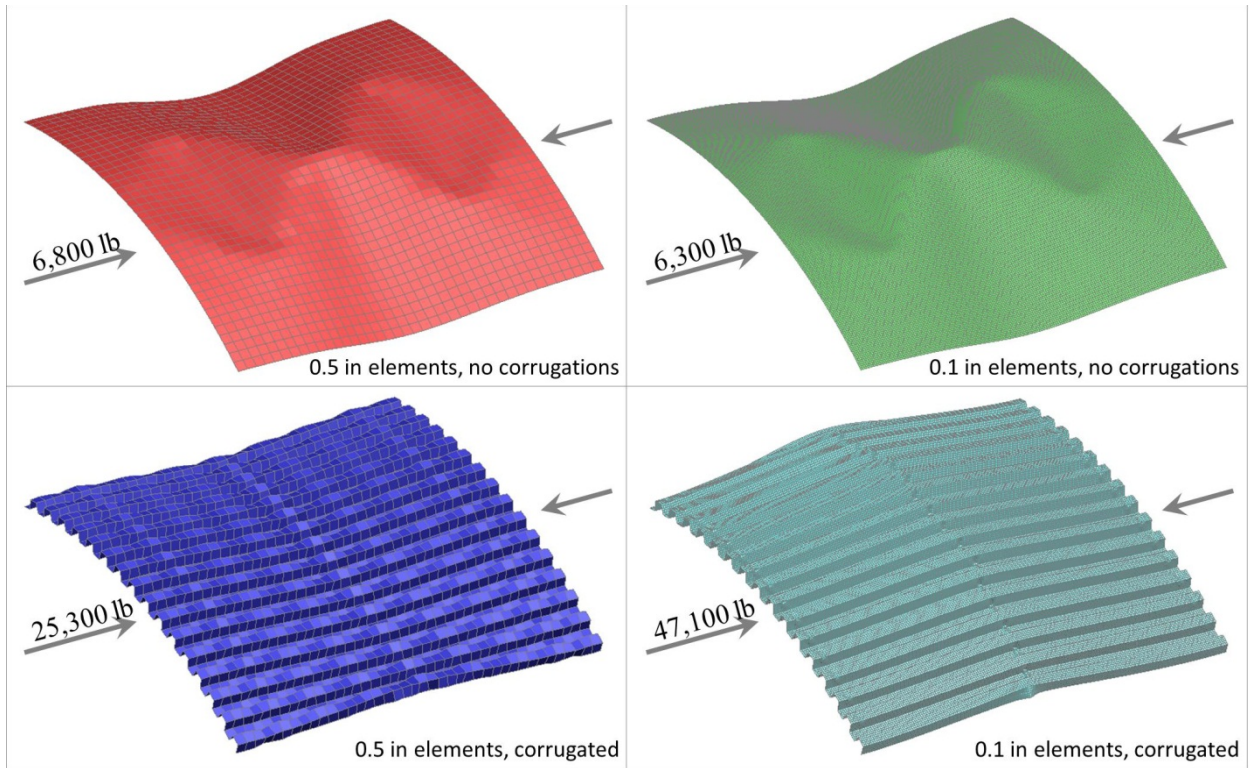


Figure H1. Force-displacement Curves for Corrugation Modeling Test

Figure H2 shows that in the analyses without corrugations, the form of the deformation was many times larger than the element sizes, so the results were similar between the 0.5-inch mesh and the 0.1-inch mesh.

Adding corrugations increased the load carrying capacity significantly. Two important observations were made for the analyses of corrugations:

- 1) The coarser mesh analysis suffered from what appears to be a numerical effect, with local waves appearing along the corrugations at a displacement of 0.17 inches. This resulted in an immediate reduction in capacity and stiffness. Figure H3 shows the waves in detail. It is interesting to note that this effect did not occur in the crippling load test analysis, perhaps because the elements had a different aspect ratio or the roof was additionally restrained by longitudinal stiffeners.
- 2) The second important observation for the analyses of corrugations is the difference in failure mode. The coarse meshed model experienced ductile failure as a gradually increasing buckle developed. The fine meshed model, on the other hand, experienced relatively sudden failure as local folding occurred. Figure H4 shows that this folding resulted in a sudden and ongoing reduction in the load carrying capacity. The reason the fine model folded locally while the coarse model did not is that the characteristic length of the fold feature was less than the 0.5-inch element length of the coarse model.



**Figure H2. Buckling Shapes at a Displacement of 0.2 in and Maximum Load
 Top Left 0.5 in, No Corrugations; Top Right 0.1 in, No Corrugations;
 Bottom Left, 0.5 in, Corrugated; Bottom Right 0.1 in Corrugated
 (All panels have the same cross-sectional area and underwent the same displacement.)**

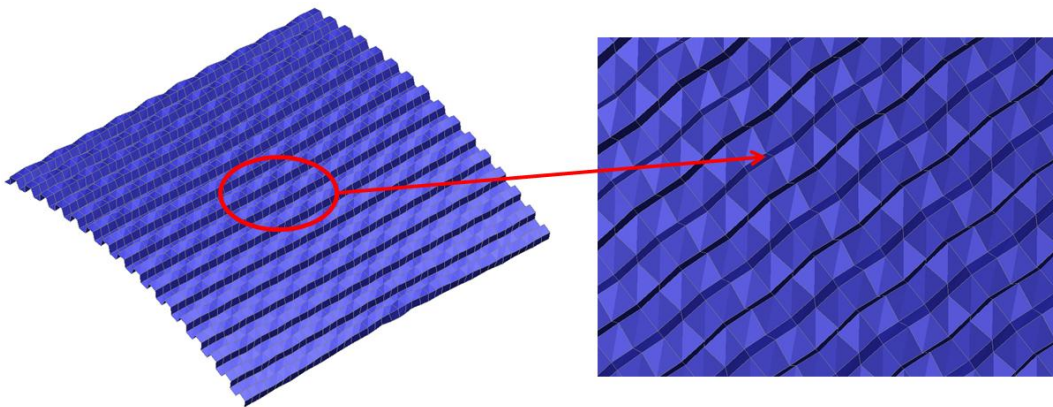


Figure H3. Local Waves in the Coarse Mesh Corrugation Analysis



Figure H4. Local Folding in the Fine Meshed Corrugated Analysis

This test shows the importance of validating the method used to model corrugated sheets, specifically noting:

- The presence of corrugations results in fundamentally different behavior than is seen in flat sheets.
- Certain mesh sizes can create erroneous numerical weaknesses.
- The element size must be significantly less than the characteristic length of any fold feature that might occur.

H.3 Spot Weld Failure

The failure modes of spot welds are complex and are notoriously challenging to a FE- model. These failures can be highly influential on the overall failure characteristics of the railcar if the main structural members (e.g., side sill and center sill) are made up of composite sections connected with spot welds.

Initially, the spot welds were all modeled as 0.2 in diameter with no failure. This formulation gave the results presented in Section 5. Investigations into the effect of introducing failure and varying the size of the spot welds showed that both can have a sizable impact on the failure behavior of the railcar.

Figure H5 compares the total load versus displacement characteristics of these three cases:

- The original model used for the crippling load predictions.
- The same model with failure introduced for the spot welds at 5-percent strain.
- A version with failure at 5 percent and the diameter of the spot welds increased by a factor of two.

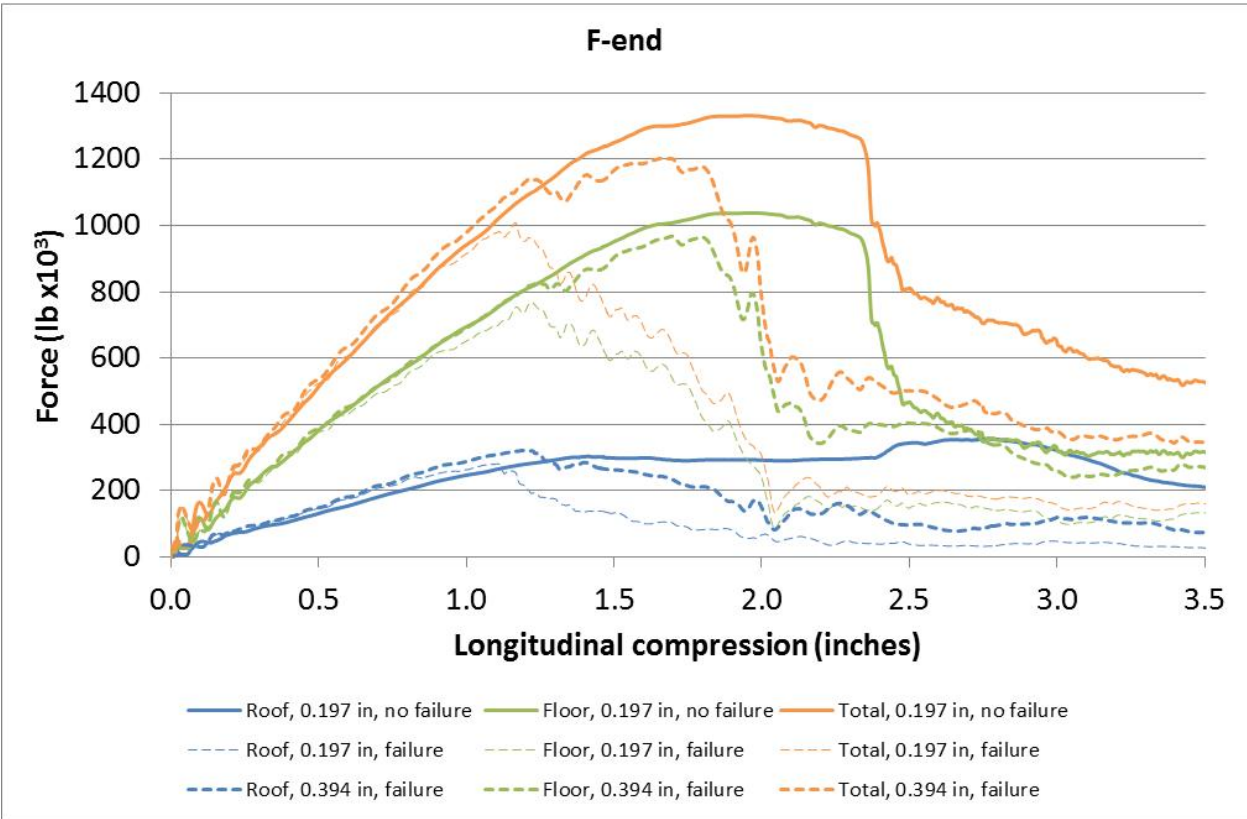
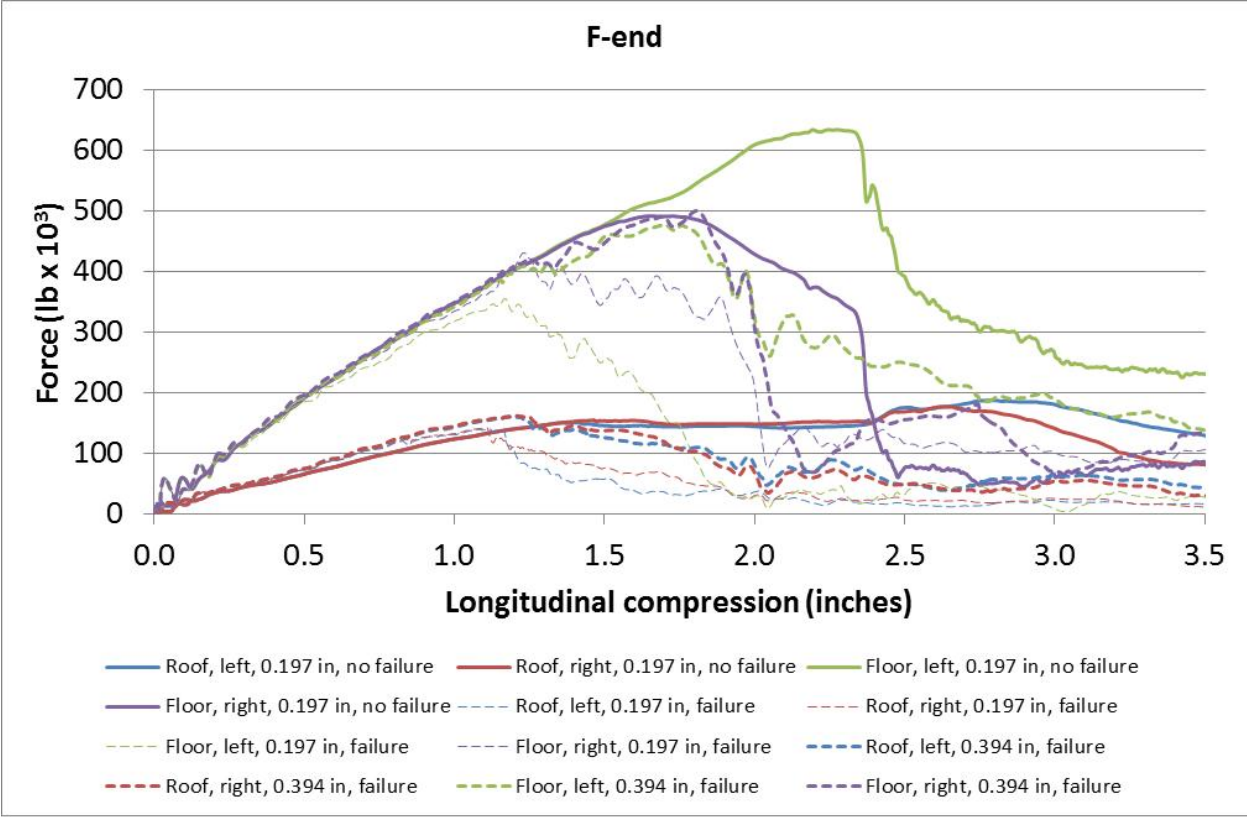


Figure H5. Effect of Spot Weld Formulation on the Overall Performance of the Railcar

It is clear that the characterization of spot welds is extremely influential and should be calibrated to the actual spot weld behavior to capture the overall behavior of the railcar.

In practice, this can only be done by carrying out physical tests on typical spot weld details and matching the analysis formulation to these results. Of course, any individual railcar is likely to have many spot weld details, with different numbers of metal layers, different thicknesses of materials, and different diameters of weld, and each of these would need to be tested and matched.

Specific characteristics that need to be accounted for include:

- Elastic behavior under axial loading due to dishing of the parent material
- Elastic behavior under shear loading
- Plastic deformation of the parent material
- Tearing of the parent material

Much research has been done on modeling spot welds and increasingly complex setups are used. This analysis used single beam elements to represent spot welds. To capture the behavior accurately, some analysts suggest using single solid elements or even multiple solid elements. These increase the complexity of the model and impart a penalty on analysis time.

H.4 Loading Rate and Damping

During the crippling load test, the railcar is loaded relatively slowly, which allows time for the car to stabilize and permits the test personnel to address any events. To keep run times to a reasonable level during FEA, loads must be applied much faster, but the analyst must not be too aggressive. If loading is applied too quickly, buckles do not have time to fully develop at a constant load.

Overly aggressive loading can also cause dynamic overshoot. This was found to be particularly pertinent to the 800,000-lb load test. Dynamic overshoot can be addressed during post-processing for 800,000-lb load analyses but would change the steady-state final condition when operating in the plastic range.

Damping can be effectively used to reduce or eliminate dynamic overshoot but can lead (as Appendix E describes) to a lag in the force-displacement curves.

Figure H6 compares force-displacement crippling curves with damping, without damping, and with reduced loading rate (also without damping). There is some effect on the results, though in this case it is small.

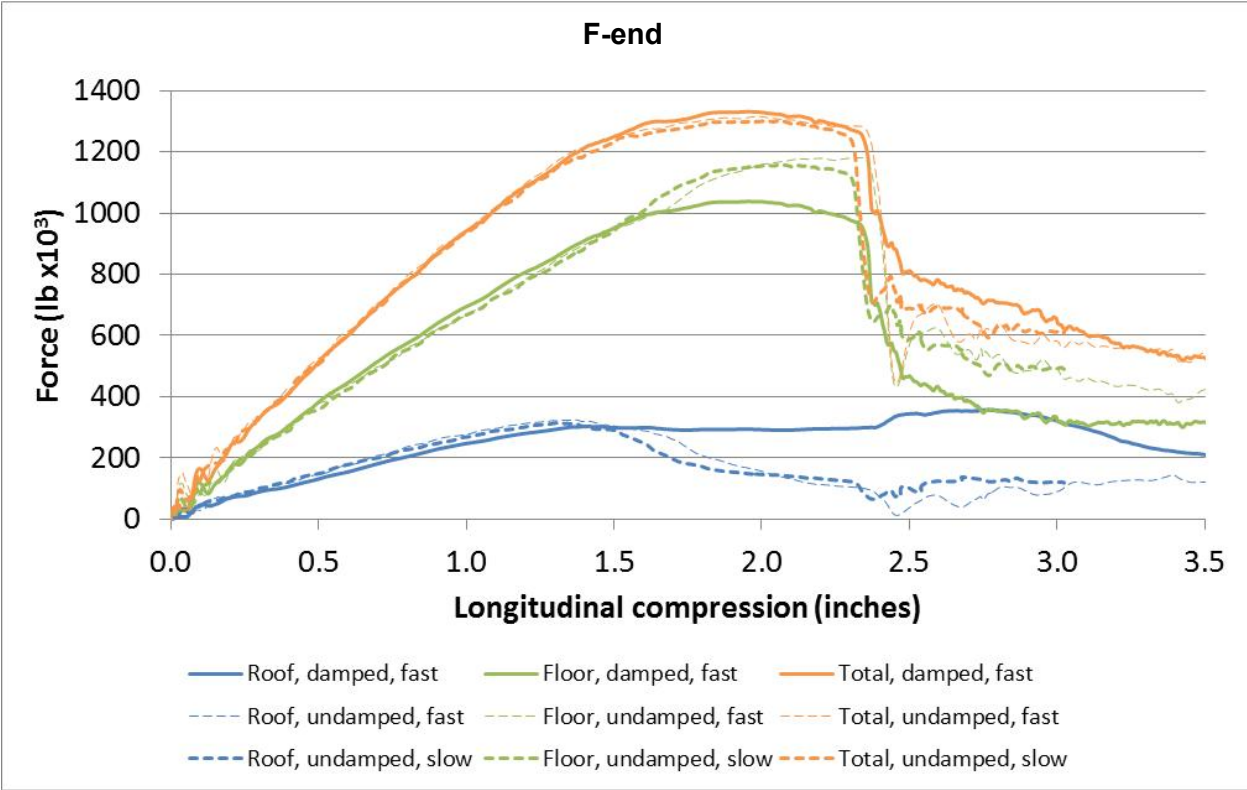
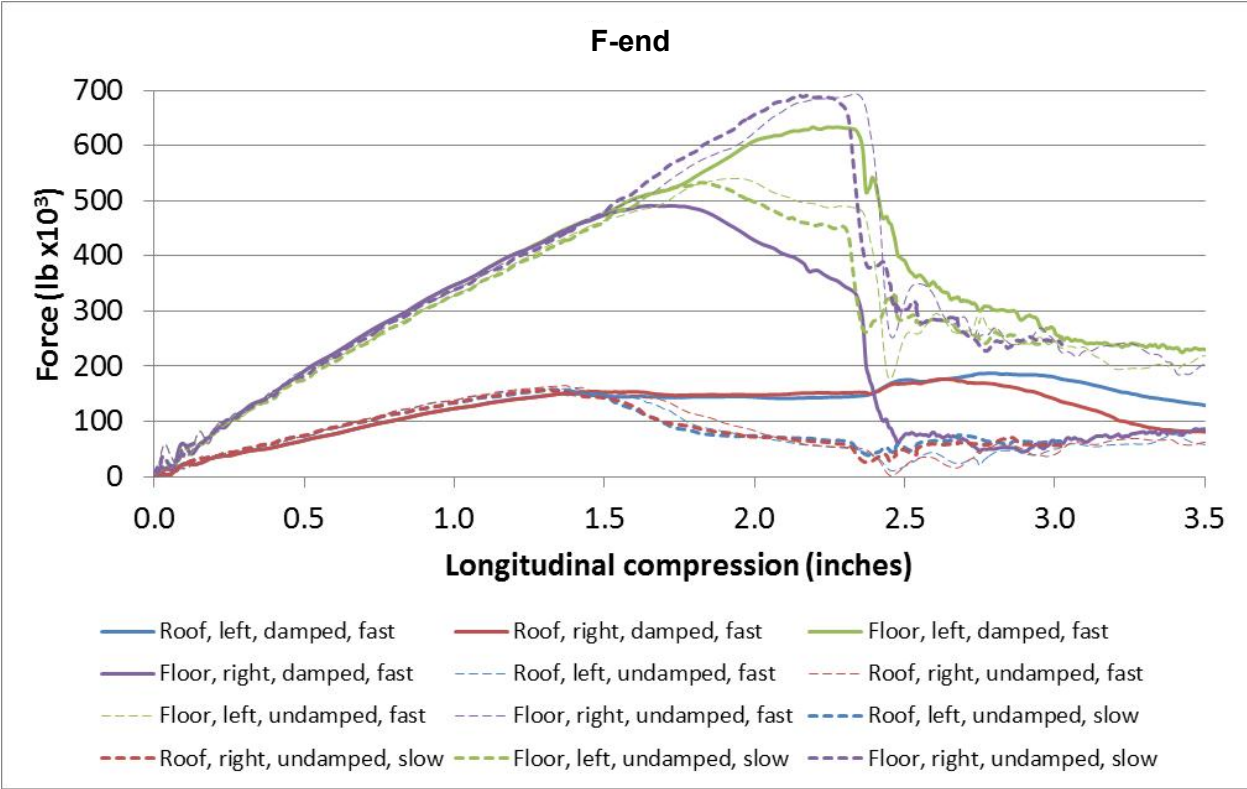


Figure H6. Effect of Loading Rate and Damping on the Overall Performance of the Railcar

H.5 Other Factors

There are other factors that may affect the behavior of railcars in crippling load tests. While some factors only apply to simulated predictions (e.g., it may be necessary to use a particularly fine mesh in areas that buckle to avoid overstating the local stiffness of the component), others also apply to physical crippling load tests. Arup investigated the effects of several such factors by altering the simulation model as follows:

- Varying the thickness of the steel
- Misaligning the railcar within the testing rig
- Adding minor initial imperfections in the geometry, such as local buckling in the side sills up to ¼ inch
- Applying the load at a slight incline
- Loading up one loading point slightly before the others
- Changing the stiffness of the truck springs

This last factor — the stiffness of the truck springs — had a marked effect on the 800,000-lb load test, where there was greater vertical bowing of the railcar but much less effect in the crippling load test (where the railcar remains largely horizontal along its length). As seen in Figure H7, all these factors were found to have a relatively small impact on the results (i.e., <5percent).

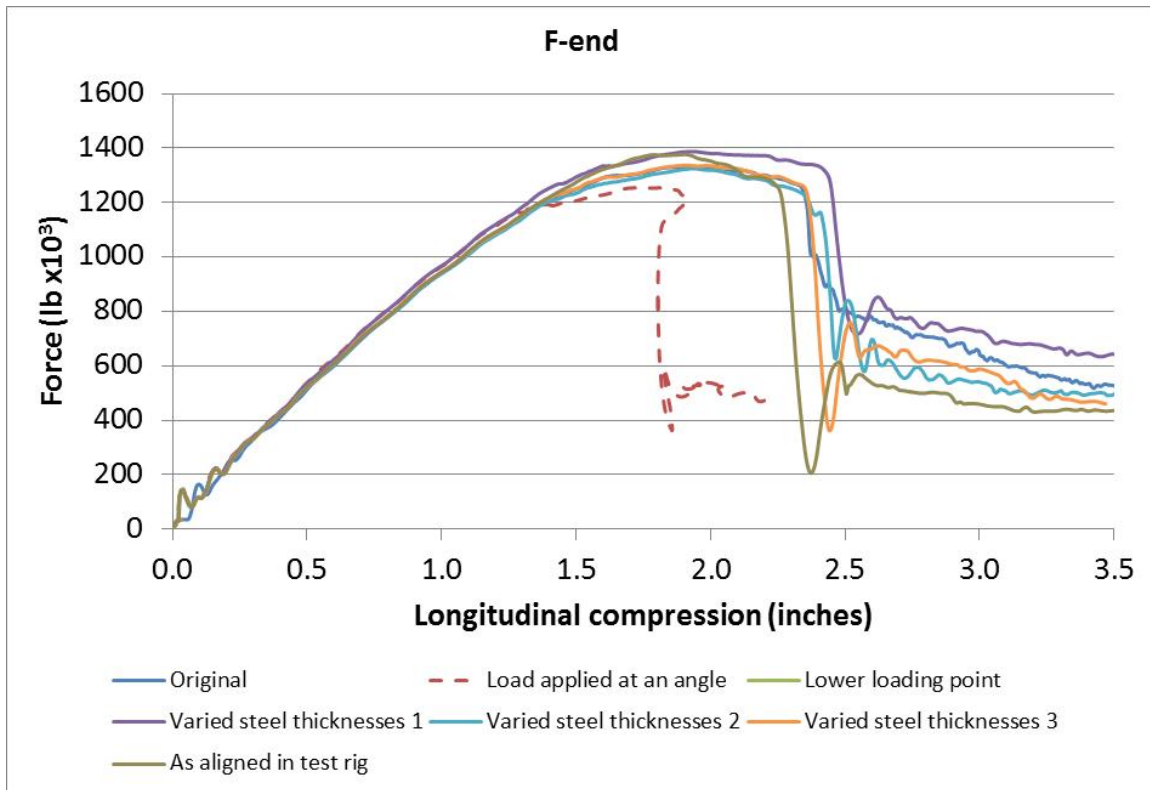


Figure H7. Effect of Other Factors on the Overall Performance of the Railcar

Appendix I – 800,000-pound and Crippling Load Tests Post-processing (Arup FE Model)

Aligning local and global axes

During the 800,000-pound and crippling load tests, and to a lesser extent, the analysis, the railcar underwent rigid body displacement. In other words, the whole railcar rotated relative to a fixed global coordinate system, independent of the deformation of the railcar. To make the results of the 800,000-pound and crippling load tests and their analyses comparable, the rigid body motion must be disaggregated and removed.

To do this, the midpoints between the lower CEM pockets at each end were used as reference points. The axis of the railcar was defined as the line between these two points, as Figure I1 shows.

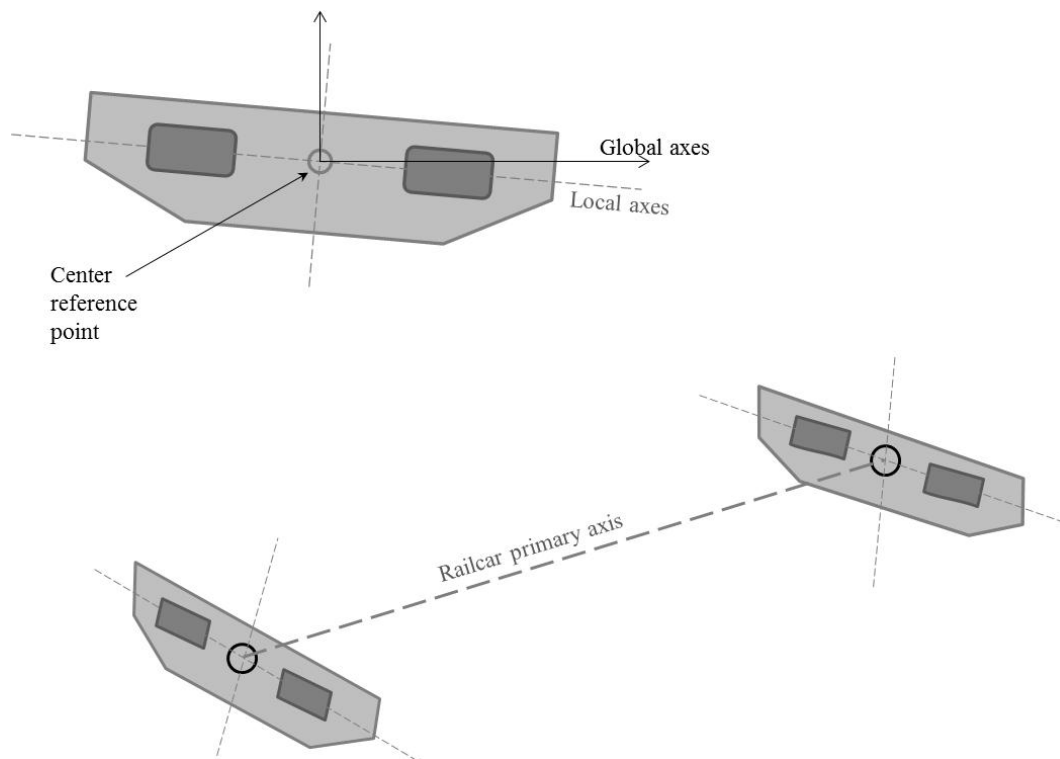


Figure I1. Local Axis Definitions for Deformed Railcar

All vertical deflections were adjusted so that the primary axis of the railcar was aligned with the global axis, with the vertical deflection of the two reference points at zero. In addition, the railcar was rotated around the primary axis so that the local transverse axes were equal distances from the global transverse axis, as Figure I2 shows.

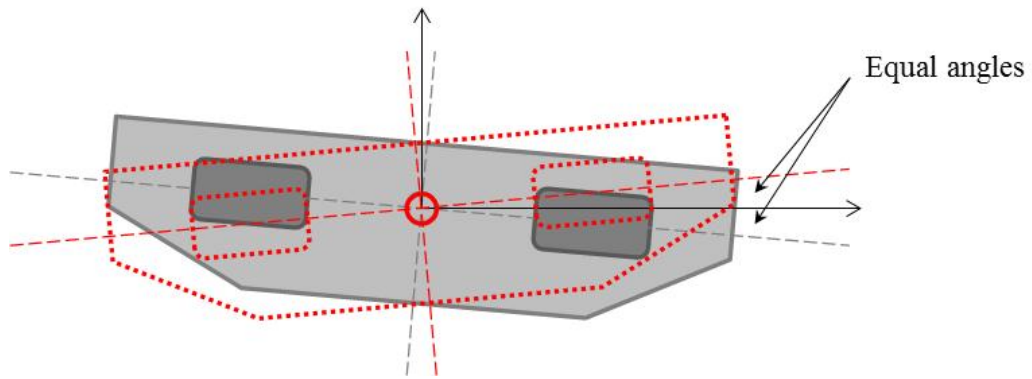


Figure 12. Orientation of the Railcar around the Primary Axis

Lateral deflections were adjusted so that the primary axis was aligned with the global axis.
Axial deflections were adjusted so that the displacement at the fixed end was zero.

Appendix J – Model and Analysis Setup (Volpe FE Model)

Most of the elements in Volpe’s FE model were fully-integrated quadrilateral shell elements. A limited number of reduced-integration quadrilateral shell elements and triangular shell elements were used. Rigid shell elements were used to model the plates used to introduce load into the carbody structure. Beam elements were used to model some superstructure members and to model the brackets where the string pots attached to the car during the tests. A breakdown of the elements used in Volpe’s FE model is provided in Table J1.

Table J1. Breakdown of Element Types in Volpe FE Model

Element Type	Element Description	Number of Elements
B31	Deformable beam	3,254
MASS	Mass	8
R3D4	Rigid shell	720
RNODE3D	Rigid body reference point	47
S3R	Triangular shell	1,944
S4	Quadrilateral shell, full integration	757,384
S4R	Quadrilateral shell, reduced integration	286
Total		763,643

This model simplified the representation of the roof structure. In the actual M1 railcar, the roof panel consists of a series of corrugations. The Volpe FE model modeled the roof as a non-corrugated plate in order to reduce the runtime of the model. It was expected that this simplification in the model would have a minimal effect on the behavior of the car during the 800,000-lb load simulation, as the load path through the occupant volume was generally through the underframe of the car. In the crippling load test, where loads were applied directly to the roof structure, it was expected that modeling the roof as non-corrugated would result in the model predicting a lower roof buckling load than that measured during the test. However, owing to the structural similarities between the M1 passenger car and previously tested Budd Pioneer passenger cars, it was anticipated that the overall crippling strength of the car would only be slightly affected, as the crippling load was expected to be determined by the strength of the underframe for the M1 [6].

Boundary Conditions and Constraints

Loads were introduced into the car through the use of rigid plates at the F-end of the model. Similarly, longitudinal restraint was provided through corresponding rigid plates at the B-end of the model. For the 800,000-lb load simulation, only the load plates at floor-level were used both to introduce loads and to restrain the car. In the crippling load simulation, the floor-level and roof-level load plates on the F-end of the car and B-end of the car were used.

In the 800,000-lb simulation, the model was loaded through its floor-level energy absorbers, similar to the loading in the test. Based on carbody roll, which was measured during the test, asymmetric loading conditions were applied to the model in an attempt to replicate the asymmetric vertical displacements measured during the test. The load plates on the F-end of the model were given a 10-degree angle, relative to the vertical. Additionally, the plates on the left side of the car were given a vertical upward displacement of 0.5” and the plates on the right side of the car were given a vertical upward displacement of 0.2”. These boundary conditions are summarized in Table J2.

Table J2. Loading Conditions for Volpe’s 800,000 pound FE Model

	Vertical Displacement (inches)	Longitudinal Displacement (inches)	Angle
F-End Left	0.5	-1.19	10 degrees
F-End Right	0.2	-1.19	10 degrees
B-End Left	0.5	0	0
B-End Right	0.2	0	0

No additional boundary conditions or constraints were placed on the car during the 800,000-lb simulation.

In the crippling simulation, the model was loaded through both its floor-level and roof-level energy absorbers. Because loading the car at both the roof and floor tends to result in moments that partially cancel each other out, significant bending of the underframe was not expected during this test. The load plates in the crippling FE model were only given prescribed longitudinal displacements. The longitudinal displacements on the load plates in Volpe’s crippling FE model are shown in Table J3.

Table J3. Loading Conditions for Volpe’s Crippling FE Model

	Longitudinal Displacement (inches)
F-End Left Floor	2.5
F-End Right Floor	2.5
F-End Left Roof	2.5
F-End Right Roof	2.5
B-End Left Floor	0
B-End Right Floor	0
B-End Left Roof	0
B-End Right Roof	0

Each load plate was given a prescribed displacement vs. time relationship. A nonlinear displacement-time behavior was defined, so that the load plates moved slowly at the beginning of the simulation and increased with time. The normalized displacement behavior was defined as the square of the normalized time at each 10 percent increment of normalized time. The square relationship was chosen over a simple linear relationship, which reduced the kinetic energy introduced into the model at the beginning of the simulation. By gradually introducing the initial loads, the model stabilized more quickly. As the model began to deform and develop strain energy, the speed of the load plates could be increased without introducing dynamic effects into the model. The prescribed displacement-time relationship is shown in Figure J1.

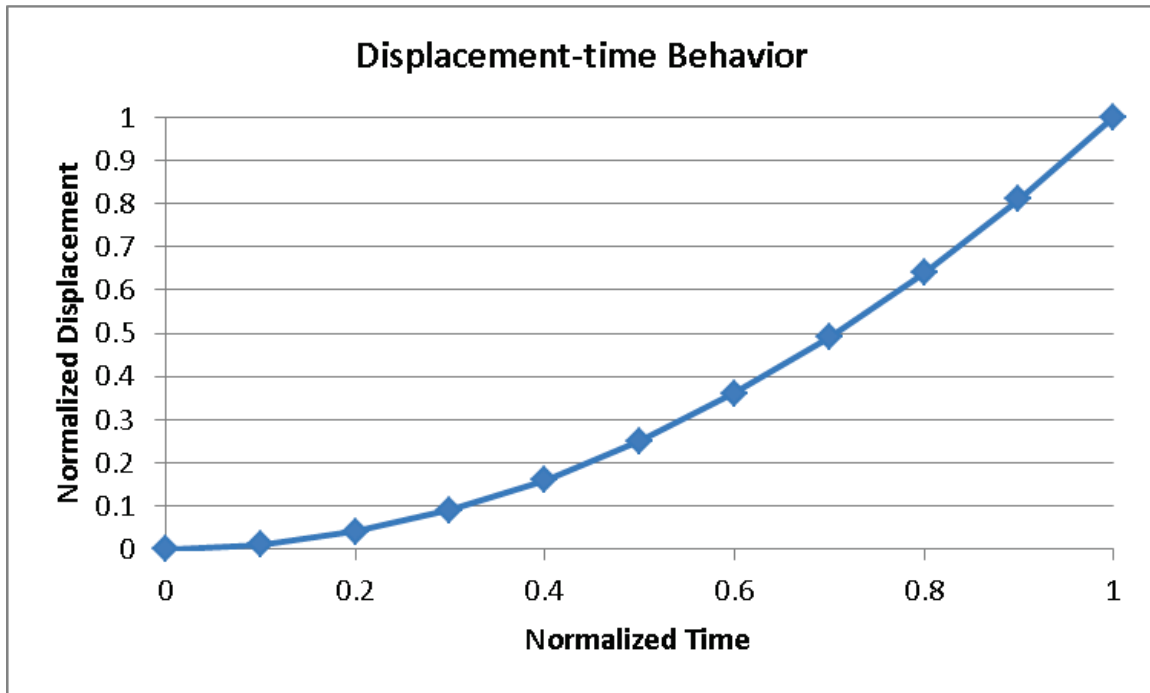


Figure J1. Prescribed Displacement-time Behavior in Volpe 800-kip FE Model

Because the displacement-time behavior was defined as an input to the model, the forces applied at each loading or reaction location were calculated by the Abaqus/Explicit solver. One consequence of using a nonlinear displacement-time behavior to apply the load to the car is seen in the force-time history shown in Figure J2. The Abaqus/Explicit solver performs a linear interpolation between points of defined displacement. Since the displacement-time history is defined using a square relationship, each defined point corresponds to a change in slope between the previous segment and the next segment. This results in a jump in the force at each 10 percent increment of normalized time, corresponding to the point at which the slope of the displacement-time relationship changed. The force quickly drops following each spike, indicating this artifact of the model is not having a global effect on the response to the applied force.

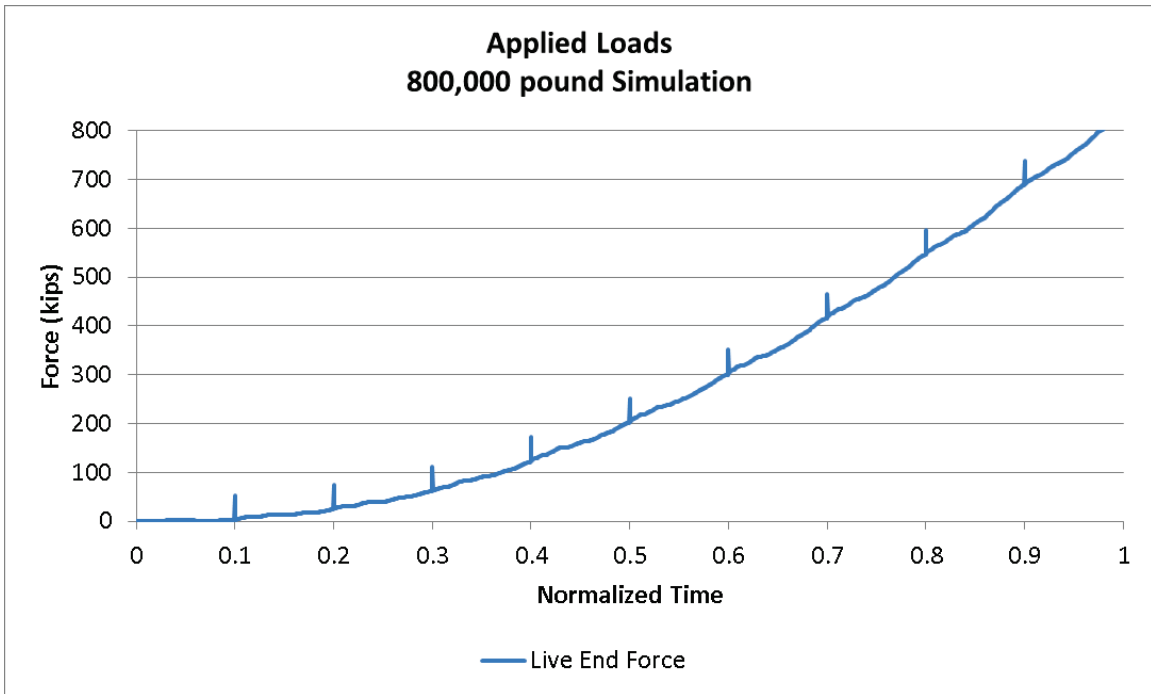


Figure J2. Applied Loads versus Normalized Time, Volpe 800-kip Simulation

In the crippling model, a smoothing technique was applied to the amplitude curve, which eliminated the spikes from those data. The applied load from the crippling simulation is plotted against normalized time in Figure J3.

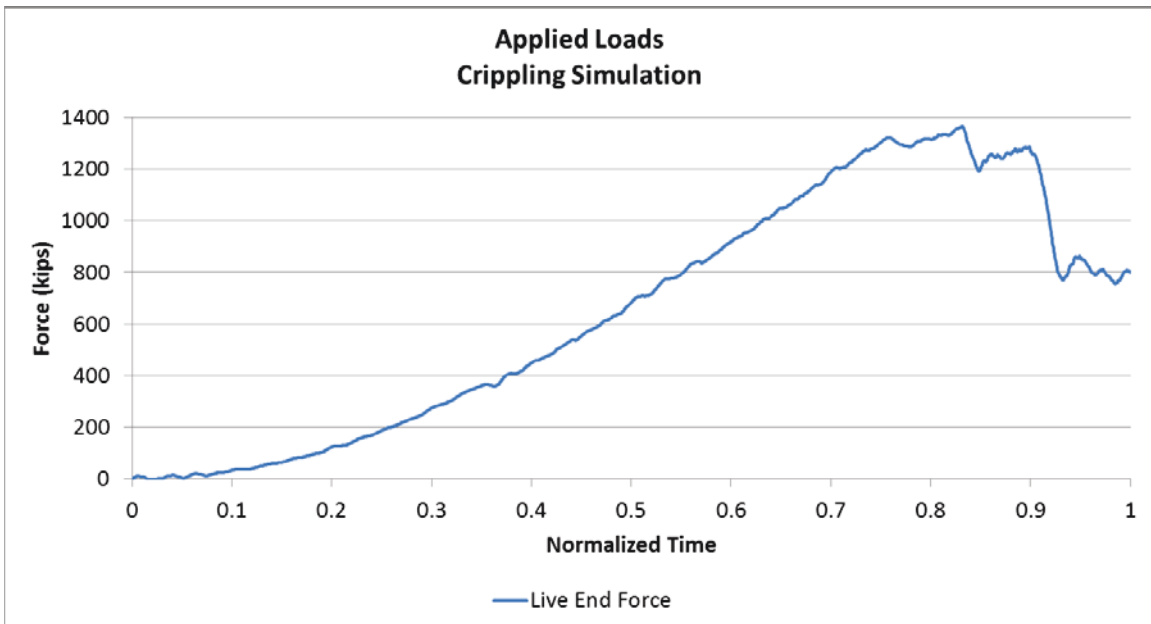


Figure J3. Applied Loads versus Normalized Time, Volpe Crippling Simulation

Appendix K – Material Formulations (Volpe FE Model)

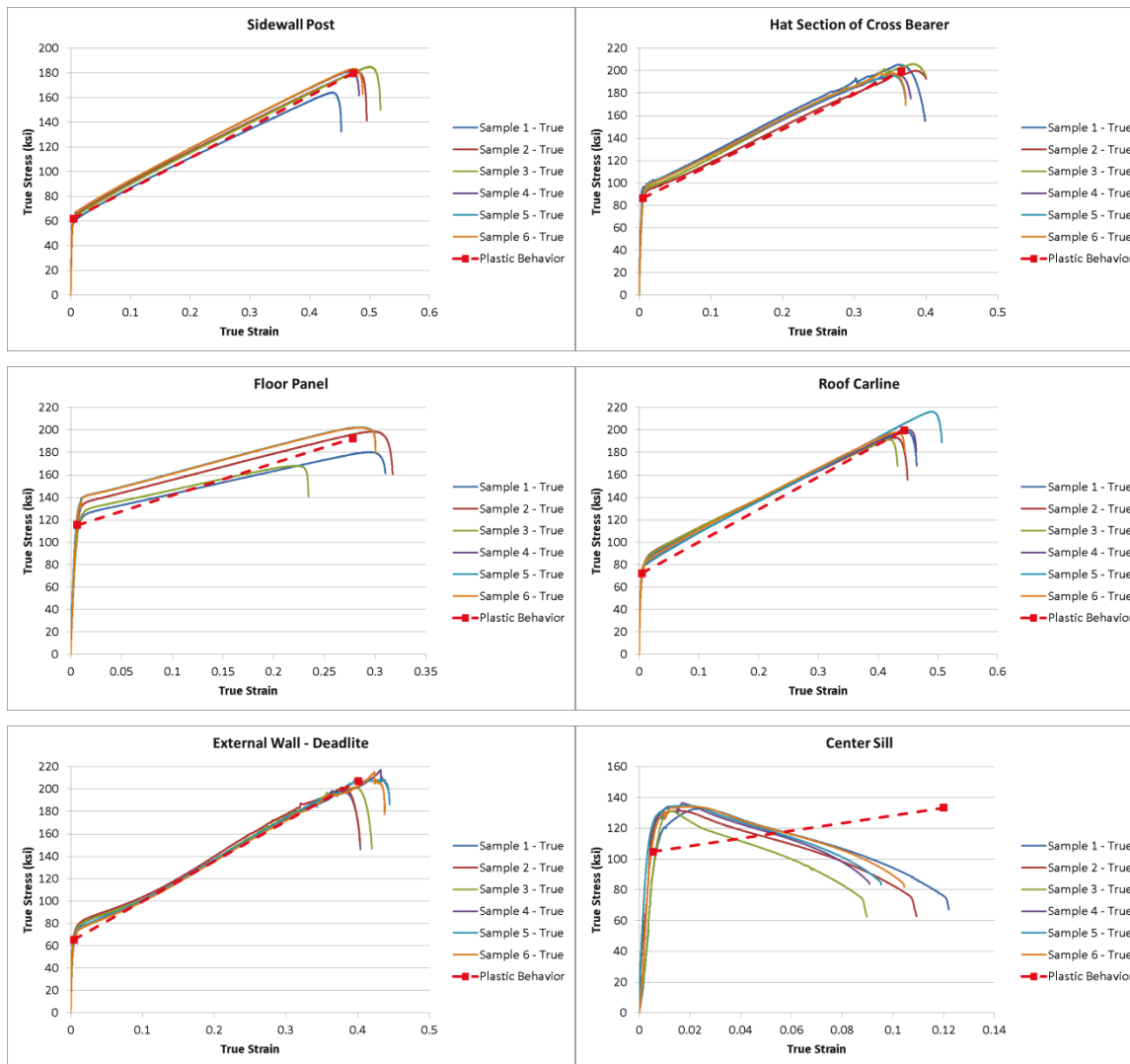
Within the Abaqus/Explicit software, metal plasticity is defined as a function of true plastic strain and true stress. The results of the tensile testing of materials from a companion M1 car were reported as engineering stress and engineering strain. Equations K1 and K2 were used to convert the engineering stress-strain data into the format required for input to Abaqus.

Equations K1 & K2. True Stress and True Plastic Strain

$$\sigma_{\text{true}} = \sigma_{\text{nom}}(1 + \epsilon_{\text{nom}})$$

$$\epsilon_{\text{ln}}^{\text{pl}} = \ln(1 + \epsilon_{\text{nom}}) - \frac{\sigma_{\text{true}}}{E}$$

Bi-linear elastic-plastic behavior was entered into the FE model, based upon the average yield strength, ultimate strength, and strain at failure for each type of material. The plastic behavior of each material type is shown in Figure K1 as a dashed line, plotted alongside the coupon test data.



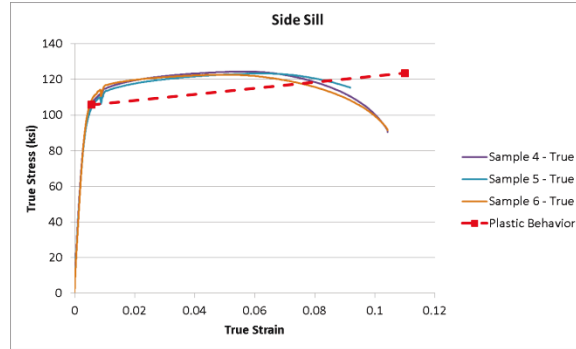


Figure K1. Material Coupon Data and Plastic Behavior Input to Volpe FE Model

The center sill and side sill materials were treated differently from the other materials based on the results of the tensile tests. These two materials experienced failure at a much lower strain than any other materials. Additionally, the ultimate strengths of these two materials did not correspond to the maximum elongation. For these two materials, the yield point was obtained conventionally, through a 0.2-percent offset. The second point used to define the bi-linear behavior is located at the average maximum true strain and the average maximum true stress.

In addition to the materials that were tested, other materials were defined in the FE model. Figure K3, the plastic behaviors assigned to these materials.

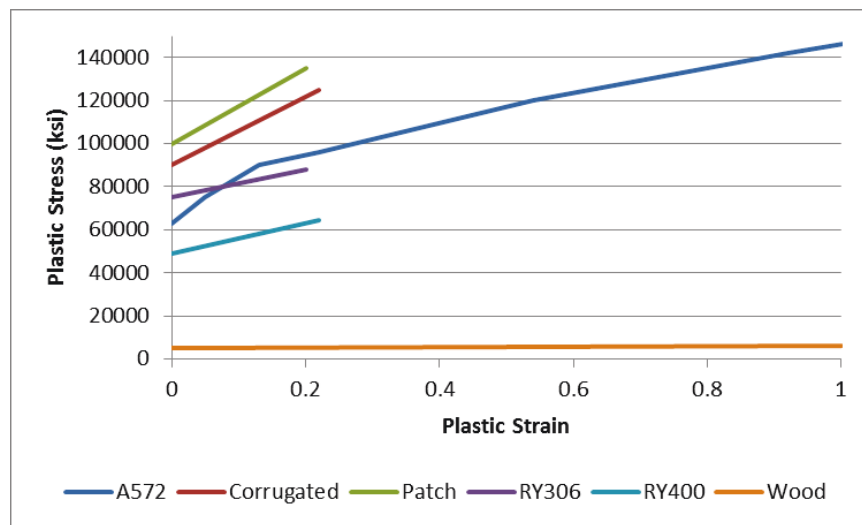
















Figure K3. Additional Materials in Volpe FE Model

The following figures show the distribution of materials throughout the FE model.

<input checked="" type="checkbox"/>	A572-50	
<input checked="" type="checkbox"/>	CENTER-SILL-TEST	
<input checked="" type="checkbox"/>	CORRUGATED	
<input checked="" type="checkbox"/>	DEADLITE-TEST	
<input checked="" type="checkbox"/>	ELASTIC-STEEL	
<input checked="" type="checkbox"/>	FLOOR-PANEL-TEST	
<input checked="" type="checkbox"/>	HAT-SECTION-CROSS-BEARER-TEST	
<input checked="" type="checkbox"/>	PATCH	
<input checked="" type="checkbox"/>	ROOF-CARLINE-TEST	
<input checked="" type="checkbox"/>	RY306	
<input checked="" type="checkbox"/>	RY400	
<input checked="" type="checkbox"/>	SIDE-SILL-TEST	
<input checked="" type="checkbox"/>	SIDEWALL-POST-TEST	
<input checked="" type="checkbox"/>	WOOD	

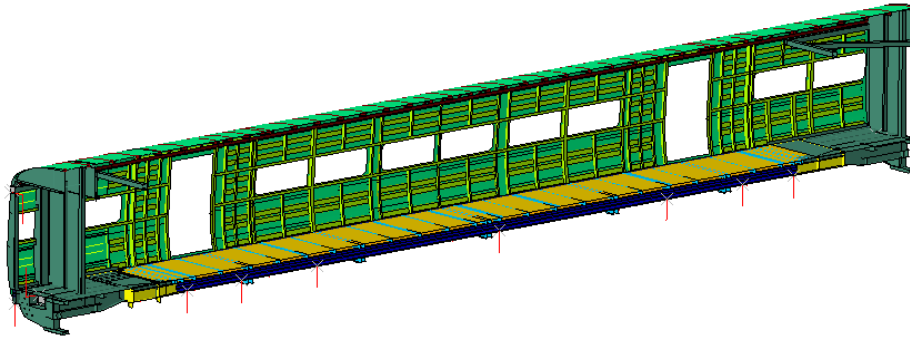


Figure K4. Overall Distribution of Materials in Volpe FE Model

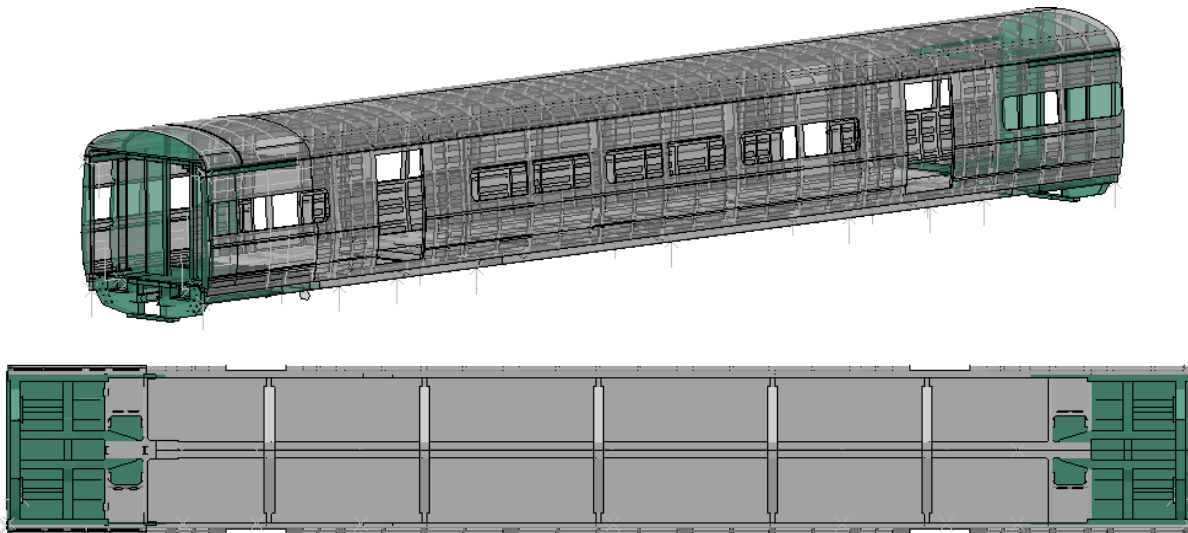


Figure K5. Distribution of A572-50 Material

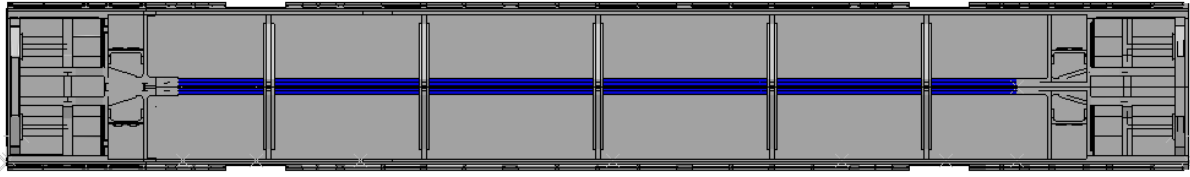


Figure K6. Distribution of *Center Sill* Material

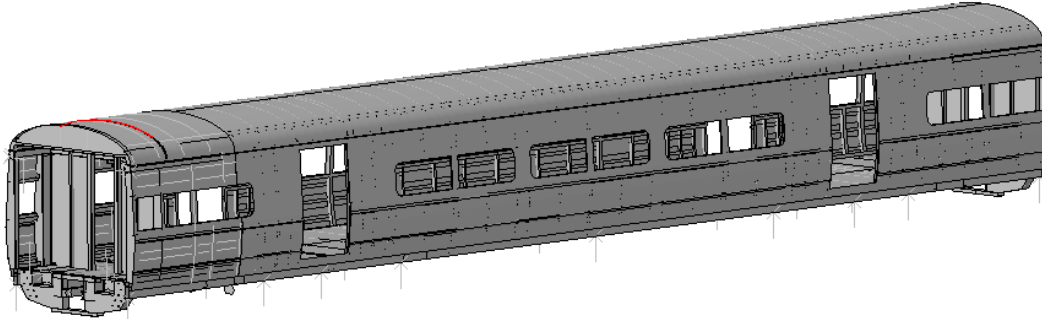


Figure K7. Distribution of *Corrugated* Material

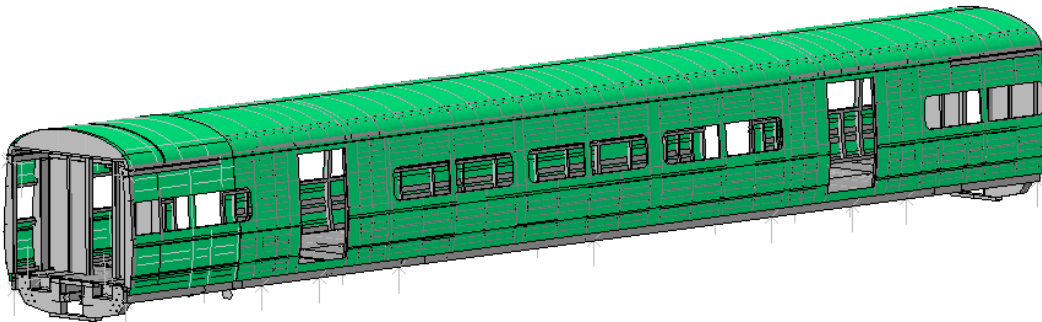


Figure K8. Distribution of *External Wall Deadlite* Material

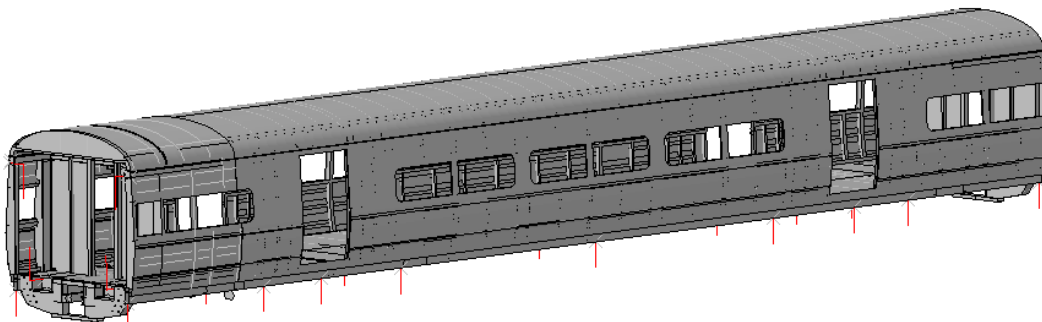


Figure K9. Distribution of *Elastic* Material

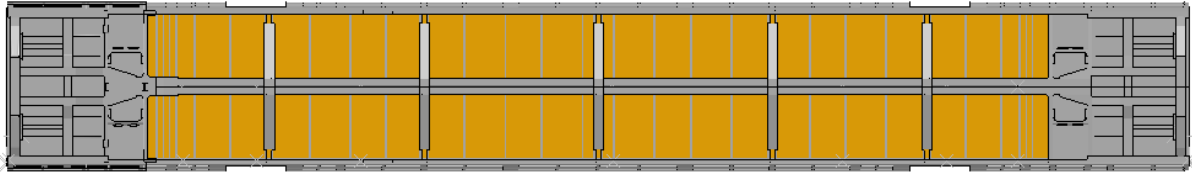


Figure K10. Distribution of *Floor Panel* Material

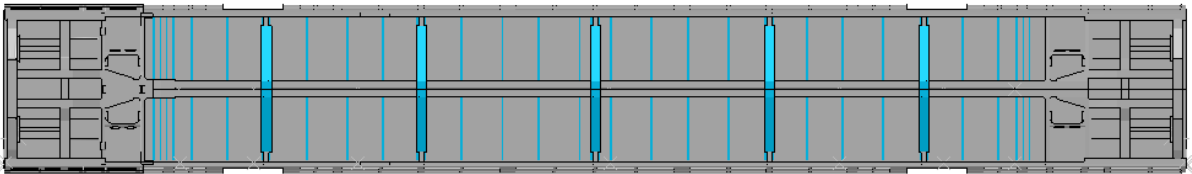


Figure K11. Distribution of *Hat Section of Cross Bearer* Material

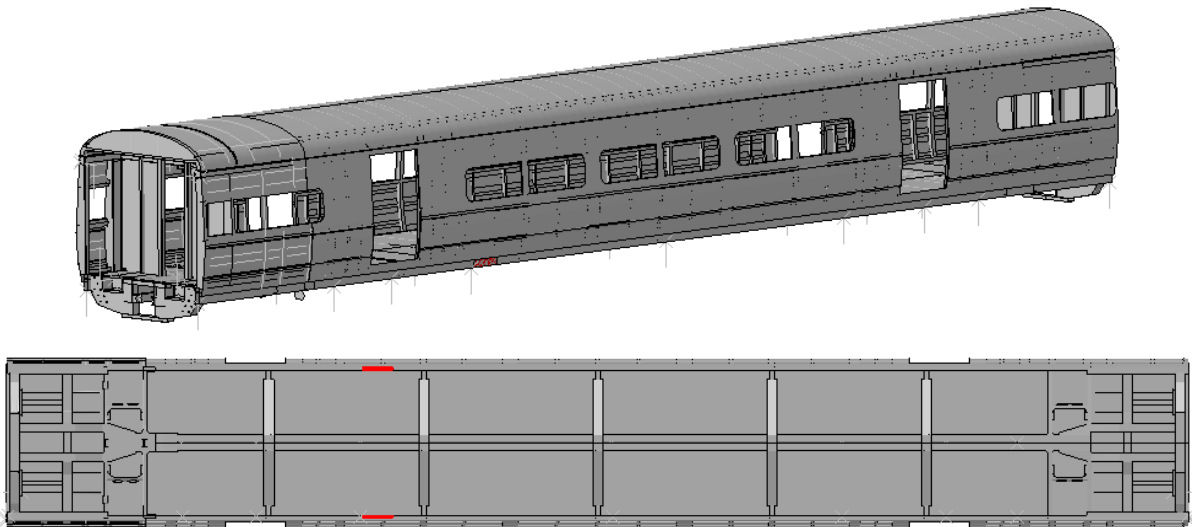


Figure K12. Distribution of *Patch* Material

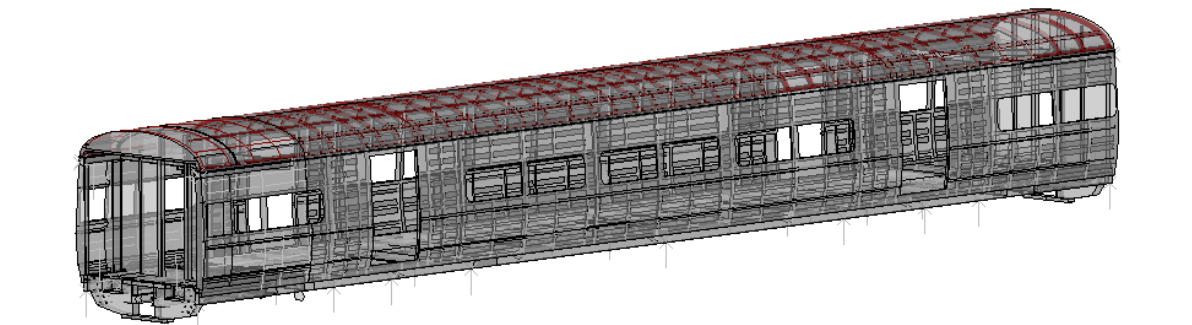


Figure K13. Distribution of *Roof Carline* Material

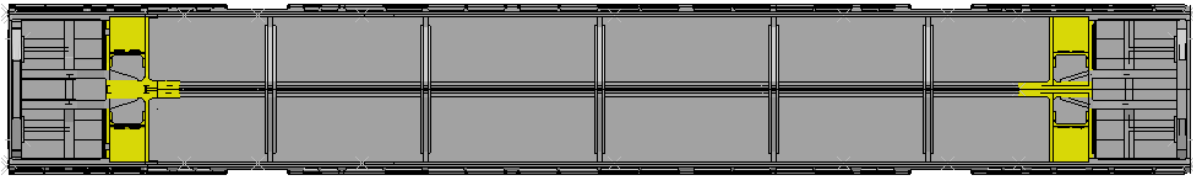


Figure K14. Distribution of *RY306* Material

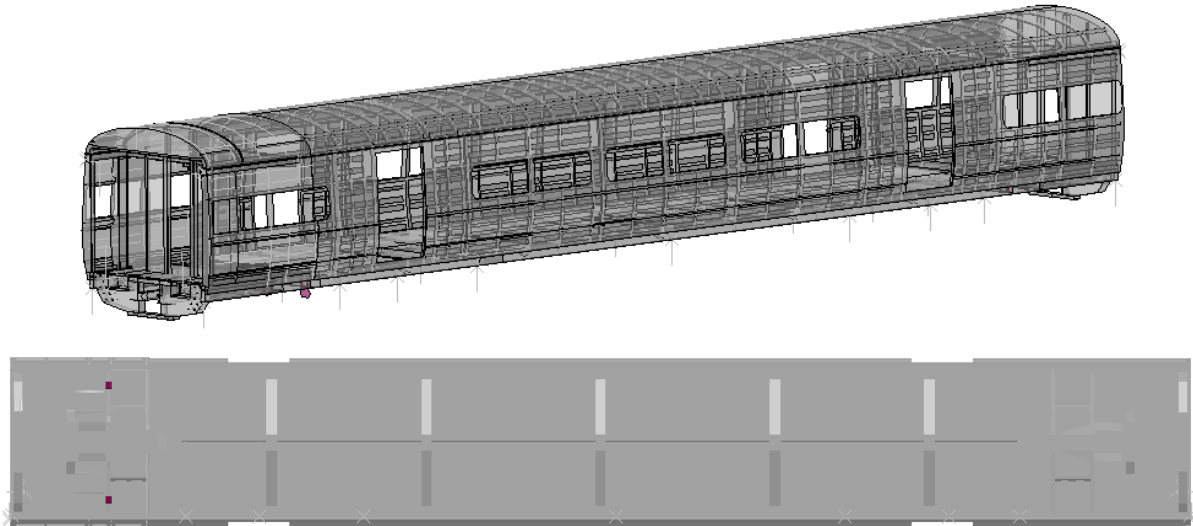


Figure K15. Distribution of *RY400* Material

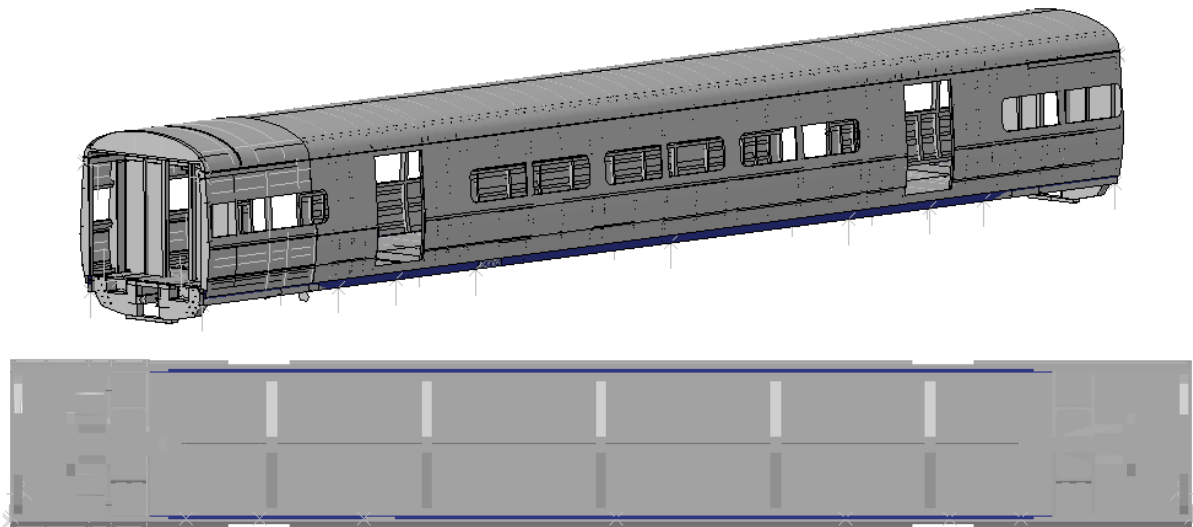


Figure K16. Distribution of *Side-Sill-Test* Material

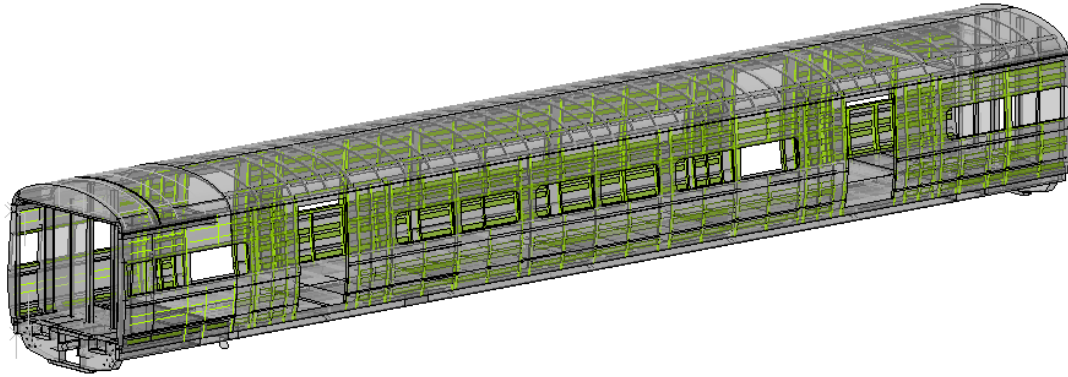


Figure K17. Distribution of *Sidewall Post* Material

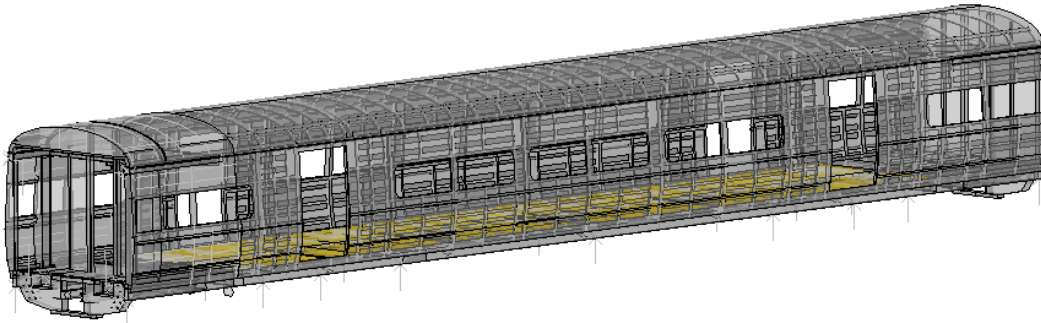
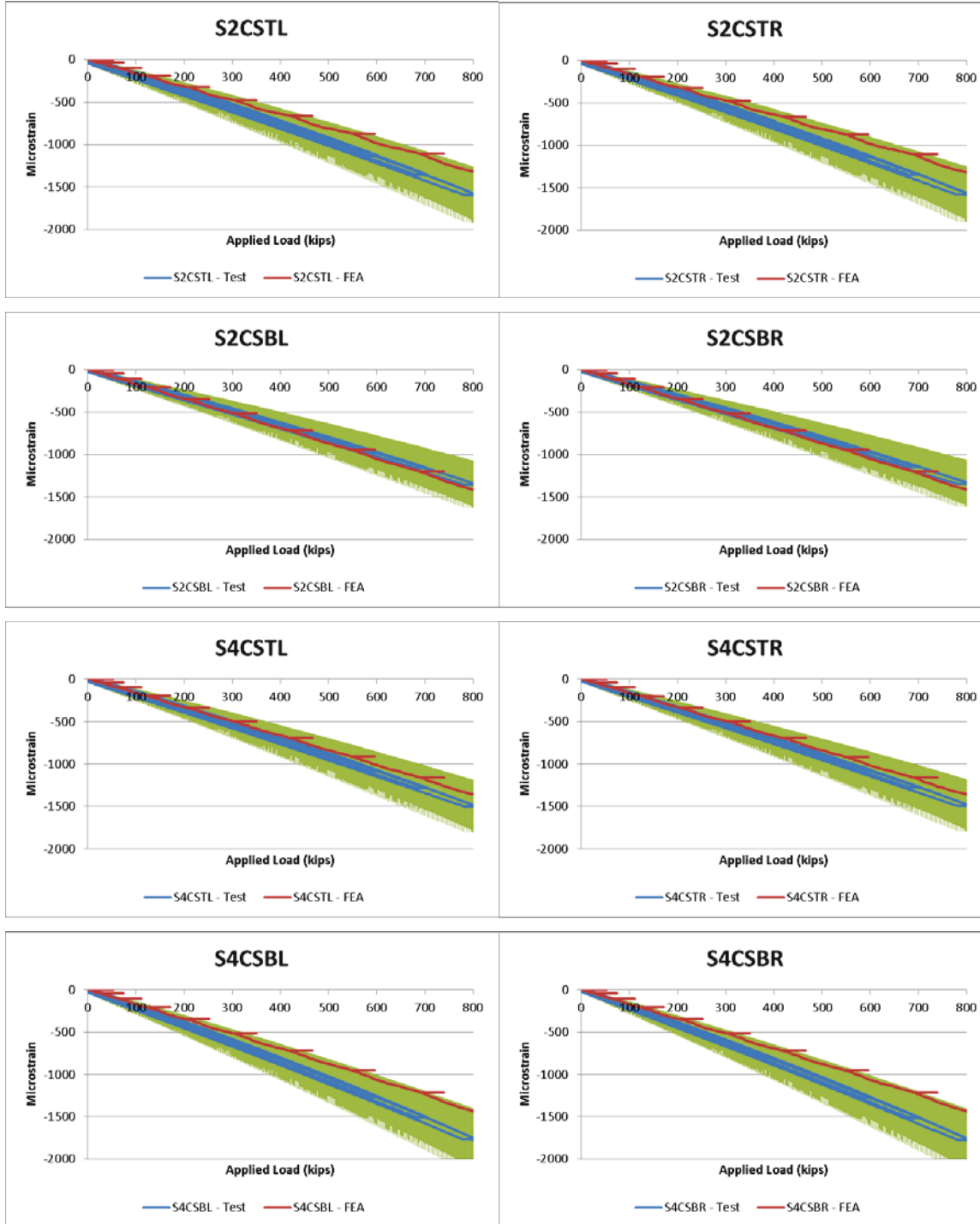


Figure K18. Distribution of *Wood* Material

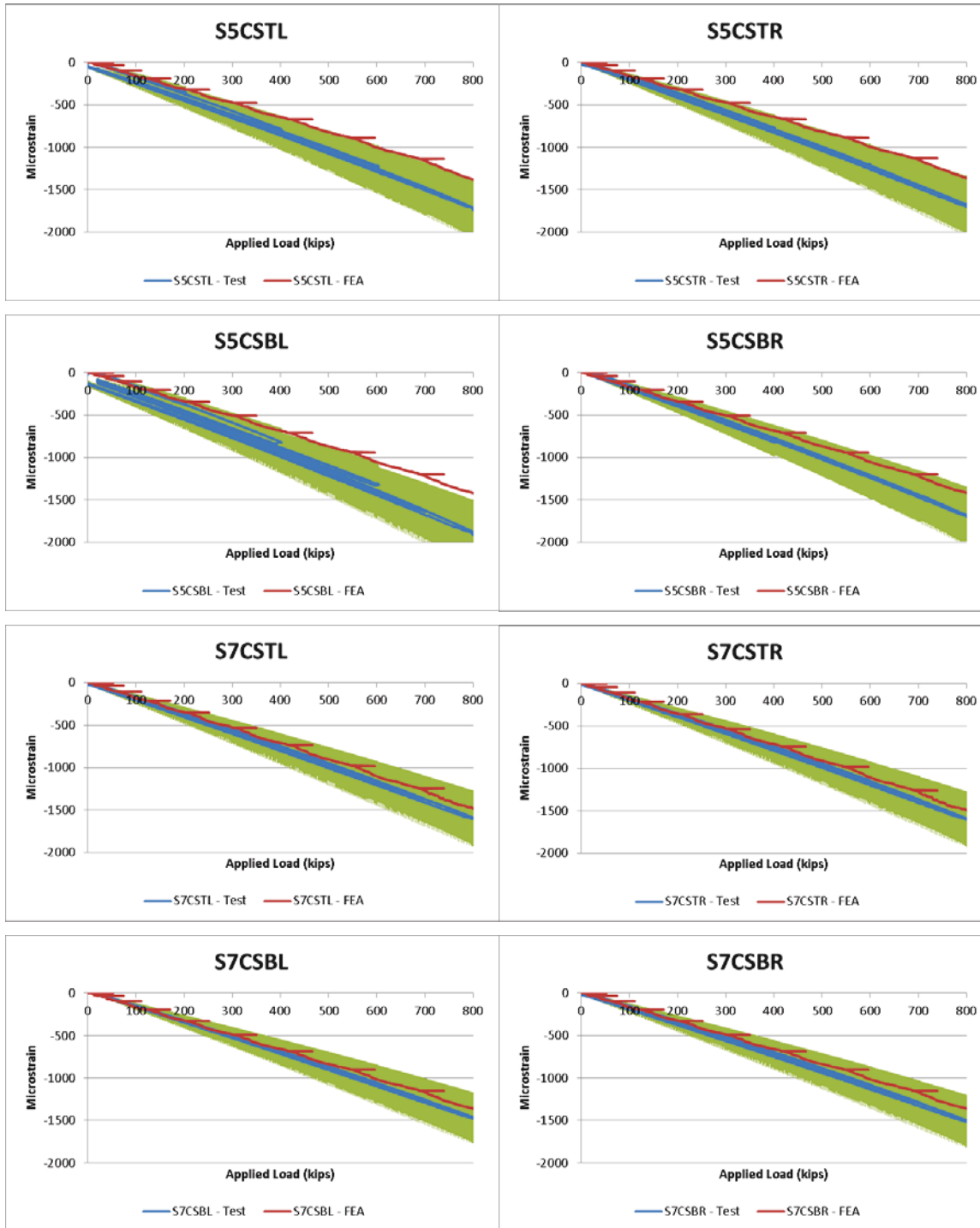
Appendix L – 800,000-pound Load Analysis and Test Results (Volpe FE Model)

Strain Results

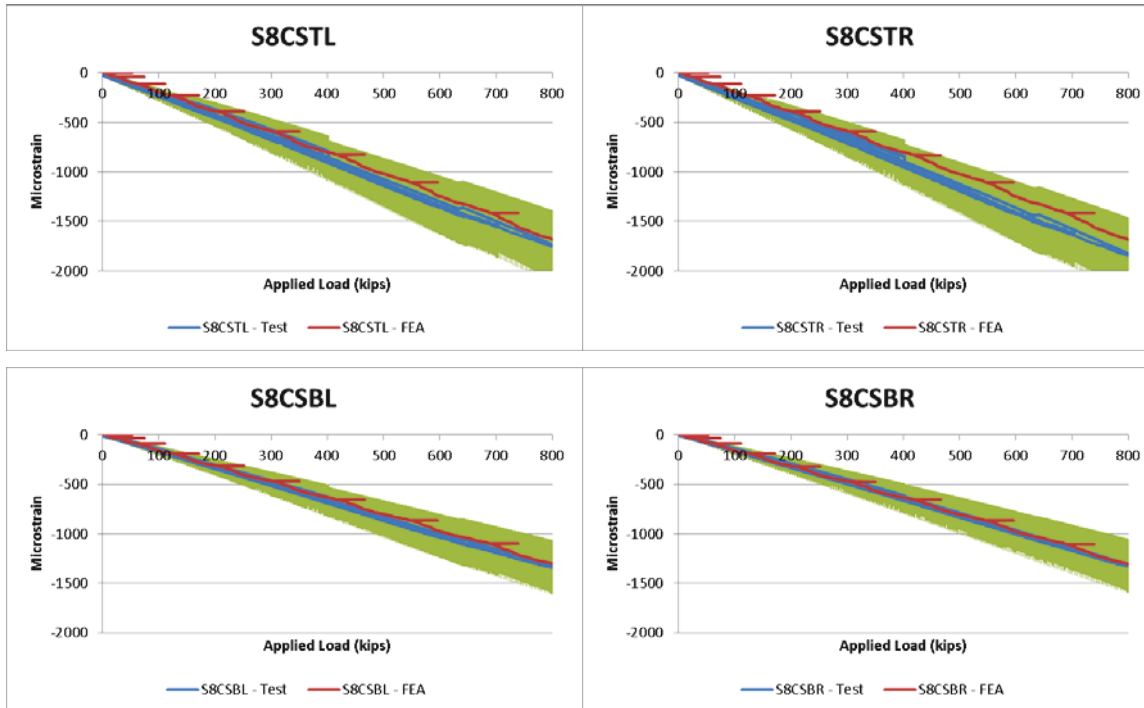
Center Sill



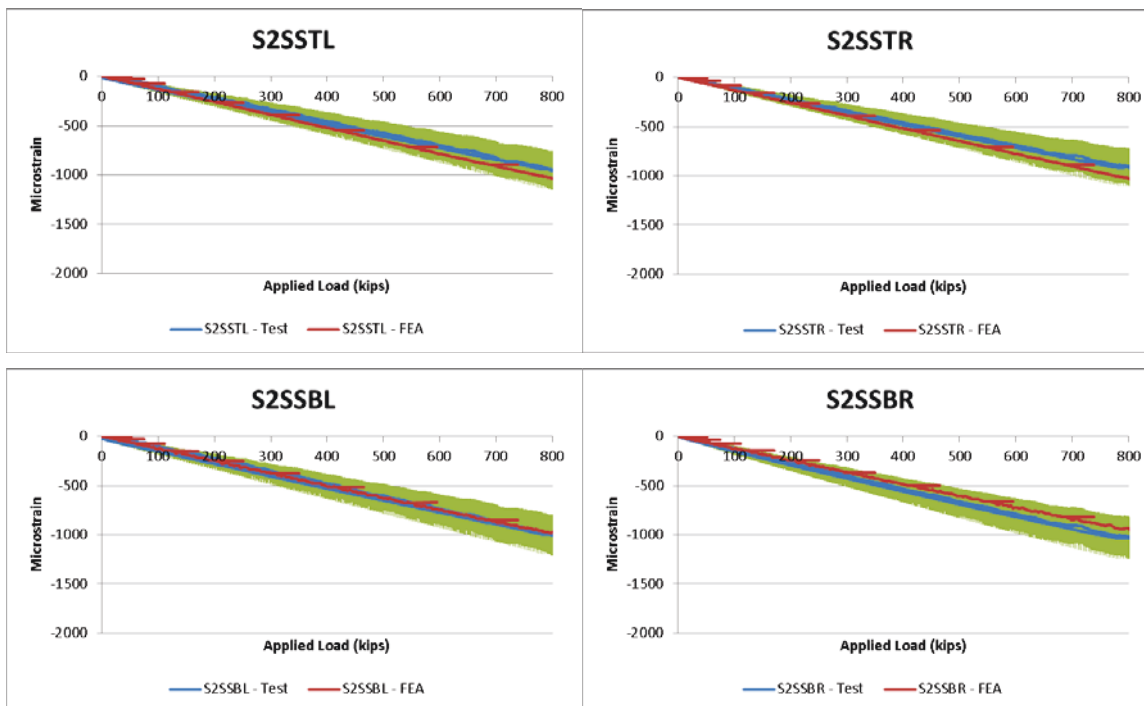
Center Sill (continued)



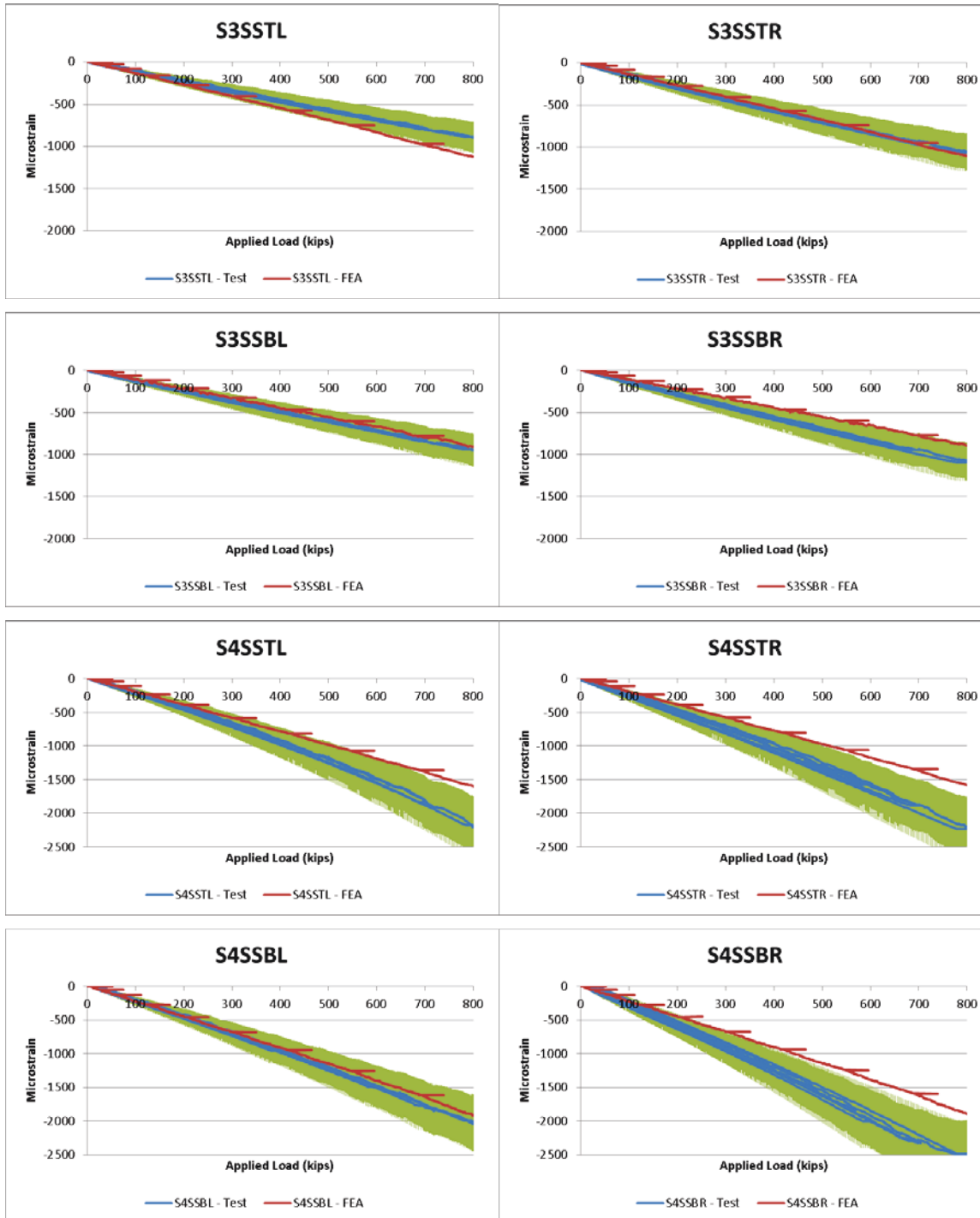
Center Sill (continued)



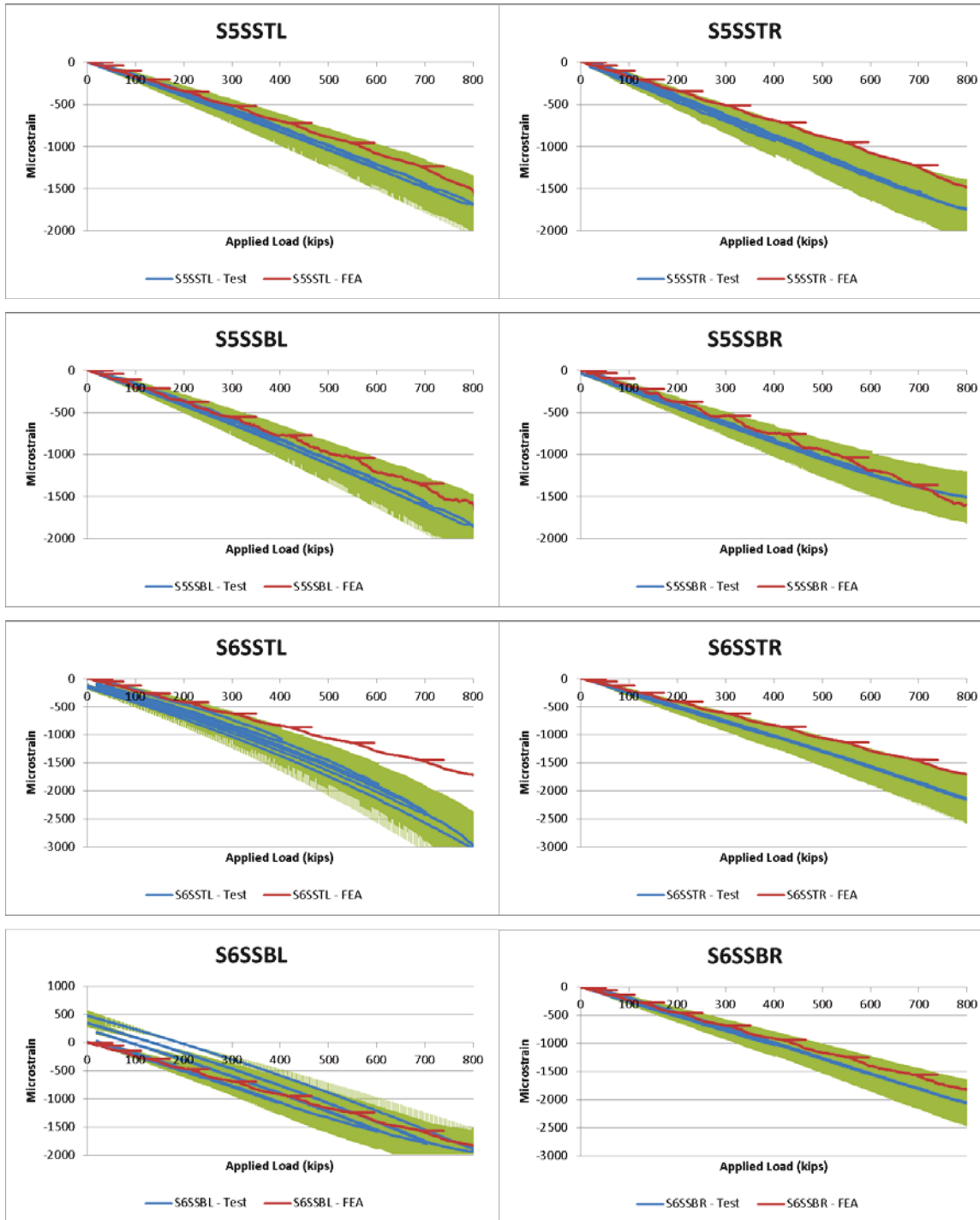
Side Sills



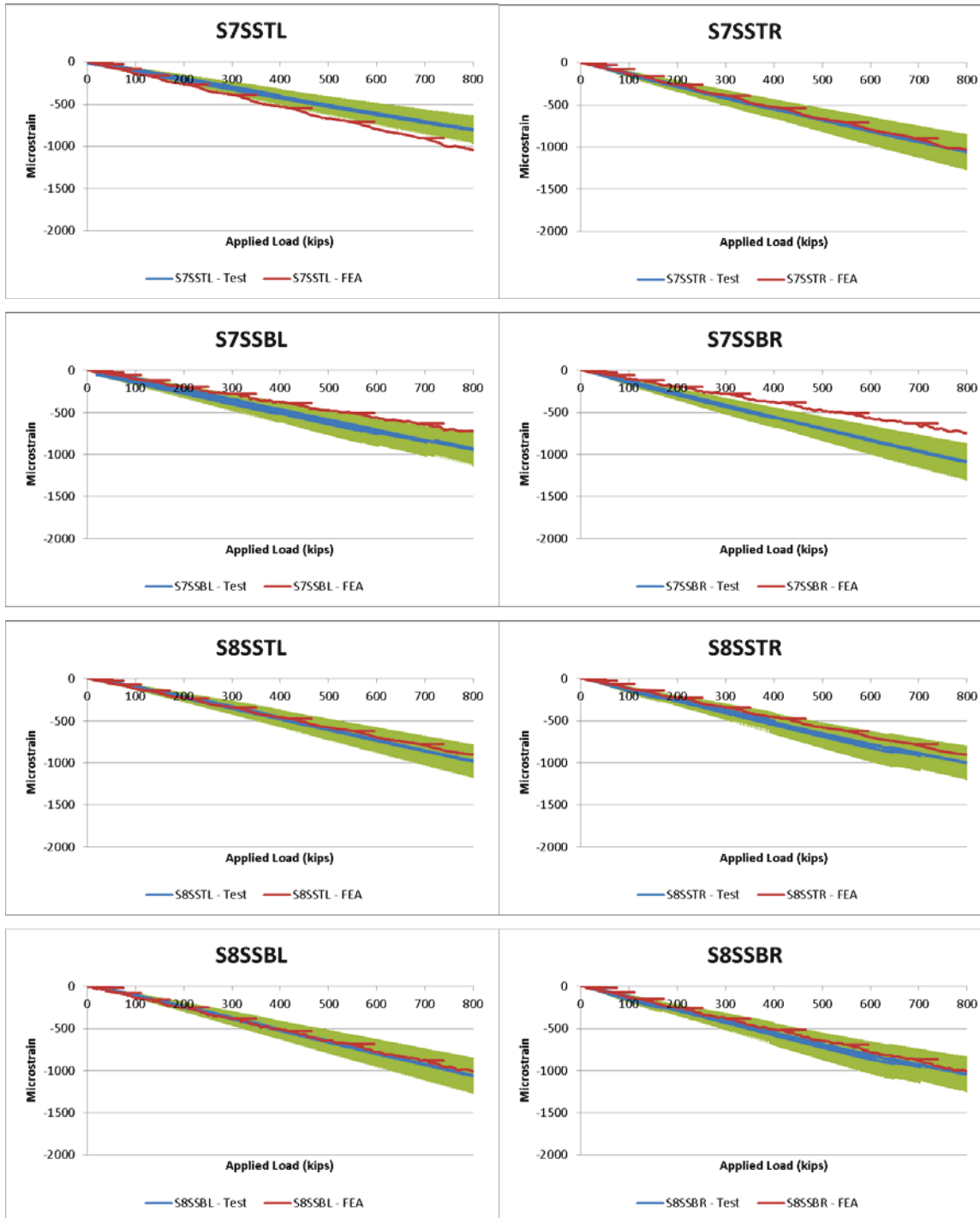
Side Sills (continued)



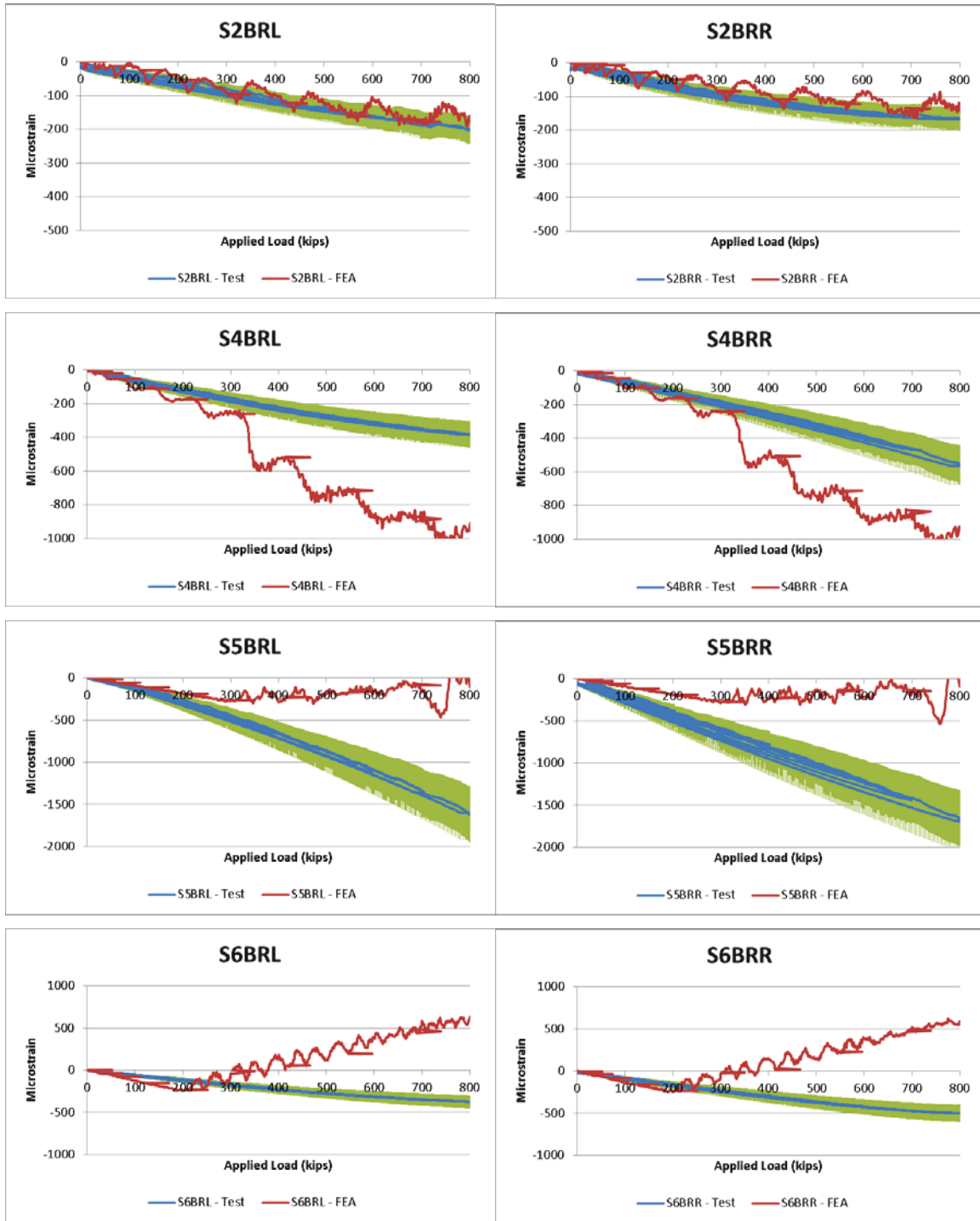
Side Sills (continued)



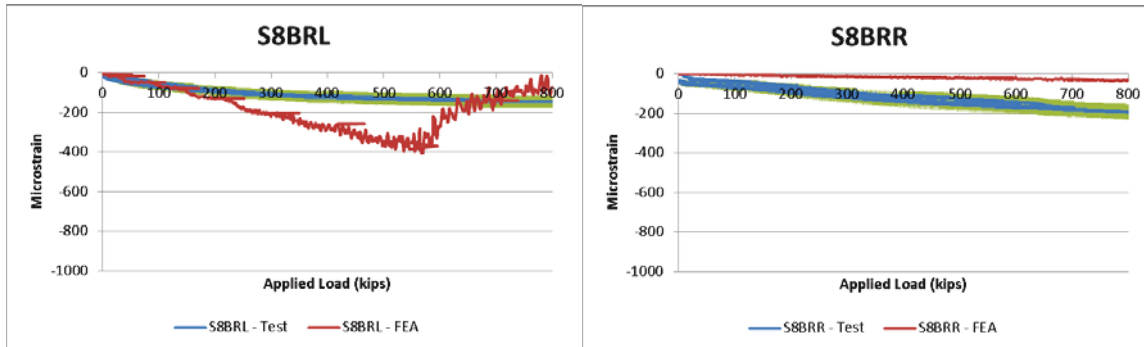
Side Sills (continued)



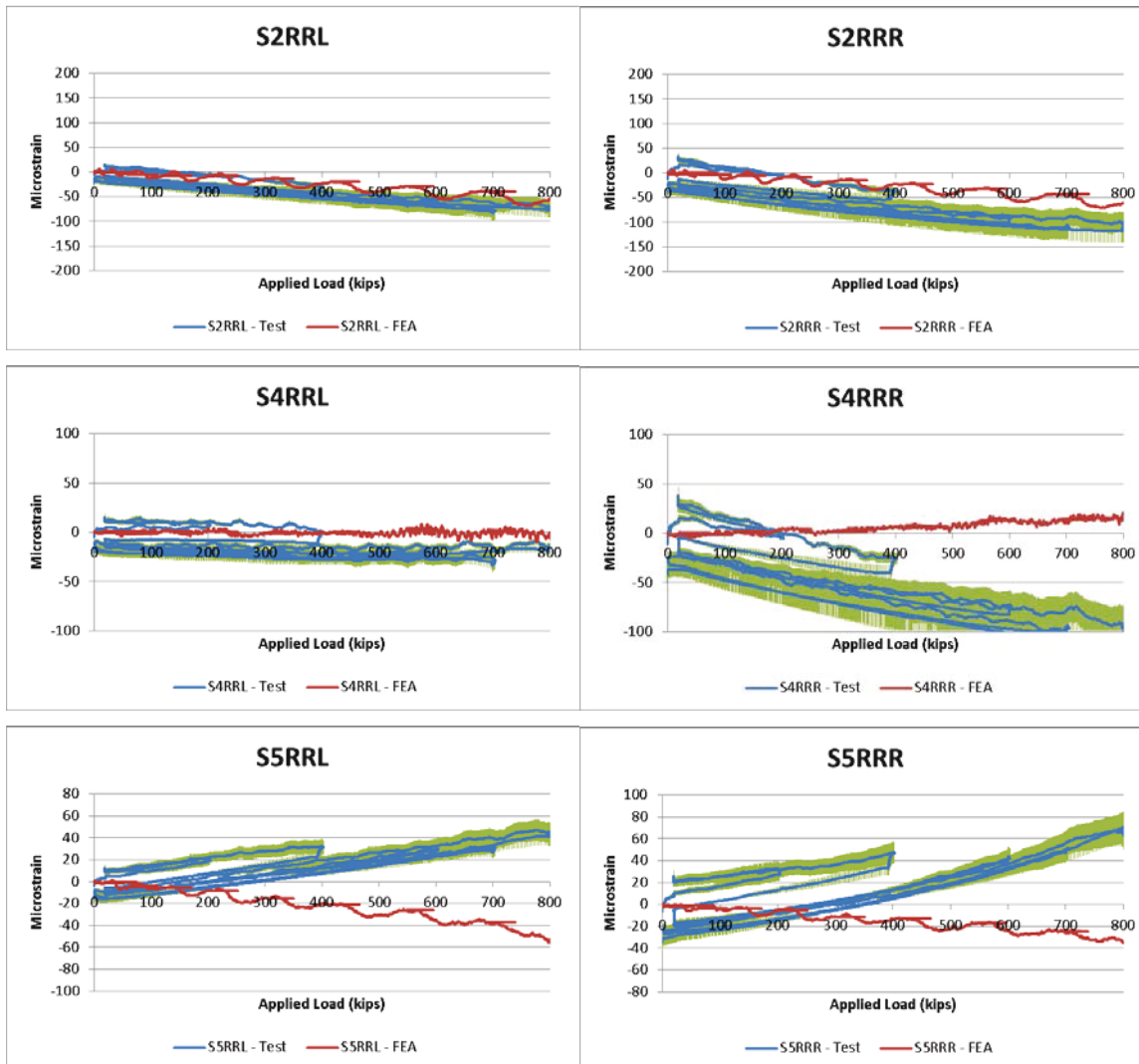
Belt Rails



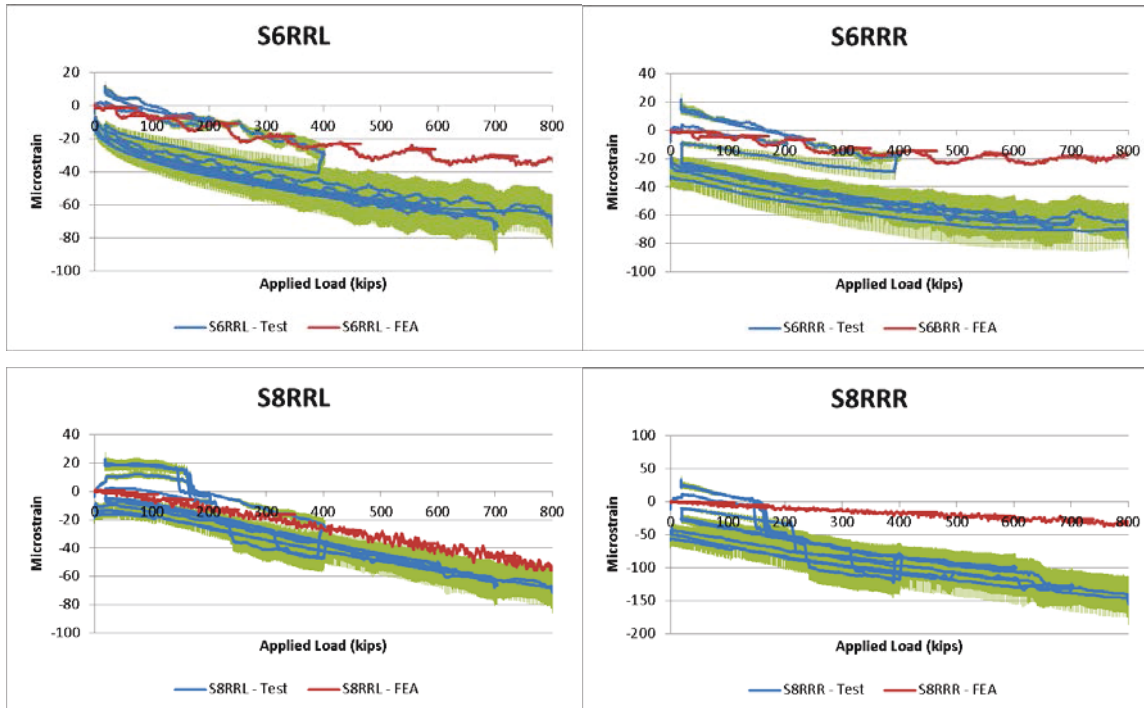
Belt Rails (continued)



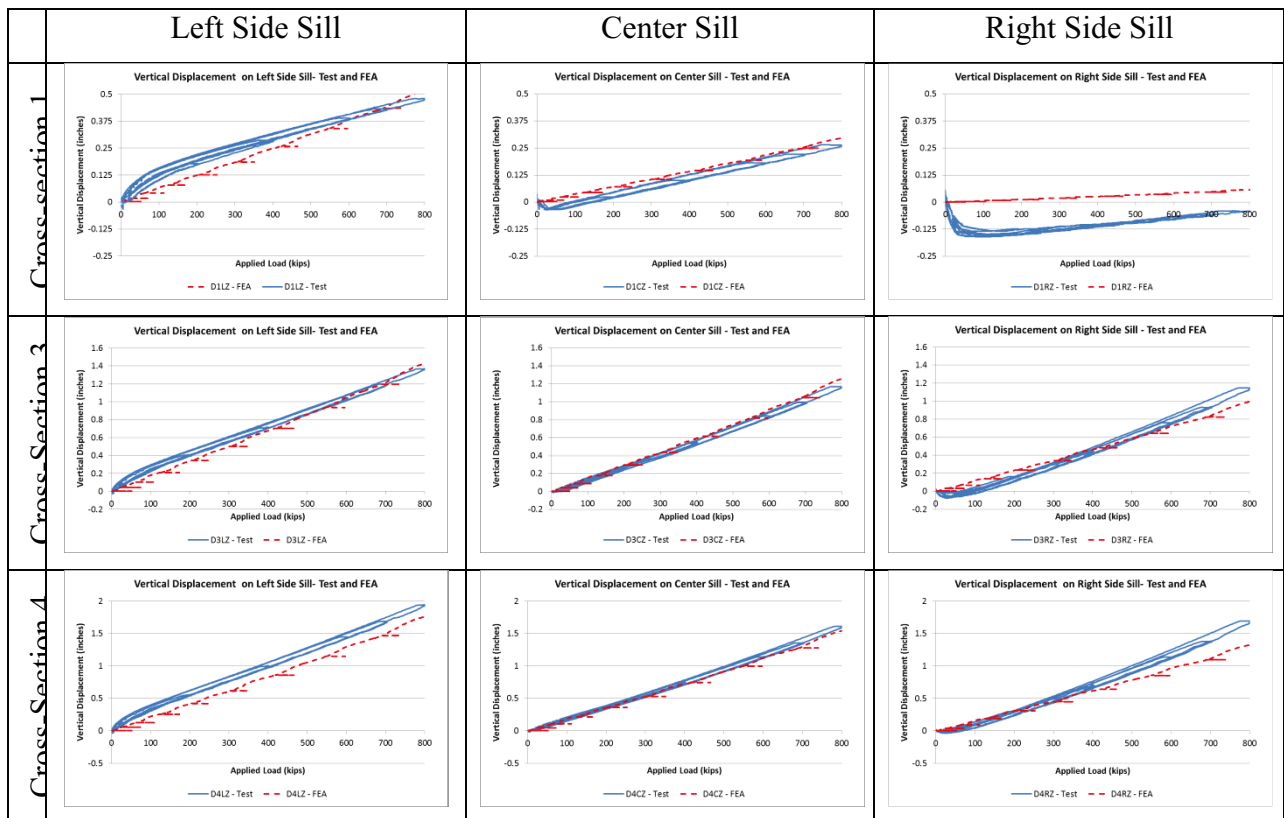
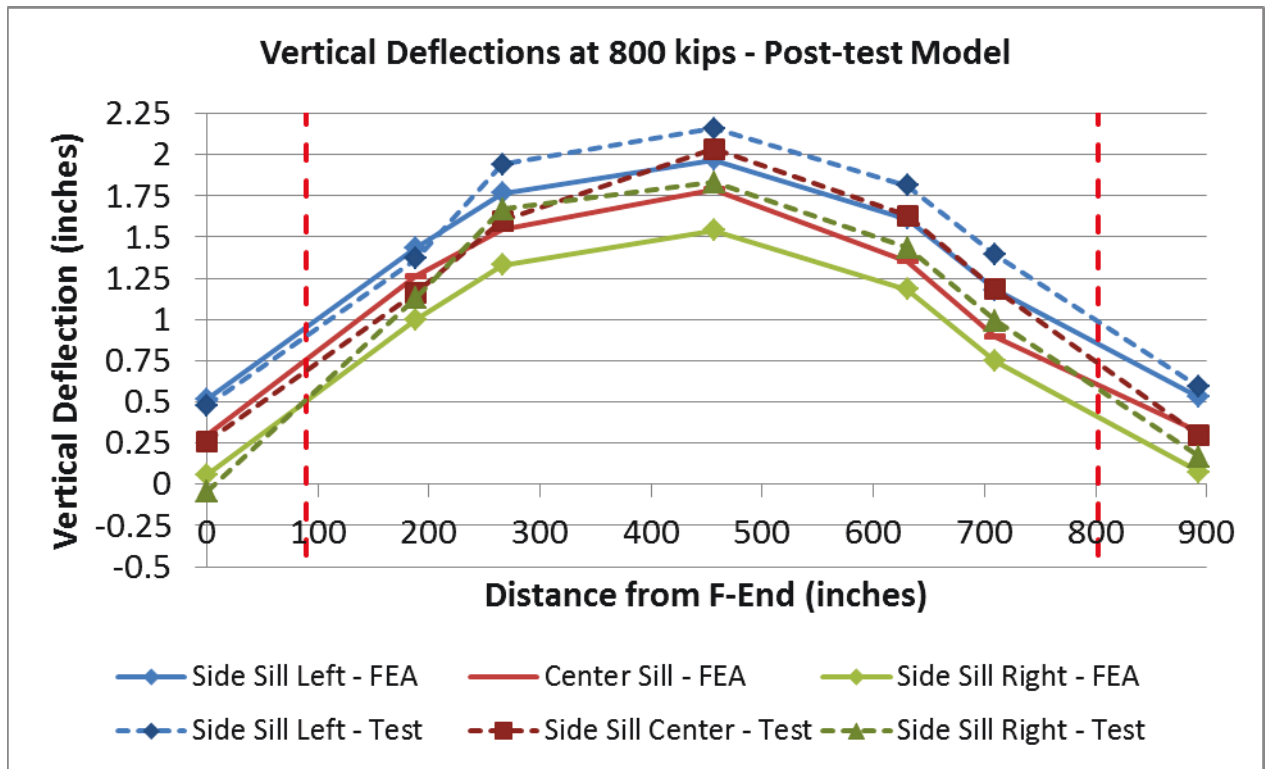
Roof Rails

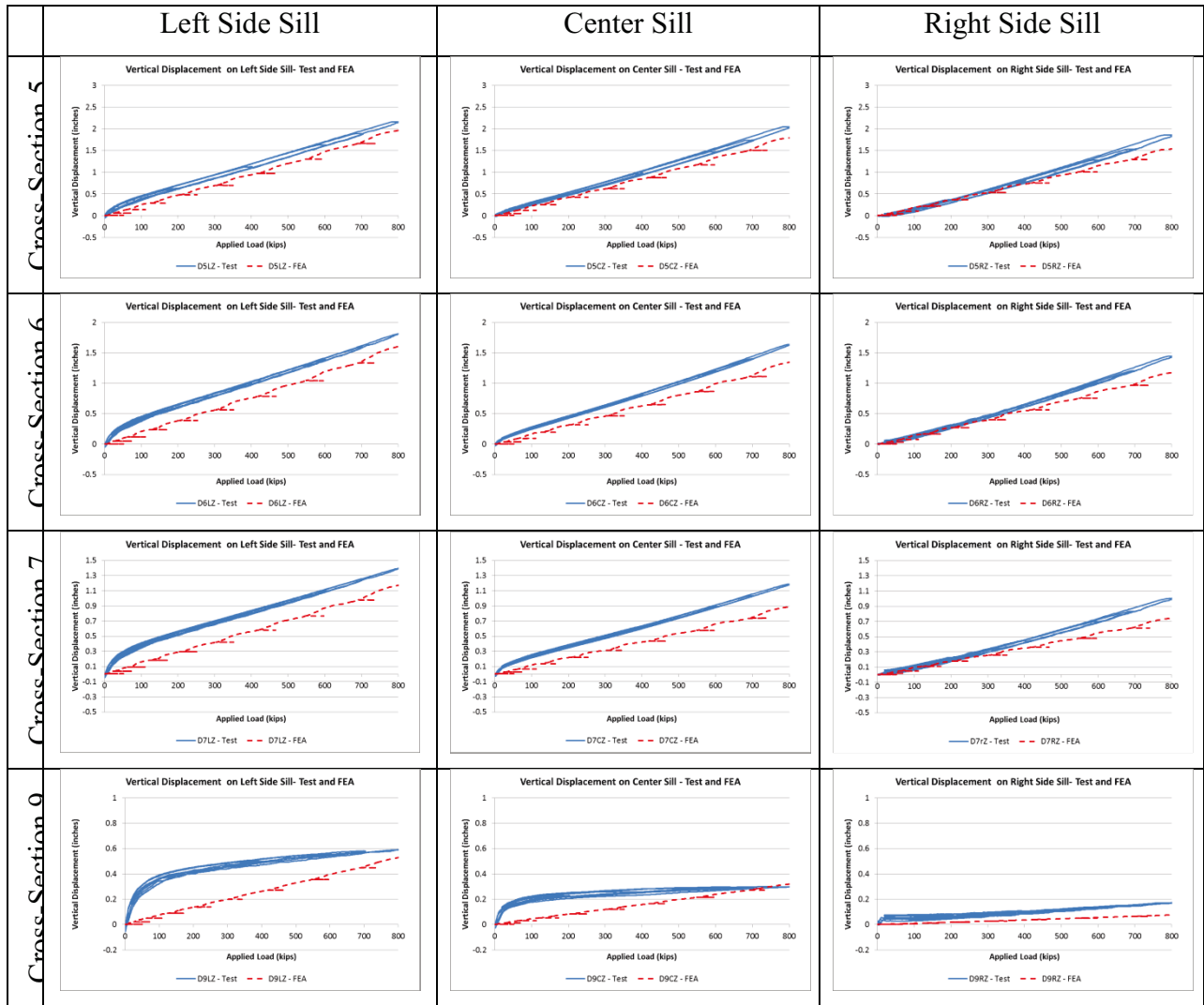


Roof Rails (continued)



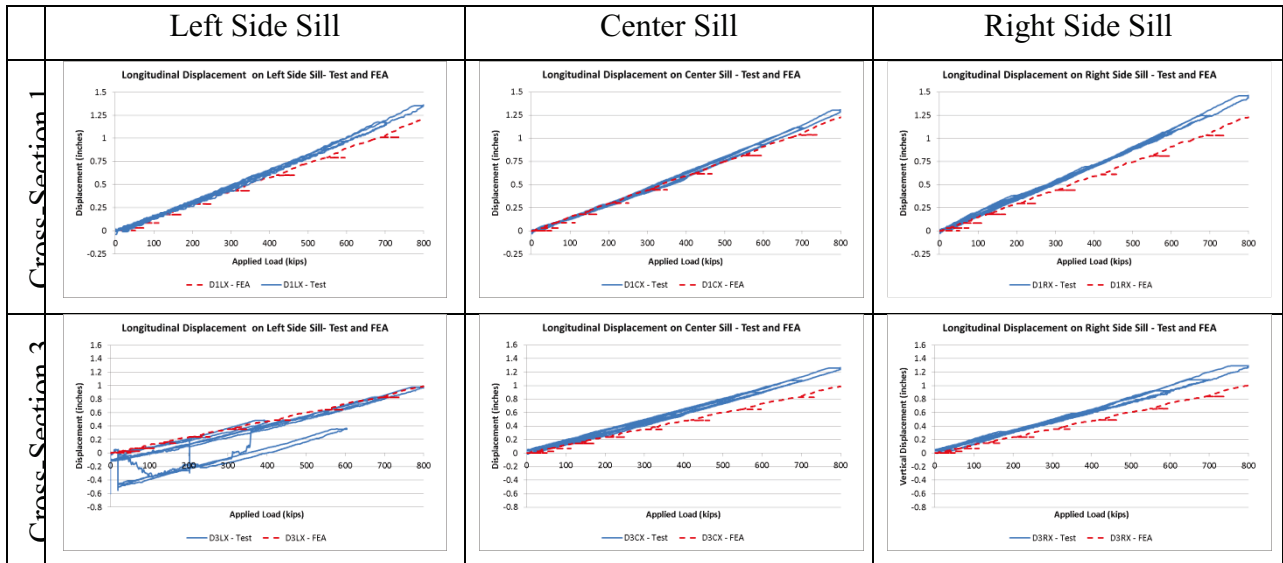
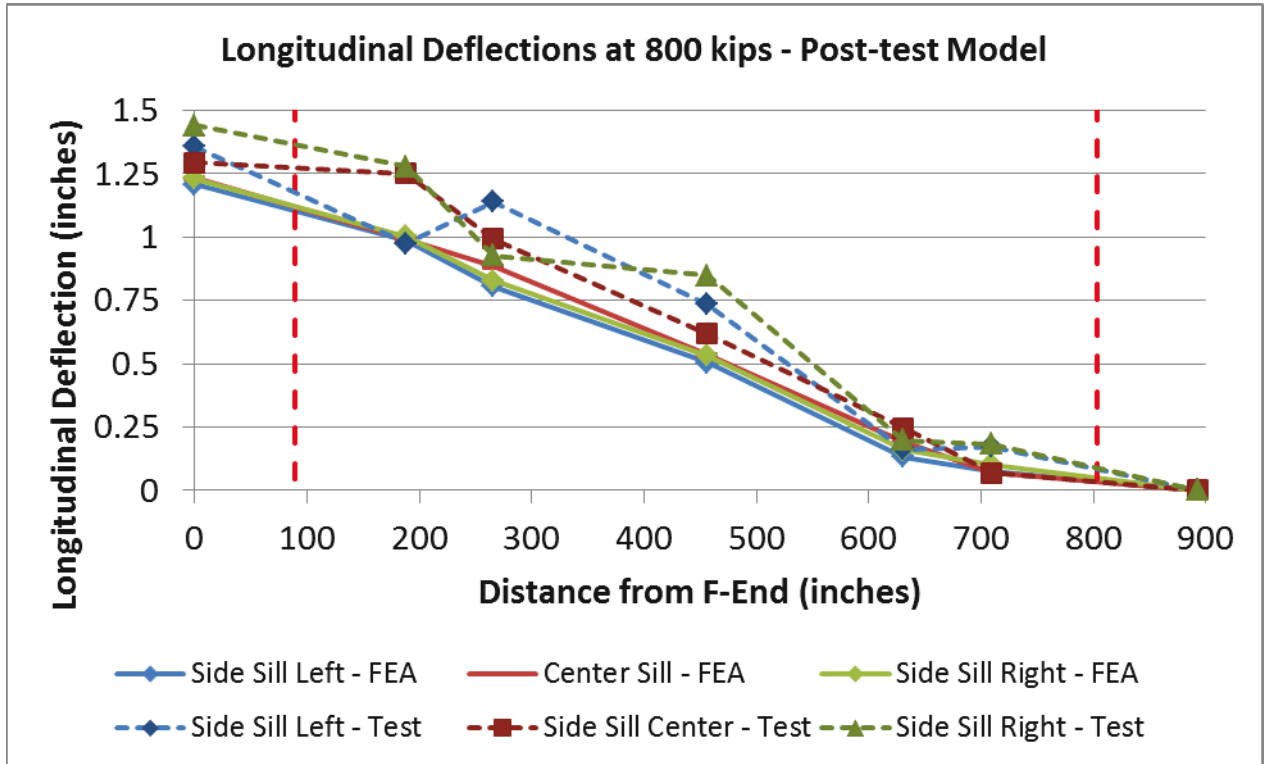
Vertical Displacement Results

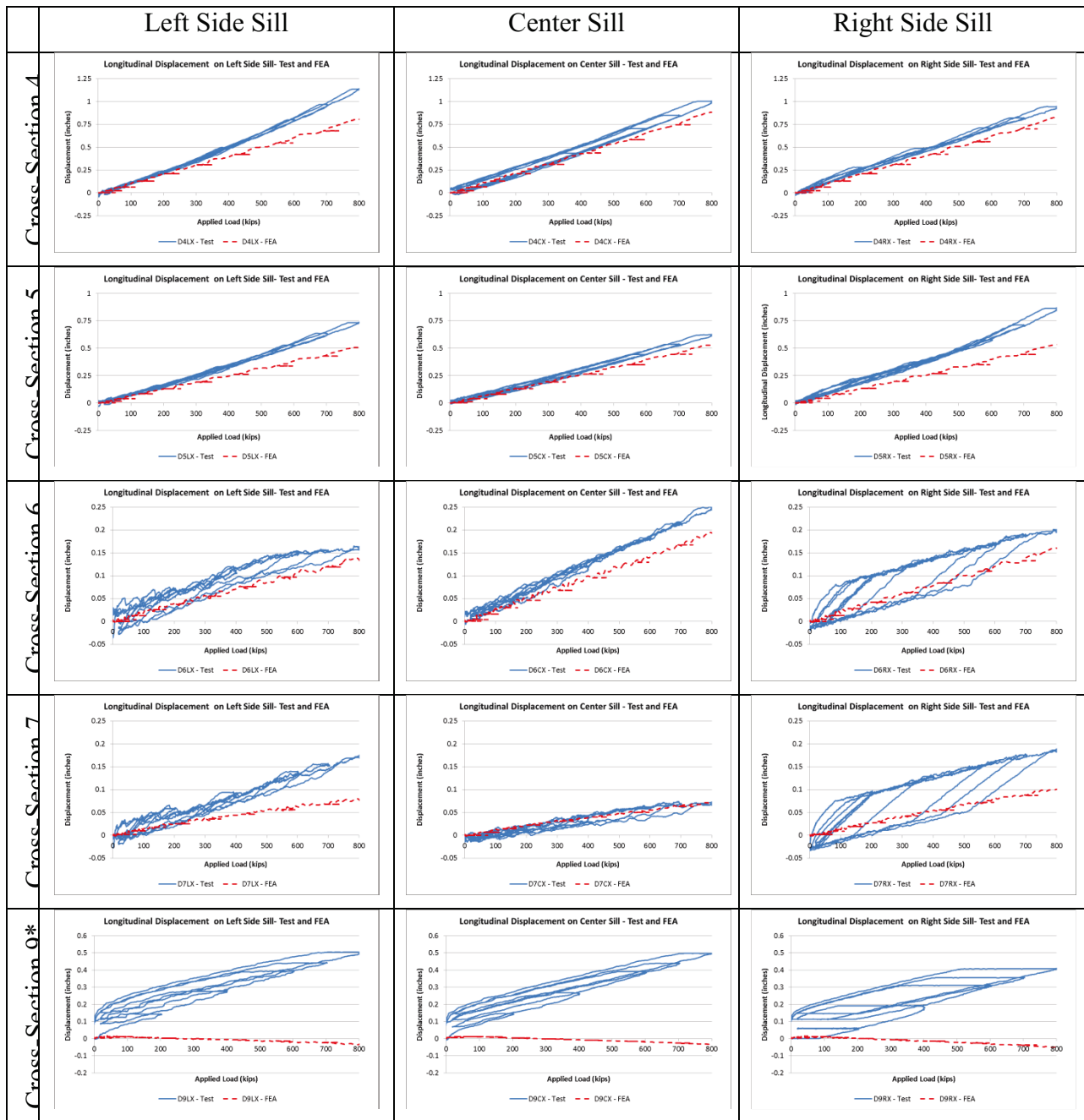




Longitudinal Displacement Results

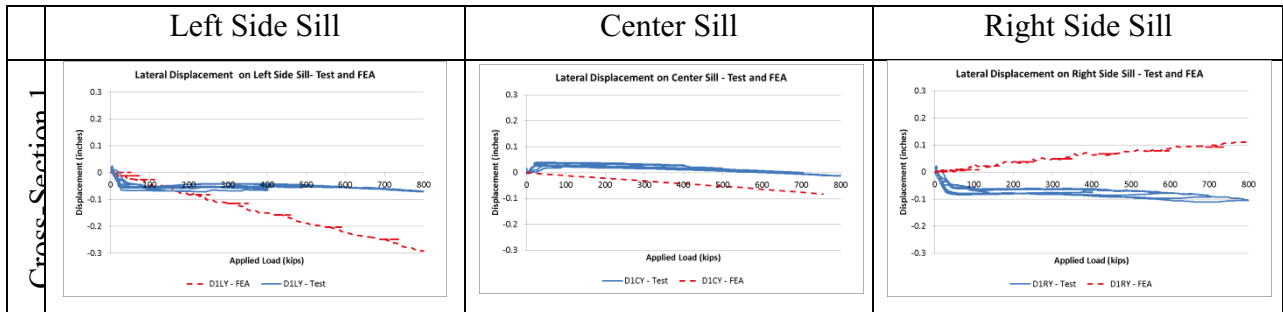
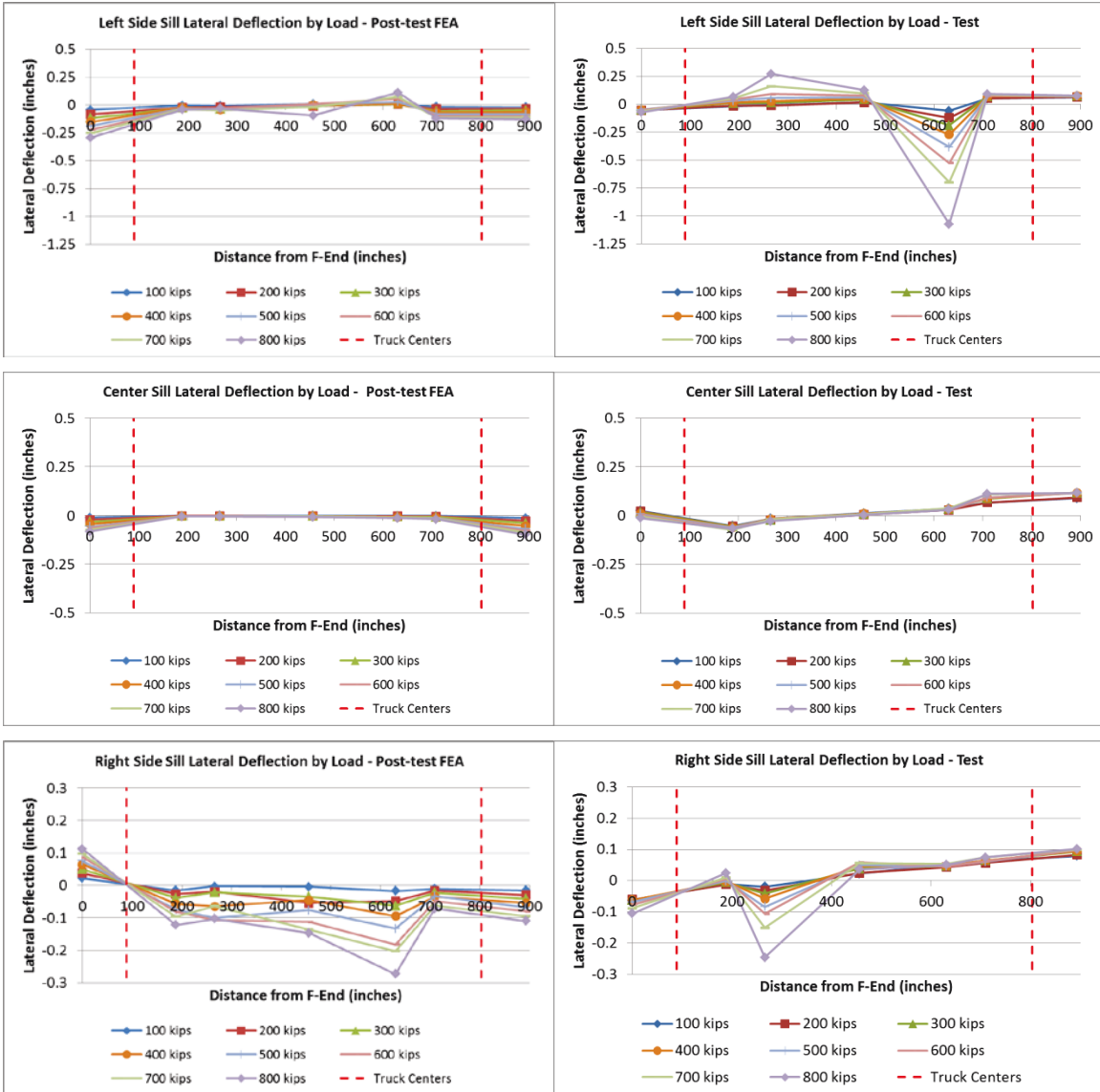
The displacement results from both the FE model and the test have been processed. Because the longitudinal displacement data from the test are comprised of both compression of the car and expansion of the frame, the longitudinal displacements at the B-end of the car have been subtracted from all other longitudinal displacement measurements. The left, center, and right side longitudinal measurements at all cross-sections have been reduced by subtracting D9LX, D9CX, and D9RX from both the test and the FEA results.

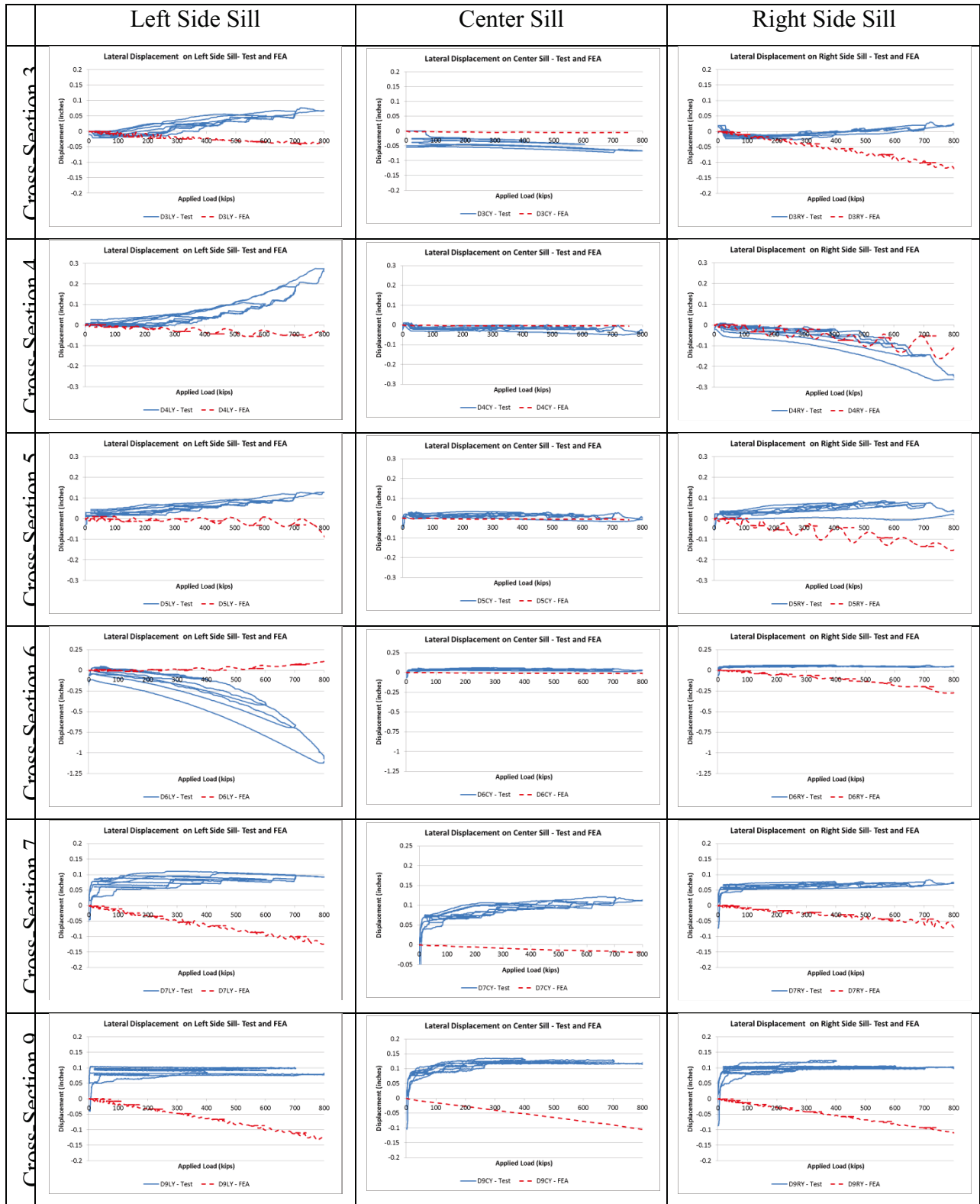




*Longitudinal data at Cross-Section 9 do not have B-end displacements subtracted, as these measurements are used as the B-end displacements.

Lateral Displacement Results





Appendix M – Analysis Verification (Volpe FE Model)

The ETF's *Criteria and Procedures* report established thresholds for determining if a slow, dynamic finite element simulation is sufficiently free from dynamic effects to be considered quasi-static. The ETF adopted two criteria for making this determination:

Condition One

For a given simulated load rate, the load at the live end of the model should be the same as the load at the fixed end. Load at the reaction end may vary by up to ± 5 percent of the load at the live end of the model for the analysis to be considered quasi-static.

Condition Two

The ratio of kinetic energy to strain energy within the structure should be small (<5 percent). The ratio of kinetic energy-to-strain energy may exceed 5 percent during the first 10 percent of the total simulation time without invalidating the analysis as quasi-static

Note that while the ETF *Criteria and Procedures* only requires demonstration using one of the above two conditions, as a part of this research program both methods were applied to Volpe's FE model. For evaluation of Condition One, Volpe's FE model experiences loads within the $\pm 5\%$ envelope for the majority of the simulated time. Over the first 20 percent of the simulation, the forces are outside of this envelope, owing to the low magnitude of the live end load and the consequently small size of the envelope. Over the majority of the loading range, the forces are in close agreement at the live end and the rear end of the model. The live and reaction end forces calculated in Volpe's FE model are shown in Figure M1.

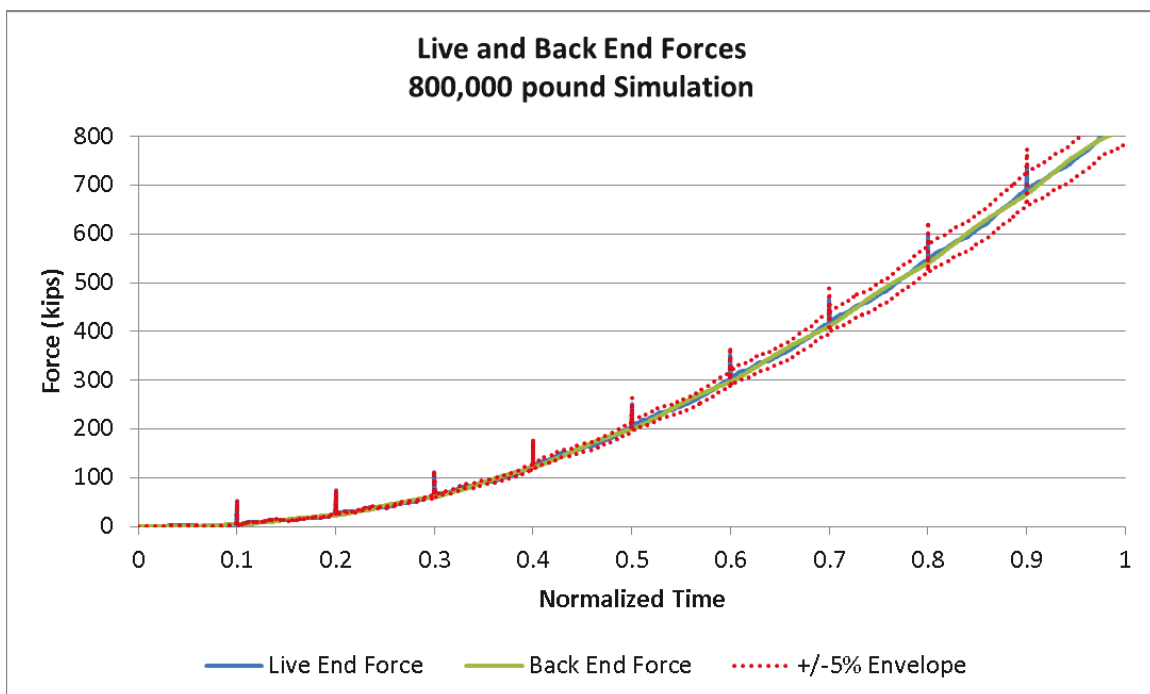


Figure M1. Live and Reaction End Forces on Volpe FE Model, 800-kip Simulation

The ratio of kinetic energy to internal energy in the Volpe FE model is plotted against normalized simulation time in Figure M2. Note that the vertical axis in this figure uses a logarithmic scale. Volpe’s FE model experiences a kinetic energy to strain energy ratio that does not drop below the 5 percent limit until approximately 20 percent of the normalized simulation time. While this takes longer than the recommended first 10 percent of the simulation time, the energy ratio has dropped well below 5 percent as the load approaches the target load of 800,000 pounds. Therefore, the initial rapid loading may be considered allowable, as the model is behaving in a quasi-static manner for the duration of the loading period.

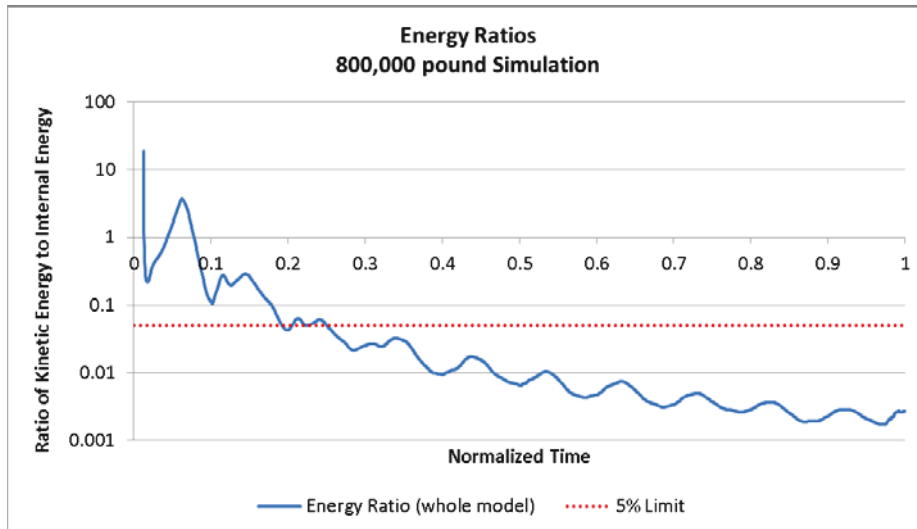


Figure M2. Energy Ratio for Volpe FE Model, 800-kip Simulation

Similar comparisons were made with the model that was used in the crippling simulation. Figure M3 displays a plot containing the live end force, the reaction end force, and a +/-5% envelope on the live end force plotted against normalized time. There is very good agreement between the live and reaction end forces throughout the simulation, and particularly at the higher loads as they approach crippling. Therefore, the simulation may be considered quasi-static using the force comparison method.

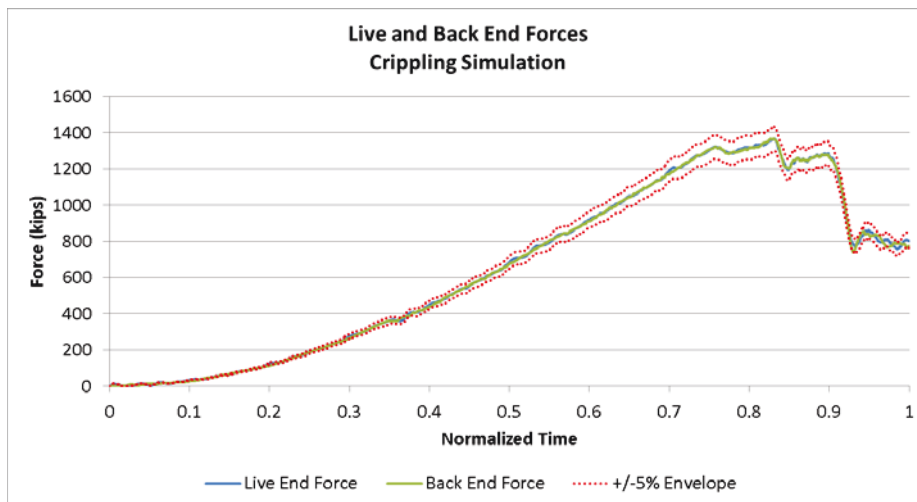


Figure M3. Live and Back End Forces on Volpe FE Model, Crippling Simulation

Figure M4 is a plot of the ratio of kinetic energy to internal energy for the whole FE model. Note that the kinetic energy in this plot will include not only the kinetic energy in the deformable carbody, but also the kinetic energy present in each of the load application plates on the F-end. The vertical axis on this plot uses a logarithmic scale, as the energy ratio spans several orders of magnitude. The energy ratio drops below the target ratio of 5 percent at a normalized time of approximately 15 percent of the total simulation time. While this slightly exceeds the ETF's target for the energy ratio to drop below 5 percent in the first 10 percent of the normalized time, the ratio remains well below the 5 percent limit throughout the duration of the simulation.

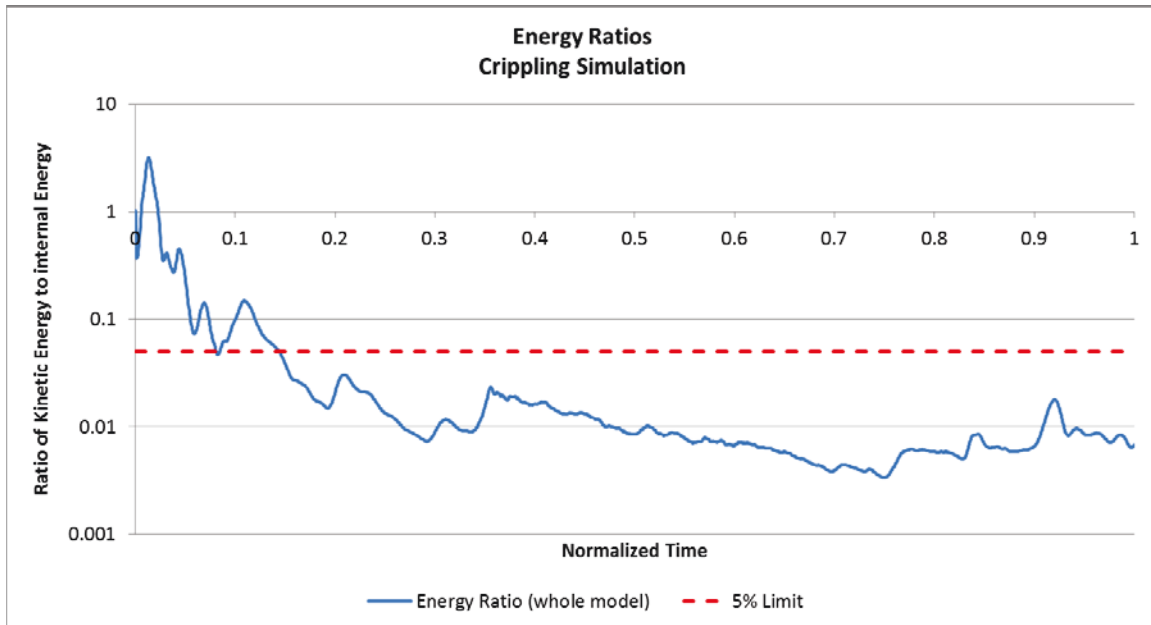
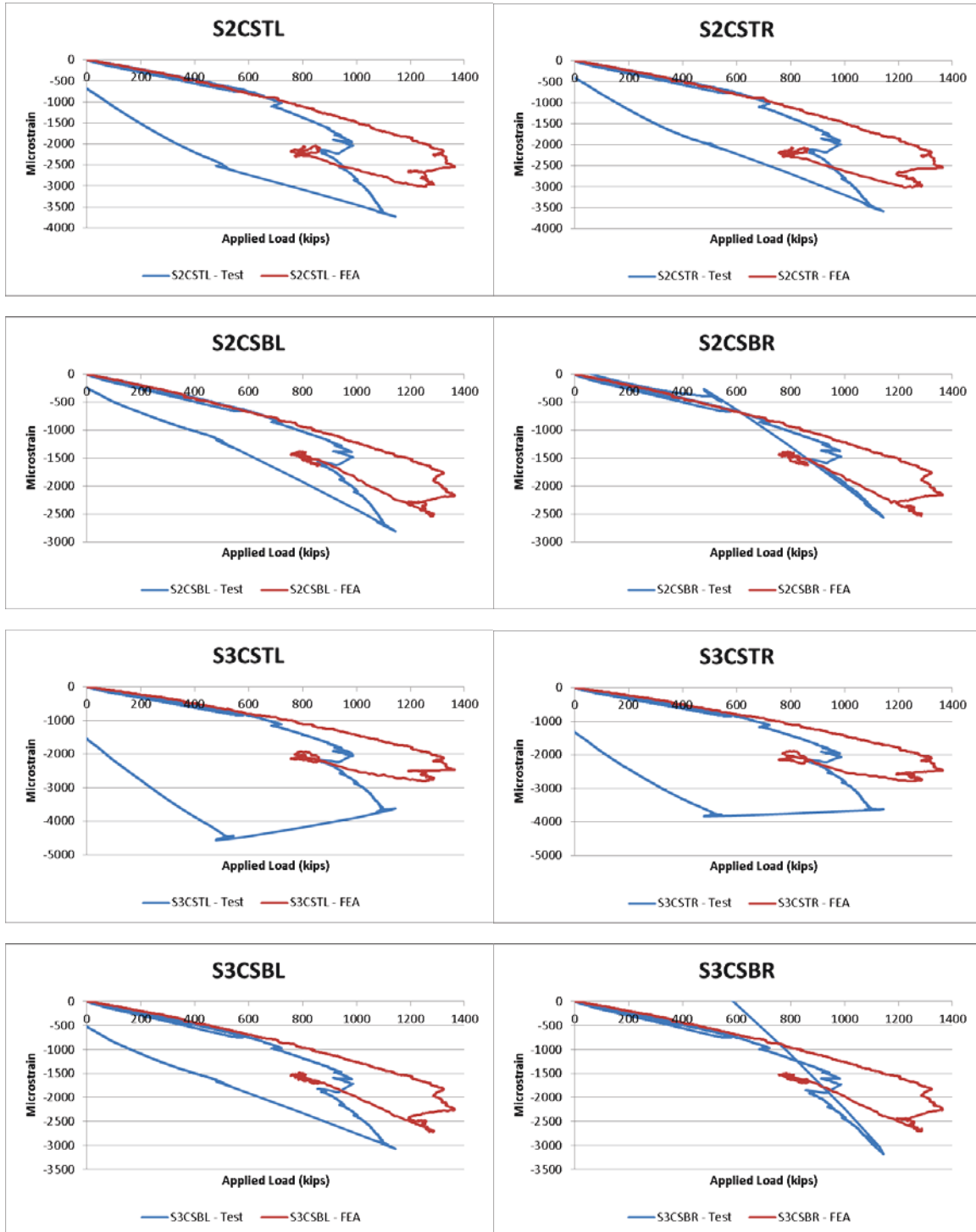


Figure M4. Energy Ratio for Volpe FE Model, Crippling Simulation

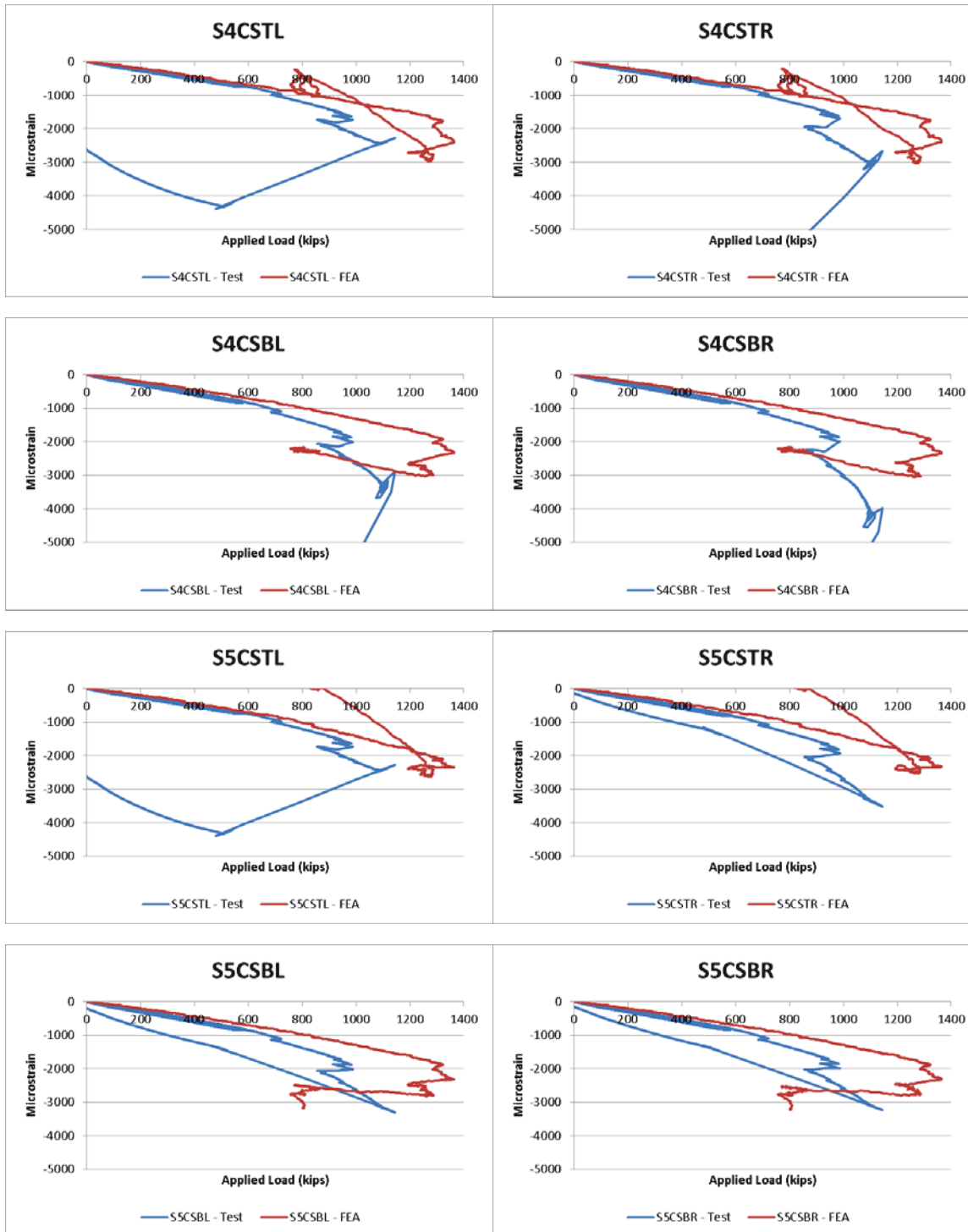
Appendix N – Crippling Load Analysis and Test Results (Volpe FE Model)

Strain Results

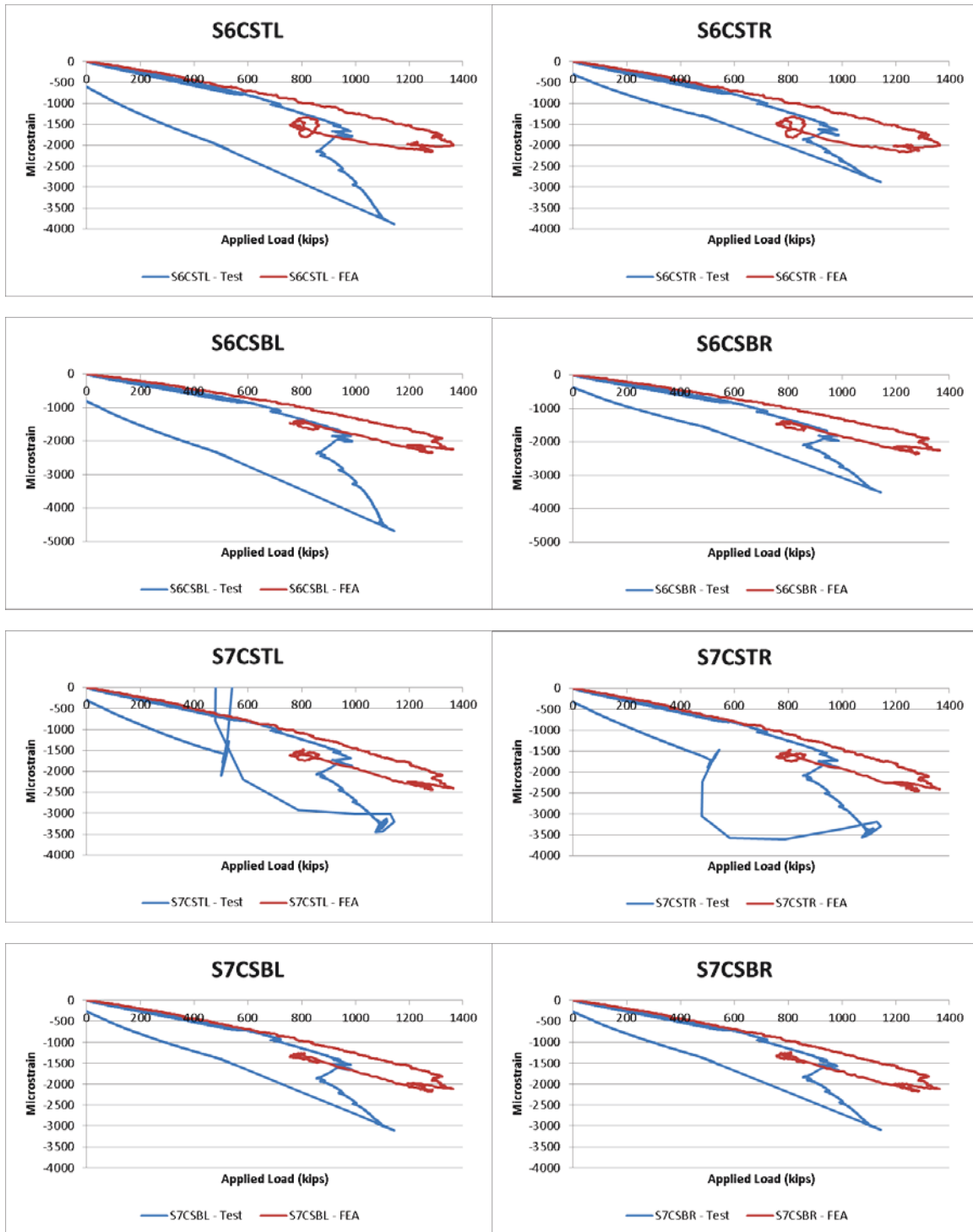
Center Sill



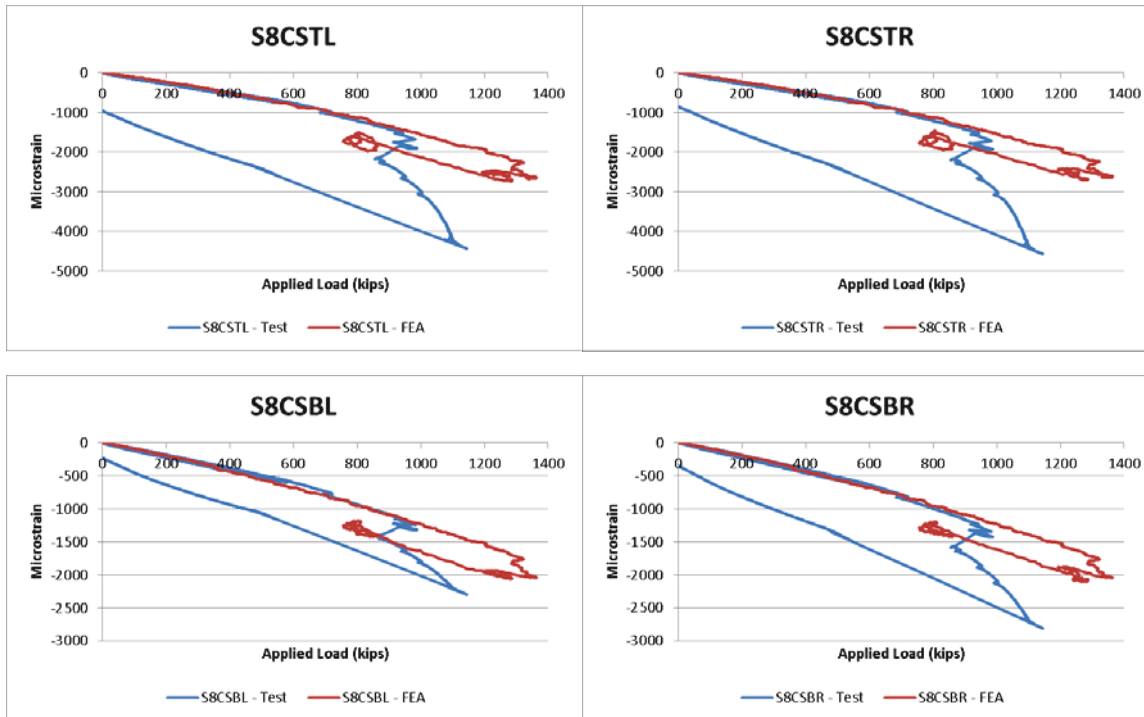
Center Sill (continued)



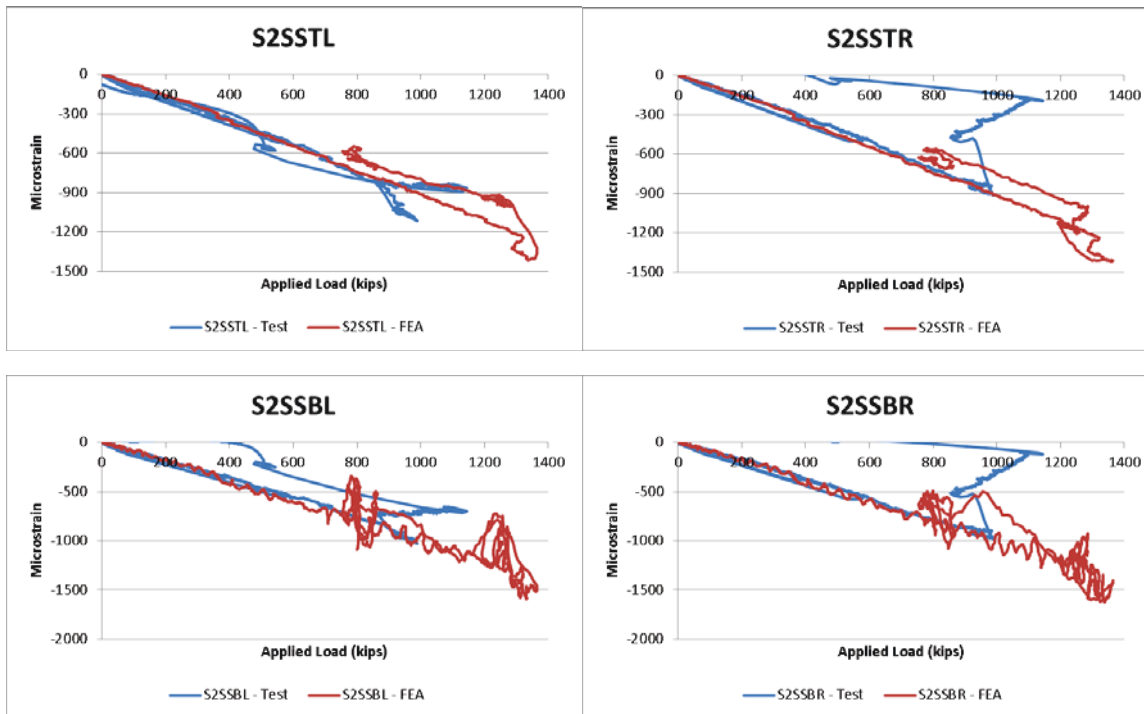
Center Sill (continued)



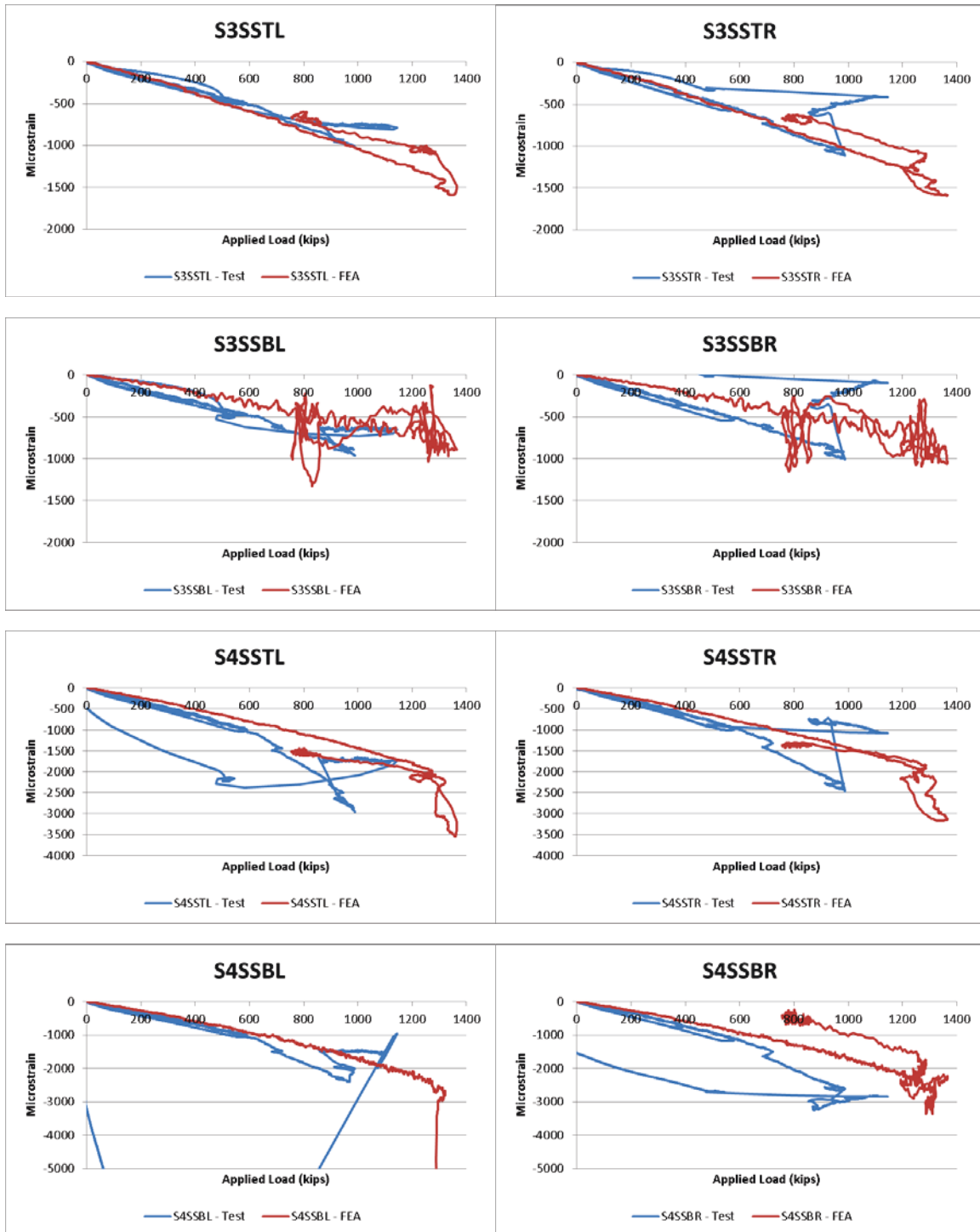
Center Sill (continued)



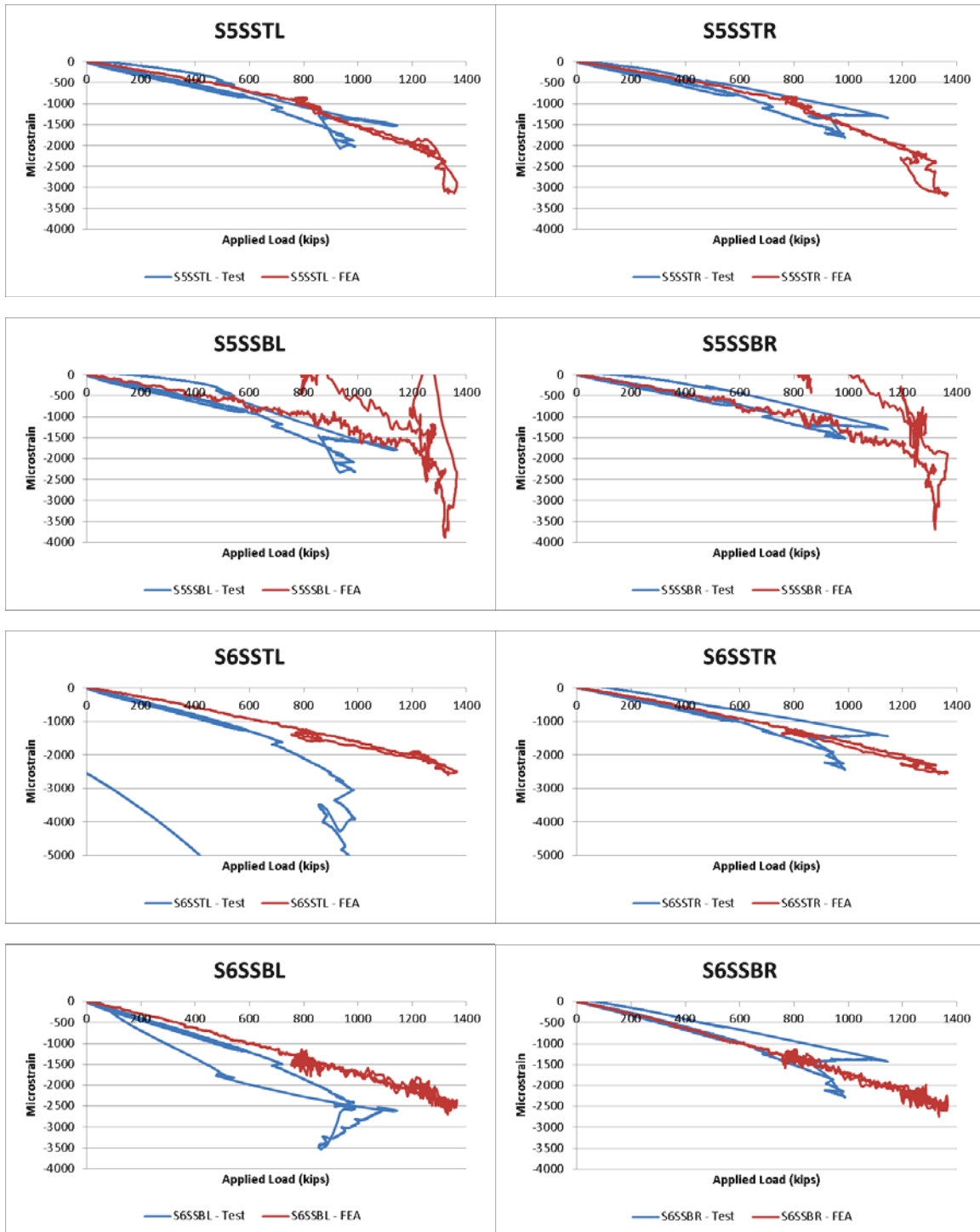
Side Sills



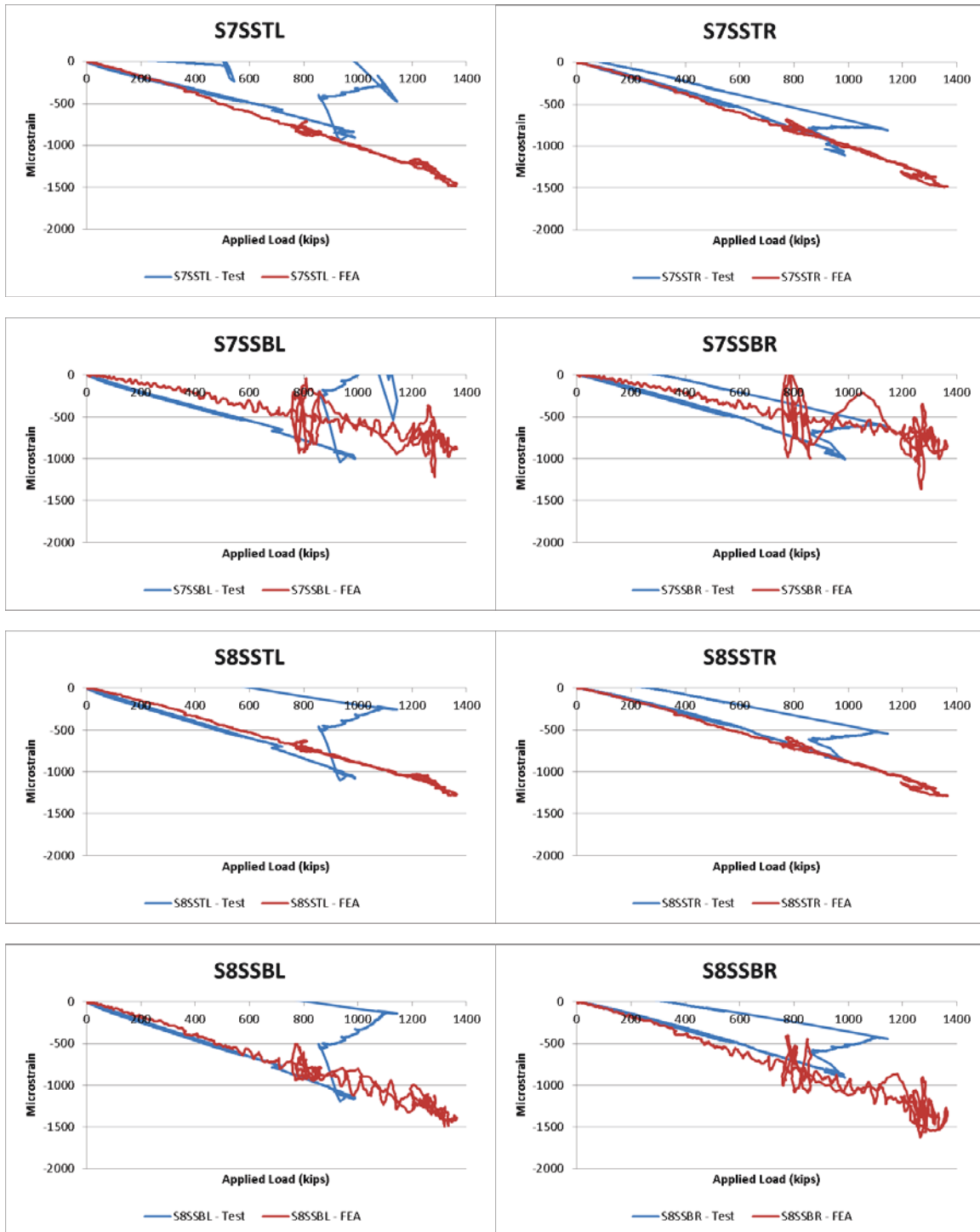
Side Sills (continued)



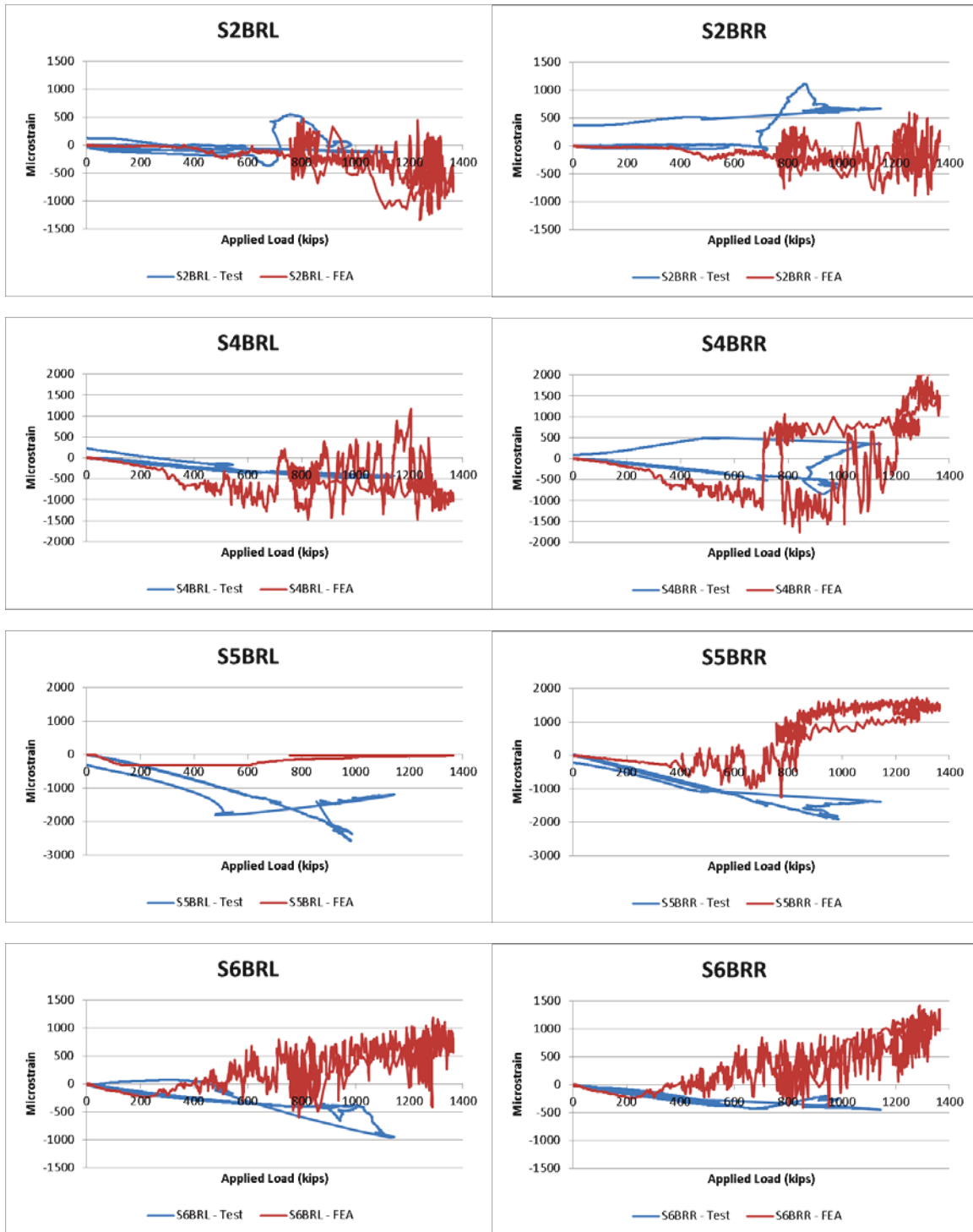
Side Sills (continued)



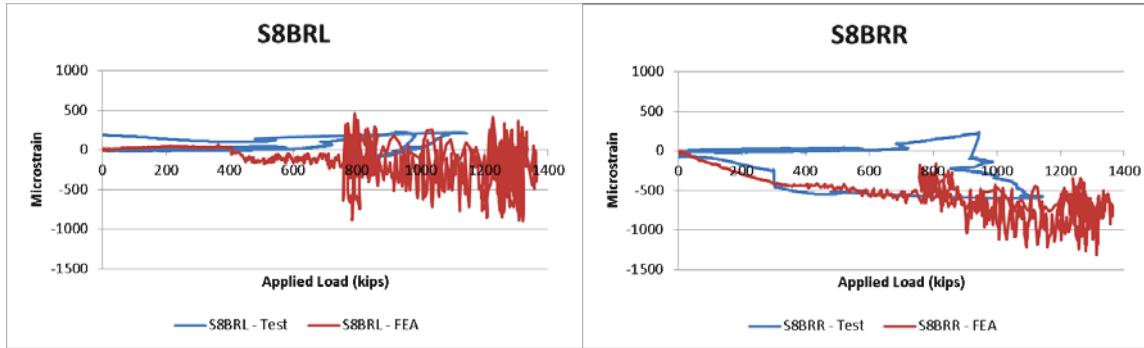
Side Sills (continued)



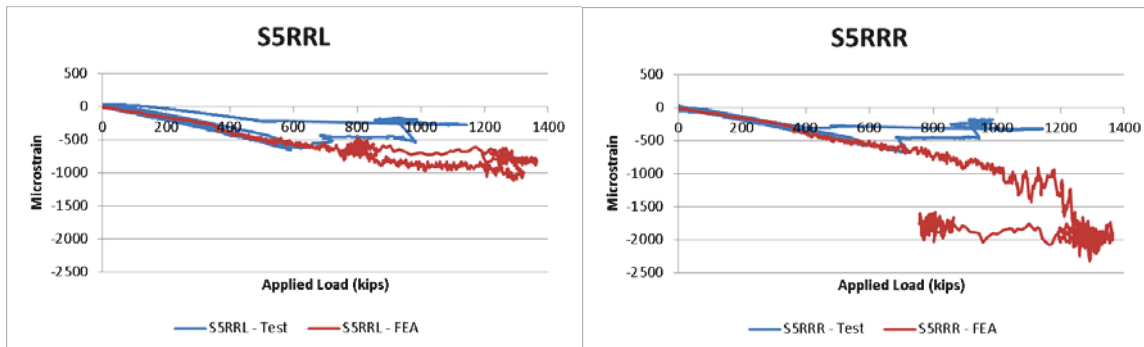
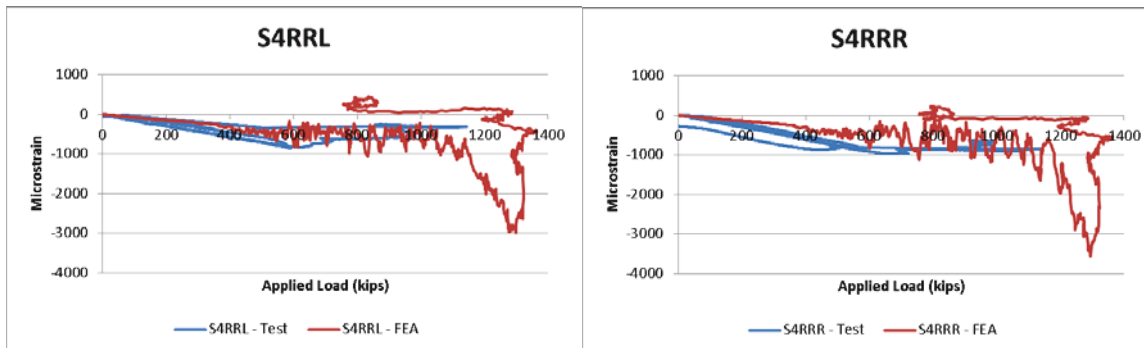
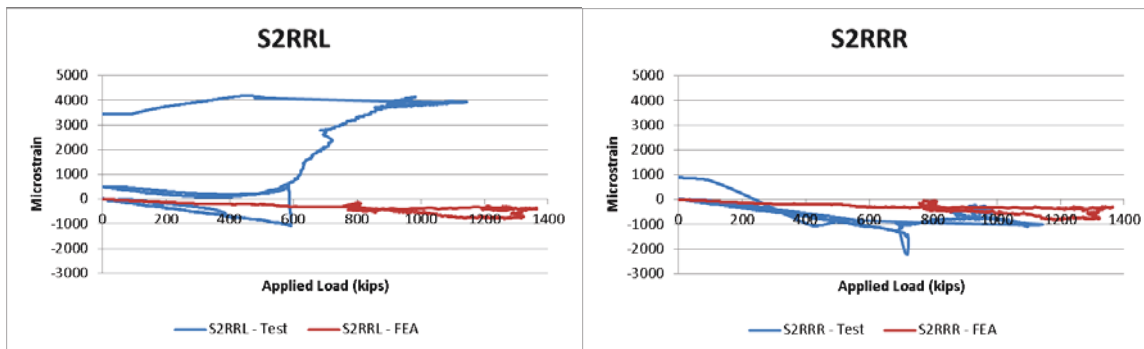
Belt Rails



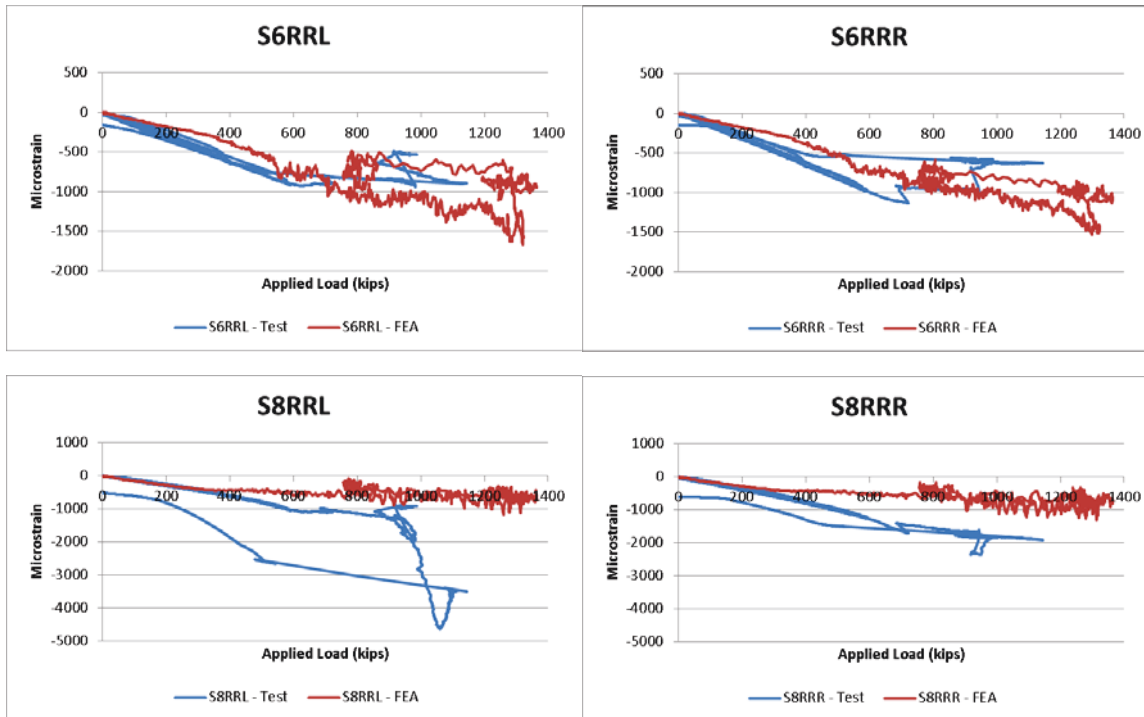
Belt Rails (continued)



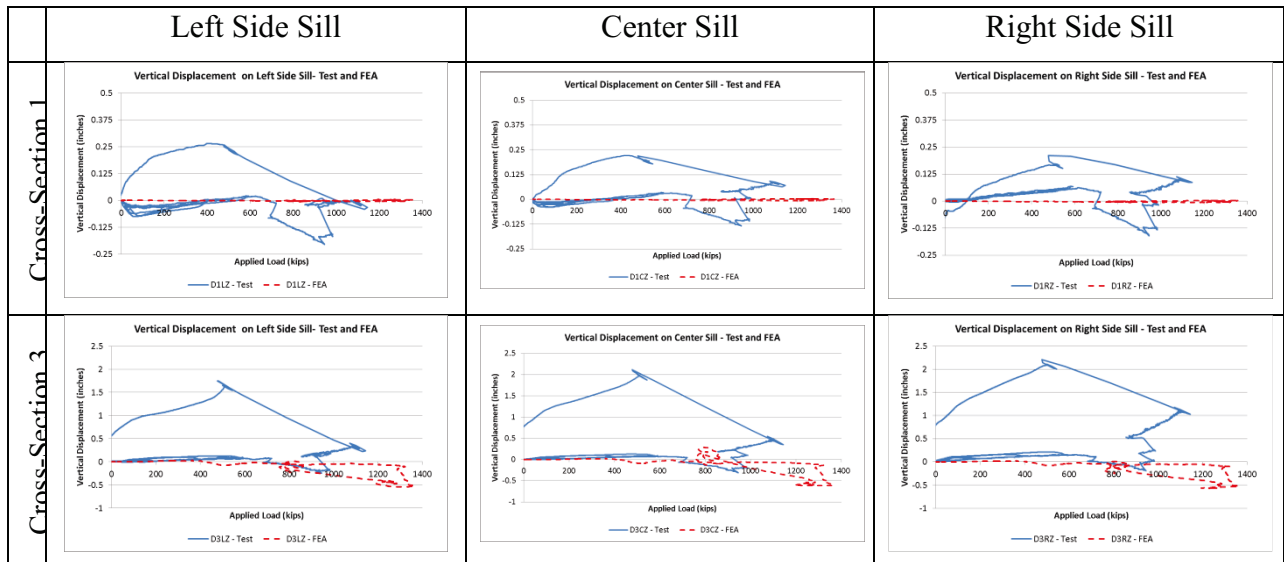
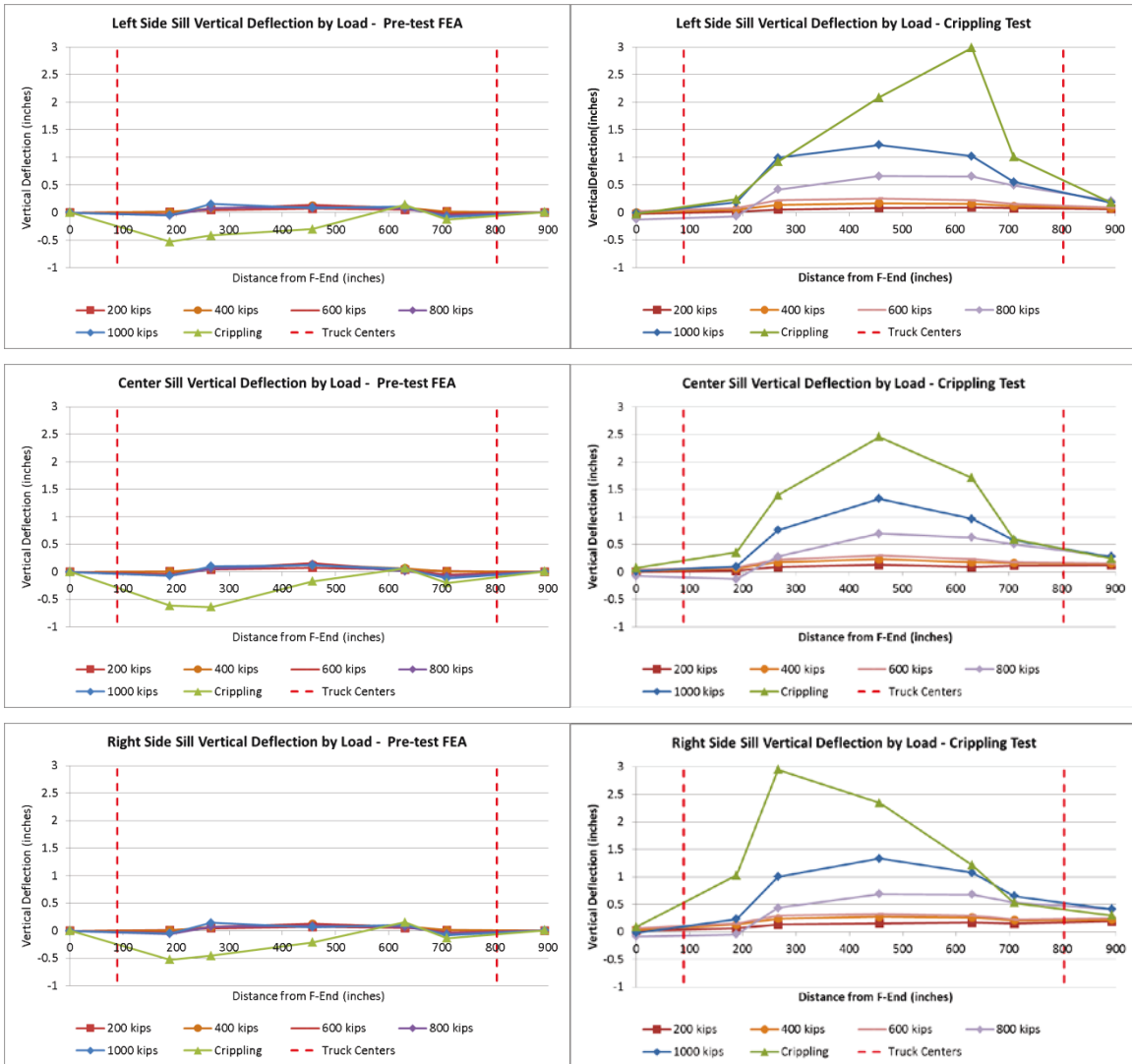
Roof Rails

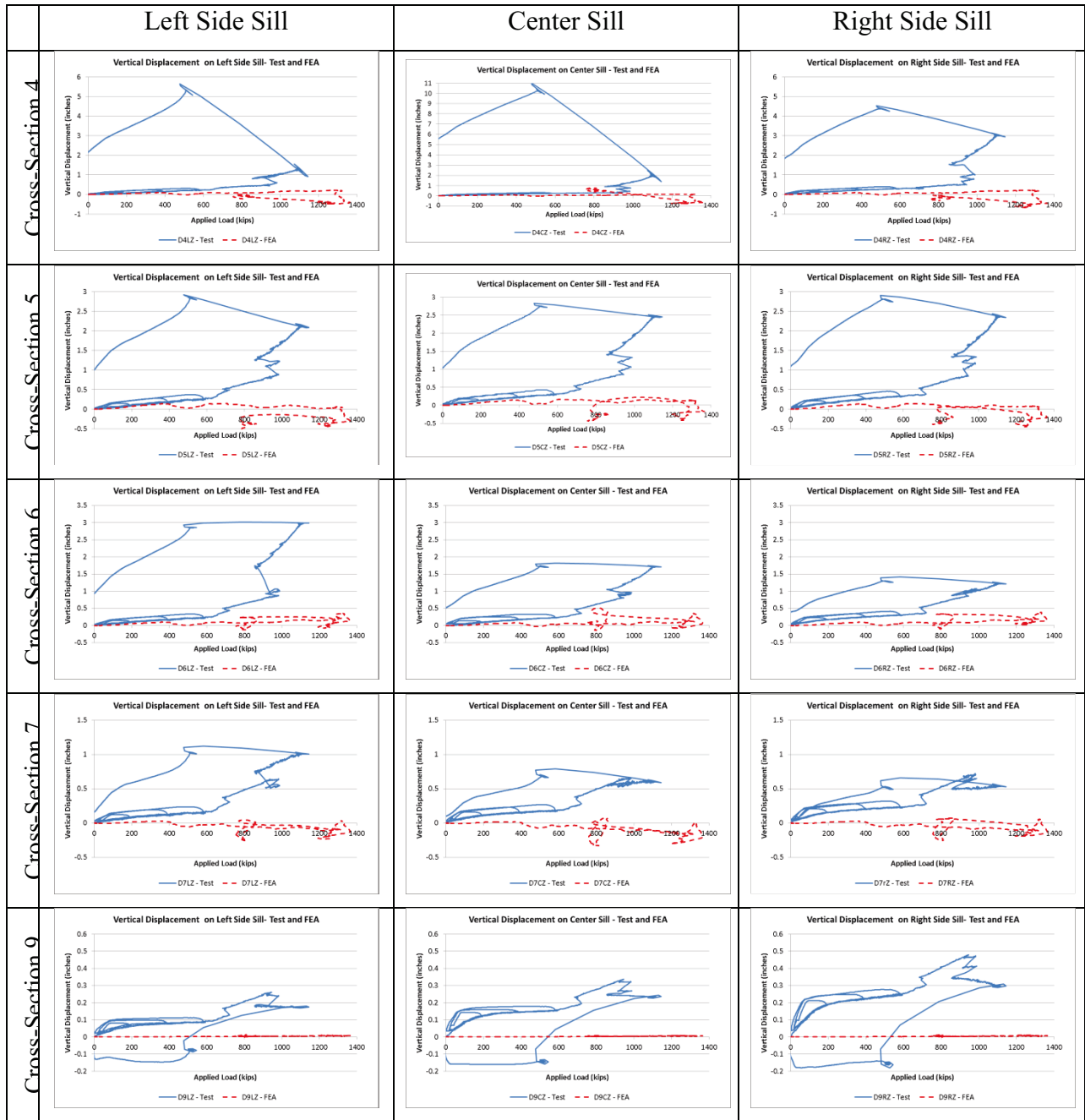


Roof Rails (continued)



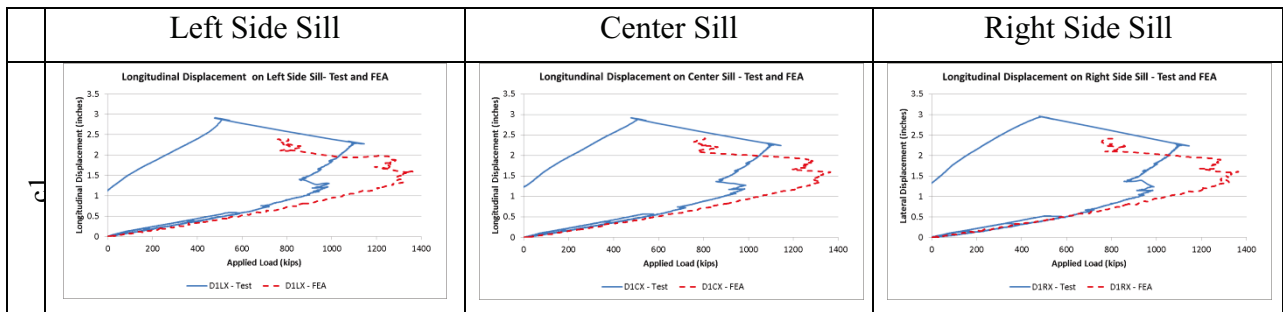
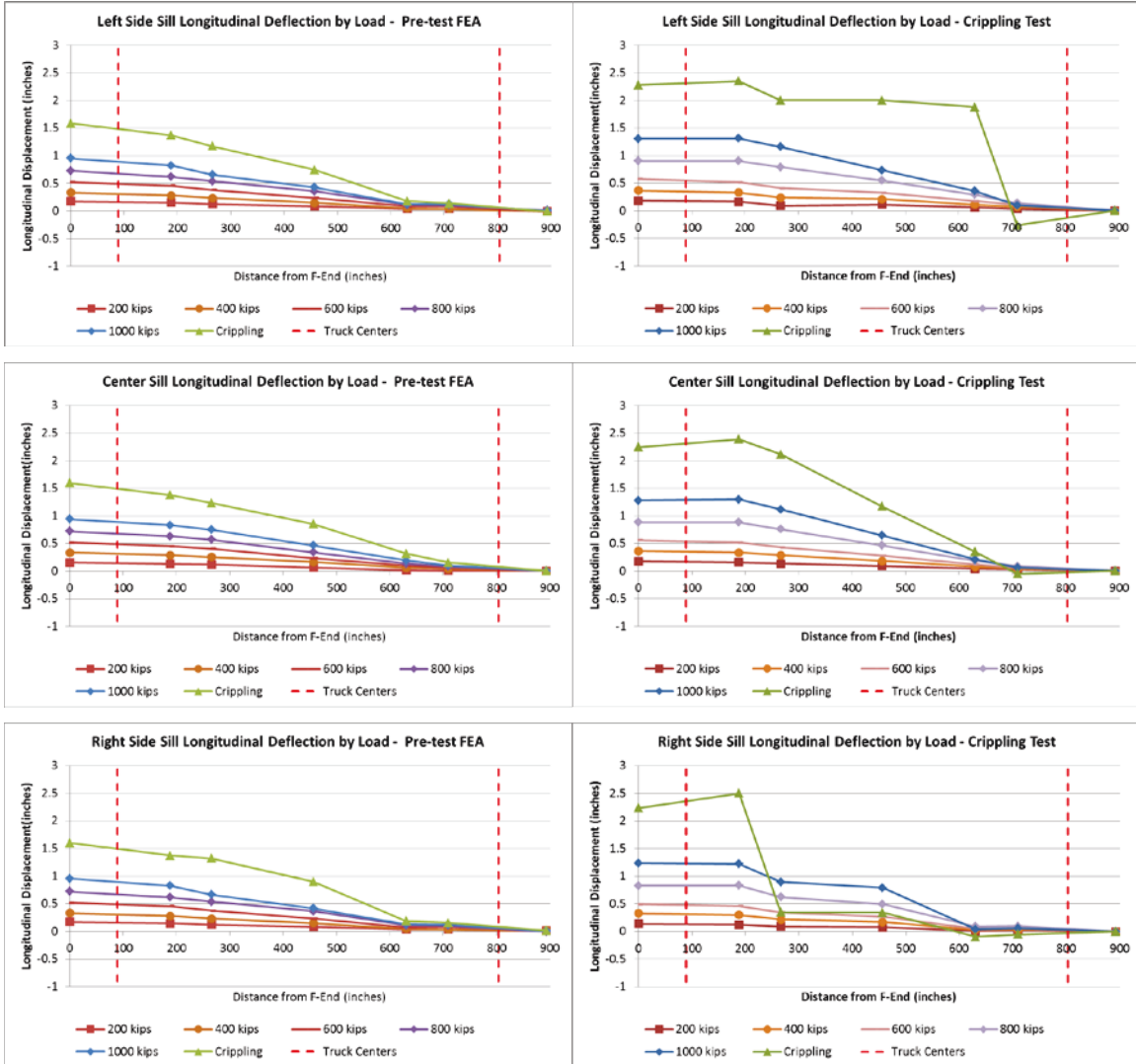
Vertical Displacement Results

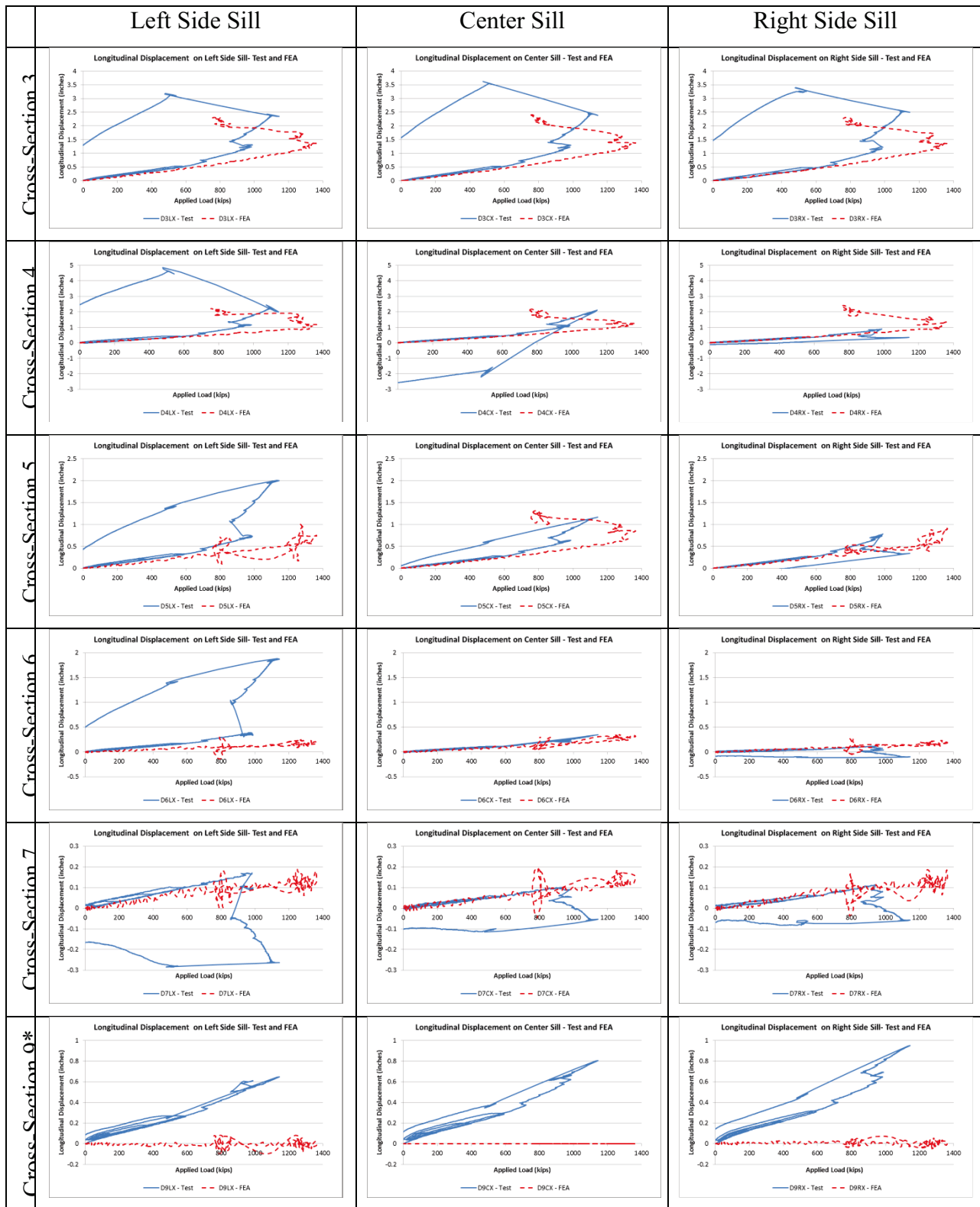




Longitudinal Displacement Results

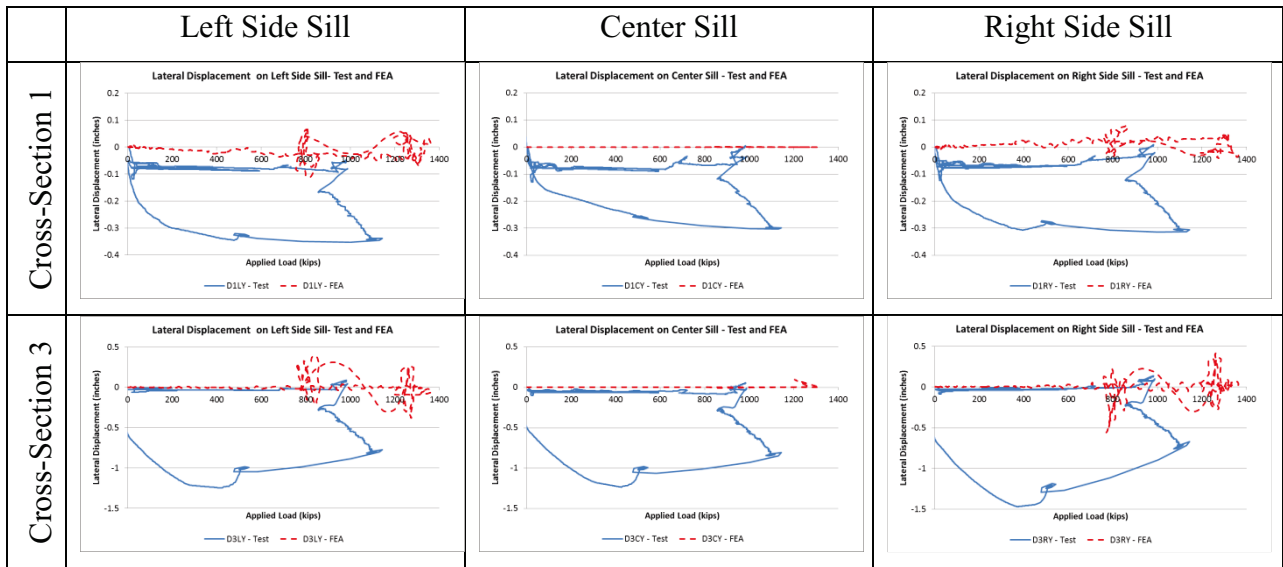
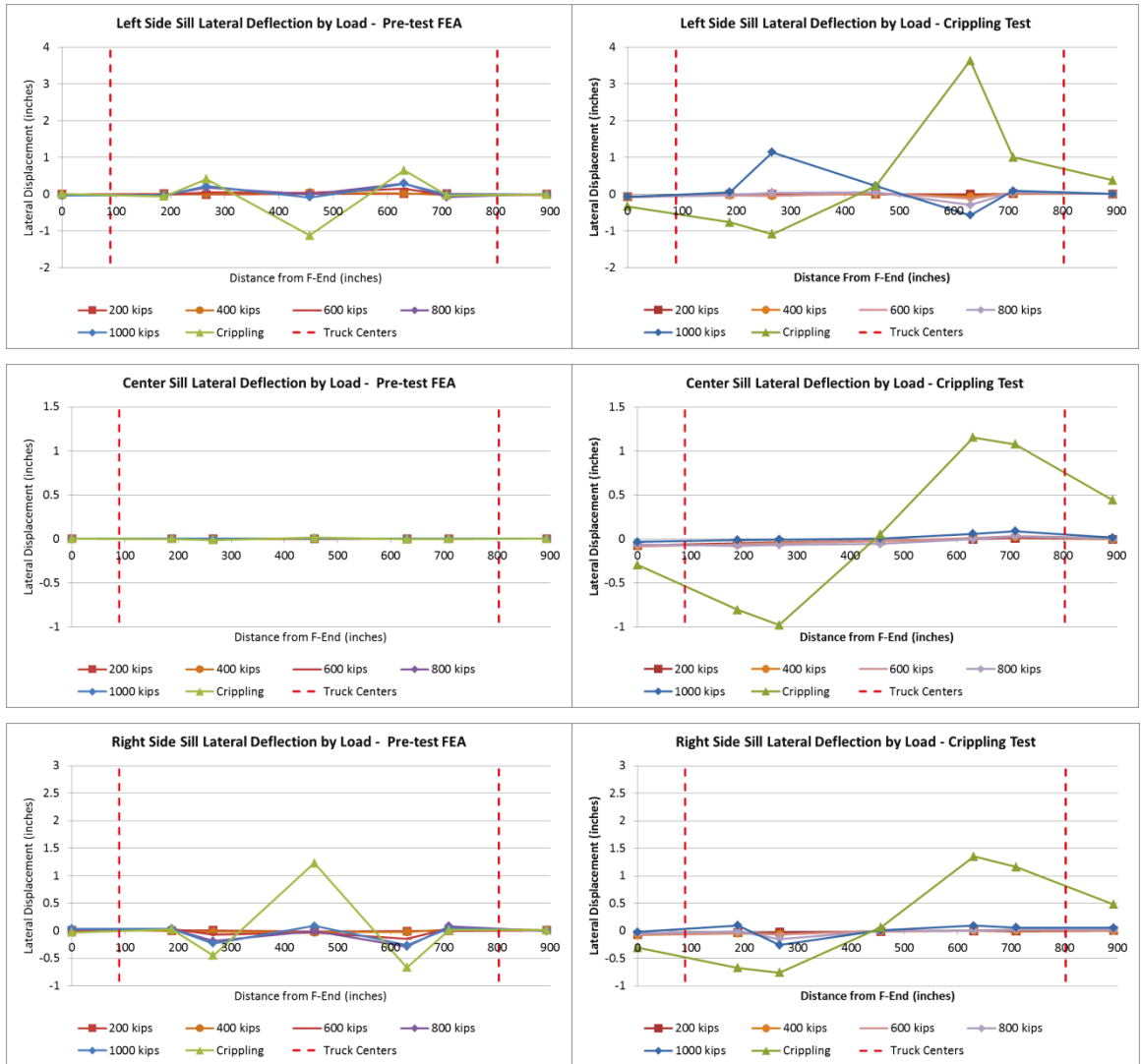
The displacement results from both the FE model and the test have been processed as follows. Because the longitudinal displacement data from the test are comprised of both compression of the car and expansion of the frame, the longitudinal displacements at the B-end of the car have been subtracted from all other longitudinal displacement measurements. The left, center, and right side longitudinal measurements at all cross-sections have been reduced by subtracting D9LX, D9CX, and D9RX, respectively, from both the test and FEA results.

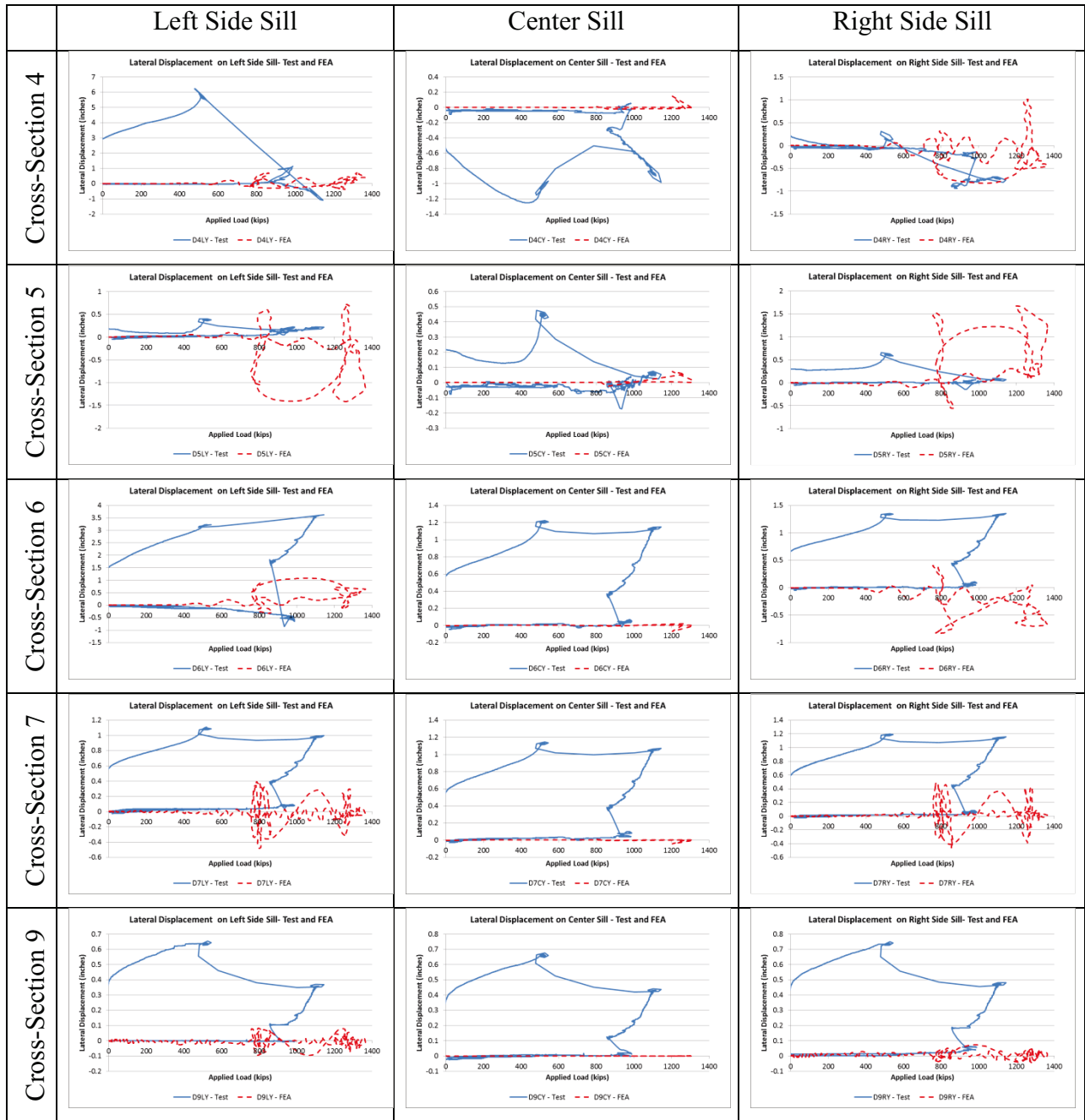




*Longitudinal data at Cross-Section 9 do not have B-end displacements subtracted, as these measurements are used as the B-end displacements.

Lateral Displacement Results





Appendix O – Discussion of Future Work

Before allowing FEA to be used in the railcar certification process, TTCI and Arup recommends that the modeling requirements should be further developed for this kind of analysis by doing the following:

- Investigation into modeling spot welds
- Investigation into the requirements for capturing post-buckling behavior in a variety of typical component types
- Preparation of a methodology requirements document, defining minimum requirements to ensure the accuracy of a FEA for predicting crippling loads

O.1 Modeling Spot Welds

Physical tests should be conducted on a range of spot welded connections that are typical in railcar construction then match the FE analyses to the results. The following items should be considered:

- Different numbers of layers in the connection
- Varying thickness of welded components, including mismatched thicknesses
- Varying sizes of spot weld
- Varying spacing of spot welds
- Loading in shear, tension and a combination

An initial literature review would be valuable, since the automotive industry has already done a substantial amount of work in this field.

O.2 Capturing Post-Buckling Behavior

The effect of mesh density, element formulation, material definition, and loading rate on the buckling behavior of channels, curved and flat corrugated panels, and other common railcar structural members should be investigated.

Initially, these tasks could be done by using FEA and should be validated by physical testing. The physical tests should be conducted on individual components and not a complete railcar.

O.3 Methodology Requirements Document

As shown in this document, minor changes in the modeling procedures of a FEA can have a significant and non-conservative impact on nonlinear crippling load predictions. Furthermore, the effects are not necessarily revealed during an elastic analysis. As such, strict requirements for setting up and validating nonlinear FEA are essential to ensure the accuracy of the results and to prevent under-strength railcars from being used in the United States.

Abbreviations and Acronyms

Arup	Arup North America Ltd
CFR	Code of Federal Regulations
CEM	crash energy management
ETF	Engineering Task Force
FE	finite element
FEA	finite element analysis
FRA	Federal Railroad Administration
LVDT	linear variable differential transformers
OVI	Occupied Volume Integrity
RSAC	Railroad Safety Advisory Committee
TTCI	Transportation Technology Center, Inc.
VLL	vertical, lateral, longitudinal
Volpe	John A. Volpe National Transportation Systems Center